Dissertation

Azobenzenes and Imines as Molecular Switches on Gold(111): Structure, Excitonic Coupling, and Photoisomerization

Daniel Brete

im Fachbereich Physik der
Freien Universität Berlin
eingereichte Dissertation
2016

This work was conducted at the Max-Born-Institut für Nichtlineare Optik und Kurzzeitspektroskopie, Berlin and at the Freie Universität Berlin in the group of Prof. Dr. Martin Weinelt.

1. Gutachter:	Prof. Dr. Martin Weinelt (Betreuer)
2. Gutachter:	Prof. Dr. Wolfgang Kuch

Tag der Disputation: 26. Februar 2016

Contents

Chapter 1

Introduction

Azobenzene derivatives, better known as azo dyes, found many applications as dyes in the past in areas as diverse as textiles, inks, and rewritable DVDs. Their attractiveness is due to the possibility to tune their properties by substitution in a wide range. Especially their optical absorption can be tuned from the ultraviolet to red. Furthermore, many azobenzenes are remarkably stable in ambient conditions. Most notably this class of dyes is very resistant to photobleaching.

More recently another property attracted the interest of the scientific community: Azobenzene exists in two configurations: *cis* and *trans* (Fig. 1.1). The isomers can be photochemically converted into each other. Thus, azobenzenes can be considered molecular switches.

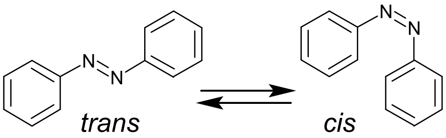

Figure 1.1: *trans* and *cis* isomers of azobenzene.

The aim of this work is to investigate the photoisomerization of azobenzene based molecular switches at a surface. Such systems could allow to change the surface properties such as polarity, chemical reactivity, or charge transfer characteristics at interfaces reversibly upon illumination with light of different colours.

Self-assembled monolayers (SAMs) are a concept to form defined monolayers on a surface. Alkanethiolate SAMs on gold are one of the most widely studied type of SAMs [1]. They form spontaneously upon the immersion of gold substrates into a solution of the thiol. The thiol head group of the SAM forming compound has a specific affinity for the gold substrate. The driving force for the chemisorption is the formation of the strong gold–sulphur bond. The thiol head group of the compound has no affinity for the tails; thus, the process comes to a halt when the surface is completely covered. This process leads to the formation of a defined monolayer. Intermolecular interactions within the layer between the tails of the molecules lead to the formation of an ordered layer.

In this work we investigate azobenzene alkanethiolate SAMs, i.e. SAMs in which the alkanethiolate is used as a linker to attach the azobenzene chromophore to the surface (Fig. 1.2). For physisorbed layers of azobenzene derivatives vapour-deposited on metal surfaces it has been shown that the photoisomerization is suppressed due to a coupling of the chromophore with the substrate [2]. In contrast, in the SAMs the alkane linker chain effectively decouples the chromophore from the surface. In addition, SAMs—unlike physisorbed azobenzenes—are stable in ambient conditions. The remarkable stability of these SAMs makes them attractive for applications and

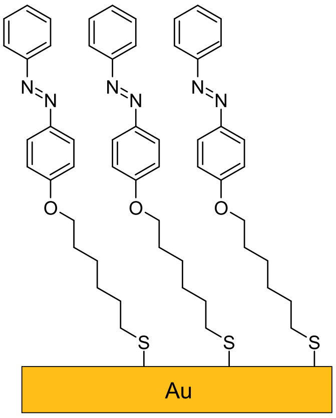

Figure 1.2: Self-assembled monolayer of an azobenzene alkanethiolate.

greatly facilitates their investigation.

To ensure the SAMs are chemically pure—a basic prerequisite for defined SAMs—we have to verify that all molecules are bound to the surface via their thiolate head-group, and no unbound thiols are left on the sample. This is especially important in the context of this work as we will show that the ordered structure in the SAM substantially influences the optical and photoisomerization properties. Therefore, residual unbound molecules must be excluded in order to obtain reliable results. X-ray photoemission spectroscopy (XPS) allows to probe the sulphur head-group and distinguish between bound and unbound sulphur. Throughout this work S2p XPS was used to ensure the quality of the SAMs investigated.

UV/vis spectroscopy allows to investigate the optical transitions that are relevant for the photoisomerization of azobenzenes and to monitor the photoisomerization process. This is a routine technique for azobenzenes in solution. SAMs, however, are produced on nontransparent gold substrates, and thus can not be investigated by transmission mode spectroscopy. Hence, azobenzene alkanethiolate SAMs have been investigated on thin semi-transparent gold substrates [3–6]. These films, however, consist of gold clusters on quartz [7, 8] unlike the single-crystal-like substrates required to obtain well ordered SAMs. In the cause of this work, it turned out that the optical properties, and especially the photoisomerization behaviour, of SAMs on transparent cluster films may differ substantially from those of SAMs on defined Au(111) surfaces [9, 10].

In order to investigate the optical properties of SAMs on nontransparent Au(111) surfaces differential-reflectance (DR) spectroscopy was used. In DR spectroscopy the change in reflectance of the substrate caused by the adsorbate is obtained from measurements of the substrate with and without adsorbate. DR spectroscopy of SAMs is a demanding experiment. The difference in reflectance caused by the SAM is only of the order of $1 \cdot 10^{-2}$, and the changes to be monitored during the photoisomerization are even smaller. This is small compared to the reflectivity of gold, therefore, a spectrometer with a large dynamic range is required. DR spectroscopy so far has primarily been used for epitaxial multilayer films [11, 12]. Conventionally DR spectroscopy is conducted with near-normal incidence and unpolarized light. So far azobenzene alkanethiolate SAMs have only been studied under these conditions [13–15]. In these SAMs the transition dipole moments (TDMs) of the main absorption bands are oriented nearly normal to the surface, and thus are hardly visible in near-normal incidence. Therefore, we designed a reflectance unit, which allows to measure DR spectra with polarized light and an angle of incidence of 45°. In conjunction with a high-performance UV/vis spectrometer we obtained spectra with a significantly increased signal-to-noise ratio compared to previous works.

Absorbance spectra in solution generally can be understood as spectra of individual molecules. In crystals or adsorbate layers, however, we observe spectra of an ensemble. The wavelength of the light is much longer than the intermolecular distances. Therefore, we have to consider an ensemble of indistinguishable particles that is collectively excited. In the molecular exciton model developed by Davydov [16, 17] and Kasha and coworkers [18–20] it is assumed that, while the molecular orbitals of the individual molecules do not overlap, the states of the individual molecules are coupled via Coulomb interactions. Thus, the energies of the excited states of the ensemble differ from those of the individual molecule. The resulting excitonic bands can be derived from the TDMs of the individual molecules. The absorbance energies of the excitonic bands and the selection rules for their excitation depend on the relative orientations of the TDMs of the individual molecules. For the SAMs investigated in this work we observed pronounced excitonic coupling. For the molecules forming these SAMs the orientations of the TDMs with respect to the individual chromophores are known from DFT calculations. In order to obtain the relative orientations of these TDMs in the SAM, a structural model of the molecules on the surface is needed. Near-edge X-ray fine-structure (NEXAFS) spectroscopy is a well established technique to determine the orientation of the chromophore with respect to the surface. In combination with the unit cell known from AFM experiments reported in the literature such a structural model can be constructed.

For single component azobenzene alkanethiolate SAMs we observed no photoisomerization, even though they are sufficiently decoupled from the surface. The failure of azobenzene SAMs to isomerize has been attributed to steric hindrance [6]. In how far the excitonic coupling contributes to this effect is discussed in detail in 5.2.5. However, both effects should be reduced by increasing the intermolecular distance. One approach to increase the distance are mixed SAMs in which the chromophore-carrying alkanethiolates are diluted by unsubstituted alkanethiolates acting as spacer molecules. One method to produce mixed SAMs is coadsorption from solutions of a mixture of two thiols. The composition of such mixed SAMs depends on the different interactions between the two pairs of like molecules and between unlike molecules. Generally preferential adsorption of one species is observed. This preferential adsorption often is so strong that layers produced from mixed solutions solely consist of one of the two components. Thus, in order to achieve mixing on the surface, the interactions between unlike and the two kinds of like molecules need to be of the same magnitude. Hence, mixing of very similar molecules provides a high chance of success. In a first mixing experiment two azobenzene alkanethiols, which differ only by a substituent on the chromophore, were employed. DR spectra of these mixed SAMs, comprising two chromophores with slightly differing absorption energies, allows to study the excitonic coupling in a two-component SAM. Furthermore, the contribution of inter- and intramolecular effects to chemical shifts in XP spectra can be studied in these SAMs. In a second mixing experiment the diluted chromophore SAMs, proposed above, comprising azobenzene alkanethiolates with a long (C11) alkyl chain and an unsubstituted alkanethiolate as spacer were investigated. Here the alkyl chains ensure similar interactions between like and unlike molecules. For both types of mixed SAMs quantitative XPS allows to investigate the composition of the SAMs as a function of the ratio of the two components in solution. We will present a thermodynamic model describing this relation. In both cases preferential adsorption of one component was observed.

In prior works investigating SAMs of diluted azobenzene chromophores these

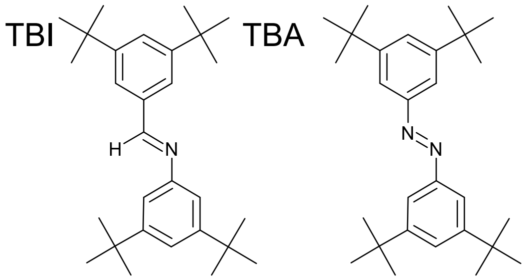

Figure 1.3: Structural formulas of TBI ((*E*)-3,5-di-*tert*-butyl-N-(3,5-di-*tert*-butyl-benzylidene)aniline) and TBA (*E*-3,3',5,5'-tetra-*tert*-butyl-azobenzene)

were prepared from asymmetric disulphides comprising the chromophore and the spacer chain to ensure both components are delivered to the surface [14, 15, 21]. Similar SAMs were produced by coadsorption of chromophore and spacer [24–26]. In contrast to SAMs from disulphides, where a fixed 1:1 ratio between chromophore and spacer is obtained, the coadsorption method also used in this work allows to produce mixed chromophore SAMs with arbitrary composition. In contrast to the works cited above we determined the composition of the SAMs and the orientation of the chromophores. In the diluted chromophore SAMs we investigated the influence of the dilution on the molecular orientation, excitonic coupling, and photoisomerization behaviour. Already for a minor dilution we could, indeed, demonstrate efficient photoisomerization upon illumination with UV light. Unlike in solution the reverse process induced by blue light is almost complete. We suggest a cooperative mechanism to explain this observation.

So far we have discussed chemisorbed azobenzene SAMs, which are decoupled from the surface by a linker chain. TBA (Fig. 1.3) physisorbed on gold is a system where the azobenzene chromophore is partially decoupled from the surface by *tert*-butyl substituents. In the cause of this work (but not part of this thesis), we could demonstrate that TBA undergoes photoisomerization on the surface [27, 28].

Aromatic imines are compounds similar to azobenzenes. The imine group (-CH=N-) is isoelectrical to the diazo group (-N=N-). TBI (Fig. 1.3) is the imine analogue to the azobenzene derivative TBA. To our surprise physisorbed on gold TBI forms two different stable monolayers: an all-*cis* and an all-*trans* layer. We employed thermal desorption spectroscopy (TDS) to monitor the temperature and coverage dependent isomerization in TBI layers. The conformation and adsorption geometry in the layers were investigated by NEXAFS spectroscopy. Thermal isomerization of TBI is enabled by the lower *trans*-*cis* isomerization barrier in imines compared to azobenzenes. We show that the conformational transitions are driven by the higher packing density of the less stable *cis* isomer and the higher adsorption energy of the *trans* isomer. The isomerization into the *cis* isomer as a response to the higher packing density can not be understood on the level of single molecules interacting with the substrate, but is an ensemble effect.

Content of this Work This work is organized as follows: In Chap. 2 the molecular structure, UV/vis spectra, electronic structure, and photoisomerization behaviour of azobenzene derivatives in solution are summarized. Chapter 3 contains a short overview of the properties of SAMs. In particular the use of XP spectroscopy as a means to investigate the chemical purity of these layers will be discussed. In Chap. 4 the experimental methods used in this work are described. XPS and NEXAFS are described with a focus on the practical analysis of spectra. TDS and DRS are briefly introduced. In Chap. 5 results on azobenzene thiolate SAMs are presented. We start with a discussion on single component SAMs, before we come to the two-component systems including the photoisomerizable mixed chromophore SAM. The chapter contains a general introduction into the research on azobenzene SAMs, introductory sections describing the different single- and two-component SAMs, and further references. In Chap. 6 the temperature and coverage dependent isomerization of the imine TBI is presented. A Chapter on methods an materials (Chap. 7) gives details on the sample preparation and experimental conditions. In the cause of this work, an evaporator for organic molecules was developed. The design and characterisation are detailed in Appendix A.

Chapter 2

Azobenzene Derivatives

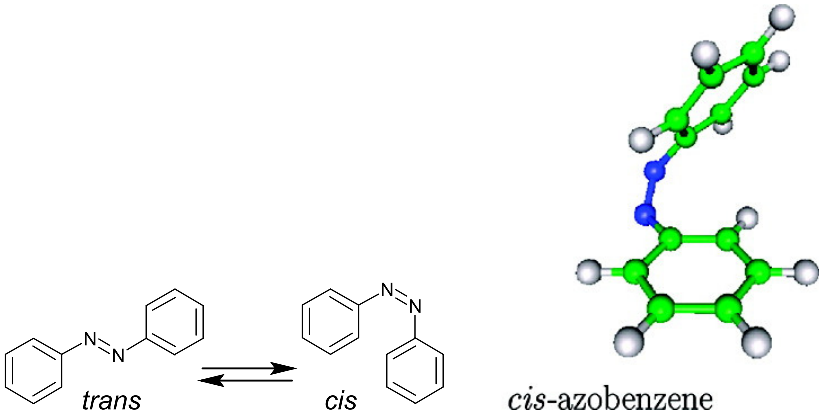

Figure 2.1: *trans* and *cis* forms of azobenzene. Image of 3D structure from [29].

Molecular Structure Azobenzene exists in two conformers: The thermodynamically stable *trans* (E) form and the metastable *cis* (Z) form (Fig. 2.1). *trans*-Azobenzene is planar in the crystalline phase and in the gas phase. In solution generally a planar conformation is assumed. However, in polar solvents a twisted conformation might be preferred [30].

Sterically a flat conformation is not possible for *cis*-azobenzene; thus the two phenyl rings must be twisted with respect to each other. An NNCC dihedral angle, that is the twist angle of the phenyl rings around their C-N bond, of 56° was obtained by X-ray diffraction for crystalline cis-azobenzene [31]. Similar angles were obtained by calculations of the free molecule [32].

UV/vis Spectra in Solution and Electronic Structure Figure 2.2 shows the frontier orbitals of *trans*-azobenzene. The HOMO mainly consists of the nitrogen lone pairs and is nonbonding. The HOMO-1 and the LUMO are of π and $\pi^\star$ type [34].

In the discussion of the UV-spectra and the photoisomerization in solution we do not use spectra of unsubstituted azobenzene itself but of the derivative H-Az6 (structure Fig. 2.5), one of the compounds investigated in this work. Figure 2.3 shows UV/vis spectra of the two isomers in solution.

Azobenzenes have three bands of accessible singlet states in the UV/vis region. These can be assigned to the following transitions [34, 35]: The most intense absorp-

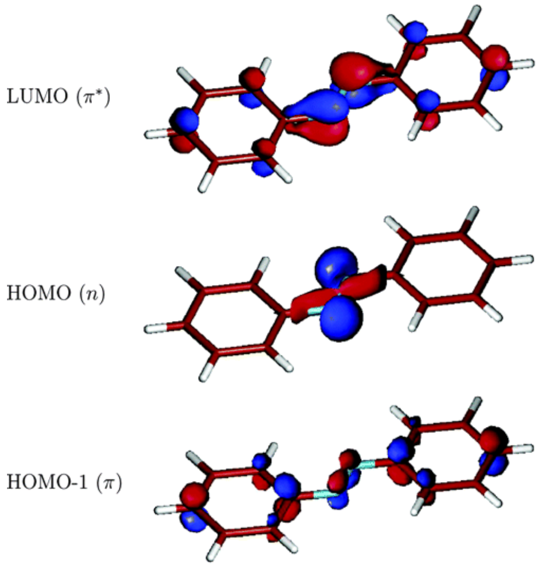

Figure 2.2: Frontier orbitals of *trans*-azobenzene. Image from [33].

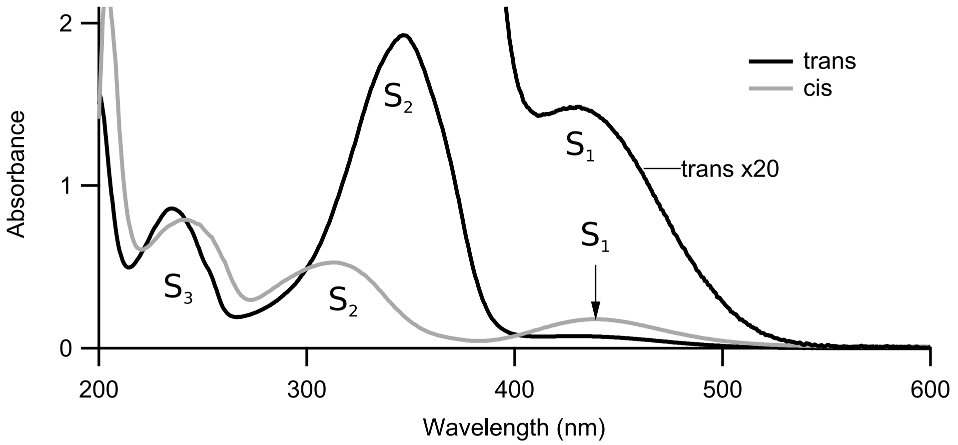

Figure 2.3: Absorbance spectra of the *cis* and *trans*-form of H-Az6 in ethanol. Modified image from the author's *Diplomarbeit* [8].

tion is the S_2 transition which is assigned to a HOMO-1→LUMO ($\pi \rightarrow \pi^\star$) transition. The S_3 transition is assigned to higher $\pi \rightarrow \pi^\star$ transitions. The S_1 transition is assigned to a HOMO→LUMO ($n \rightarrow \pi^\star$) transition. This transition is symmetry-forbidden by dipole selection rules in *trans*-azobenzene. However, it is weakly visible due to molecular vibrations [36]. In H-Az6 it is more intense due to the asymmetric substitution.

In the spectrum of the *cis* form the S_2 transition is much weaker and blue shifted compared to the *trans* form. The S_1 transition has an increased intensity in the *cis* form as it is now allowed. The apparent shift of the S_1 transition is mainly caused by the tail of the S_2 transition on which this peak is superimposed in the *trans* form.

The optical transition dipole moments of the *trans* form $\mu(S_2)$ and $\mu(S_3)$ lie in the aromatic plane. $\mu(S_2)$ is oriented along the long axis of the molecule, while $\mu(S_3)$ is approximately parallel to the N=N bond (Fig. 5.12).

A more detailed description of the electronic structure of azobenzene is given by Conti et al. [35].

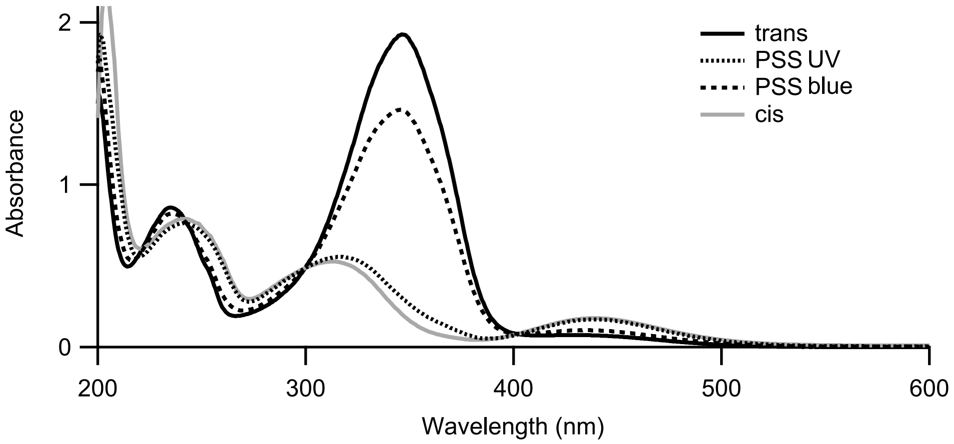

Figure 2.4: Photoisomersiation of H-Az6 in Ethanol: A solution of the *trans* conformer is illuminated at 350 nm inducing the *cis*/*trans* isomerisation until a photostationary state (PSS UV) is reached. Illumination with blue (>400 nm) light induces the back reaction until the photostationary state (PSS blue) is reached. The photoisomerisation is reversible only between these two states. Modified image from the author's *Diplomarbeit* [8].

Photoisomeriation Figure 2.4 demonstrates the photoisomerization of H-Az6 in solution. A solution of the *trans* form is irradiated with UV light until no further change in the spectrum was observed, i.e. the photostationary state (PSS) was reached. The composition of this UV PSS is dominated by the *cis* form. However, the PSS still contains a residual amount of the *trans* form as is evident by comparing the spectra of the PSS and the pure *cis* form. Irradiation with blue light leads to another PSS, which is dominated by the *trans* form, but contains a significant amount of the *cis* form. By illumination with the two colours in turns the photoisomerization is reversible between the two PSSs. The thermodynamically stable pure *trans* state can only be reobtained thermally. The pure *cis* form can not be obtained photochemically; thus it was prepared chromatographically (cf. Sec. 7.5).

The efficiency of the photoisomerization is described by the absorption cross section and the photoisomerization quantum yield. The *absorption* cross section $\sigma(\lambda)$ at a given wavelength is proportional to the absorbance of the solution. It is a measure of the probability to reach a certain excited state. The photoisomerization quantum yield Φ of that excited state is the probability of the excited state to decay into the desired isomer. The *photoisomerization* cross section

$$\sigma^{\mathrm{iso}} = \sigma\Phi \tag{2.1}$$

is determined by these two factors. It describes the probability of a molecule to isomerize, when it is exposed to light.

The composition in the photostationary state is depending on these quantities and is given in the following: For a reversible photochemical reaction A $\rightleftarrows$ B the rate constants of the forward and back reactions are given by:

$$k_{\mathrm{A}\to\mathrm{B}} = J\sigma_{\mathrm{A}}\Phi_{\mathrm{A}\to\mathrm{B}} \quad ; \quad k_{\mathrm{B}\to\mathrm{A}} = J\sigma_{\mathrm{B}}\Phi_{\mathrm{B}\to\mathrm{A}} \tag{2.2}$$

where J is the photon flux. The equilibrium constant K and thus the composition in the photostationary state is determined by the ratio of the two rate constants:

$$K = \frac{c_{\mathrm{B}}}{c_{\mathrm{A}}} = \frac{k_{\mathrm{A}\to\mathrm{B}}}{k_{\mathrm{B}\to\mathrm{A}}} = \frac{\sigma_{\mathrm{A}}\Phi_{\mathrm{A}\to\mathrm{B}}}{\sigma_{\mathrm{B}}\Phi_{\mathrm{B}\to\mathrm{A}}} = \frac{\sigma^{\mathrm{iso}}_{\mathrm{A}\to\mathrm{B}}}{\sigma^{\mathrm{iso}}_{\mathrm{B}\to\mathrm{A}}} \tag{2.3}$$

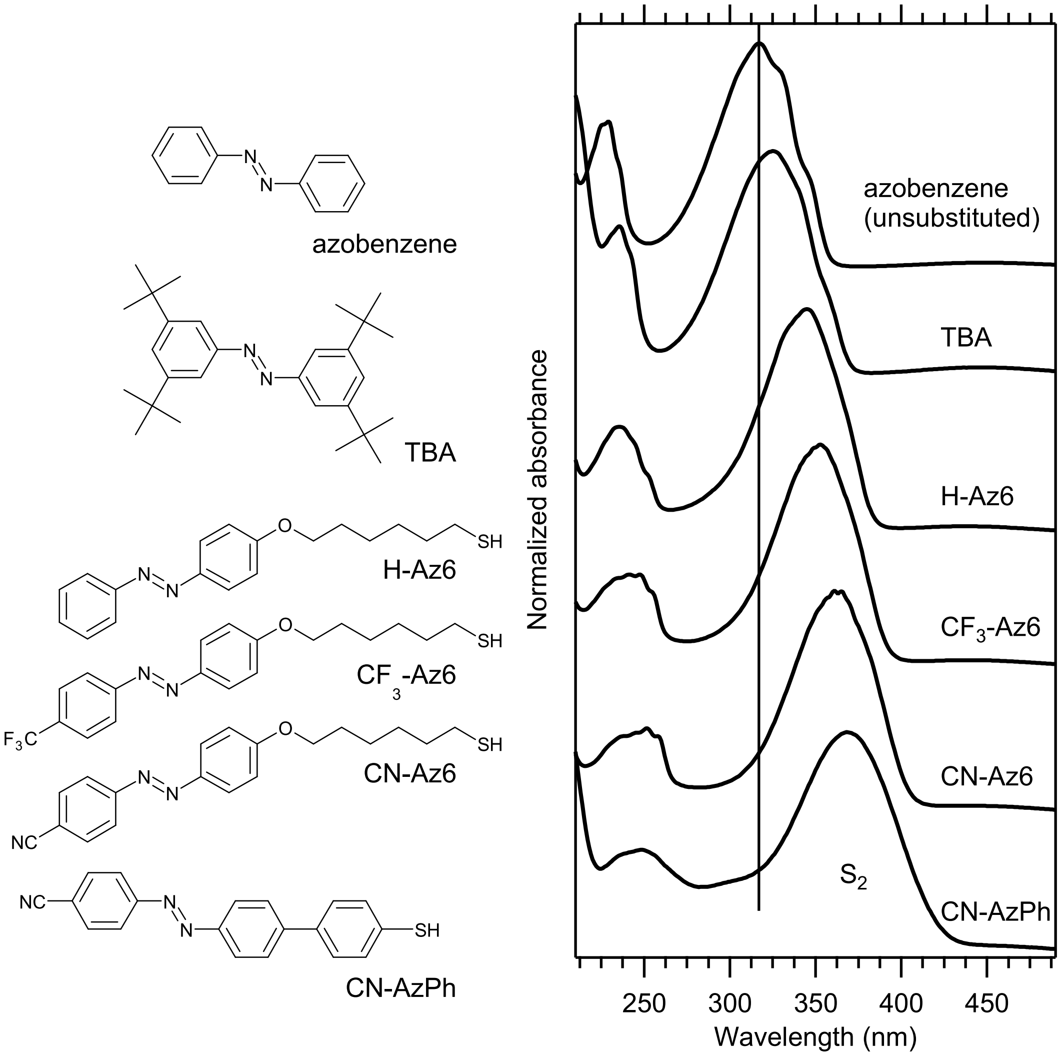

Figure 2.5: Substitution Effects: UV/vis spectra of the *trans* forms of azobenzene and azobenzene derivatives in cyclohexane. The absorbance was normalized in the maxima of the S2 absorption.

It is independent of the photon flux. The above equation is valid, if a thermal back reaction is slow compared to the photochemical process. If the thermal back reaction can not be neglected, it can be included into the model [37].

The absorption cross sections in Eq. 2.3 explain why the UV PSS contains only little of the *trans* form even though $\Phi_{cis \rightarrow trans}$ is larger [38] than $\Phi_{trans \rightarrow cis}$: When illuminating in the maximum or right of the S_2 band of the *trans* form, the *cis* form has a much smaller absorption cross section than the *trans* form due to the blueshift of the S_2 band in the *cis* form. In contrast the yield of the *cis*-*trans* isomerization by blue light can not be optimized by choosing an optimal wavelength, because there is no significant shift of the S_1 transition between *trans* and *cis* form.

Bandara and Burdette [38] and Dokic et al. [39] give an overview on the mechanisms of the photoisomerization of azobenzenes in solution and the dependence of the quantum yield on the substitution and solvent.

Influence of Substituents on Spectra The position of the absorption bands and thus the colour of azobenzenes can be tuned by adding substituents to the azobenzene

	S_2	
	(nm)	(eV)
azobenzene	317	3.91
TBA	325	3.81
H-Az6	345	3.59
CF_3-Az6	353	3.51
CN-Az6	361	3.43
CN-AzPh	369	3.36

Table 2.1: Substitution Effects: S_2 band positions are maxima directly read from Fig. 2.5.

Table 2.2: Solvatochromic Effect: Band positions are maxima directly read from Fig. 2.6, dielectric constant ϵ_r and dipole moments of solvent molecules μ from [41], $E_T(30)$ values from [42].

	S_2		ϵ_r	μ	$E_T(30)$
	(nm)	(eV)		(D)	(kcal mol^{-1})
cyclohexane	368	3.37	2.0	0.0	30.9
methyl *tert*-butyl ether (MTBE)	370	3.35			34.7
butanone	372	3.33	18.6	2.8	41.3
ethanol	372	3.33	25.3	1.7	51.9
benzene	374	3.32	2.3	0.0	34.3
2-methoxyethanol	376	3.30	17.2	2.4	52.0
THF	380	3.26	7.5	1.8	37.4

skeleton. Figure 2.5 shows spectra of unsubstituted azobenzene and the derivatives studied in this work. Table 2.1 lists the corresponding S_2 band positions. The substitution leads to a redshift of the S_2 band. Substituents that have a mesomeric effect, i.e. interact with the aromatic system, have the largest influence on the spectrum. H-Az6 compared to azobenzene is an example, where the +M effect of the ether oxygen leads to a large shift. CN-Az6 is an example for a push-pull azobenzene. Here the electron donating (+M) effect of the ether oxygen is combined with the CN group as a mesomeric electron acceptor (-M effect) leading to an even larger redshift. The effect of substituents that have no mesomeric interaction with the aromatic system is comparatively small. This is illustrated by CF_3-Az6 compared to CN-Az6. The CF_3 group in CF_3-Az6 which possesses a strong inductive electron withdrawing (-I) effect, however, the red shift is significantly smaller than in CN-Az6.

The substitution not only influences the spectra but also has an influence on the isomerization kinetics and mechanisms [39]. In some push-pull azobenzenes, for example, the isomerization mechanism changes depending on the solvent and the half-life of the *cis* form changes by three orders of magnitude [40].

Solvatochromic Effect Different solvents may interact differently with the ground state and optically excited states, leading to changes in the spectra of the dye. This solvatochromic effect is illustrated in Fig. 2.6, which shows spectra of CN-AzPh in various solvents. Cyclohexane is a solvent with no dipole moment, low dielectric constant, and reduced Van-der-Waals interactions with alkyl chains. Thus, we assume that this solvent interacts little with the dye and we take the spectra in this solvent as the reference.

Solvent effects are usually discussed in terms of solvent polarities. However, chem-

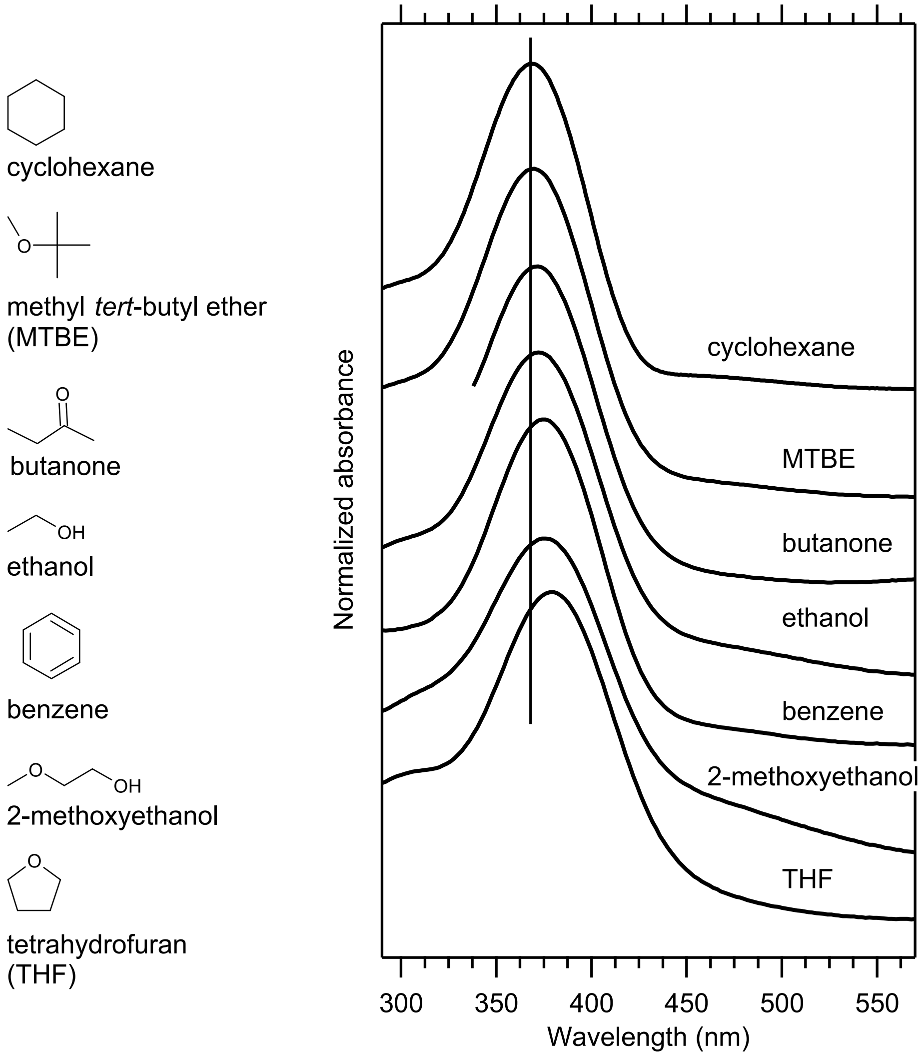

Figure 2.6: Effect of the solvent on the S_2 band position of CN-AzPh: The absorbance was normalized in the maximum of the S2 absorption.

ical behaviour only poorly correlates with the dielectric constant ϵ_r or dipole moment μ of the solvent. Therefore, empirical polarity scales based on the solvatochromic effect have been developed in chemistry. The $E_{\mathrm{T}}(30)$ scale is the most prominent of these. Reichardt [42] gives a good review on solvatochromic effects and empirical polarity scales.

The position of the S_2 transition in various solvents correlates neither with the dielectric constant or dipole moment nor with the $E_{\mathrm{T}}(30)$ scale. Most notably the aromatic solvent benzene, which has a similar polarity as cyclohexane on all three scales, causes a peak shift larger than that caused by the polar solvent ethanol. Hence, the solvatochromic effect in this case is dominated by specific interactions between the solvent and the solute.

Chapter 3

Self-Assembled Monolayers

Self-assembled monolayers (SAMs) are typically formed by immersing a substrate into a solution of the SAM-forming compound. The SAM-forming compound possesses a head group, i.e. is a chemical functionality with a specific affinity for the substrate. The head group binds to the surface and thereby forms an organic adlayer on the substrate. A defined monolayer is formed, because once the surface is fully covered, the process comes to a halt. The adsorbate organizes spontaneously in a crystalline or semicrystalline structure.

We will limit our discussion to thiolate based SAMs on gold(111) surfaces. This kind of SAMs is reviewed in [1, 43]. Thiolate SAMs on gold can be produced in ambient conditions by immersing a gold substrate into a solution of the thiol. After the adsorption process the sample is removed from the solution, rinsed to remove excess thiol, and dried.

Mechanism of SAM Formation The sulphur head group of the thiol binds to the gold substrate and forms the strong gold thiolate bond ($44\,\mathrm{kcal\,mol^{-1}} \equiv 1.9\,\mathrm{eV}$) [44]:

$$\mathrm{Au + HS(CH_2)_nX \xrightarrow{-1/2\,H_2} Au - S(CH_2)_nX} \tag{3.1}$$

Disulphides, which are often present in the adsorption solution due to oxidation, lead to the same gold thiolate as thiols:

$$\mathrm{Au + 1/2\,X(CH_2)_nSS(CH_2)_nX \longrightarrow Au - S(CH_2)_nX} \tag{3.2}$$

Thus, this impurity does not necessarily impair the quality of the SAM. Disulphides can also be used directly to produce SAMs (cf. Sec. 7.2.5.5).

For simple alkanethiols kinetic studies show 2 distinct kinetic steps: An initial step during which the surface is covered, which takes minutes in 1 mM solutions and completes within about 2 h at 0.1 mM [45]. This initial step is followed by a slower crystallisation and healing process. A self-exchange experiment, in which ^{35}S labelled long chain alkanethiolate SAMs are exposed to solutions of the same unlabelled thiol [46], gives some hints on the mechanisms of SAM formation. Most notably it shows that after an initial period of < 24 h the self-exchange rate is drastically reduced. This may be interpreted as the completion of a healing process during which defect sites necessary for the exchange are cured. Typically 24 h are assumed to be sufficient to form well ordered SAMs at room temperature; thus immersion times of 20–24 h were used throughout this work. More details on the SAM preparation are given in Chap. 7.2.5. More detailed mechanistic studies have been conducted for SAM formation in the gas phase [1].

Substrates On gold single crystals the (111) surface can be prepared by sputter anneal cycles. In this way large terraces are obtained. The (111) surface is known to exhibit the so called herringbone reconstruction [47, 48]. For SAM formation generally 100–300 nm thick polycrystalline gold films vapour deposited on glass, silicon wafers or mica are used. Suitable annealing protocols allow to produce Au/mica substrates with large Au(111) terraces of a few hundred nm in width [49] similar to the surfaces of single crystals. Such substrates are commercially available and were used in this work. SAMs have also been investigated on thinner semitransparent gold films; however, their properties may differ from SAMs on single-crystal-like substrates (cf. Sec. 5.2.4).

Adsorption solutions Ethanol is the most commonly used solvent for alkanethiolate SAM formation and was used for most types of SAMs in this work. Solutions with a thiol concentration of 0.1–10 mM are usually employed. The higher concentrations are more common in experiments with simple and readily available alkanethiols. For more complex thiols 0.1 mM are preferred to make economical use of the precious compounds. This is also the concentration generally used for the SAMs in this work.

In typical experiments a concentration of 0.1 mM corresponds to a more than 130-fold excess of thiol for simple alkanethiols.[1] Thus, the concentration in solution can be assumed to remain constant during the adsorption.

The S-Au Bond and Purity of the SAM The S-Au bond is most commonly investigated by XPS. Figure 3.1 shows a spectrum of a sample exhibiting all commonly encountered sulphur species in a SAM. It can be decomposed into 4 doublets corresponding to the following 3 sulphur species:

The doublet at about 162.0 eV is assigned to the alkyl-thiolate sulphur, i.e. the sulphur bound to gold. The spectrum of a perfect SAM should only show this component.

The doublet at 163.4 eV is assigned to free thiol or disulphide [50]. Free thiols and disulphides both have XPS binding energies in the range 163–164 eV. Disulphides, which are formed by oxidation of thiols, are a common impurity in thiols. They are usually less soluble than the thiol, and thus are more difficult to rinse off the sample. The occurrence of this peak at 163 eV is a sign for ineffective rinsing during SAM preparation. The sample shown was prepared from a disulphide solution and was not rinsed in order to show the effect.

We can not assign the broad doublet at 164.5 eV. The binding energy above that of the disulphide suggests sulphur in higher oxidation states but partly oxidized disulphides have significantly higher binding energies [51]. However, the assignment is not relevant for this work as we never observed this component when trying to produce clean SAMs.

The doublet at 161 eV is commonly assigned to atomic sulphur [52]; however, also other interpretations have been suggested, especially thiolates at different binding sites [53, 54]. These explanations are not mutual exclusive. For the samples analysed in this work the species leading to the signal at 161 eV is present on the Au/mica

---

[1] We used about 1 ml per cm^2 of sample and assume a footprint of 0.22 nm^2 (cf. Sec. 5.5.2) per molecule on the surface for simple alkanethiols. More complex thiolates have larger footprints.

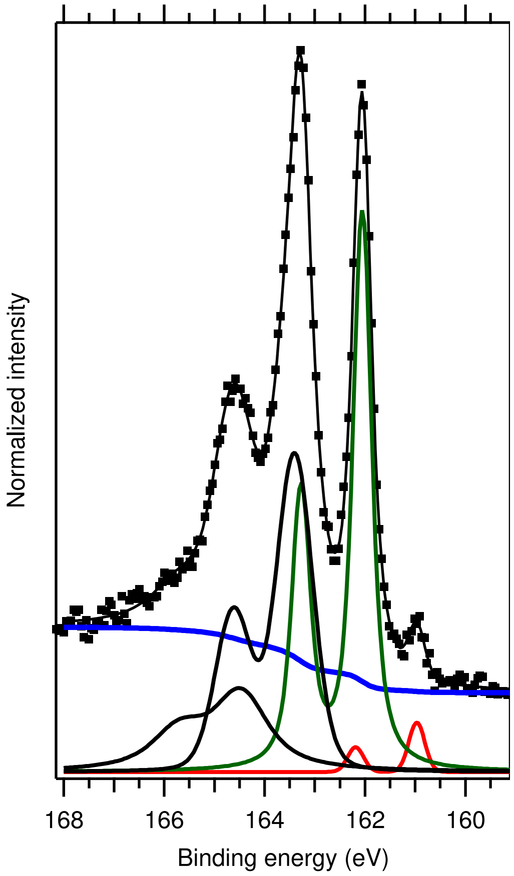

Figure 3.1: S2p XPS spectrum of a sample showing all commonly encountered sulphur species in SAMs: The peak structure was decomposed into 4 Voigt doublets on a Shirley type background. sample: SAM prepared from the symmetric disulphide corresponding to CN-Az6 prepared from a solution in toluene/ethanol 1:1 without rinsing.

substrates already before the SAM is produced. This is corroborated by the following experiments: In SAMs prepared by evaporation of the thiol in UHV, where the clean crystal was not exposed to air before the SAM formation, the peak is not present [28, p. 47]. Figure 3.2 shows XP spectra of a gold substrate before and after SAM formation in solution. The spectrum of the pristine Au/mica substrate (exposed to air) shows the doublet at 161 eV among other components. After formation of the SAM this component is reduced to less than 4% of the total peak area. Due to the strong dampening of the S2p signal by the SAM, this does not necessarily indicate that this species has been displaced. As well the initial amount of this species may have been low compared to the amount of thiolate sulphur in the SAM.

The C1s spectrum shown in the same figure demonstrates that carbon containing contaminants are effectively displaced by the SAM. The nature of the contaminants varies from batch to batch and immersing the substrate into ethanol does not remove the contaminants, but changes their composition. The effective displacement of the contaminants can be explained by the energetic gain of the Au-S bond formation in addition to strong attractive interactions between the alkyl chains. The relevance of the attractive interactions in the backbone is illustrated by an experiment in which an adamantanethiolate SAM is displaced by alkanethiols, because the backbone interactions in the adamantanethiolate are weak compared to the attractive forces in the resulting alkanethiolate SAM [55].

Structural Quality of the SAM [1] So far we have discussed the purity of the SAM, i.e. the absence of chemical species different from the desired gold thiolate. Even a pure SAM has structural defects, like isolated vacancies, i.e. single missing

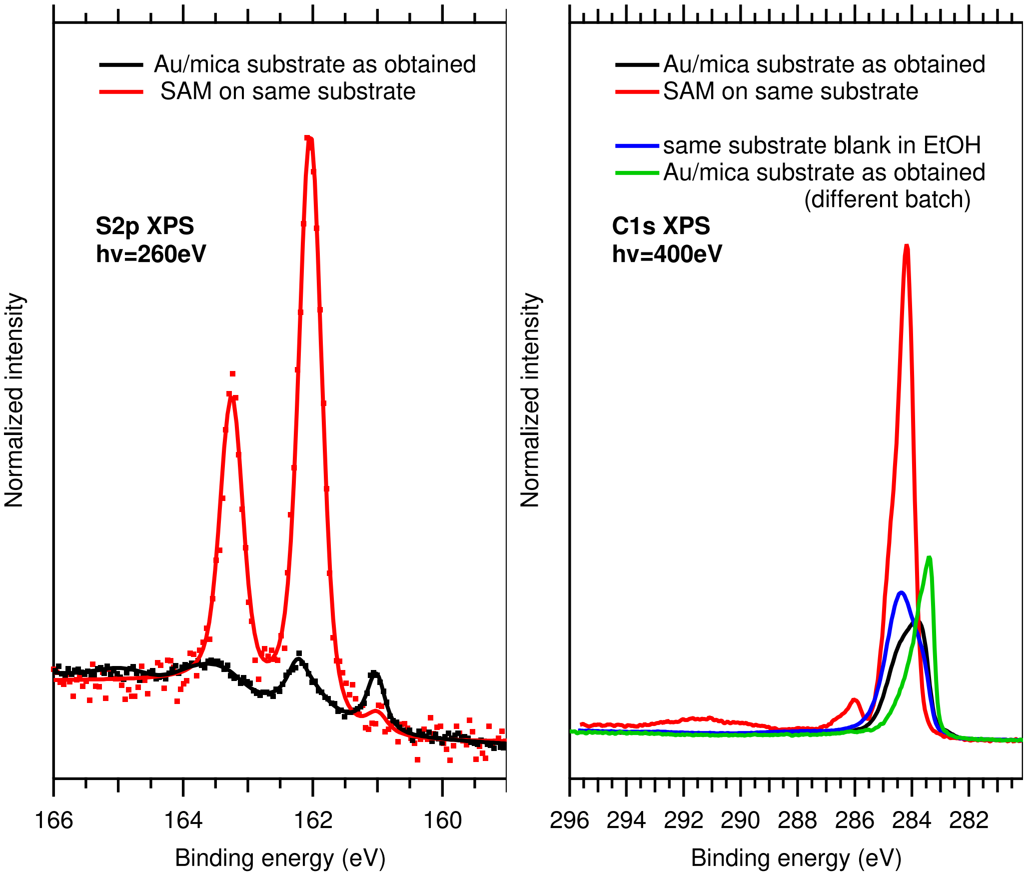

Figure 3.2: S2p and C1s XPS of an Au/mica substrate as obtained *(black)* and of an H-Az6 SAM grown on the same substrate *(red)*: Additional C1s spectra are shown of the same substrate immersed for 24 h in ethanol and of a pristine substrate from a different batch. The C1s spectra of blanks were variable from batch to batch, whereas S2p spectra of blanks were very similar for different batches of substrates. S2p spectra of blanks were fitted with 3 Voigt doublets on a Shirley type background resulting in sharp doublett at 161.0 eV width a width of 0.4 eV and wider dubletts at 162.0 eV and 163.4 eV. The spectrum of the SAM was fitted with two doublets: In addition to the doublet at 162.0 eV a second doublet at 161.0 eV with less than 4% of the total peak area was obtained. Peak intensities were normalized to the right background; thus peak intensities between different spectra can not be compared.

molecules, missing rows or defect regions at domain boundaries. Larger scale depressions, which are frequently observed, are no real defects. They are vacancy islands of mono- or di-atomic depth in the gold substrate, which are covered by the SAM forming thiolate.

Mixed SAMS Several methods have been demonstrated to deliver mixed SAMs, i.e SAMs comprising of two different thiolates that form a statistical mixture on the surface. We limit our discussion to coadsorption from solution and the use of asymmetric disulphides. The adsorption of asymmetric disulphides (R_1SSR_2) is assumed to ensure a 1:1 mixture of the two components in the SAM, even though for special cases deviations from the 1:1 composition [56] and phase separation [57] have been reported.

The most frequently followed approach, which we also used in this work, is the formation of mixed SAMs by coadsorption from a solution of two thiols. An advantage of coadsorption over the disulphide approach is that the composition at the surface can be controlled by the composition of the solution. Coadsorption of simple alkanethiols have been extensively studied by Bain and coworkers [45, 58–62]. They investigated the influence of substituents, solvents, and the length of the alkyl chains on the relation between composition in solution and in the SAM. Generally preferential adsorption of one component is observed and may be so strong that in equilibrium only one component is found in the SAM. Preferential adsorption should be less pronounced, when the interactions of different molecules in the SAM are similar. In the mixed chromophore experiment (cf. Sec. 5.4) this was achieved by mixing very similar thiols, which only differ in one substituent. In the diluted chromophore experiment (cf. Sec. 5.5), long-chain alkane-thiols with and without chromophore head-group are employed. We assume that in this system the interactions between the alkyl chains, which are identical in both components, limit the preferential adsorption.

In coadsorption experiments the composition of the adsorption solutions is described in terms of mole fractions. The mole fraction χ_i of component i is defined as the ratio of molecules of i to the total number of (relevant) molecules. It is related to the concentrations c_i as follows:

$$\chi_i = \frac{N_i}{\sum_j N_j} = \frac{c_i}{\sum_j c_j} \tag{3.3}$$

Thus, for a mixture of 2 thiols A and B the mole fraction of thiol A is:

$$\chi_\mathrm{A} = \frac{c_\mathrm{A}}{c_\mathrm{A} + c_\mathrm{B}} \tag{3.4}$$

When the composition of the SAM is investigated as a function of the composition of the adsorption solution, adsorption solutions with a constant total thiol concentration $c_\mathrm{A} + c_\mathrm{B}$ are used.

The composition of the mixed SAM is described in the same way by the *surface mole fractions* χ^ads in contrast to mole fractions χ^sol in the adsorption solution. This quantity is especially usefull when the total numer of molecules in the SAM is constant, i.e. when we have a 1:1 exchange reaction:

$$\mathrm{A}^\mathrm{ads} + \mathrm{B}^\mathrm{sol} \rightleftharpoons \mathrm{A}^\mathrm{sol} + \mathrm{B}^\mathrm{ads} \tag{3.5}$$

Thus, both components have the same space requirement or footprint in the SAM.

When the footprints of the two components are different, and thus the total number of molecules in the SAM depends on its composition, it may be more appropriate to describe the composition by the relative coverage Θ of component A. Θ is defined as the ratio of the number of molecules of component A in the mixed SAM to number of molecules in a single component SAM of component A:

$$\Theta = \frac{N_\mathrm{A}}{N_\mathrm{A}^\text{pure A SAM}} \tag{3.6}$$

We will discuss models describing the composition of the SAM as a function of the composition of the solution in 5.4.1 and in 5.5.2. Literature specific to mixed azobenzene/spacer SAMs will be discussed in 5.5.

Chapter 4

Experimental Techniques

4.1 X-ray Photoemission Spectroscopy (XPS)

In this work XPS, also named ESCA (Electron Spectroscopy for Chemical Analysis), was used to determine the chemical composition of (sub-) monolayers of organic adsorbates on gold. In XPS core electrons are emitted by absorption of X-rays with constant photon energy while the number of emitted electrons is recorded as a function of their energy. Hüfner [63] gives a good introduction to photoelectron spectroscopy. The application of XPS to adsorbates was reviewed by Nilsson [64]. In the following we will briefly discuss some aspects of the technique relevant for the analysis of the XP spectra in this work.

4.1.1 Set-up

Laboratory X-ray sources for XPS make use of the K_α radiation of Aluminium (1486.7 eV) or Magnesium (1253.6 eV). The radiation emitted by these sources is nonpolarized. In contrast, in synchrotron experiments polarized radiation with arbitrary photon energy is available.

In this work two set-ups were used: one comprising a monochromatised AlK_α laboratory source[1] and a mobile chamber used at the synchrotron facility BESSY II. Both set-ups were equipped with a hemispherical electron analyser. The synchrotron source with its high flux, tunable photon energy, and low spectral bandwidth allows to record high resolution spectra in minutes; whereas it takes about an hour to record a spectrum with lower resolution and more noise using the laboratory source. However, because the lab source is constantly available, it is more suitable for tasks like the optimisation of sample preparations. In addition, the spectra recorded using the laboratory source were found to be more suitable for the quantification of the different species in the mixing experiments (cf. Sec. 4.1.9).

The measurement geometry for the laboratory set-up is shown in Fig. 4.1(a). The measurement geometry chosen for XPS experiments with synchrotron radiation, shown in Fig. 4.1(b) is based on the following considerations: As photoelectrons are emitted primarily in the direction of the electric field, the polarization should be in direction of electron detection. In order to achieve maximum sensitivity and minimal backgrounds the interaction of the emitted photoelectrons with the layer needs to be minimised. Thus, a near normal emission geometry, i.e. the surface

---

[1] The laboratory source is available by the collaborative research centre 658. It is maintained and run by my colleague D. Przyrembel, who performed all lab-based XPS measurements shown in this work.

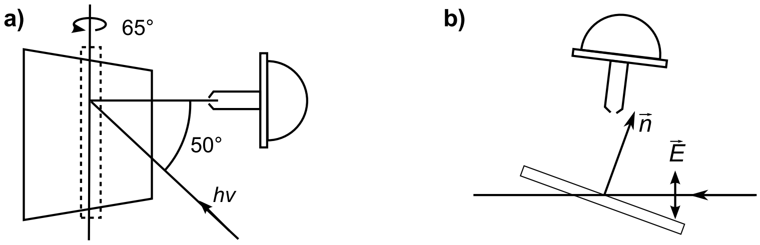

Figure 4.1: Geometries used for XPS measurements: **a)** using the laboratory source: View from the side. In order to increase the interaction of the X-rays a glancing incidence geometry is chosen. Therefore the sample is rotated by 65° out of the normal emission position. This results in a 65° off-normal emission angle. **b)** using synchrotron radiation: View from the side. The X-rays impinge on the sample in glancing incidence from the right and are vertically polarized. Thus, the electric field is nearly parallel to the sample normal. The electrons are detected in near normal emission from the top. Exact angles are given in Fig. 4.9.

normal pointing towards the electron analyser is desirable. This set-up was mainly used at beamlines where the polarization of the radiation could be switched from vertical (for XPS measurements) to horizontal. Thus, NEXAFS experiments, where horizontal polarization is preferred (cf. Sec. 4.2.3.1) could be performed in rapid sequence with XPS measurements on the same sample. The influence of the photon energy and polarization on the XP-spectra will be discussed later in this section.

4.1.2 Electron Energy Referencing

In photoemission of *free atoms* the photon energy $h\nu$ is partly used to overcome the binding Energy $\tilde{E}_{\mathrm{bind}}$ of the emitted electron. The remaining energy is the kinetic Energy E_{kin} of the photoelectrons:

$$h\nu = \tilde{E}_{\mathrm{bind}} + E_{\mathrm{kin}} \tag{4.1}$$

In *conductors*, however, the binding energy E_{bind} is defined with respect to the Fermi level. Thus, the workfunktion of the sample ϕ_{s} reduces the kinetic energy of the electron *in front of the sample* $E^{\mathrm{s}}_{\mathrm{kin}}$:

$$E^{\mathrm{s}}_{\mathrm{kin}} = h\nu - E_{\mathrm{bind}} - \phi_{\mathrm{s}} \tag{4.2}$$

Analyser and sample are connected to the same ground. Thus, their Fermi levels are aligned (Fig. 4.2). Therefore, a potential difference exists between the vacuum levels in front of the sample and in front of the analyser. Hence, the kinetic energy in front of the analyser $E^{\mathrm{a}}_{\mathrm{kin}}$ differs from that in front of the sample $E^{\mathrm{s}}_{\mathrm{kin}}$. Thus, we obtain for the kinetic energy observed by the analyser:

$$E^{\mathrm{a}}_{\mathrm{kin}} = h\nu - E_{\mathrm{bind}} - \phi_{\mathrm{a}} \tag{4.3}$$

In practise, the binding energy E_{bind} of core-levels is determined from the energy difference to a reference level with known binding energy $E^{\mathrm{ref}}_{\mathrm{bind}}$.

$$E_{\mathrm{bind}} = E^{\mathrm{ref}}_{\mathrm{bind}} + E^{\mathrm{ref}}_{\mathrm{kin}} - E_{\mathrm{kin}} \tag{4.4}$$

Throughout this work the bulk component of the Au4f$_{7/2}$ peak of the gold substrate at a binding energy of 83.95 eV [65] was used as reference level.

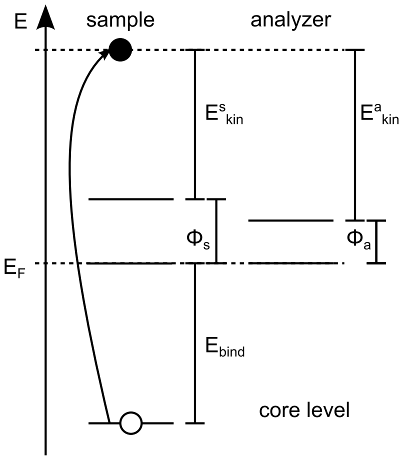

Figure 4.2: Energy levels for a conductor in photoemission spectroscopy.

4.1.3 Doublets, Spin-orbit splitting

In this work photoemission from the C1s, N1s, O1s, S2p and Au4f levels were investigated.

Photoemission from the S2p levels results in a double peak structure due to a final state effect. The final state is an S atom with a core hole in the 2p level. Thus, the total spin of the final state is $S = 1/2$. Due to the spin-orbit coupling the 2p levels are not degenerate any more. In L-S coupling the level splits into the states $j = l \pm s = 1/2, 3/2$. These states possess a $(2j + 1)$ fold degeneracy. I.e.

$$\text{for } j = 1/2 : m_j = \pm 1/2 \quad \text{and for } j = 3/2 : m_j = \pm 1/2, \pm 3/2. \tag{4.5}$$

This results in a doublet with an amplitude ratio of $2p_{3/2} : 2p_{1/2} = 2 : 1$. For the Au4f levels in the same way a splitting into the $4f_{7/2}$ and $4f_{5/2}$ with an amplitude ratio of 4:3 is obtained.

The 1s levels have a total orbital angular momentum of $L = 0$; thus the 1s core hole states are degenerate and a singlet is observed.

4.1.4 XPS-satellites (Shake-Up)

In the photoemission process a valence electron may be excited at the expense of the energy of the emitted photoelectron. For atoms and small molecules the final state generally has a higher energy than the final state of direct photoemission. Thus, in the vicinity of the direct photoemission peak the participating photoelectrons are observed as satellite peaks with apparent higher binding energy. However, in more complex molecules shake-ups with negative binding energy shifts are possible [66].

4.1.5 Peak Shape

The shape of photoemission peaks is influenced by several factors. The finite lifetime of the core-hole leads to a Lorentzian; whereas vibrational progression, inhomogeneous broadening, and instrumental effects (resolution of the electron analyser and spectral width of the radiation used to excite the electrons) lead to a further broadening of the peak, described by the convolution with a Gaussian. This convolution is known as Voigt function and has no analytical solution:

$$\text{Lorentzian:}\quad g_{\mathrm{L}}(\nu-\hat{\nu},\gamma_{\mathrm{L}}) = \frac{1}{\pi}\frac{\gamma_{\mathrm{L}}}{(\nu-\hat{\nu})^2+\gamma_{\mathrm{L}}^2} \tag{4.6}$$

$$\text{Gaussian:}\quad g_{\mathrm{G}}(\nu-\hat{\nu},\gamma_{\mathrm{G}}) = \tfrac{1}{\gamma_{\mathrm{G}}}\sqrt{\tfrac{\ln 2}{\pi}}\cdot\exp\left(-\ln 2\left(\frac{\nu-\hat{\nu}}{\gamma_{\mathrm{G}}}\right)^2\right) \tag{4.7}$$

$$\text{Voigt peak:}\quad g_{\mathrm{V}}(\nu-\hat{\nu},\gamma_{\mathrm{V}}) = \int_{-\infty}^{\infty} d\nu' g_{\mathrm{L}}(\nu-\nu',\gamma_{\mathrm{L}})\cdot g_{\mathrm{G}}(\nu'-\hat{\nu},\gamma_{\mathrm{G}}) \tag{4.8}$$

In the above formulas the distributions are given for a peak located at the position $\hat{\nu}$ and are defined in view of 4.1.11 using their respective *half* width (at *h*alf maximum) $\gamma_{\mathrm{V,\,G,\,L}}$.

In the literature, sum, product, and linear combination of Gaussian and Lorentzian are frequently encountered. These are analytical approximations to the Voigt function rather than different peak shapes and can be replaced by numerical approximations of the Voigt function, which were used in this work (cf. Sec. 4.1.11).

The Voigt shape gives a good description of the *primary* photoemission peak. Generally asymmetrical line shapes with a tail towards lower binding energies are observed. They are caused by backgrounds that depend on the peak as described below. Alternatively, (part of) the background can be considered as part of the peak leading to asymmetric line-shapes, like the Doniach-Sunjic [67] peak profile.

4.1.6 Background

The primary photoelectrons experience losses due to inelastic scattering. Excitation of discrete levels, like shake-ups or the excitation of intrinsic plasmons, lead to satellite peaks coupled to the primary peak.

In contrast, scattering processes like excitation of phonons and vibrations or the formation of electron-hole pairs allow quasi continuous energy losses thus leading to a background that increases stepwise underneath the peaks (Fig. 4.3). Shirley [68] developed a widely used model for this kind of background. His model uses a background proportional to the integral over the peak starting at a binding energy below the onset of the peak. In the original Shirley procedure the background is determined by an iterative method using the measured data directly. Whereas we integrated the peak model function (cf. Sec. 4.1.11), thus allowing to find the proportionality factor in the same fit together with the peak parameters.

In addition to this background formed by inelastically scattered electrons of the primary peak a smooth background component is observed. It is caused by secondary electrons released by photoemission processes with binding energies below the current peak. This contribution can be modelled as constant or linear over the range of a peak.

Generally, in this work a combination of linear and Shirley type background was used. The amount of Shirley type background depends on the position of the atom probed in the layer. The longer the way the photoelectron has to travel through the layer, the larger the contribution to the inelastic background. Figure 4.3 shows S2p spectra of 2 different SAMs. In both, the S atoms are located at the bottom of the adsorbate. Thus, the photoelectrons have to travel through the whole layer, and therefore the amount of inelastically scattered electrons compared to the peak amplitude is larger in the thicker layer.

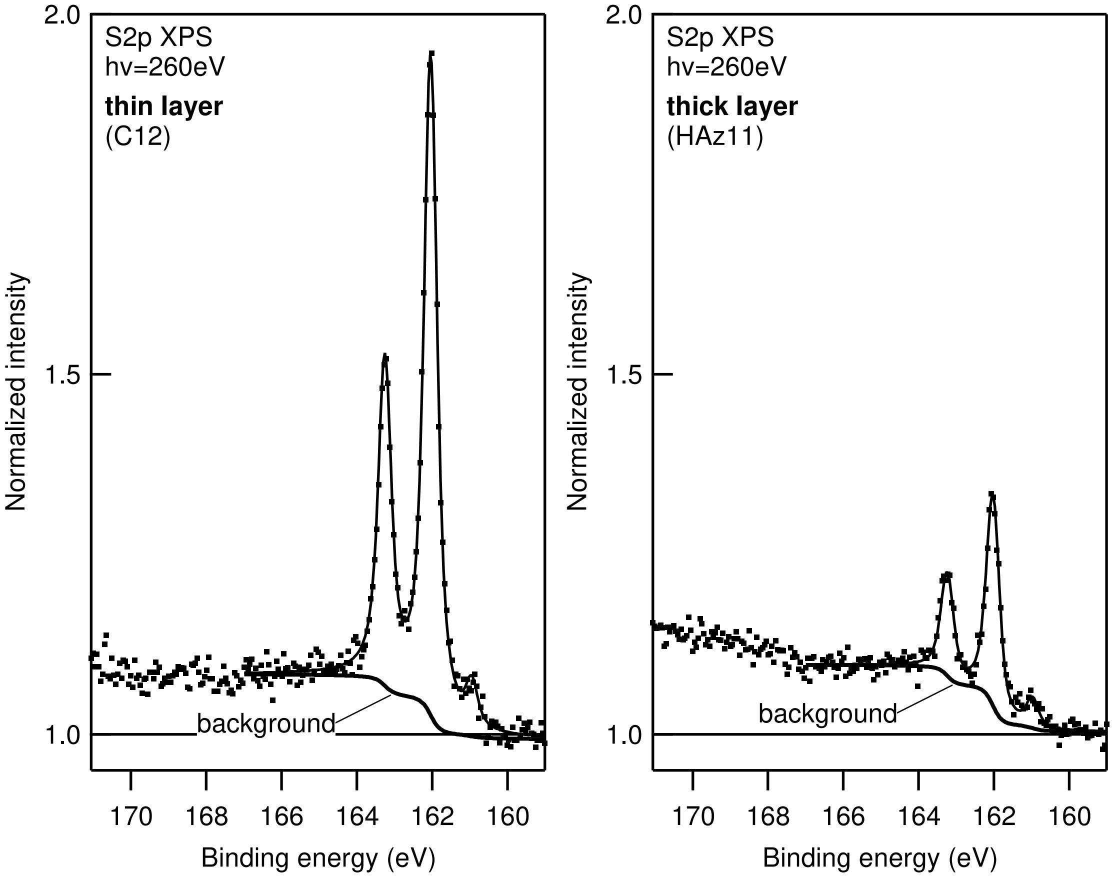

Figure 4.3: Dependence of the XPS background on the thickness of the adsorbate layer: S2p spectra of a thin and a thick SAM on Gold. The spectra were fitted with two doublets and a Shirley type background (cf. Sec. 4.1.11). The spectra were normalized to the low binding energy (right) background. I.e. the secondary electron background, that is approximated as a constant over the fitting range, has an intensity of about 1. On top we see the Shirley type background that increases stepwise with the peaks and describes the inelastically scattered electrons of the primary peaks. Due to the low kinetic energy of about 100 eV of the photoelectrons the contribution of this part of the background is substantial. Since the S atom is located at the bottom of the SAM in both samples, the photoelectrons have to travel through the whole layer. Thus, the ratio of the peak intensity to both components of the background is much higher for the thin layer than for the thick layer. samples: thin layer: C12 SAM, thick layer: HAz11 SAM.

The secondary electron contribution, which mainly originates from photoelectrons of the substrate,[2] also increases with the layer thickness. This becomes apparent as a smaller peak in the spectrum of the thicker layer, because the spectra in the figure were normalized at the right background, i.e. to the secondary electron background.

4.1.7 Choice of Photon Energy

As the photoemission cross section of s levels decreases with increasing photon energy,[3] energies short above the binding energy of the electrons to be probed yield maximum sensitivity. The escape depth of the photoelectrons is limited by scattering

---

[2] e.g. Au4f. C and N atoms in the layer are not excited by the 260 eV radiation used to probe S.

[3] For the S2p levels the maximum cross section is only shortly above the binding energy.

in the layer. Scattering is maximal for electron energies of about 100 eV. Therefore, the surface sensitivity of the method is maximal for these energies. An example is the surface component of the Au4f peaks of the substrate, that increases with decreasing photon energy compared to the bulk component [69].

However, this argument is not relevant if the adsorbate to be investigated consists of other elements than the substrate, as it is the case for the SAMs on gold investigated in this work. Nonetheless in the synchrotron experiments the photon energy was chosen to yield 100 eV electrons, because this energy is low enough to yield a high photoemission cross section but sufficiently high to avoid resonant photoemission and to ensure the peaks are out of the secondary electron tail of the background. The binding energies of the relevant peaks of the elements in the organic adsorbates range from about 163 eV (S2p) to 543 eV (O1s). Thus, different photon energies for each element were used.

The intense scattering of the 100 eV electrons leads to an attenuation that depends strongly on the position of the core they were emitted from in the layer. Figure 4.4 (top) demonstrates the increased attenuation of electrons emitted deeper in the layer: The compound shown possesses 1 nitrogen atom in the CN group at the top of the layer and 2 in the N=N bridge in the middle of the chromophore. The atoms in the N=N bridge are almost equivalent and their contribution to the spectrum can be described by a single peak. Thus, the spectrum can be decomposed into two peaks. The peak attributed to the CN group at the top of the layer accounts for 63% of the total peak area, even though the CN group comprises only 1 of the 3 nitrogen atoms. The intense scattering at these photon energies also leads to the large Shirley-type contribution to the background that is observed in the spectra recorded using the synchrotron source. In contrast, for spectra recorded using the laboratory AlK_α source the kinetic energies for the relevant peaks are about 1 keV. Here much less scattering takes place in the adsorbate layer and the Shirley-type component of the background is smaller and could often be neglected, whereas the secondary electron background is much higher.

4.1.8 Choice of polarization

In contrast to XPS experiments, where a polarization of the electrical field parallel to the direction of electron detection is preferred, in NEXAFS experiments a polarization with the electrical field perpendicular to the direction of electron detection is desirable (cf. Sec. 4.2.3.1). This would correspond to horizontally polarized radiation in Fig. 4.1(b). As not all synchrotron beamlines allow rotation of the polarization we investigated the effect of the polarization on the XP-spectra.

Figure 4.4 shows N1s XP-spectra recorded on the same sample with the preferred vertical polarization and with horizontal polarization. The peak to background ratio is much higher in the spectra recorded with the preferred, vertical polarization. This is the expected behaviour and is explained as follows: Both components of the background—the Shirley component comprising the inelastically scattered electrons and the linear component comprising secondary electrons—have a wide distribution of escape directions, while the photoemission takes place mainly in the direction of the electric field. Thus, when using vertical polarization, photoemission takes place mainly in the direction of the detector and the peaks are enhanced with respect to the background. In contrast, when using horizontal polarization, photoemission takes place mainly in directions perpendicular to the direction of the detector and the background is enhanced.

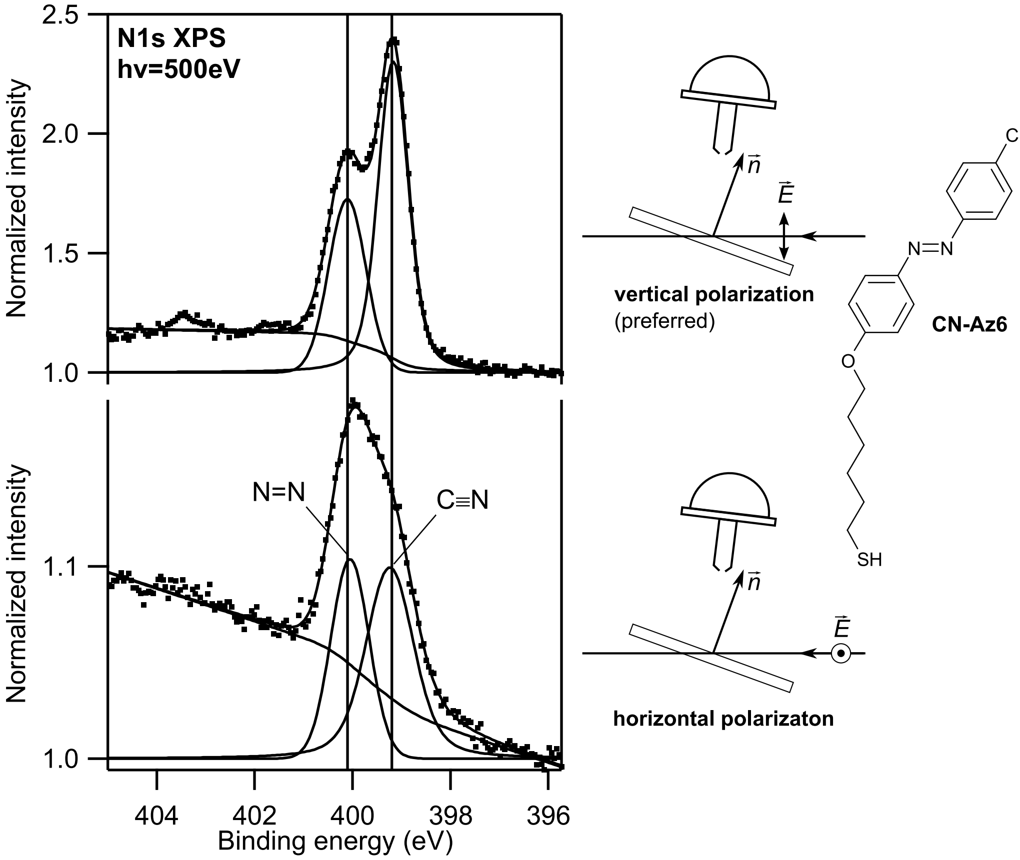

	NN			CN		
	position/eV	fwhm/eV	area	position/eV	fwhm/eV	area
vertical	400.10±0.05	0.90±01	37%	399.20±0.05	0.73	63%
horizontal	400.05±0.05	0.90±01	44%	399.20±0.05	1.14	56%

Figure 4.4: N1s spectra recorded using vertically and horizontally polarized radiation. The spectra were measured on the same sample. Intensities were normalized to the right background. Note the different scales! Even though the peak structures appears different, both spectra can be decomposed into two peaks at the same positions. sample: SAM of CN-Az6 on gold/mica, full discussion of spectral features cf. Sec. 5.2.1.

In the example, the peak shape is also affected. This is mainly caused by the CN peak which is broadened while the NN peak does not change its width. The reasons are not clear to the author.

4.1.9 Quantification

We want to use XPS to answer quantitative questions like, “What is the composition of the layer in a mixed SAM made up of two different molecules?”, or “How much of an undesired impurity is present on the sample?”

Quantitative XPS is based on the fact, that the photoemission cross section for core electrons is independent of the chemical environment of the core. Thus, the number of emitted photoelectrons is proportional to the amount of the respective species on the surface and hence can be used to quantify that species. However, the photoelectron signal is attenuated depending on the position of the atom in the layer. This presents one of the major difficulties in the quantitative analysis of adlayers.

As the electron signal is proportional to the incident intensity, the photon flux needs to be sufficiently constant during a series of measurements or the electron signal has to be normalized to the flux. The flux of the laboratory source decreases as the source ages. Thus, when the samples in a series can not be measured subsequently to minimize the effect, the electron signal has to be normalized to a standard measured in regular intervals.

The electron signal is proportional to the amount of a certain species on the surface, but the proportionality factor is unknown. In order to obtain relative coverages, the peak integrals have to be set into relation to a reference, i.e. a sample with a defined full monolayer.

For some special cases the analysis is simplified. If only the ratio of 2 species on the same sample is required, no standards or references are needed. An example are the S2p spectra of the SAM samples which generally could be decomposed into 3 peaks assigned to the desired bound thiolate, atomic sulphur, and unbound thiole (cf. Sec. 3). The sulphur of the bound thiolate is located directly at the gold interface, and we assume that the atomic sulphur is also residing directly at the interface, and hence the photoelectrons will experience the same attenuation by the layer. Therefore, the ratio of the two peak integrals should directly correspond to the ratio of the two sulphur species. Possible unbound thiole sulphur will be located on top or in the layer. Thus, the respective photoelectrons will be attenuated less. Hence, the ratio of the unbound to bound thiol integrals will give an upper limit for the amount of the undesired unbound thiol on the sample.

In the CF_3-Az6/CN-Az6 mixed SAM experiment (cf. Sec. 5.4) the mixed SAM consists of two almost identical components and the mixed SAM has the same structure as the 2 single component SAMs. Thus, we can assume the same attenuation for photoelectrons from the substrate for all samples. Therefore, the Au4f peak of the gold substrate could be used as an internal standard to eliminate variations in the photon flux (cf. Sec. 5.4.1).

Generally, the attenuation of the photoelectrons and thus the differences in the attenuation are less in the high kinetic energy spectra recorded with the laboratory source, than for the low kinetic energy in the spectra recorded using the synchrotron source. This allowed us to quantify the amount of H-Az11 in the H-Az11/C12 mixed SAM experiment. Here the signal of the nitrogen atoms located in the upper part of the layers was used even though the structure and thickness oft the mixed layer is different from the single component SAM used as reference. However, as the photoelectrons from the substrate have to travel through the whole layer and thus are affected more by the different attenuation, in this case the use of a substrate peak as flux standard did not seam advisable (cf. Sec. 5.5.1).

We found that spectra recorded using the synchrotron source were not suitable for quantitative analysis other than relative intensities within the same spectrum. Sample to sample variation for the same type of sample were large and did not improve when normalized to the Au4f substrate peak. The lower kinetic energy and hence larger relative difference of the peaks of the adlayer to the Au4f substrate peak may play a role. In addition, unlike the lab source with its broad illuminated area on the sample, the synchrotron beam creates a small spot on the sample that has to be carefully overlapped with the focus of the analyser. Here small variations in the sample position may impair the overlap.

4.1.10 Radiation Damage

X-ray exposure leads to radiation damage in organic samples. Thus, a compromise between exposure and statistical noise in the spectra has to be found. Radiation damage on organic samples can be reduced by cooling the sample [70]. Therefore, for all experiments with synchrotron radiation the sample was cooled using liquid nitrogen to below 95 K. In order to minimise exposure, for each spectrum a fresh spot on the sample was used, and the beam was blocked in between measurements. The spectra were recorded in several sweeps which were summed later; thus allowing to judge radiation damage from differences in the individual scans. Schmidt et al. [71], [28, p. 52] discuss radiation damage for the kind of SAMs investigated in this work in more detail and shows spectra demonstrating the effect.

4.1.11 Practical Analysis of XP-Spectra

Approximating the Voigt function Throughout this work, XPS peaks were modelled using the Voigt function. As the Voigt function has no analytical representation it was numerically evaluated. We used the rational approximation by J. Humlicek, described by F. Schreier [72], implemented in the data analysis software *Igor Pro*, and described in its documentation [73].

For the approximation, the convolution (Eq. 4.8) that describes the Voigt function is written as [72, 74]:

$$g_v(\nu - \hat{\nu}, \gamma_{\mathrm{G}}) = \frac{\sqrt{\ln 2/\pi}}{\gamma_{\mathrm{G}}} K(x, y); \quad K(x, y) = \frac{y}{\pi} \int_{-\infty}^{\infty} \frac{e^{-t^2}}{(x-t)^2 + y^2} \mathrm{d}t \tag{4.9}$$

Where $K(x, y)$ is the function actually approximated.[4] Its parameters are defined as:

$$x = \frac{\sqrt{\ln 2}}{\gamma_{\mathrm{G}}}(\nu - \hat{\nu}) \quad \text{and} \quad y = \sqrt{\ln 2}\frac{\gamma_{\mathrm{L}}}{\gamma_{\mathrm{G}}} \tag{4.10}$$

Peak Model Thus, a single Voigt peak at position $\hat{\nu}$ is described by

$$\mathrm{singlet}(\nu; \hat{\nu}, a, w, y) = a\ K\big(w(\nu - \hat{\nu}), y\big) \tag{4.11}$$

where the amplitude parameter a, the width parameter w and the shape parameter y typically are free parameters in the fit. Fitting peaks using these parameters, rather than γ_{L} and γ_{G}, for describing width and shape of the peak has the advantage that w and y are less correlated than the two widths. The fit parameters obtained in this way can be converted to the usually desired parameters area and $\gamma_{\mathrm{V,\,G,\,L}}$ using the formulas given in [73].[5] In cases where peaks are to be fitted, e.g. with a constant Gaussian width γ_{G} the peak function has to be parametrised using $\gamma_{\mathrm{G,L}}$.

For the S2p and Au4f peaks doublets of two Voigt peaks with common width, shape, and amplitude parameters were used. The ratio r of the two components was fixed to the theoretical value and a constant doublet splitting s was used:

$$\mathrm{doublet}(\nu; \hat{\nu}, a, w, y; r, s) = \mathrm{singlet}(\nu; \hat{\nu}, a, w, y) + r \cdot \mathrm{singlet}(\nu; \hat{\nu} + s, a, w, y) \tag{4.12}$$

---

[4] This is the function voigt(x,y) in Igor Pro.

[5] Note that in here and in [73] the *half* width at half maximum γ is used.

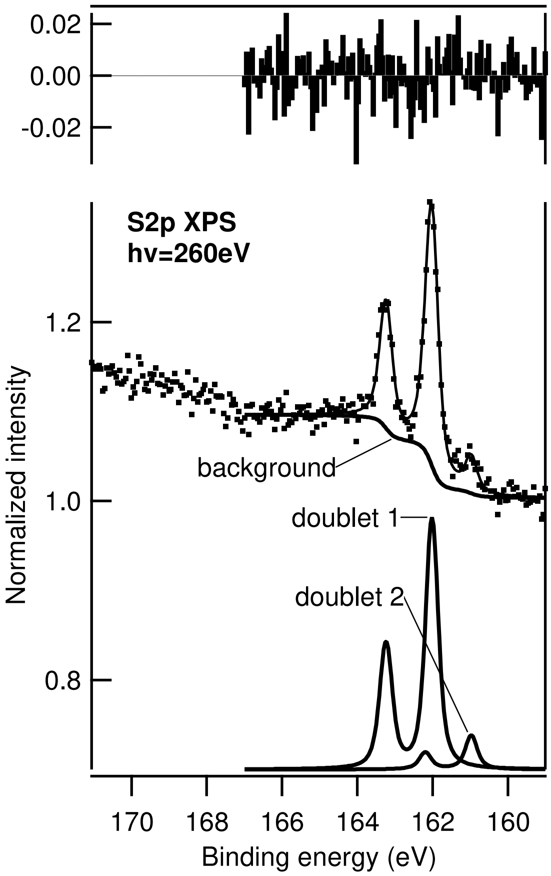

Figure 4.5: Decomposition and fit residuals of an S2p XPS spectrum: The peak is decomposed into two Voigt doublets and a Shirley type background. No slope in the linear component was required. Thus, $m = 0$ was held fixed during the fit. The residuals show that the data is well described by the model. Intensities were normalized to the right background. sample: SAM of H-Az11 on gold/mica.

Background Model Generally a combination of linear and Shirley type background was used. Rather than determining the Shirley background from the measured data as described in the original procedure [68] the peak model was integrated:

$$\text{background}(\nu; \text{peak parameters}) = m\nu + b + p\int_{\infty}^{\nu} \mathrm{d}\nu' \text{peaks}(\nu'; \text{peak parameters}) \tag{4.13}$$

This allows to determine the background parameters m, b, and p together with the peak parameters in the same fit.

Fit Example In order to decompose the S2p spectrum in the example (Fig. 4.5) into two doublets the following peak function was used

$$\begin{aligned}\text{peaks}(\nu; \hat{\nu}_{1,2}, a_{1,2}, w_{1,2}, y_{1,2}; r, s) &= \text{doublet}(\nu; \hat{\nu}_1, a_1, w_1, y_1; r, s) \\ &+ \text{doublet}(\nu; \hat{\nu}_2, a_2, w_2, y_2; r, s)\end{aligned} \tag{4.14}$$

Thus, the complete model to be fitted including linear and Shirley type background is:

$$\begin{aligned}&\text{fitfunction}(\nu; m, b, p, \hat{\nu}_{1,2}, a_{1,2}, w_{1,2}, y_{1,2}; r, s) \\ &\quad = m\nu + b + p\int_{\infty}^{\nu} \mathrm{d}\nu' \ \text{peaks}(\nu; \hat{\nu}_{1,2}, a_{1,2}, w_{1,2}, y_{1,2}; r, s) \\ &\quad + \text{peaks}(\nu; \hat{\nu}_{1,2}, a_{1,2}, w_{1,2}, y_{1,2}; r, s)\end{aligned} \tag{4.15}$$

The parameters $m, b, p, \hat{\nu}_{1,2}, a_{1,2}, w_{1,2}, y_{1,2}$ were free parameters, $r = 1/2$ and $s = 1.22\,\mathrm{eV}$ were constants. s was obtained from previous fits of a single doublett to spectra that could be well described using only 1 peak.

4.2 NEXAFS Spectroscopy

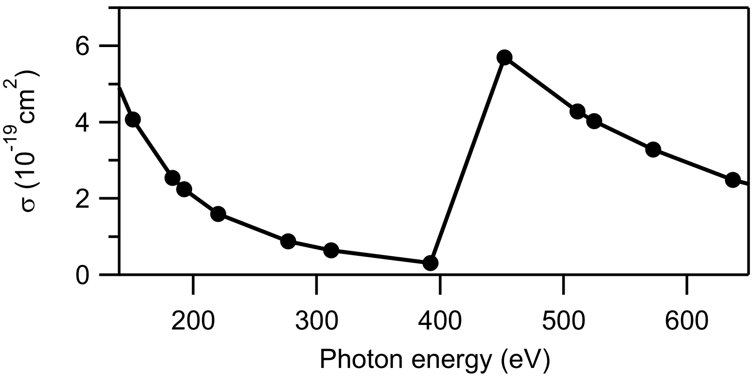

Figure 4.6: N1s atomic absorption coefficient σ as a function of photon energy: Data from [75].

The principles and details of Near Edge X-Ray Absorption Fine Structure (NEXAFS) spectroscopy are described in the classical book by Stöhr [76]. Here we will only briefly summarise some general aspects and focus on the discussion of aspects specific for this work, i.e. the specific sample geometry of our set-up; processing of Auger yield spectra for the specific case of adsorbates on gold; and the determination of the orientation of the adsorbate molecules on the surface.

In X-ray absorption spectroscopy the absorption is measured as a function of photon energy and polarization of the X-rays. The intensity of the absorption is described by the photoelectron cross section σ. Using Fermis Golden Rule in dipole approximation the following expression can be derived [76, eq. 2.8]:

$$\sigma = \frac{4\pi^2\hbar^2}{m_e^2}\frac{e^2}{\hbar c}\frac{1}{h\nu}\left|\langle f|\vec{e}\cdot\vec{p}|i\rangle\right|^2 \rho(E_f) \tag{4.16}$$

Where $\vec{e}$ is the unit vector pointing in direction of the electric field; $\vec{p}$ is the momentum operator; and $|i\rangle$ and $|f\rangle$ are the initial and final states; $\rho(E_f)$ is the density of final states.

Figure 4.6 shows the photoabsorption cross section of nitrogen. At about 400 eV the ionisation potential of the 1s electrons is reached and photoemission from the 1s level becomes possible and the cross section increases sharply. This feature is known as the N1s photoemission *edge*. The nonzero cross section in the pre-edge region is due to photoemission from valence levels.

For photon energies above the ionisation potential there always exists a vacuum state that is compatible with the selection rules for the transition. Thus, direct photoemission occurs. For light elements the initial state is always a 1s level; for direct photoemission, the final states in Eq. 4.16 are free electron states. The cross section for direct photoemission smoothly decreases with increasing photon energy.

4.2.1 Spectral Features

In NEXAFS Spectroscopy the X-ray absorption in the vicinity of the edge is investigated. Figure 4.7 shows such a spectrum. In addition to the direct photoemission edge, resonances are observed. In a molecular orbital picture, resonances are transitions into unoccupied molecular orbitals. In the pre-edge region the final states lie below the ionisation potential, i.e. are bound states. For resonances above the edge

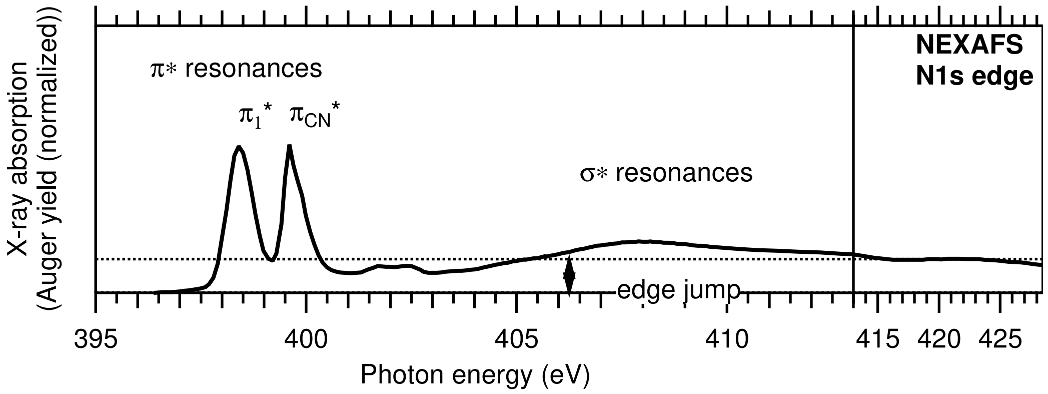

Figure 4.7: N1s NEXAFS spectrum: sample: CN-Az6 SAM on gold, magic angle spectrum, complete NEXAFS data: Fig. 5.5.

the final states lie above the ionisation potential, i.e. are unbound states. They subsequently decay into free electron states. The states above the ionisation potential can also be described by scattering of free electrons at potential wells, where the electrons are trapped by the potential shape, but have a probability to tunnel out of the well. This description leads to the term *shape resonance.*

Molecular orbitals can be classified according to their symmetry:

π **Orbitals** possess a nodal plane and are antisymmetric with respect to this plane. The π bonds in double and triple bonds and aromatic systems are formed of the p orbitals of the involved atoms. In aromatic systems the bonding π (and antibonding $\pi^\star$) orbitals are delocalised and have the same nodal plane, which is the plane of the aromatic ring. The corresponding antibonding orbitals are denoted $\pi^\star$ orbitals and have the same symmetry. $\pi^\star$ resonances are transitions to these orbitals. Typically $\pi^\star$ orbitals are bound states. Therefore, these resonances are usually sharp.[6] The excited state subsequently decays by fluorescence or Auger decay. For light elements Auger decay is the dominating process and limits the lifetime of the excitation and the line width of the resonance. For nitrogen a lifetime of about 6 fs corresponding to a line width of 0.1 eV has been estimated [76, p. 14]. Vibrational broadening leads to the observed fwhm of ≈ 0.7 eV for the N1s $\pi^\star$ resonances in the example spectrum in Fig. 4.7.

σ **Orbitals** are symmetric with respect to a symmetry plane through the bond axis and possess no nodal plane. In organic molecules the single bonds and the first bonds of multiple bonds and aromatic systems are σ bonds. Their orbitals have a localised character and a lower energy than those of the π bonds. Correspondingly, the antibonding $\sigma^\star$ orbitals have higher energies than the $\pi^\star$ orbitals and typically lie above the ionisation potential. Thus, the $\sigma^\star$ orbitals are observed on top of the direct photoemission background. Due to the overlap with the vacuum states, i.e. the states of free electrons, these excited states have a reduced lifetime and are correspondingly broad. Even though the σ orbitals of single bonds are localised, the $\sigma^\star$ orbitals of different bonds may overlap and thus may hybridise.

---

[6] The broad $\pi^\star$ structures in C1s NEXAFS spectra presented in this work are the result of overlapping excitations at all the different C cores of the aromatic system.

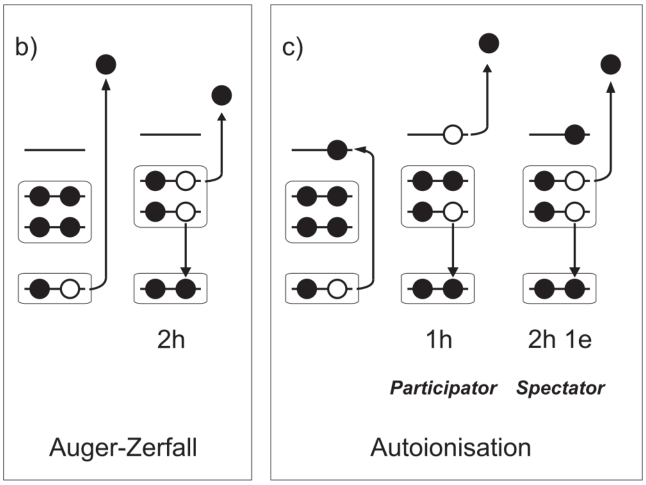

Figure 4.8: Auger decay in carbon: *left: Normal Auger decay, i.e. following direct photoemission:* An X-ray photon is absorbed and a 1s electron is emitted, i.e. excited into an unbound state. An atom with 1 core hole remains. In the Auger decay an electron from the valence orbitals fills the hole and the energy is transferred to a second valence electron, the Auger electron. The Auger electron is emitted. The kinetic energy of the Auger electron is independent of the photon energy initially used to create the core hole. *right: Auger decay following resonant excitation, i.e. autoionisation:* An X-ray photon is absorbed and excites a 1s electron into a resonance. The core hole is then filled by a valence electron. The energy is either transferred to the excited electron (participator decay) or another valence electron (spectator decay). The participator decay leads to the same final state with a single hole in the valence band as direct photoemission from the valence band. Thus, the participator electron has the same kinetic energy as the corresponding photoelectron. The electron emitted in the spectator autoionisation process has an energy slightly higher than the one of the normal Auger process. When NEXAFS resonances are excited, the electrons detected in Auger yield stem from autoionisation processes. (Figure from [28])

NEXAFS-Spectra of Large Molecules The simplest approach to describe the spectra of large molecules is the building block approach. Here the spectrum of a molecule is described as a linear combination of spectra of $\sigma^\star$ and $\pi^\star$ resonances associated with diatomic building blocks. Obviously, this approach is of limited use for the large conjugated aromatic systems present in the molecules investigated in this work. However, it is still useful to understand differences caused by substituents that add localised features to a larger system.

For the interpretation of the spectra in this work the results of ground state molecular orbital calculations were used. The LUMOs obtained in this way can still be classified according to their symmetry as π-type.

While in this work simulations of NEXAFS spectra were not available, spectra of azobenzene derivatives have been simulated using the StoBe code [77].

4.2.2 Detection Principles

For adsorbates on surfaces X-ray absorption is normally detected through electrons emitted by secondary processes. For light elements like carbon and nitrogen, Auger decay is the main secondary process, much favoured over fluorescence, the main decay channel of heavy elements. We assume the amount of Auger electrons created is proportional to the X-ray absorption cross section above the pre-edge threshold. The Auger process is summarised in Fig. 4.8. Commonly three methods are used to detect the electrons emitted in the X-ray absorption process: Auger electron yield, partial electron yield and total electron yield. They are described and compared in great detail in [76]. Here we will only give a brief overview.

Auger Yield This is the method used in this work and will be described in more detail in Sec. 4.2.3. In this method the Auger electrons emitted by the sample are detected by the same electron analyser as used for XPS. It is set to the fixed energy of the Auger electrons while the photon energy is scanned. Unfortunately the detection window of the hemispherical electron analyser is only a fraction of the width of the Auger peak. This and the limited acceptance angle lead to a relatively low sensitivity. On the other hand, of all the methods discussed here, this method should have the most favourable signal to background ratio as only few electrons having the same energy as the Auger electrons originating in other processes, add to the recorded signal.

Partial Electron Yield In partial electron yield all electrons with a kinetic energy above a threshold energy set below the Auger energy are counted using a retarding grid detector. This technique is more sensitive than the Auger yield method for several reasons: The whole Auger peak is within the detection range and the retarding grid analyser has a larger acceptance angle than the hemispherical electron analyser used for Auger yield. In addition, Auger electrons that experienced an energy loss due to inelastic scattering are also detected. However, photoelectrons and secondary electrons created by absorption processes other than the absorption edge of interest also contribute to the signal. Thus, the increased sensitivity compared to the Auger yield method comes at the expense of a larger background.

Total Electron Yield In total electron yield the sample current is measured, i.e. all electrons leaving the sample contribute to the signal. This method gives the largest signal as all secondary electrons of the initial Auger process are recorded and no electrons are lost due to a limited angular acceptance of a detector. However, this is at the expense of a very large background. Typically only about 1% of the signal originates from the adsorbate [76, p. 128]. The background mainly consists of secondary electrons of the substrate.

4.2.3 Practical Auger Yield NEXAFS

4.2.3.1 Set-up and Electron Detection

The set-up is the same as used for XPS. The detection geometry is shown in Fig. 4.9. In contrast to the XPS measurements, horizontally polarized X-rays are used. This is to reduce the contribution of photoelectrons to the measured signal, as they are primarily emitted in the direction of the electric field. For polarization dependent measurements the sample can be rotated around the direction of incidence. Typically spectra were recorded in the s- and p- polarized geometry shown and at an intermediate rotation, the magic angle (cf. Sec. 4.2.5). The emitted Auger electrons were detected from the top using the same hemispherical analyser as used for XPS.

The electron analyser was set to a fixed detection energy for each edge and maximum pass energy to give the widest possible detection window and maximum transmission. Figure 4.10 shows the detection window and electron spectra recorded for various photon energies in the NEXAFS range. In the post-edge region above the resonances the spectrum predominantly consists of the broad Auger peaks caused by

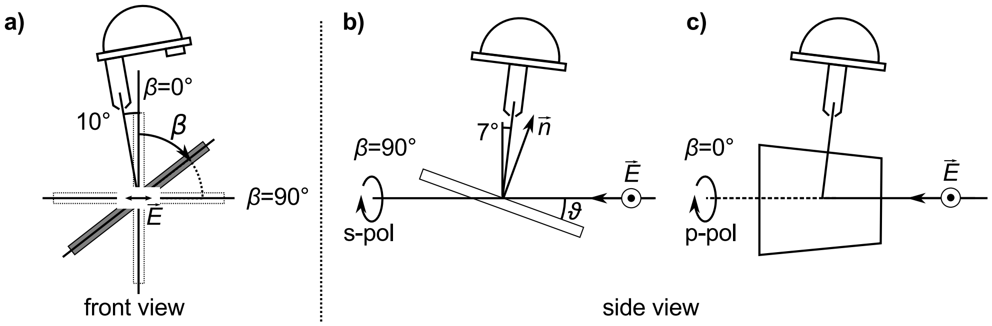

Figure 4.9: NEXAFS measurement geometry: **a)** *View onto the sample in direction of the X-ray beam.* The sample can be rotated around the direction of incidence. β is the sample rotation. Radiation with horizontal polarization is used. Thus, the emitted Auger electrons are detected in a direction nearly perpendicular to the electric field, minimising the contribution of photoelectrons to the signal. **b, c)** *View from the side.* **b)** *sample orientation for s-polarized measurements:* The sample is tilted by ϑ=20° with respect to the direction of incidence in order to create a spot on the sample. The paper plane is the plane of incidence. **c)** *sample orientation for p-polarized measurements:* The sample is rotated by 90° compared to b). Now the plane of incidence is perpendicular to the paper plane and thus the radiation is p-polarized. The analyser is rotated by 10° out of the paper plane (see a)) so that electrons can be detected from the top in this geometry. For some measurements angles of β up to 20° were used in order to facilitate electron detection further. In all cases the radiation is predominantly p-polarized, with a small s-polarized component. Hence, the spectra are denoted p-pol. For the calculation of the molecular orientation always the actual value of β was used.

the normal Auger effect following direct photoemission. In the pre-edge region the $\pi^\star$ resonances decay via autoionisation (cf. Fig. 4.8). The spectator peak is shifted towards higher electron energies with respect to the Auger peak. The detection window is small compared to the broad peaks. Thus, while scanning the photon energy in the NEXAFS spectrum, the Auger (autoionisation) peaks may partly move out of the window. This may lead to distortions in the spectrum, i.e. the relative intensities of different resonances in the spectrum may be affected. However, this does not affect the relative intensities of the same resonance for different polarizations, which is important for the determination of the molecular orientation.

NEXAFS spectra were recorded by scanning the photon energy stepwise. After each data point a photo diode is moved into the beam and the diode current, which is needed for the normalisation, is measured. The diode is left in the beam to act as a beam block while undulator and monochromator of the beamline are moved to the next energy to minimize X-ray exposure of the sample.

In order to minimize the effect of beamdamage for the most relevant features further, the photon energy range was split in up to 4 overlapping intervals that were scanned with different step width: First the $\pi^\star$ resonances required for the molecular orientation were scanned with high step density, the post edge region was scanned last with lower resolution. Also to reduce beamdamage, as discussed in Sec. 4.1.10, samples were kept below 100 K, were placed out of the focus of the beam and for each scan a fresh spot on the sample was used. A repeated scan on the same spot usually showed minor changes in the spectrum only.

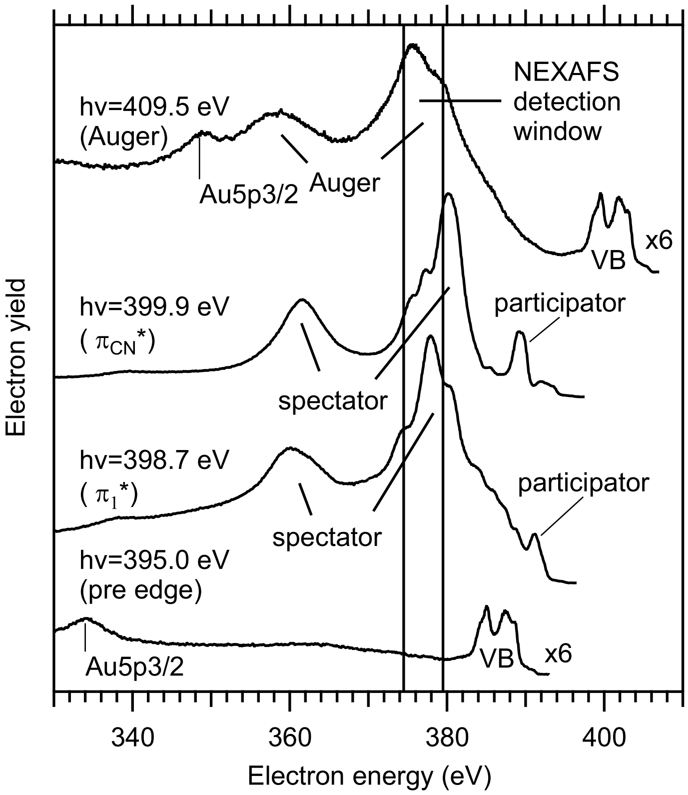

Figure 4.10: Electron spectra corresponding to the N1s NEXAFS spectra in Fig. 4.7: For photon energies in the post-edge region (*top*) direct photoemission takes place and the subsequent Auger emission is observed in the electron spectrum. The KLL Auger structure has a 2-fold structure caused by the different energies from which the valence electrons may be emitted. In addition, the $Au5p_{3/2}$ photoemission peak and photoemission from the valence band (VB) is observed. In the pre-edge region below the $\pi^\star$ resonances (*bottom*) the photon energy is not sufficient to excite N1s core electrons. Thus, no Auger emission occurs and only the $Au5p_{3/2}$ and VB photoemission peaks are observed at electron energies that moved with the photon energy. In the pre-edge region short before the edge (*middle, bottom*) $\pi^\star$ resonances are excited. These states decay by autoionisation. The main decay channel is spectator decay and the resulting structure exhibits a similar 2-fold structure as the Auger peak. The structure is superimposed by participator peaks. A prominent participator peak is observed right of the spectator structure. The $Au5p_{3/2}$ and VB photoemission peaks are only weakly visible in these spectra, as their intensity is small compared to the autoionisation features. The spectator peaks of the $\pi^\star$ resonances are shifted with respect to the Auger peak and each other. Because the electron detection window is small compared to the peak structures, only a small part of the electrons are recorded and the Auger/resonant photoemission peaks move over the detection window while the NEXAFS spectrum is scanned. This may lead to distortions in the NEXAFS spectrum. Note that the top and bottom spectrum have been enlarged as indicated because of the lower intensities before and after the resonance. sample: CN-Az6 SAM on gold.

4.2.3.2 Normalisation and Background Correction

The raw spectra acquired as described above, need to be normalized for further analysis. Various options for the normalisation and background correction for different kinds of samples (and detection methods) are discussed in detail in [76]. Here we will focus on the method used in this work for the specific case of adsorbates on gold measured in Auger yield.

The incident X-ray flux of the beameline varies with the energy of the radiation and time. Therefore, the electron yield $A(h\nu)$ needs to be divided by the photon flux, i.e. the number of photons per unit time at the time when the datapoint was measured.

The diode current $d(h\nu)$ recorded after each datapoint is proportional to the photon flux and the photon energy. We neglect the photon energy dependence for the energy range of a NEXAFS spectrum.[7] Therefore, we can normalize the electron signal to the photon flux by dividing by the diode current and obtain:

$$A_{\text{norm1}}(h\nu) = \frac{A(h\nu)}{d(h\nu)} \tag{4.17}$$

This signal still contains the secondary electron background, that we assume to be in first order independent of the photon energy. At photon energies below the resonances no Auger electrons are created, and thus the signal is the pure background. This pre edge intensity is subtracted in the 2nd step of the normalisation:

$$A_{\text{norm2}}(h\nu) = A_{\text{norm1}}(h\nu) - A_{\text{norm1}}(h\nu_{\text{pre}}) \tag{4.18}$$

For the determination of the molecular orientation, spectra are recorded in different sample geometries with different detection efficiencies for the Auger electrons. Above the resonances the spectrum is flat and the photoemission probability from the anisotropic 1s levels is independent of the orientation of the electric field vector of the radiation. Therefore, the theoretical X-ray absorption should be the same. This allows to normalize the spectra at an arbitary point E_{post} in the post edge region to give an edge jump of 1:

$$A_{\text{norm3}}(h\nu) = \frac{A_{\text{norm2}}(h\nu)}{A_{\text{norm2}}(h\nu_{\text{post}})} \tag{4.19}$$

Figure 4.11 shows the raw electron signal, the diode current and the normalized spectrum for a SAM on gold as an example.

The normalisation procedure described here has been applied to all NEXAFS data in this work. For some C1s spectra additional false light effects were corrected (cf. Sec. 4.2.3.3).

Limitations The electron background of the substrate is not completely constant. The contribution of secondary electrons, following processes with binding energies much below the photon energy, increases with the photon energy.[8] This contribution,

---

[7] The energy dependence of the sensitivity of the photo diode leads to an error for C1s spectra of up to 15%. It could easily be taken into account in future works by dividing the electron signal additionally by the photon energy. However, all spectra are affected in the same way and the $\pi^\star$ resonances used to compute orientational angles are at the beginning of the spectrum and therefore less affected.

[8] This may have been compensated in part by not taking into account the energy dependence of the sensitivity of the photo diode.

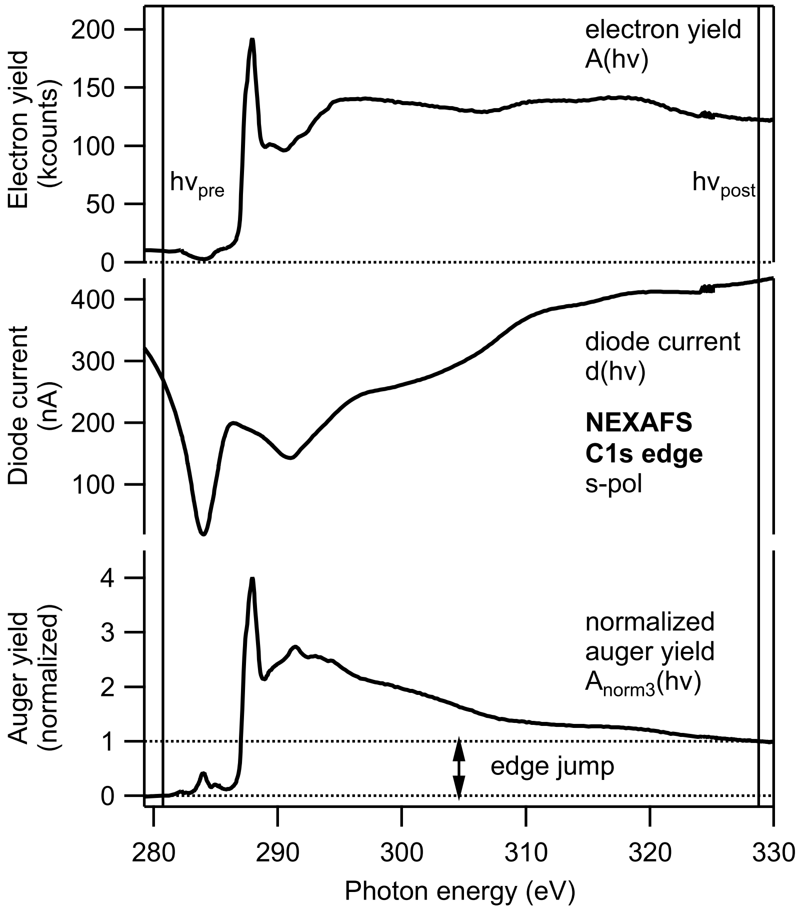

Figure 4.11: Normalisation of NEXAFS spectra: raw signal of Auger electron yield *(top)*, diode current used as measure of the photon flux *(middle)*, normalized spectrum as described in the text *(bottom)*. The feature at 284 eV in the normalized spectrum is an artefact due to the carbon dip (cf. Sec. 4.2.3.3). sample: C12 SAM on gold, complete NEXAFS data: Fig. 5.5.

however, is smooth. In contrast, direct photo emission peaks (XPS peaks) that move through the detection window when the photon energy is scanned may cause additional features. They may appear as peaks in the NEXAFS spectrum, because the kinetic energy of the photo electrons changes with the photon energy, while the detector is set to the fixed kinetic energy of the Auger electrons. The photon energy at which the photoemission peak appears is given by:

$$h\nu = E_{\text{kin}} + E_{\text{bind}} + \Phi \tag{4.20}$$

Where E_{kin} is the nominal electron energy of the analyser used to detect the Auger electrons, E_{bind} the binding energy of the photoemission peak and Φ the workfunktion of the analyser. These effects can be reduced by subtracting a clean substrate spectrum.[76, Chap. 5] For the case of gold there is only the weak $5p_{3/2}$ photoemission peak with $E_{\text{bind}} = 57\,\text{eV}$[78] appearing at about $h\nu = 320\,\text{eV}$ in the C1s NEXAFS. ($E_{\text{kin}}^{\text{nominal}} = 259\,\text{eV}$). This peak becomes only visible at low coverages, i.e. in the case of TBI (6.3). In the N1s NEXAFS range gold has no photoemission peak. Therefore, no correction in addition to the normalisation procedure shown above was applied.

The normalisation to an edge jump of 1 (Eq. 4.19) is based on the assumption that the X-ray absorption in the post-edge region is independent of the polarization,

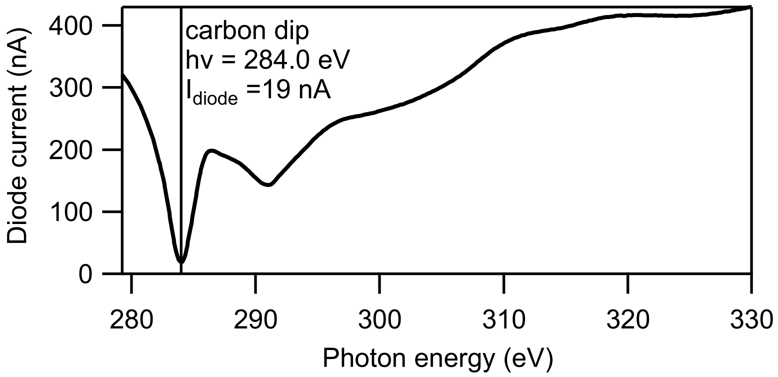

Figure 4.12: Diode current as a function of photon energy around the K-edge of Carbon.

i.e. the orientation of the electric field. In the experiment, however, the sample is rotated instead of the polarization. Thus, the orientation of the sample with respect to the analyser changes (cf. Fig. 4.9). Hence, the path of the detected Auger electrons through the adsorbate layer changes. This leads to differences in attenuation of the detected electrons for atoms with different positions in the layer. This effect may slightly distort the polarization dependence of a resonance.

4.2.3.3 X-ray Flux at the C1s Edge (Carbon Dip)

As described in 4.2.3.1, the signal of the photo diode is recorded in parallel to the Auger-electron signal as a measure of the beamline X-ray flux. The diode current is proportional to the photon flux.[9] Figure 4.12 shows the diode current as a function of photon energy around the K-edge of carbon. We observe a decrease of the photon flux by more than one order of magnitude around the minimum at 284 eV. This phenomenon is known as *carbon dip*. It is caused by elemental carbon that builds up on the X-ray optics in the beamline due to radiolysis of CO present in the vacuum system. These carbon layers, of course, absorb strongly at the C K-edge.

At first glance this reduction in intensity should not influence the NEXAFS spectra, as they are normalized to the flux by dividing through the diode current. However, the synchrotron radiation is not entirely monochromatic, but contains some false light, mainly the 2nd and 3d harmonic of the undulator that pass the monochromator in 2nd and 3rd order. In the carbon dip the intensity of the fundamental is attenuated drastically whereas the higher harmonics are not affected. Therefore, their relative contribution, which can normally be neglected, becomes notable. Due to the higher photon energy the false light generates more than proportional secondary electrons in the Auger detection window. Thus, the false light contribution to the electron signal is more than proportional.

Correction of the Electron Signal The false light contribution to the electron signal in the Auger detection window consists mainly of secondary electrons of other processes. In order to estimate the magnitude of this contribution we record an electron spectrum at a photon energy $h\nu_{\mathrm{pre}} = 281\,\mathrm{eV}$ with the same analyser settings as for NEXAFS. This photon energy is located in the pre-edge region close to the minimum of the carbon dip. Figure 4.13 shows such a spectrum.

---

[9] and the photon energy, which we can assume constant over the energy range depicted.

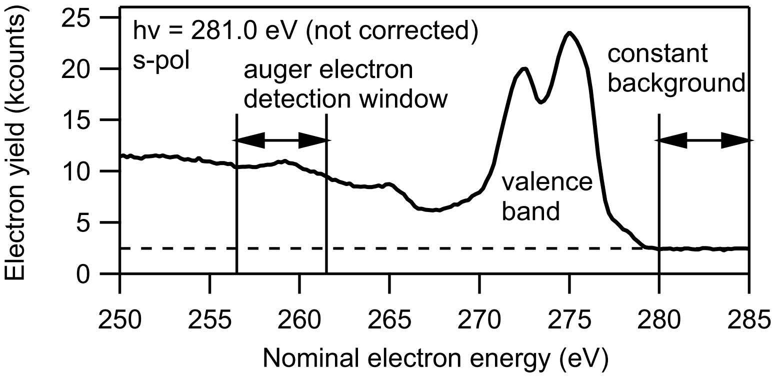

Figure 4.13: Electron spectrum recorded at a photon energy close to the minimum of the carbon dip: sample: C12 SAM on Gold.

In the figure and in the following, electron energies are uncorrected as measured. Electron energies referenced to the Fermi level would be approx. 4 eV larger.[10]

Above 280 eV nominal electron energy the photon energy is below the electron energy and there is no contribution of the fundamental to the electron spectrum. The flat spectrum in this region thus consists solely of the false light contribution. Towards lower kinetic energies the magnitude of these secondary electrons will rise. However, over the small region to the Auger detection energy we assume the false light contribution as constant and thereby obtain an approximation for the false light contribution to the NEXAFS electron signal on the low side.

In order to correct the Auger electron signal for the contribution of the false light, we assume that the absolute contribution of the false light is sufficiently constant over the energy region of the NEXAFS spectrum. We take the ratio r_A of the background above 280 eV to the mean electron signal in the Auger electron detection window. In order to obtain the corrected NEXAFS electron signal A_{corr} we subtract:

$$A_{\mathrm{corr}}(h\nu) = A_{\mathrm{raw}}(h\nu) - r_A A_{\mathrm{raw}}(h\nu_{\mathrm{pre}}) \tag{4.21}$$

In practise we did not use values at single points, but means of intervals around these points.[11] The correction r_A was obtained individually for all measurement geometries and on each sample. For SAM samples r_A was in the range 20 to 27%.

Correction of the Diode Current The diode current is of course also affected by the false light. However, the contribution is smaller for the diode current and sufficient correction was obtained without correcting the diode current. The following method was attempted to correct the diode current, but for reasons not yet understood let to an overestimation of the false light contribution and was therefore not used in the analysis:

For the energy range of the C1s NEXAFS the undulator is operated in the 1st harmonic and the monochromator is operated in the 1st order. The main contributions to the false light are the higher orders of the monochromator. If the monochromator is set to $h\nu_1$ in the 1st order, in the 2nd and 3rd order also radiation with energies $h\nu_2 = 2h\nu_1$ and

---

[10] To obtain energies referenced to the Fermi level, the nominal values need to be corrected by the work function of the analyser and errors in its energy calibration, which are high for the large path energy used to detect the Auger electrons in NEXAFS.

[11] The following regions were used: for r_A: ±2.5 eV around the Auger detection energy i.e. [280,285] eV i.e. the width of the Auger electron detection window, for $A_{\mathrm{raw}}(h\nu_{\mathrm{pre}}\,\mathrm{eV})$ the same interval as for the normalisation was used, i.e. $A([280, 281]\,\mathrm{eV})$.

$h\nu_3 = 3h\nu_1$ will pass through the monochromator. These energies coincide with the 2nd and 3rd harmonic of the undulator.[12]

For the correction, electron spectra of the 4f levels of a gold sample were recorded with the photon energy set to the minimum of the carbon dip $h\nu_1 = h\nu_\mathrm{C}$. With the argument above the total diode current d_1 can be written as.

$$d_1 = d_1^1 + d_1^2 + d_1^3 \tag{4.22}$$

Where d_1^1, d_1^2 and d_1^3 are the contributions of the 1st, 2nd and 3rd harmonic to the diode current. Correspondingly the photoelectron spectrum contains the 4f peaks of gold three times. We name the peak integrals A_1^1, A_1^2 and A_1^3.

Due to differences in the cross section and analyser transmittance depending on the photon energy the diode current can not be directly decomposed using the photo electron signals. In order to obtain the ratios of diode current to photoelectron signal, the following additional measurements are performed. The photon energy of the beamline is set to $h\nu_2 = 2h\nu_C$, however with the undulator operated in the 3rd harmonic. Now the 2nd order of the monochromator corresponds to the 6th harmonic and the 3rd order to the 9th harmonic and there is no carbon dip attenuation of the desired energy. Therefore, we can assume the radiation to be monochromatic and the diode current to be proportional to the photo electron signal and we obtain:

$$d_2 \propto A_2 \quad \text{and similar for } h\nu_3 = 3h\nu_\mathrm{C}\text{:} \quad d_3 \propto A_3 \tag{4.23}$$

Using these relations we obtain:

$$d_1^2 = \frac{A_1^2}{A_2} d_2 \quad ; \quad d_1^3 = \frac{A_1^3}{A_3} d_3 \tag{4.24}$$

For the relative contribution of the false light in the carbon dip r_d we thus obtain:

$$r_d = \frac{d_1^2 + d_1^3}{d_1} = \frac{1}{d_1}\left(\frac{A_1^2}{A_2} d_2 + \frac{A_1^3}{A_3} d_3\right) \tag{4.25}$$

Similar to (4.21) we assume that the absolute contribution of the false light to the diode current is constant over the region of the NEXAFS spectrum and obtain for the corrected diode current:

$$d_\mathrm{corr}(h\nu) = d_\mathrm{raw}(h\nu) - r_d d_\mathrm{raw}(h\nu_\mathrm{C}) \tag{4.26}$$

We obtained $r_d = 0.85$. This value leads to an overestimation. As the measurements for the diode current correction were only performed once we can not say whether these measurements were erroneous or there is a flaw in the assumptions used for the correction.

Effect of the Correction Figure 4.14 shows the low energy region of a NEXAFS spectrum of C12, a sample that does not contain any aromatic systems and therefore has no resonances near the carbon dip. A corrected and an uncorrected spectrum are shown. The artefact caused by the carbon dip and the effect of the correction of the electron signal are clearly visible. This correction is especially important for low coverage samples with aromatic systems, i.e. TBI (cf. Sec. 6.3).

4.2.4 Photon Energy Calibration

At the C1s edge the photon energy was calibrated using highly oriented pyrolytic graphite HOPG as a reference sample. Figure 4.15 shows NEXAFS spectra of the

---

[12] In the middle of the beam, the radiation leaving the undulator should only contain the odd harmonics, however, in the marginal region of the beam the even harmonics are also present. The experiment shows that the 2nd order can not be neglected. This is resonable as the 2nd harmonic coincides with the 2nd order of the monochromator, which has a higher transmission then the 3rd order. Thus, the contribution of the 2nd harmonic to the falselight is enhanced with respect to the 3rd.

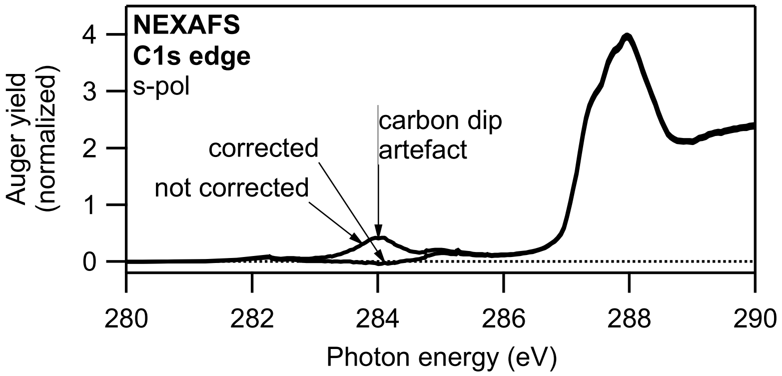

Figure 4.14: Effect of false light correction at the C1s edge: Uncorrected spectrum and spectrum corrected for the false light contribution in the electron signal. The artefact caused by the carbon dip and the effect of the correction are clearly visible. sample: SAM of C12 on gold/mica. The full spectrum is shown in Fig. 5.5.

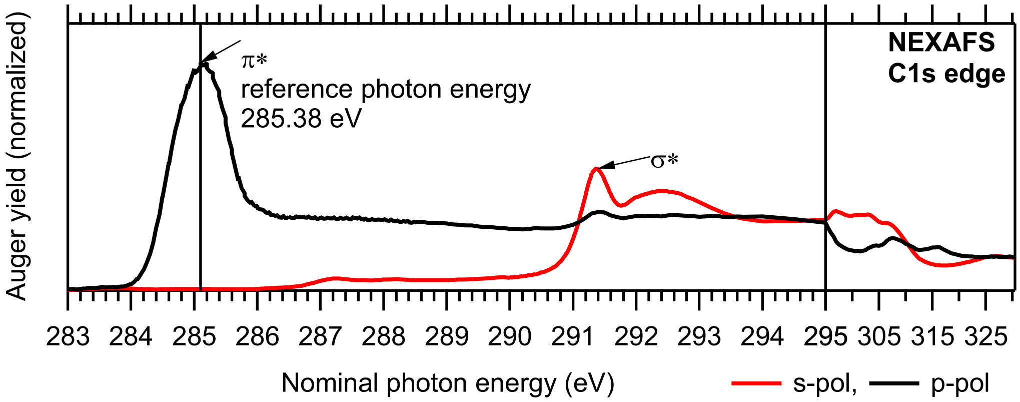

Figure 4.15: C1s NEXAFS spectra of highly oriented pyrolytic graphite (HOPG) used for photon energy calibration at the C1s edge.

reference sample. The layers of the graphite were oriented in the sample plane and therefore also the aromatic rings. Therefore, the $\pi^\star$-transition is only visible in the p-pol spectrum, while the $\sigma^\star$ structure is only visible in the s-pol spectrum. The $\pi^\star$ peak at $285.38 \pm 0.05\,\text{eV}$ [79] is used as reference for the calibration by an offset. The calibration was conducted once per beamtime.

At the N1s edge the photon energy can be calibrated using elemental N_2 in a gas cell and detecting the transmission using a photodiode. Unfortunately this calibration was not available during the cause of this work. In order to make spectra of different beamtimes comparable offsets were applied so that the same $\pi^\star$ feature on the same kind of sample appears at the same position. One beamtime was arbitrarily chosen as reference. The same technique was used at the carbon edge for beamtimes where no reference sample had been measured to indirectly calibrate the spectra to the graphite reference.

Energy corrections were always below 0.5 eV (Details in Sec. 7.8).

4.2.5 Determination of Molecular Orientation

The dependence of the X-ray absorption on the orientation of the electric field allows to determine molecular orientations from measurements of the absorption intensities for different orientations of the sample surface to the electric field $\vec{E}$ of the linearly

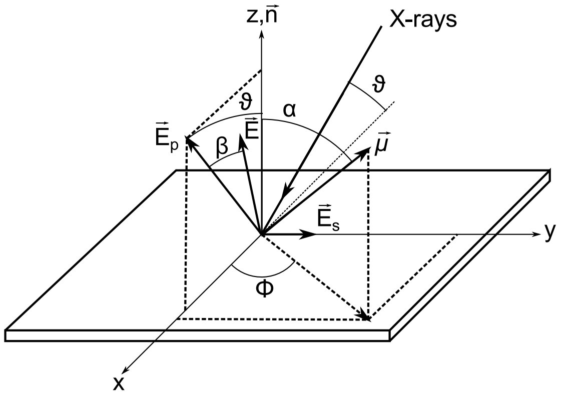

Figure 4.16: Definition of the angles used to calculate the molecular orientation: The coordinate system is the sample coordinate system. The surface normal $\vec{n}$ is the z-axis. The X-rays incide in the (x, z) plane. ϑ is the angle between the incidence direction and the x-axis. $\vec{E}$ is the electric field vector of the linearly polarized radiation. β is the angle by which $\vec{E}$ is rotated out of the incidence plane (x, z). β and ϑ are the same as in Fig. 4.9. $\vec{E}$ can be decomposed into a component parallel to the incidence plane $\vec{E}_p$ and a component perpendicular to the incidence plane $\vec{E}_s$. ϑ is also the polar angle of $\vec{E}_p$. $\vec{\mu}$ is the transition dipole moment of the NEXAFS resonance α is its polar angle, i.e. the angle between $\vec{\mu}$ and the surface normal that is to be determined. ϕ is the orbital vectors azimuthal angle.

polarized X-rays.

The transition matrix element in Eq. 4.16 can be rewritten using the dipole operator and replacing the unit vector $\vec{e}$ with the electrical field vector $\vec{E}$ itself. Thus, the transition intensity I is proportional to the projection of the electrical field vector $\vec{E}$ onto the transition dipole moment $\vec{\mu}$:

$$I \propto \left| \langle f \, | \vec{E} \cdot \vec{r} \, | \, i \rangle \right|^2 = \left| \vec{E} \cdot \langle f | \vec{r} | i \rangle \right|^2 = \left(\vec{E} \cdot \vec{\mu} \right)^2 \tag{4.27}$$

In the case of $\pi^\star$ resonances, i.e. transitions from isotropic 1s orbitals to $\pi^\star$ orbitals, the transition dipole moment $\vec{\mu}$ points in the direction of the normal of the aromatic plane. Thus, Eq. 4.27 allows us to obtain the angle α between the normal of the aromatic plane and the surface normal of the sample.

The determination of molecular orientations of adsorbed molecules from the angular dependence of NEXAFS resonances has been developed by Stöhr and Outka [76, 80]. The expressions were adapted by Schmidt [28] to our measurement geometry.

Figure 4.16 defines the angles β and ϑ, which are controlled in the experiment (cf. Fig. 4.9), and the coordinate system used in the following derivation. In this coordinate system, the sought angle α is the polar angle of the transition dipole moment $\vec{\mu}$; ϕ is its azimuthal angle. Transforming to Cartesian coordinates we obtain:

$$\vec{\mu} = \mu \begin{pmatrix} \sin\alpha\cos\phi \\ \sin\alpha\sin\phi \\ \cos\alpha \end{pmatrix} \tag{4.28}$$

In order to express the direction of the electrical field vector $\vec{E}$ in terms of the experimental angles we first decompose it into its components parallel and perpendicular to the plane of incidence $\vec{E}_p$ and $\vec{E}_s$. The representation of the two components in spherical coordinates is read from the figure and converted to Cartesian coordinates:

$$\vec{E} = \vec{E}_\mathrm{p} + \vec{E}_\mathrm{s} = E_\mathrm{p} \begin{pmatrix} \sin\vartheta\cos 0 \\ \sin\vartheta\sin 0 \\ \cos\vartheta \end{pmatrix} + E_\mathrm{s} \begin{pmatrix} 0 \\ 1 \\ 0 \end{pmatrix} \tag{4.29}$$

Using $E_\mathrm{p} = E\cos\beta$ and $E_\mathrm{s} = E\sin\beta$ we obtain:

$$\vec{E} = E \begin{pmatrix} \cos\beta\sin\vartheta \\ \sin\beta \\ \cos\beta\cos\vartheta \end{pmatrix} \tag{4.30}$$

Now we can execute the inner product (Eq. 4.27) and obtain:

$$I \propto \left(\vec{E}\cdot\vec{\mu}\right)^2 \propto (\cos\beta\sin\vartheta\sin\alpha\cos\phi + \sin\beta\sin\alpha\sin\phi + \cos\beta\cos\vartheta\cos\alpha)^2 \tag{4.31}$$

This expression still contains the azimuthal angle ϕ. For the systems investigated in this work the azimuthal dependence is eliminated by the substrate symmetry. We assume that adsorbed molecules form domains on the substrate with preferential orientation. However, depending on the substrate symmetry there will be several equivalent orientations. For threefold and higher substrate symmetry it can be shown that the contributions from different domains average out and the same result as for random azimuthal orientation is obtained [80]. All samples were on gold(111), which has a threefold symmetry. Thus, we may average over the azimuthal angle Φ by integration:

$$I(\beta) \propto \sin^2\alpha\ \left(1 - 3\cos^2\vartheta\cos^2\beta\right) + 2\cos^2\vartheta\cos^2\beta \tag{4.32}$$

Unfortunately the synchrotron radiation is not entirely polarized. Therefore, we have to take the limited degree of polarization into account. The electrical field vector can be decomposed into a component with the desired horizontal polarization E_h and a component with the perpendicular (vertical) polarization E_v. The degree of polarization P is defined as the ratio of the *intensity* with the desired polarization to the total intensity:

$$P = \frac{E_h^2}{E_h^2 + E_v^2} \tag{4.33}$$

$I(\beta)$ is the absorbed intensity for perfectly polarized light. We obtain for the absorbed intensity $I(\beta, P)$ with light with a degree of polarization P.

$$I(\beta, P) = PI(\beta) + (1-P)I(\beta - 90^\circ) \tag{4.34}$$

With the proportionality constant C we obtain:

$$\begin{aligned} I(\beta,P) = C\,\big[&P\left(\sin^2\alpha\left(1 - 3\cos^2\beta\cos^2\vartheta\right) + 2\cos^2\beta\cos^2\vartheta\right) \\ &+(1-P)\left(\sin^2\alpha\left(1 - 3\sin^2\beta\cos^2\vartheta\right) + 2\sin^2\beta\cos^2\vartheta\right)\big] \end{aligned} \tag{4.35}$$

Thus, α can be obtained from the absorbance ratio r of two measurements for two different orientations of the sample β_1 and β_2:

$$r = \frac{I(\beta_1, P)}{I(\beta_2, P)} \tag{4.36}$$

Figure 4.17 shows ratios of the absorption in the s-pol geometry to the p-pol geometry for various degrees of polarization.

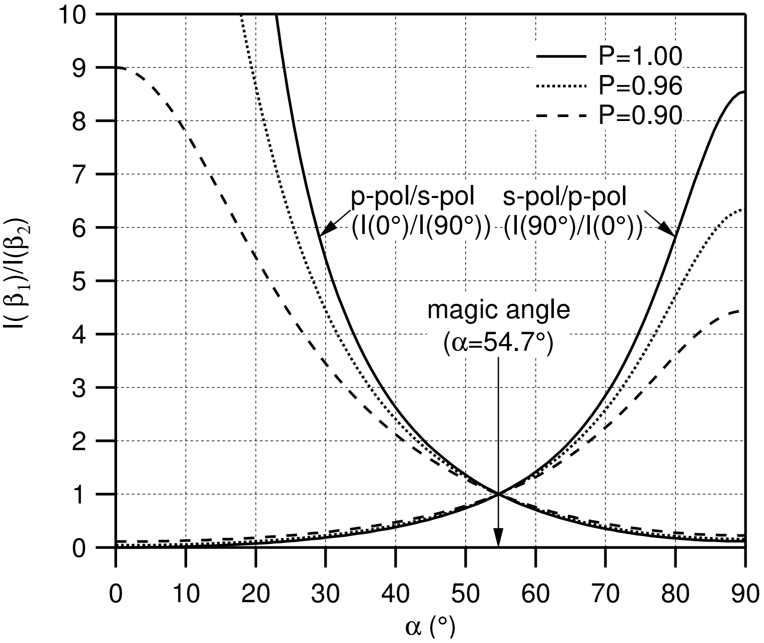

Figure 4.17: Ratio r of the X-ray absorption in the s ($\beta = 90°$) and p ($\beta = 0°$) polarized geometry (depicted in Fig. 4.9), computed according to Eq. 4.35 and Eq. 4.36 for $\vartheta = 20°$. The dependence on the degree of polarization is shown. Throughout this work a degree of polarization of $P = 0.96$ was assumed.

Practical Determination of the Molecular Orientation Figure 4.18 shows C1s NEXAFS spectra for an aromatic adsorbate on gold for different polarizations. We want to obtain the orientation of the aromatic system from the angular dependence of the $\pi^\star$ resonances. The $\pi^\star$ resonances form a complex pattern due to the overlapping of the transitions from all the different carbon cores in the aromatic system. However, as all the transitions belong to the same system, their transition dipole moments point in the same direction. In the top graph the ratio of the s- to the p-polarized spectrum is shown. It is approximately constant over the whole $\pi^\star$ structure. This corroborates that the different contributions to the structure show the same angular dependence. From the ratio the oriental angle α is obtained by solving Eq. 4.36 numerically for α. Figure 4.17 shows this relation. In order to use the data from all three orientations β Eq. 4.35 was fitted directly to the absorption intensities with C and the sought angle α as free parameters. As intensities for the ratio or the fits, the integrals of the spectra over the marked integration window were used.

Magic Angle We look again at Eq. 4.32 the absorbed intensity for 100% polarized radiation:

$$I(\beta) \propto \sin^2\alpha \, \left(1 - 3\cos^2\vartheta\cos^2\beta\right) + 2\cos^2\vartheta\cos^2\beta$$

For $\sin^2\alpha = 2/3$ the absorbed intensity is independent of the sample rotation β. For this *magic angle* $\alpha_{\text{magic}} = 54.7°$ the orientation of vector orbitals can not be distinguished from an isotropic distribution of orbital vectors. Thus, a measurement yielding a value close to the magic angle may either indicate a layer of ordered molecules with this orientation or a lack of order.

There also exists a sample rotation β for which the absorbed intensity is inde-

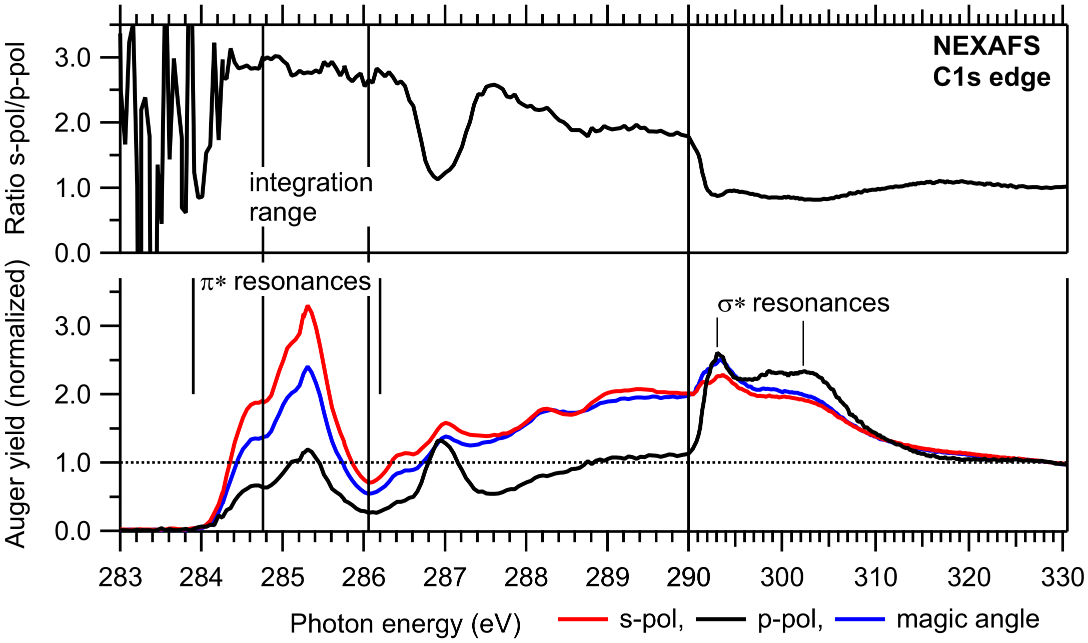

Figure 4.18: NEXAFS spectra of an azobenzene derivative on gold. Measured in the s-pol geometry (red) and p-pol geometry (black). The planar aromatic system of this compound leads to a range of overlapping $\pi^\star$resonances. The $\pi^\star$orbitals involved possess a common nodal plane. Thus, the ratio of these two spectra (top) is constant over the overlapping $\pi^\star$-resonances. Therefore, the angle α between the surface normal and the normal of the aromatic plane (orbital vector of the $\pi^\star$-orbitals) can be obtained without decomposing the resonances. Often in addition to the s-pol and p-pol spectra, spectra with an intermediate value of β were acquired. The peaks were integrated over the marked integration range and the obtained areas were fitted as a function of β according to (Eq. 4.35). sample: SAM of H-Az11 on gold.

pendent of the molecular orientation. This is the case for

$$\left(1 - 3\cos^2\vartheta\cos^2\beta\right) = 0 \tag{4.37}$$

For our set-up with $\vartheta = 20°$ we obtain $\beta_{\text{magic}} = 52.1°$.

These values were obtained for $P = 1$. For the case $\vartheta = 0°$ the two magic angles have the same value $\alpha_{\text{magic}} = \beta_{\text{magic}} = 54.7°$. We note that β_{magic} in contrast to α_{magic} depends on the degree of polarization.

4.3 Thermal Desorption Spectroscopy (TDS)

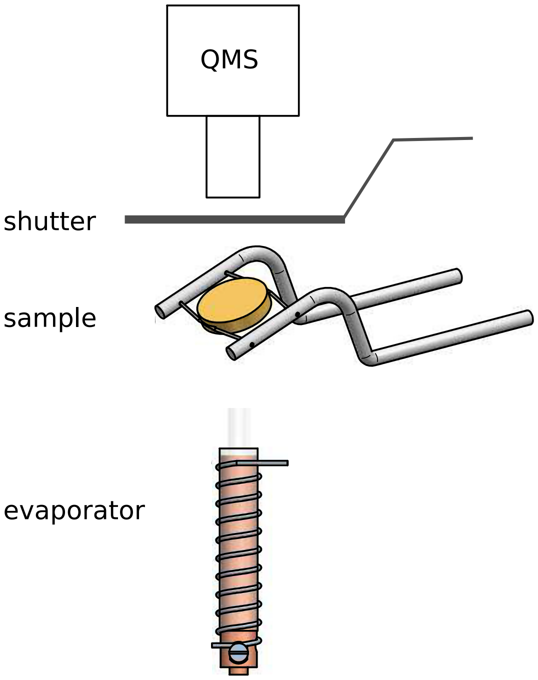

Figure 4.19: TDS set-up: The evaporator is positioned underneath the quadrupole mass-spectrometer (QMS). This allows to record mass spectra of the evaporated molecules when the sample is retracted. A shutter protects the QMS during sample preparation. The sample is rotated for deposition of the organic molecules.

Thermal desorption spectroscopy (TDS), also known as temperature programmed desorption (TPD) is a technique to investigate adsorbate layers. A mass spectrometer is used to analyse the molecules that desorb when the substrate is heated. This technique can be used to obtain binding energies of the adsorbed molecules [81]. Another application is to quantify the amount of adsorbate on a sample. In this work the technique will be used to compare the density of adsorbate monolayers with different structures.

Figure 4.19 shows a schematic of the set-up used to deposit organic layers by thermal evaporation onto the crystal and record TD spectra of the so-formed layers: The evaporator is positioned underneath the quadrupole mass spectrometer (QMS). This allows to record mass spectra of the evaporated molecules and determine the flux of the evaporator, when the sample is retracted. The sample is mounted with tantalum wire to tantalum bars attached to a liquid nitrogen cooled copper block. To heat the sample, a current is applied to the wires. This design ensures a minimal surface of the sample holder. Thereby, artefacts in the TD spectra caused by molecules desorbing from the sample holder, when the crystal is heated, are minimized.

In the following we will describe the process using data obtained for the adsorbate TBI on Au(111) discussed in detail in Chap. 6:

Figure 4.20 shows a mass spectrum of the compound to be deposited on the sample. Because the mass of the parent ion, i.e. the ion of the nondissociated molecule exceeds the range of the QMS used for the experiment, we choose a prominent fragment ion for the TDS (*tert*-butyl, M^{+}=57 amu). The residual gas spectrum shown in the bottom part of the figure shows no features at this mass.

For deposition the cooled sample is turned face down and the QMS is protected by a shutter. After deposition the sample is retracted, turned face up again, and a linear heating ramp is started while the desorbing molecules are detected by the QMS as explained in Fig. 4.21. In order to obtain an undistorted spectrum it is crucial that the temperature does not deviate from the linear ramp.

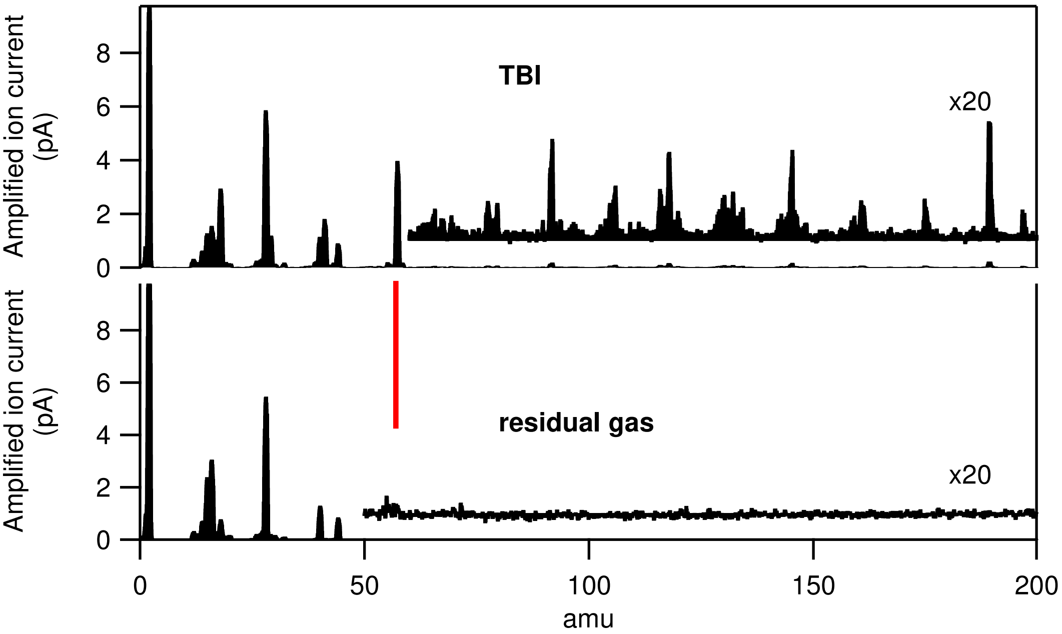

Figure 4.20: Mass spectrum of Adsorbate and Residual Gas.

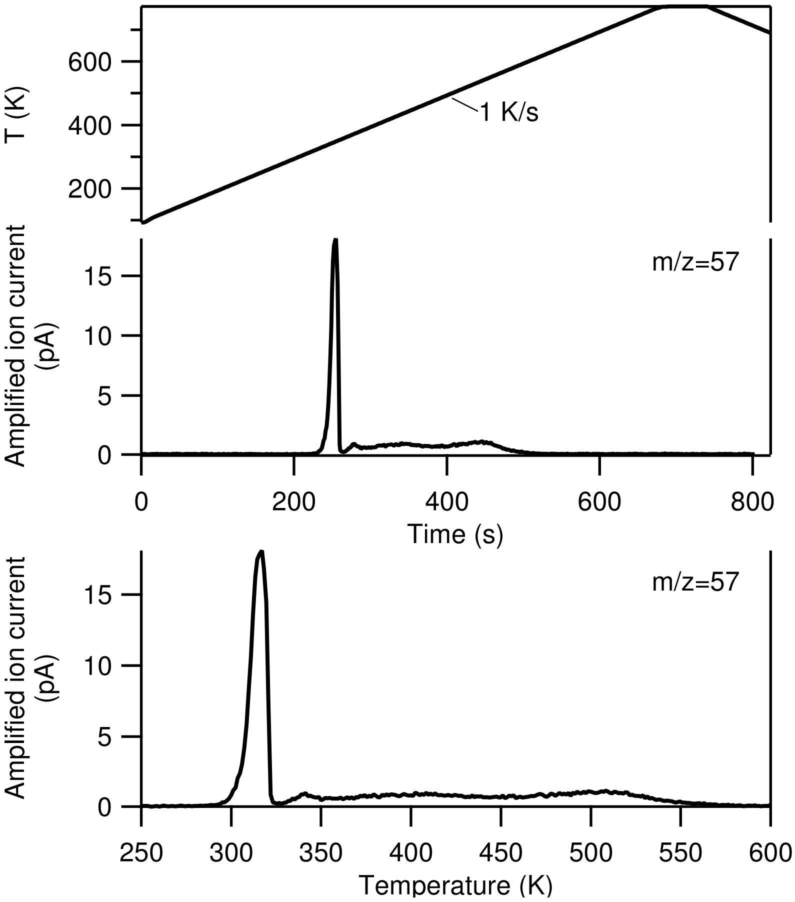

Figure 4.21: Thermal desorption spectroscopy (TDS): The substrate with the organic adlayer to be investigated is heated using a linear heat ramp controlled by a PID controller. *(top)*, while the ion current for the fixed mass of the desired ion is recorded as a function of time *(middle)*. Later the two curves are combined to give the ion current as a function of temperature, the actual TD spectrum *(bottom)*.

4.4 Differential Reflectance Spectroscopy (DRS)

In Differential Reflectance Spectroscopy the change in the specular reflectivity caused by an adsorbate on a reflective substrate—in this work a SAM on a gold substrate—is investigated. The application of this technique to thin films is well described by Forker and co-workers [11]. Here we only give a brief description of the set-up used in this work and the relevant photometric quantities.

Before we discuss DRS we briefly summarize how transmission mode spectra are recorded. The *transmission* T of a sample or optical path is defined as the ratio of the transmitted intensity I_t and the incident intensity I_0 the corresponding absorbance A is given by:

$$T = \frac{I_\mathrm{t}}{I_0}; \quad A = -\lg T \tag{4.38}$$

In a double beam spectrometer the measurement light is split into sample and reference beam with approximately equal intensity. The raw transmission T_raw is the ratio of the intensity in the sample I_s and reference beam I_r. It is corrected for intensity differences between the two beams by dividing the raw transmission T_raw by a reference measurement T_0 without a sample in the beam. Thus, we obtain for the transmission T of the sample:

$$T = \frac{T_\mathrm{raw}}{T_0}; \quad A = A_\mathrm{raw} - A_0 \tag{4.39}$$

Taking the ratio of the transmissions corresponds to the subtraction of the absorbances of the two measurements commonly referred to as *baseline subtraction.*

DRS is based on the measurement of the specular reflectance R of the sample. The reflectance is defined analogue to the transmittance as the ratio of the reflected intensity I_R to the the incident intensity I_0:

$$R = \frac{I_\mathrm{R}}{I_0} \tag{4.40}$$

We are interested in the difference between the reflectance of the substrate with R^1_sample and without R^0_sample adsorbate. In analogy to the absorbance A the DRS spectra are plotted as

$$-\Delta \lg(R) = -(\lg R^1_\mathrm{sample} - \lg R^0_\mathrm{sample}) \tag{4.41}$$

In order to measure this quantity a home build reflectance unit was installed in the double beam spectrometer (Fig. 4.22). The reflectance of the sample is measured at a fixed angle of incidence of 45°. Rotatable linear polarizers allow measurements with s- or p-polarized light. The electric field vector of s-polarized light is parallel to the sample surface, whereas p-polarized light at 45° has components parallel and perpendicular to the surface. Thus, DRS measurements with polarized light allow to obtain information about the orientation of the optical transition dipole moments in the adsorbate.

The reference beam contains no additional optical elements. The sample beam is guided by 3 aluminium mirrors onto the sample and back onto its original path. Thus, the absorbance of the sample beam is given by:

$$A = -\lg(3 \cdot R_\mathrm{mirror} \cdot R_\mathrm{sample}) \tag{4.42}$$

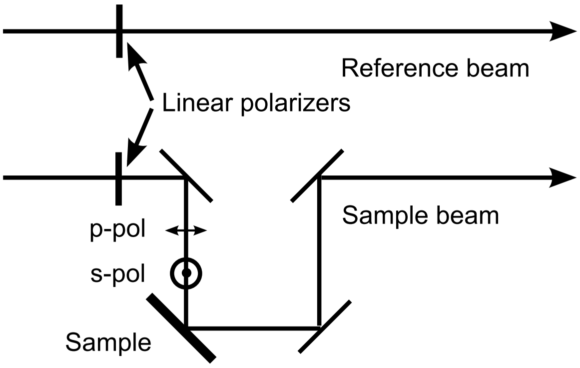

Figure 4.22: Differential reflectance unit for double beam spectrometer. image from [82, SI].

The difference in absorbance ΔA in the sample beam for the sample with and without adsorbate is thus:

$$\begin{aligned} \Delta A &= -\left(\lg(3\cdot R_{\text{mirror}}\cdot R^1_{\text{sample}}) - \lg(3\cdot R_{\text{mirror}}\cdot R^0_{\text{sample}})\right)\\ &= -\left(\lg R^1_{\text{sample}} - \lg R^0_{\text{sample}}\right)\\ &= -\Delta\lg(R) \end{aligned} \tag{4.43}$$

In this difference the reflectivity of the mirrors cancel out. For the same reason there is no need to record a baseline.

In the literature [11]

$$\frac{\Delta R}{R} = \frac{R^1_{\text{sample}} - R^0_{\text{sample}}}{R^0_{\text{sample}}} \tag{4.44}$$

is also commonly used to describe the differential reflectivity. In first order—a valid approximation for thin films—this expression is proportional to Eq. 4.43.

Figure 4.23 (top) shows the absorbance (Eq. 4.42) of the sample beam for the substrate with and without adsorbate. The resulting DR spectrum is shown in the bottom of the figure. The changes in reflectivity are small compared to the measured signal. In order to measure them reliably, the following points were considered in the design of the measurement set-up:

Subtle differences between different substrates or in the position of the substrate may spoil the measurement. Thus, the reference spectrum was always measured on the same substrate prior to deposition of the adsorbate, and a sample holder was designed to allow for exact repositioning of the substrate after adsorption of the adlayer.

As the adsorption process used to form the SAMs investigated in this work takes about a day, good stability of the measurements is required. This is ensured by the use of a double beam spectrometer, where time dependent changes in the intensity of the measurement light cancel out between sample and reference beam.

A conventional spectrometer set-up with monochromator before the sample and a photomultiplier as detector was chosen, because it offers a larger dynamic range than spectrometers that illuminate the sample with white light and record the spectrum in one shot using a CCD array. The large dynamic range is achieved by adjusting the amplification of the detector signal to the A/D-converter for each wavelength while the spectrum is scanned. For the case of molecular switches this set-up has the further advantage, that the loss in the monochromator occurs before the sample, and thus the light sensitive samples are exposed to less light than in one-shot CCD spectrometers.

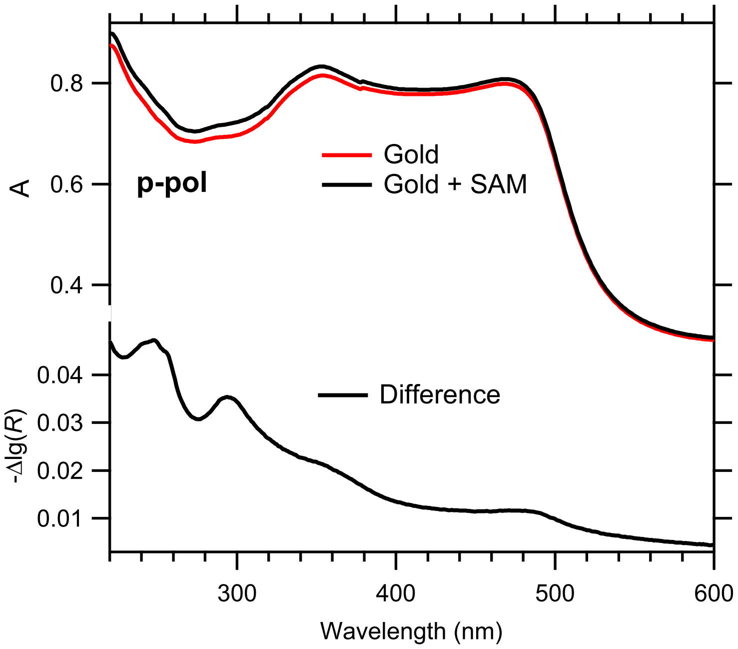

Figure 4.23: DRS Example: Absorbance of the sample beam (Eq. 4.42) for sample with and without adsorbate *(top)*. The DR spectrum is the difference (Eq. 4.43) *(bottom)*. sample: H-Az11 SAM on gold (Sec. 5.5), image from [82, SI]

Chapter 5

Azobenzene SAMs

5.1 Introduction

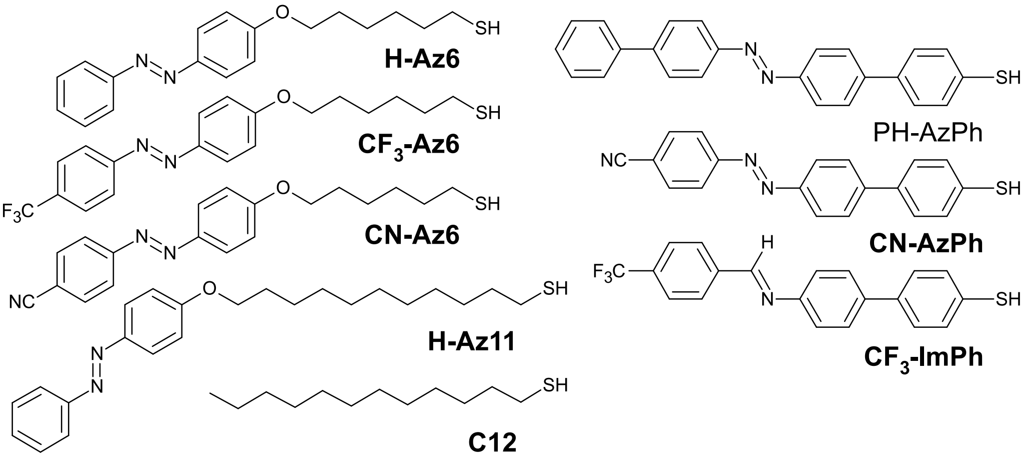

Figure 5.1: SAM forming azobenzene thiols investigated in this work.

Self-assembled monolayers are a promising approach to functionalize surfaces. The aim of this work is to integrate molecular switches into SAMs. Such systems could allow to change the surface properties such as polarity, chemical reactivity, or charge transfer characteristics at interfaces reversibly upon illumination with light of different colours.

We focus on molecular switches derived from azobenzenes. Since the interaction of the chromophore with the metal substrate may inhibit the photoisomerization [2, 27] it is desirable to separate the azobenzene unit from the surface. Attaching the azobenzene chromophore to an alkanethiol linker allows formation of SAMs in which the interaction of the chromophore with the substrate can be tuned by varying the length of the alkanethiol linker. Furthermore, these SAMs are sufficiently stable to be investigated at ambient conditions. However, in these densely packed layers the interactions of the chromophores with each other strongly influence the optical properties of the layer and the ability to switch, as we will see.

In Sec. 5.2 we will discuss our results obtained for SAMs of H-Az6, CF_3-Az6 and CN-Az6 (Fig. 5.1) as prototypes of this chromophore linker concept. XPS was used to investigate the composition of these SAMs. Combining the molecular orientations with respect to the surface obtained from NEXAFS data with literature AFM/STM data, which provides information on the lateral structure, a model of the structure of these SAMs was developed. Differential reflectance measurements in the UV/vis range reveal strong lateral interactions of the chromophores. We demonstrate that in these systems coupling of transition dipole moments leads to excitonic band formation. These findings are further corroborated by the comparison of the DR spectra of the SAMs with optical spectra of films and aggregates formed in solution by the same compounds. The photoisomerization, however, was found to be inhibited in these systems.

For SAMs of Ph-AzPh, an azobenzene derivative with an aromatic linker, the formation of similarly densely-packed layers, which are readily photoisomerizable, had been reported [6, 83, 84]. Therefore, we also investigated SAMs with an aromatic linker. In Sec. 5.3 we present our results on CN-AzPh, an azobenzene derivative, and CF_3-ImPh, an imine, both with aromatic linkers. We were able to produce well ordered, densely packed SAMs from these compounds. However, up until now, we have no evidence for photoisomerization of these compounds.

The strong lateral interactions between the chromophores observed for the R-Az6 SAMs and the different positions of the absorption bands depending on the substituent suggest that it should be possible to tune the strength of the excitonic coupling by mixing two chromophores in one SAM. In Sec. 5.4 we report on our results on such a mixed SAM of CF_3-Az6 and CN-Az6. The similarity of the two thiols allowed us to produce mixed SAMs by coadsorption from solution. We show that both pure SAMs as well as the mixed SAM have the same structure at the surface. The different end groups were used as markers for XPS and allowed independent quantification of both components at the surface. The composition of the SAM as a function of the composition of the adsorption solution was found to be in good agreement with a simple thermodynamic model assuming attractive interactions of equal magnitude between the two pairs of like molecules and between unlike molecules. XPS peaks that shift continuously with the composition of the SAM show that no phase separation occurs in the mixed SAM. An analysis of these peak shifts further suggests that XPS peak positions for densely packed SAMs have to be described by a local potential caused by the environment of the chromophore rather than a purely intra molecular picture. The aggregate peak in the UV/vis DR spectra of these mixed SAMs shifts continuously with the composition at the surface, demonstrating that the excitonic coupling can indeed be tuned. Not unexpected, no photoisomerization was observed for these mixed SAMs.

Steric hindrance appears to be the most likely cause for the failure to photoisomerize of the R-Az6 SAMs. This view is further corroborated by the observation that azobenzene alkanethiols form photoisomerizable layers on nanoparticles where the chromophore density is reduced due to the curvature of the substrate [85], and mixed SAMs prepared form asymmetric disulphides in which the chromophores are diluted by spacer molecules [14, 15, 21–23] are readily photoisomerizable.

We focussed on mixed SAMs prepared by coadsorption from a solution of the two components, which allow to tune the dilution of the chromophore arbitrarily. In Sec. 5.5 we report on mixed SAMs prepared from H-Az11 and C12. For this system we demonstrate effective photoisomerization. The structural and electronic properties of these switching SAMs as a function of the chromophore density in the SAM were investigated extensively. In order to describe the composition of the SAM as a function of the composition of the adsorption solution the thermodynamic model was extended to allow for different interactions between like and unlike molecules.

5.2 R-Az6 SAMs

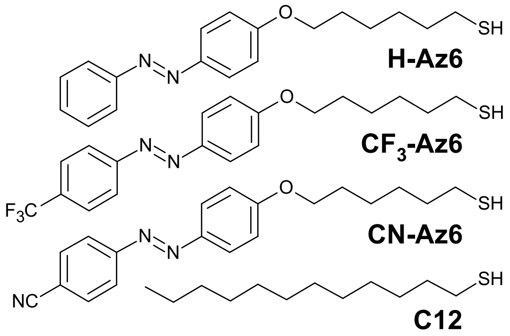

Figure 5.2: SAM forming thiols discussed in this chapter.

In this chapter SAMs of the R-Az6 type (Fig. 5.2) will be discussed. They all consist of an azobenzene chromophore bond to gold via the same hexane thiolate linker and differ only by the substituent in their tail group. This class of SAMs was our first attempt to integrate azobenzene as a molecular switch into a SAM. The results on single components SAMs discussed here also form the basis for the understanding of experiments with mixed SAMs of different R-Az6s in Sec. 5.4.

H-Az6 is the unsubstituted prototype for these compounds. The C6 linker chain is intended to decouple the chromophore from the substrate. For nitriles it has been shown by the Auger-core-hole-clock method that an upright alkyl chain isolates an excitation at the top well enough from the substrate so that its lifetime is not reduced by the substrate [86, 87].

CF$_3$-Az6 and CN-Az6 carry additional substituents intended as markers in NEXAFS experiments to give additional information on the molecular orientation. The substituents also effect the positions of the main transitions in the optical absorption spectrum of the free molecule and the SAM as we will see.

We will show that all R-Az6 compounds form densely packed SAMs, which are similar in structure and optical properties. However, the photoisomerization of the azobenzene moiety in these SAMs is very ineffective.

5.2.1 XPS

S2p Figure 5.3 shows S2p XPS spectra of the three azobenzene derivatives and C12. They were fitted using 2 doublets[1] on a background comprising linear and Shirley components. For all compounds the main component is located at a binding energy of 162.05 ± 0.01 eV and has a FWHM < 0.42 eV. A minor component is observed at 160.92 ± 0.02 eV, FWHM < 0.46 eV. We assign the main peak to bound thiolate and the minor peak to atomic sulphur as discussed in Chap. 3.

The sulphur atoms of both thiolate and atomic sulphur are located right at the gold surface. Therefore, electrons emitted from both sulphur species experience the same attenuation by the organic layer. Thus, the peak areas directly translate into the relative amounts at the surface. For all samples presented here, less than 4% of the total peak area comes from atomic sulphur.

As the sulphur is directly bound to the gold, the thiolate binding energy is pinned to the Fermi level of the gold substrate and is not affected by differences in the

---

[1] For the main component a Voigt line profile was used. Due to the low amplitude of the minor component the peak shape could not be determined by the fit. Thus, a Gaussian line profile was used for this component.

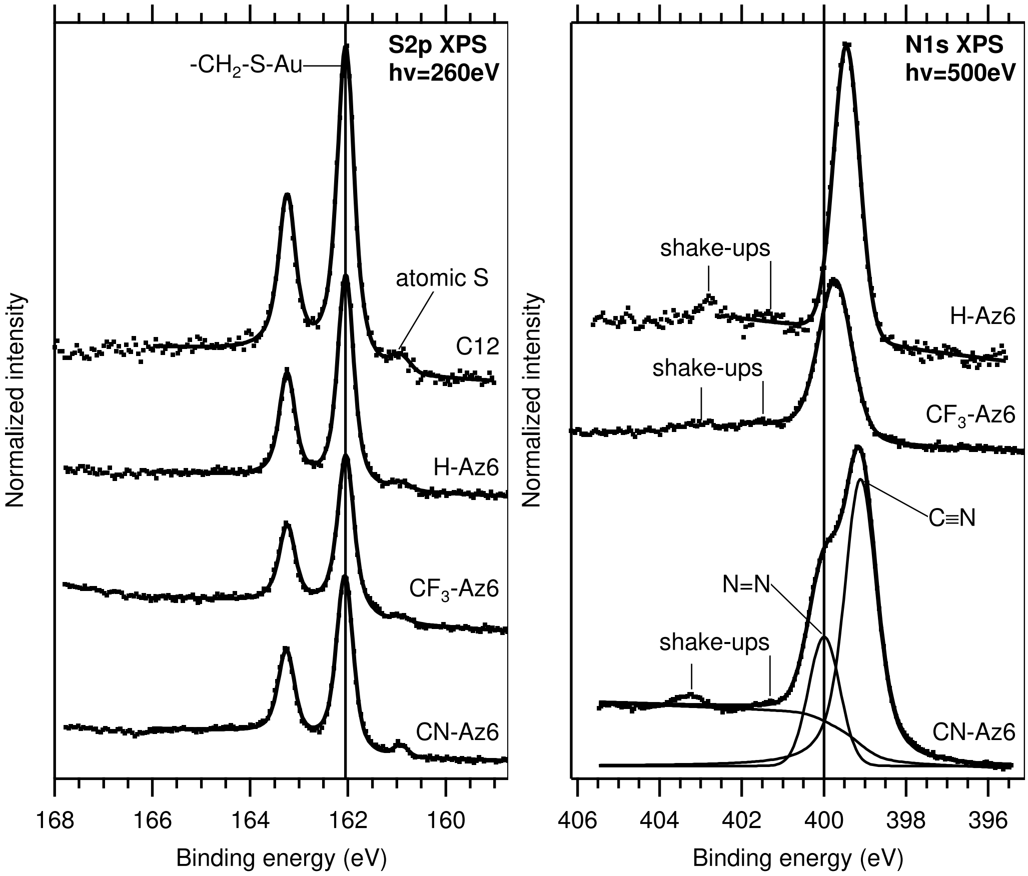

Figure 5.3: S2p and N1s XP spectra: Intensities were normalized to the right background.

work function arising from different substitutions of the chromophore. The linker chain isolates the sulphur from the chromophore and creates the same chemical environment in all cases. Therefore, the peak positions of the peaks are the same in all four compounds.

No peaks at higher binding energies are observed, showing that the samples are free of unbound thiol and disulphide. We conclude that we were able to produce clean SAMs with nondetectable amounts of unbound molecules and less than 4% of the unwanted atomic sulphur.

N1s Figure 5.3 shows N1s XPS spectra of the three azobenzene derivatives. Spectra of H-Az6 and CF_3-Az6 could be fitted using a single Voigt peak on a background comprising Shirley and linear components. CN-Az6 was fitted in the same way, but with an additional peak arising from the CN group. The peak parameters obtained from the fits are given in Tab. 5.1.

CN The peak of the CN group in CN-Az6 is well separated from the signal of the azo group present in all three compounds and can therefore be used to quantify the amount of CN-Az6 in the mixed SAM described in 5.4. At first glance it may seem counter-intuitive that the CN peak is larger than the NN peak even though there are two nitrogen atoms in the NN group but only one in the CN group. The reason is that the CN group is located directly at the surface while the NN group is located deeper in the layer. Therefore, electrons emitted from the NN group

Table 5.1: N1s XPS peak parameters: All energies in eV.

	NN BE	FW HM	CN BE	FW HM	shake ups BE (shift)[b]	BE (shift)[b]	optical transitions[a] $S_1(n\rightarrow\pi^\star)$	$S_2(\pi\rightarrow\pi^\star)$
H-Az6	399.4	0.8	—	—	401.3 (1.9)	402.8 (3.4)	2.8	3.6
CF_3-Az6	399.6	0.9	—	—	401.5 (1.9)	403.0 (3.4)	2.8	3.5
CN-Az6	400.0	0.9	399.1	0.9	401.3 (1.3)[c]	403.2 (3.2)[c]	—[d]	3.4

[a] solution in ethanol.

[b] Peak positions are maxima directly read from the spectra, shifts are given with respect to the azo (NN) peak.

[c] Due to their broad structure the shake-ups of the NN and CN photoemission peaks can not be separated. Therefore, the difference to the NN peak given here will underestimate the shift.

[d] Peak position can not be determined, because the peak is only visible as a shoulder on the S_2 transition.

are attenuated more than those from the CN group. This effect is particularly strong at the low *kinetic* energies of $\approx 100\,\text{eV}$ in this experiment using synchrotron radiation compared to data acquiered using AlK_α sources ($E_\text{kin} \approx 1\,\text{keV}$). The peak assignment is corroborated by the mixing experiment shown in Fig. 5.18.

NN peak shift In contrast to the S2p spectra where the binding energy is the same for all three compounds, the binding energy of the NN peak clearly depends on the end group of the azobenzene moiety. It shifts towards higher energies in the order H-Az6 < CF_3-Az6 < CN-Az6. The azo group is part of the chromophore and is isolated from the gold substrate by the linker chain. Therefore, the binding energy is not only sensitive to chemical shifts, but also to changes in the local potential of the neighbours. Here we will only discuss the intra-molecular contributions to the peak shift. In the discussion of the mixing experiment (5.4.1), where the same molecule can be investigated in different environments we will see that effects caused by the neighbours, either through Coulomb interaction or changes in the local potential, may be the dominating contribution to the peak shift.

The CF_3 group posses a negative inductive effect that withdraws charge from the aromatic system leading to an increased binding energy at the azo nitrogen. The CN group possess a strong mesomeric effect in addition to the inductive effect acting in the same direction. Therefore, the ability of the CN group to withdraw charge from the aromatic system is not only stronger, but also reaches further. This leads to an even stronger peak shift of the azo nitrogen.

Shake-up excitations At higher binding energies two shake-ups are observed. It is tentative to correlate their energies with optical transitions known from spectra measured in solution (Tab. 5.1).[2]

---

[2] As the shake-up is a local excitation caused by the Coulomb interaction between the emitted electron and the valence electrons, we have to compare to optical transitions in the free molecule rather than the delocalised excitation observed in the SAM. In table 5.1 we give values measured in cyclohexane. These values should give a sufficiently accurate estimation for the free molecule as it has been shown in Sec. 2 that solvatochromic effects, i.e. the variations of the band position with the solvent are much smaller than the final state effects discussed here. We assume the variation between the most polar and apolar solvent tested is of the order of the difference

Table 5.2: C1s XPS peak parameters: All energies in eV.

	p1 BE	FWHM	p2 BE	FWHM	p3 BE	FWHM	shake up BE[a]	CF_3	FWHM
C12 fit 1 peak			284.9	0.9					
H-Az6	284.2	0.6	284.6	0.8	286.1	0.8	291.4		
CF_3-Az6	284.3	0.6	284.7	0.9	286.2	0.7		291.9	0.6
CN-Az6	284.9	1.1	285.4	1.7	286.5	0.9	291.6		

[a] maxima directly read from the spectra

Following the ideas in [66] we assume that both shake-ups are related to the S_2 ($\pi \rightarrow \pi^\star$) optical transition: The final state of the shake-up is a two-hole one-electron configuration. The shake-up energy is the excitation energy in the presence of the core hole. This final state possesses 3 unpaired electrons. Because the spin of the excited electron does not flip in the shake-up, there are 2 possibilities to couple the spins of the 3 electrons leading to a 2-fold splitting of the final state and thus 2 shake-ups. The situation is similar to that of the series of $1s^{-1}2p^{-1}np^1$ shake-ups in neon, which are converging towards the two $1s^{-1}2p^{-1}$ double ionization thresholds ^1P and ^3P, which are split by 3.6 eV [88].

The shake-up energies are below the energy of the optical transition. This behaviour is not uncommon for complex molecules, where shake-up energies may even be negative [66], and can be explained by a final state effect: The S_2 transition is a transition between the HOMO-1 and LUMO. The HOMO-1 (π) is delocalized over the whole chromophore, whereas the LUMO ($\pi^\star$) has a high density at the N=N bridge, where the N1s core hole is located (Fig. 2.3). Hence, the energy of the LUMO is reduced more by the N1s core hole than that of the HOMO-1. Thus, the transition energy in the shake-up process is reduced compared to the optical transition, where the energy levels are not influenced by an additional core hole.

A participation of the S_1 (HOMO→ LUMO) transition in the shake-up appears unlikely. Because of the different symmetry of the HOMO (σ-like) and LUMO (π-like) a significant out-of-plane distortion of the molecule would be required in order to achieve sufficient overlap of the orbitals.

Shake-ups can be included in the fitting model [28, pp. 48]. However, in the present study we did not include them in favour of a simpler model.

C1s Figure 5.4 shows C1s XPS spectra of the three azobenzene derivatives and C12. The spectra were fitted using Voigt peaks on a background comprising a Shirley component and an offset only. Omitting the slope was possible because the background before and after the peaks is relatively flat and allowed to end the fitting region at 289 eV before the onset of the shake-ups and the CF_3-peak in the case of CF_3-Az6. Peak parameters obtained from the fits are given in Tab. 5.2.

C12 The spectrum of C12 shows a single structure and can be fitted with a single peak although the peak is somewhat asymmetric and a better description of the data by the fit can be achieved using two or three peaks. However, the results obtained in this way are inconsistent from spectrum to spectrum and depend on the details of the model. Heister et al. [89] investigated Cn SAMs of different chain

---

between a free molecule and a molecule in solution.

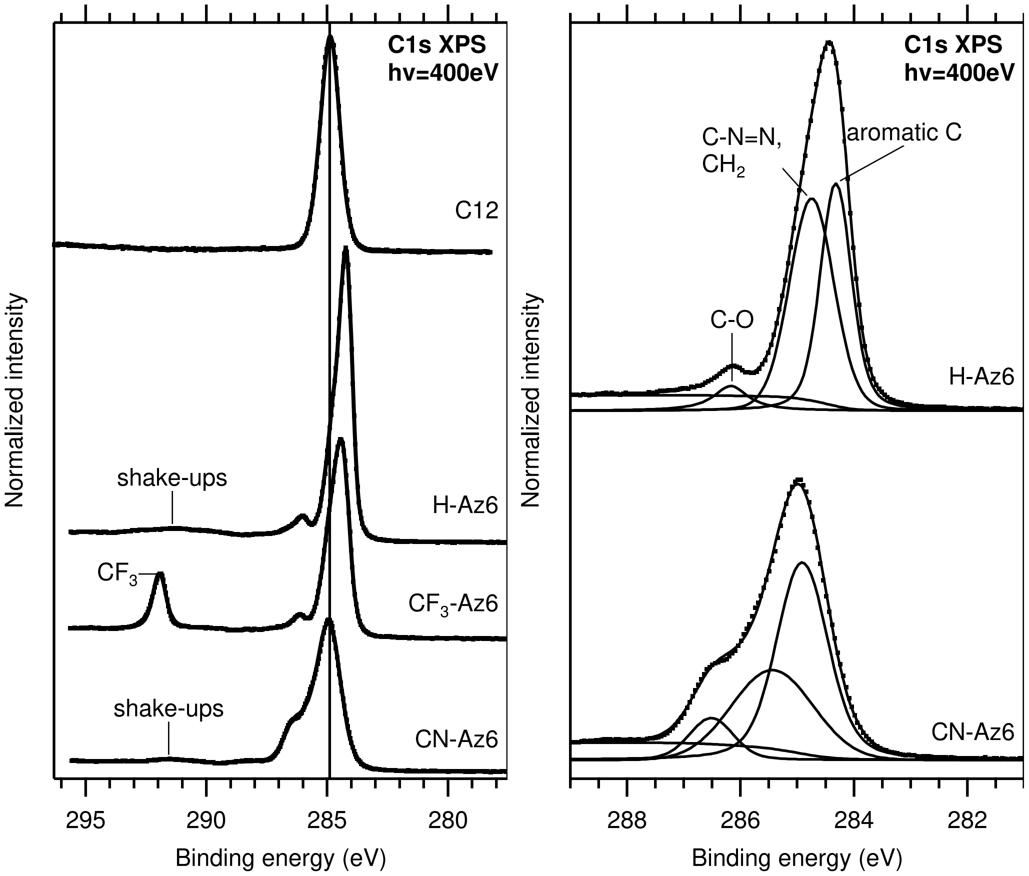

Figure 5.4: C1s XPS spectra of the R-AzO6 SAMs and C12: Intensities were normalized to the right background.

length (n=12–20) by fitting them with 3 Voigt Peaks on a polynomial background with a common Lorentzian width of 160 meV. They made the following observations: The amplitude of the low binding energy component decreases with the chain length whereas that of the high binding energy component maintains its ratio to the main component independent of the chain length. This indicates that the high binding energy components originate from carbon atoms distributed over the whole chain. The authors observe the high BE component 0.47 eV above the main component and suggested intrinsic energy losses, e.g., vibrational excitation of the CH stretch mode (≈0.35 eV) as the cause for the high binding energy component. The low energy component may be attributed to substrate mediated screening, which rapidly decreases with distance from the surface. Whether the signal of the α-carbon, which is in addition affected by the chemical shift induced by the thiolate sulphur, is located below or above the main peak is unclear [28].

We followed Heister's procedure using a linear background and the same Lorentzian width (fwhm). The results deviate considerably from those obtained by Heister et al. However, a look at the correlation matrix reveals that the peak positions and amplitudes are highly correlated.

Azobenzenes The spectrum of H-Az6 can be empirically decomposed using three Voigt peaks (Fig. 5.4 (right)). The highest binding energy peak is attributed to the carbon atoms directly bound to the oxygen. The electron withdrawing effect of the azo bridge is much smaller than that of the ether; therefore the signal of the

C atoms next to the azo nitrogen are expected together with the contributions from the linker chain in the left part of the main peak, whereas the signal of the remaining aromatic carbons is located in the right of the main peak.

About 6 eV above the main peak a broad shake-up with very low intensity is observed. It is assigned to transitions within the phenyl rings, [28] as both gas phase benzene and phenol show several shake-ups in this region [90]. The shake-ups observed for benzene adsorbed onto Ni and Cu surfaces [91] are slightly shifted and have a much lower intensity than in the gas phase.

The most prominent difference in the spectrum of CF_3-Az6 compared to H-Az6 is the additional isolated peak of the CF_3-group at about 292 eV, which was fitted independently from the main structure using a single Voigt peak. The shake-up observed for H-Az6 would fall in this region and can therefore not be resolved. The shape of the main C1s structure is almost identical to that of H-Az6. However, the structure is shifted as a whole towards higher binding energies. This shift is explained in the same way as for the N1s N=N peak.

The main peak of CN-Az6 is shifted even further, as expected due to the additional mesomeric effect of the CN group. Furthermore, the peak structure is broadened. This demonstrates that the mesomeric effect, in contrast to the inductive effect observed in CF_3-Az6, shifts charge through the whole aromatic system thereby making the different atoms more unequal. This also explains why the empirical decomposition into 3 peaks fits less well.

5.2.2 NEXAFS

Figure 5.5 shows NEXAFS spectra at the C1s and N1s edges of the three SAMs with C6 alkanethiol linker. A C1s spectrum of a pure C12 SAM, i.e. an alkanethiol without chromophore, is shown for comparison. Data were processed as described in Sec. 4.2 and Sec. 7.8.

5.2.2.1 Spectral features

C12 Since alkanethiolate SAMs are a model system of the thiol/gold type of SAMs, we start our discussion with a SAM of C12 before we go to the azobenzenealkanethiol SAMs.

Starting at low energies the first prominent feature in the C1s spectrum is a sharp resonance located at 286.7 eV only observable in the p-pol. spectrum. We assign it to a transition located at the CH_3 group. In 2PPE experiments a long lived state located above alkanethiolate SAMs has been observed [92], which is likely the same state. Even though alkanethiolate SAMs on gold have previously been investigated by NEXAFS, this resonance has not been reported [70, 93, 94]. This might be due to beam damage of the easily dissociable CH_3 group. Beam damage may be reduced in the present work compared to the published spectra due to the shutter used to shield the sample in between data points while monochromator and undulator move.

The following features have already been described by Stöhr et. al. [80] for polyethylene: The broader structure around 288 eV is interpreted as resonances of the C-H bonds of the chain. It is followed by the broad $\sigma^\star$(C-C) resonances at 293 eV and, less pronounced, at 302 eV.

A more detailed discussion of an alkanthiole spectrum for the case of decanethiole can be found in [28, pp. 58].

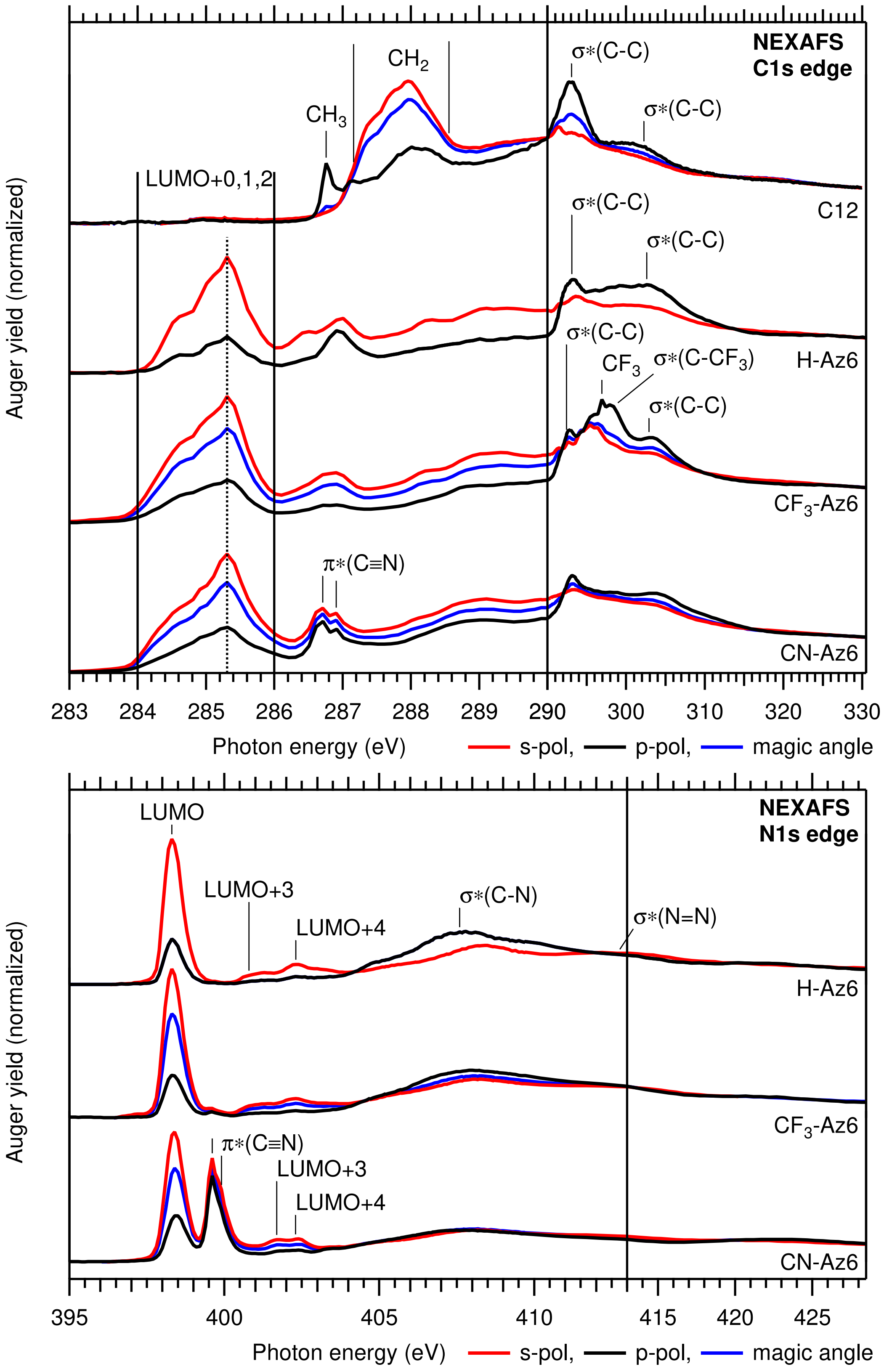

Figure 5.5: C1s and N1s NEXAFS spectra of the R-Az6 SAMs and C1s NEXAFS of C12, a pure alkanethiole, for comparison.

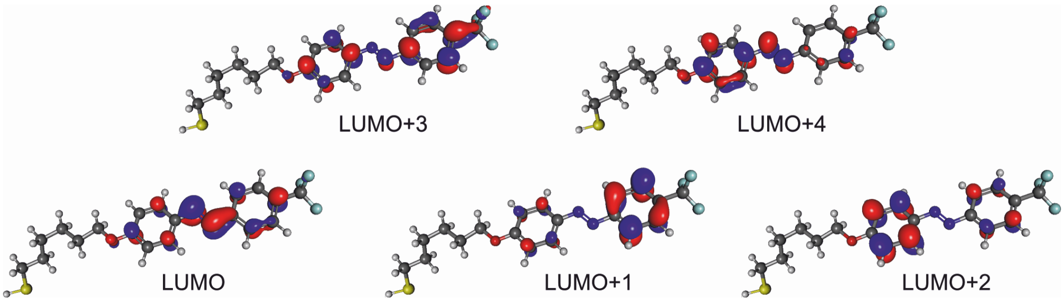

Figure 5.6: Isodensity contours for the lowest unoccupied molecular orbitals (LUMO+n) of CF_3-Az6: calculations at the DFT-B3LYP level, image from [95].

H-Az6 H-Az6, the unsubstituted azobenzenealkanethiole, is the prototype for this class of molecules. According to the building block scheme the substituents attached to the outer phenyl ring in the other two compounds will mostly add additional features to the NEXAFS spectra. Throughout the discussion we will refer to the LUMOs of the compound. They are depicted for CF_3-Az6 in Fig. 5.6 but should qualitatively describe all three compounds.

C1s At the carbon edge the lowest energy absorption structure extends from 284 to 286 eV. It is assigned to the transitions from the C1s to LUMO, LUMO+1 and LUMO+2 (LUMO+0,1,2) in the aromatic rings. The substructure with two maxima at 284.5 eV and at 285.3 eV with a shoulder at 285.0 eV does not necessarily reflect the three mentioned orbitals. The LUMO+1,2 are expected to be nearly degenerate [71] and initial state effects may play a role. As the LUMO+0,1,2 orbitals are all of $\pi^\star$ type and *trans*-azobenzene is planar, all contributions in this region exhibit the same polarization dependence, and the absorption structure can thus be used without decomposition into individual peaks to obtain the orientation angle α.

The absorption peaks up to 5 eV above the LUMO+1,2 resonance are assigned to higher lying $\pi^\star$ orbitals of the aromatic system and mixed C-H valence/Rydberg states. (The Rydberg states in benzene are observed at 287.17 and 287.92 eV [96]). Also in this region at around 288 eV resonances of the aliphatic linker chain are expected to contribute to the background as they are strongly dampened compared to the C12 SAM. An unambiguous assignment of the peaks in this region doesn't seem feasible without a theoretical calculation of the NEXAFS spectrum. Fortunately these peaks are not relevant for the determination of the molecular orientation.

Above the ionisation threshold of about 290 eV broad shape resonances are observed most pronounced at 293 eV. Even though they occur at a similar position as in the pure linker chain they mainly originate in the aromatic system, because the signal form the linker chain is strongly dampened. The broader structure observed here is similar to that of benzene [76].

N1s The N1s spectrum of H-Az6 shows a sharp $\pi^\star$ transition at 398 eV, in contrast to the threefold substructure at the carbon edge. It is attributed to the LUMO, which has a high density at the nitrogen atoms. The LUMO+1,2 are located at the phenyl rings with only little density at the azo bridge and therefore contribute only insignificantly to the N1s spectrum. The angle α can be obtained independently from the N1s to LUMO transition in the same way as for carbon.

The resonances at 401 and 402 eV are attributed to the LUMO+3 and LUMO+4. Both have significant density at the azo bridge.

Above the ionisation threshold broad $\sigma^\star$ resonances are observed at 408 and 413 eV. They can be explained by qualitatively applying the *Linear Combination of Bond Orbitals* method [76, p. 67]: Starting with the 3 localised σ bonds around the two nitrogen cores we obtain 3 localised $\sigma^\star$ orbitals. The shorter N=N double bond has a higher $\sigma^\star/\sigma$ splitting than the two longer C−N bonds. Therefore, the $\sigma^\star$(N=N) orbital will have a higher energy than the $\sigma^\star$(C-N) orbital. In the general case of nonequivalent rings on both sides of the N=N bond there are 4 relevant transitions: From both cores there are transitions to the $\sigma^\star$(N=N) and the $\sigma^\star$(C-N) of the bond neighbouring the N core. Due to their spatial overlap the $\sigma^\star$ orbitals of the N=N and C-N bonds are expected to hybridise. As the higher lying initial orbital will contribute more to the higher lying hybrid, the higher lying of the two resulting hybrid orbitals will have more $\sigma^\star$(N=N) character, while the lower lying hybrid orbital will be dominated by the $\sigma^\star$(C-N). Therefore, we mark the regions of the resulting transitions with $\sigma^\star$(N=N) and $\sigma^\star$(C-N). In addition, in this region multiple excitations and ionization thresholds related to them are expected, as seen in N_2 [76].

CF_3-Az6 The C1s spectra of CF_3-Az6 show the same features as H-Az6. The LUMO+0,1,2 structure is slightly broader. This may be due to initial state effects induced by the CF_3 group, which effect mainly the C1s to LUMO transition because the LUMO has significant density at the C atom neighbouring the CF_3 group. In contrast, the maximum of the structure formed by transitions to the LUMO+1,2 does not shift. The polarization dependence of the LUMO+0,1,2 resonances are used to obtain α, as for H-Az6.

In comparison to H-Az6, the C1s spectra show additional pronounced resonances in the energy range of $294 - -300$ eV. They are attributed to transitions from the C1s of the CF_3 group. In the C1s XPS (Fig. 5.4) the signal from the CF_3 group is shifted by about 8 eV with respect to the main C peak. This can be predominantly attributed to a chemical shift, i.e. initial state effects. Thus, a shift of the resonance of a similar size is to be expected. We observe a shift of about 10 eV. These shifted resonances could be extracted from the spectra by subtracting the corresponding spectra of H-Az6 [28]. In this work we decided to subtract a spectrum of CN-Az6 instead in order to be able to use data measured under the same conditions as the CF_3-Az6 sample. The resulting difference spectrum is shown in Fig. 5.7. The observed negative signal at around 310 eV must be caused by additional resonances of the CN group as it is not observed when H-Az6 is subtracted. [28]

The main resonances at the CF_3 group are assigned in analogy to hexafluoroethane. [97, 98] The polarization dependence of the C1s to $\sigma^\star$(C-C) transition at 298.3 eV allows us to obtain the tilt angle ϑ of the C-CF_3 bond.

The N1s spectrum is almost indistinguishable from that of H-Az6. Only above the ionisation threshold the intensity and polarization dependence of the $\sigma^\star$ resonances differs.

CN-Az6 The nitrile group contributes two additional π bonds. One with a nodal plane parallel to that of the aromatic system and one perpendicular. The former is conjugated with the aromatic system. As a result, the degeneracy of the $\pi^\star$(C≡N) resonance is lifted [99].

The transition to the $\pi^\star$ orbital of the remaining localised π bond is observed in the C1s spectrum as an additional absorption structure at 286.5 eV. This peak exhibits a vibrational progression not typically observable in delocalised orbitals. In

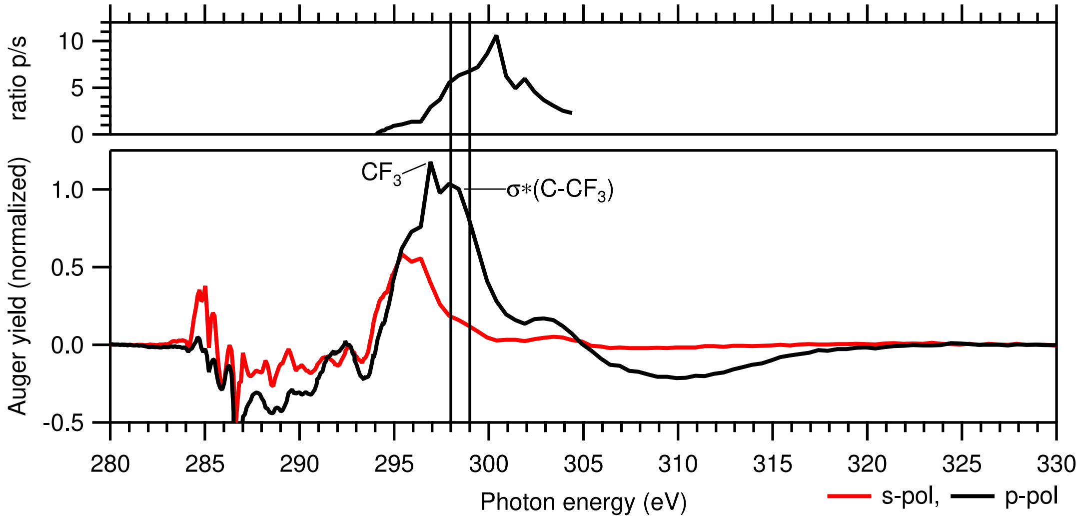

Figure 5.7: CF3 resonances of CF_3-Az6: Differences of the C1s NEXAFS spectra of CF_3-Az6 and CN-Az6 (bottom) and the ratio of the p-polarized and s-polarized spectra of these differences (top). The markers indicates the region used to calculate the angle ϑ from the polarization dependance of the $\sigma^\star$(C-CF_3) resonance. The ratio is relatively constant in this region, indicating that only orbitals with similar orientation contribute.

the N1s spectrum this transition leads to an additional isolated peak at 399.6 eV where the vibrational progression is also observed, but not resolved as well. The position and vibrational splitting are comparable to the $\pi^\star$ resonance observed for $HS(CH_2)_{16}CN$ [87] at both the C and N edge. The observed splitting of 0.25±0.05 eV is comparable with the value of 0.25 eV calculated for the CN stretch vibration. [100, 101]. This isolated transition at the N edge is used to obtain the tilt angle β.

The conjugated π bond of the (C≡N) group is part of the aromatic systems and its effect on the spectrum can not be treated with the building block model, but would require calculations for the complete aromatic system. DFT calculations and NEXAFS measurements for the related system benzonitrile can be found in [101].

The LUMO+3, which has a high density at the ring atom neighbouring the CN group, is shifted towards higher energies in CN-Az6 compared to H-Az6. Please note that we label the orbital LUMO+3 that has a similar shape to the LUMO+3 in CF_3-Az6. Due to the additional contributions of the nitrile group to the LUMO region the numbering of the orbitals would be different for CN-Az6.

The C≡N bond will also contribute an additional $\sigma^\star$ transition to the N1s spectrum. Unlike in H-Az6 and CF_3-Az6 there is hardly any polarization contrast in the $\sigma^\star$ area. As the $\sigma^\star$ orbital of the nitril (C≡N) group is expected in the same region as the resonances of the azo (N=N) group their polarization dependence partly cancels.

5.2.2.2 Molecular Orientation

As *trans*-azobenzenes are essentially planar the orientation of the chromophore is mainly described by the orientation of the aromatic plane. In the following we will discuss the orientation of the chromophore only, as the orientation of the linker chain in the SAM can not be probed effectively by NEXAFS because the signal of the linker chain is strongly dampened and superimposed on features of the chromophore.[3]

---

[3] For alkanethiol SAMs without chromophores orientations have been obtained by NEXAFS. [93], [28, p. 60]

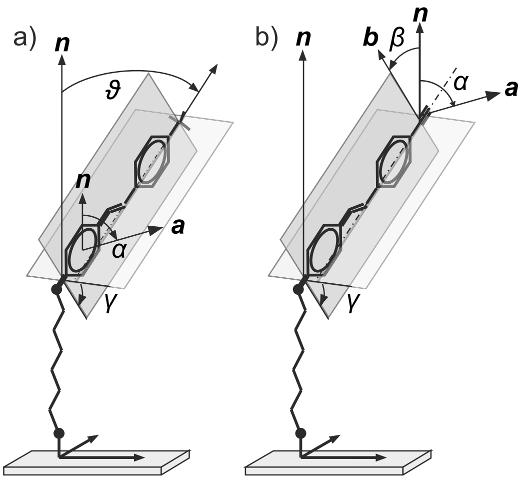

Figure 5.8: Angles describing the molecular orientation of the chromophore in R-Az6 with respect to the sample surface: **a)** CF_3-Az6, **b)** CN-Az6. **n** is the surface normal of the sample. α is the angle between the normal of the aromatic plane **a** and the surface normal **n**, ϑ is the tilt angle between the (C-CF_3) bond axis and the surface normal. γ is the twist angle of the chromophore plane around the axis of the C-O bond (parallel to the C-C≡N/C-CF_3 axis). For $\gamma = 90°$ the normal of the aromatic plane **a** is parallel to the surface. Note that the linker chain has just been drawn schematically and does not reflect the actual orientation of the chain.

The LUMO+0,1,2 are of $\pi^\star$ type; thus the transition dipole moments from the isotropic 1s orbitals to the LUMOs are normal to the aromatic plane. The angular dependence of the N1s to LUMO and the C1s to LUMO+0,1,2 transitions can be utilized to calculate the angle α between the normal **a** of the aromatic plane and the surface normal **n** (Fig. 5.8) as described in Sec. 4.2. This angle can be obtained for all azobenzenes and the values obtained at the C and N edge are denoted α_C and α_N respectively.

In CN-Az6 the orbital vector **b** of the $\pi^\star$ orbital of the localised π bond of the nitrile group is oriented perpendicular to the normal of the aromatic plane **a** and the C≡N bond axis. The transition dipole moments from the C1s and N1s core orbitals located at this bond have the same orientation as the orbital vector. Only the transition from the N1s orbital to this orbital can be isolated easily in the spectrum and it is used to obtain the angle β between **b** and the surface normal **n** in the same way as for α.

In CF_3-Az6 the C1s to $\sigma^\star$ (C-CF_3) transition can be used to obtain the tilt angle ϑ between the (C-CF_3) bond axis and the surface normal (Fig. 5.8). Figure 5.7 shows difference spectra used to obtain the polarization dependence for this transition. In addition, the ratio of the NEXAFS intensities measured with p- and s-polarized radiation is shown. In the region of the (C-CF_3) transition the ratio curve is relatively flat and only changes from 5.5 to 7.2 corresponding to $\vartheta = 25°$ to 23°. I.e. the (C-CF_3) transition does not overlap too much with other peaks with deviating polarization dependence,[4] thus making this evaluation feasible. However, as there will be contributions in the background that have a constant polarization dependence, the error is larger than estimated from the ratio curve.

γ is the twist angle of the chromophore plane around the axis of the C-O bond (parallel to the C-C≡N/C-CF_3 axis). The normal of the aromatic plane is parallel to the surface for $\gamma = 90°$.

The orientation of the chromophore plane with respect to the surface plane is defined by any two of the angles defined above. The relationships between theses angles are:

$$\cos\gamma = \frac{\cos\alpha}{\sin\vartheta}; \quad \tan\gamma = \frac{\cos\beta}{\cos\alpha}; \quad \sin^2\vartheta = \cos^2\alpha + \cos^2\beta \tag{5.1}$$

---

[4] A resonance with deviating polarization contrast located at nearly the same position as the (C-CF_3) transition would not show up as a slope in the ratio but still invalidate the analysis. In [28, p. 69] a decomposition of the structure in the region 294–303 eV has been attempted.

Table 5.3: Average orientations in the SAM. Values in parentheses were computed according to Eq. 5.1 from the measured data using the mean of α_C and α_N.

	α_C (deg)	α_N (deg)	β (deg)	γ (deg)	ϑ (deg)
H-Az6	73±5	77±5	—	—	—
CF_3-Az6	75±5	78±5	(71±10)	(57±19)	24±7
CN-Az6	72±5	73±5	59±5	(60±8)	(37±6)

Table 5.4: 2D Lattice constants obtained by AFM/STM for H-Az6, the prototype of the R-Az6 molecules discussed in this chapter, and Ph-AzPh, an azobenzene thiol with aromatic linker. Both form a herringbone structure with approximately rectangular unit cells and two molecules per cell.

		a/Å	b/Å
H-Az6	[102, 103]	6.1±0.4	7.9±0.4
	[104]	6.3±0.3	8.2±0.3
Ph-AzPh	[6]	6.5±0.5	8.9±0.5

Table 5.3 shows the average orientations obtained from the spectra.

5.2.3 Structural Model

Having analysed the orientation of the chromophore to the surface, we now come to the orientation of the molecules with respect to each other, i.e. the 2D lattice of the SAM. In AFM and STM measurements of H-Az6 on Au/mica conducted by other groups, 2 different structures were observed with the two molecules either close together or evenly spaced. However, the unit cells of both structures have the same dimensions and are nearly rectangular. For the two structures a simple herringbone structure and herringbone structure with pair-wise sandwiched molecules have been proposed. Lattice constants and references are given in Tab. 5.4. The structures are similar to those suggested for H-Az10[5] [4] and H-Az11 [105]. Figure 5.9 shows a structural model obtained by combining the unit cell obtained by AFM and the molecular orientation obtained in this work.

From the NEXAFS data, as discussed, we can conclude that the SAM consists of the *trans* form. The molecules have a preferential upright orientation. This upright

---

[5] 10-(4-(phenylazo)phenoxy)decyl-1-thiol

Figure 5.9: Structural Model for a SAM of CF_3-Az6: Note that, while α and ϑ define the orientation with respect to the surface normal, the molecule may still be moved around a cone. In addition there are two possible orientations of the N=N bridge in the chromophore plane, which can not be distinguished by our analysis of the NEXAFS spectra: one with the N=N bridge nearly parallel to the surface and one with the N=N bridge oriented upright. The image shows the latter case, even though the redshift of the S_3 aggregate peak suggests that the N=N bridge is oriented parallel to the surface (cf. Sec. 5.2.4). As the orientational angles obtained for all three R-Az6 SAMs are identical within the experimental error this model should describe all the R-Az6 SAMs. Modified figure from [9].

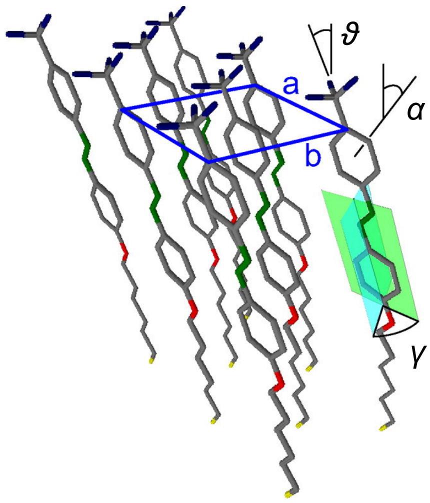

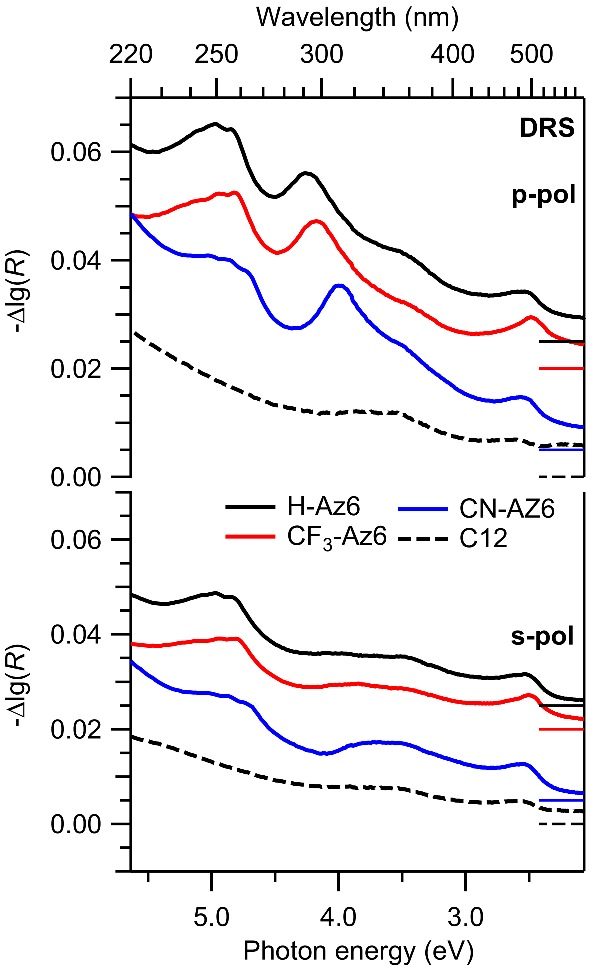

Figure 5.10: DR spectra of the R-Az6 SAMs: Spectra were vertically offset as indicated by the horizontal lines at the right.

orientation allows for a strong interaction of the alkane chains and enables the π-stacking, which leads to excitonic coupling as we shall see when we discuss the optical properties of these SAMs.

5.2.4 Optical Properties

SAMs of azobenzene derivatives on gold have been investigated by transmission mode UV/vis spectroscopy [3, 4]. This technique can only be applied to semi-transparent and thus thin ($\lesssim$ 40 nm) gold films on transparent substrates, i.e. quartz. These films, however, consist of gold clusters[6] [7, 8] on quartz unlike the thick ($\approx$ 300 nm) polycrystalline films on mica used in this work, which exhibit (111) terraces of a few 100 nm width. In the cause of this work, it turned out that the optical properties and especially the photoisomerization behaviour of SAMs on transparent cluster films may differ substantially from those of SAMs on defined Au(111) surfaces [9, 10]. Hence, the combination of results obtained by transmission mode spectroscopy on transparent substrates with results obtained by complementary methods on other substrates may be misleading.

Therefore, the optical properties of SAMs prepared on the same thick, nontransparent substrates, which were used for XPS and NEXAFS, had to be investigated.

---

[6] However, a method to prepare semitransparent gold films on silanized glass, which exhibit (111) surfaces, has been developed in the group of Rubinstein [106, 107].

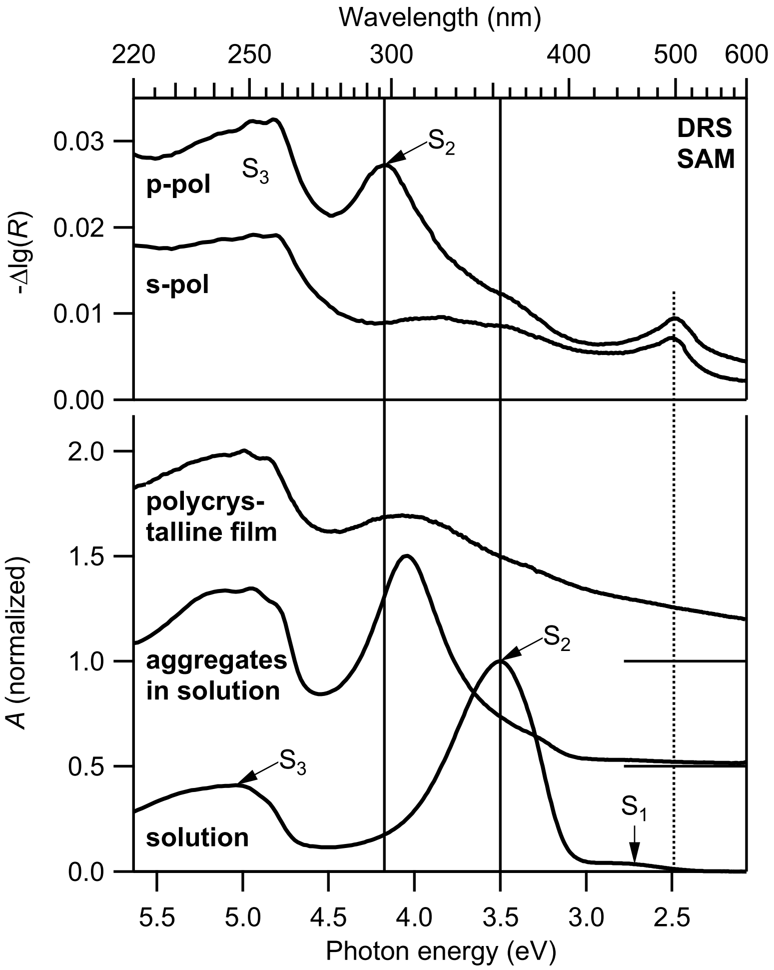

Figure 5.11: Optical spectra of CF_3-Az6: DR spectra of a SAM and absorbance spectra in ethanol, of a polycrystalline film on quartz, and of an ethanolic solution where aggregation was induced by adding water. Data for the latter two spectra from [10]. Spectra in the bottom graph were offset as indicated by the bars at the right. The peak at about 2.5 eV in the SAM spectra is an artefact as described in the text.

Differential Reflectance (DR) spectroscopy (cf. Sec. 4.4) allows to measure the change in reflectivity of the gold surface caused by the SAM. DR spectra were recorded at an angle of incidence of 45° using s- and p-polarized light.

The general shape of the DR spectra is determined by the change in reflectivity due to the SAM acting as a dielectric layer. This effect is experimentally most evident when looking at the DR spectra of C12 (Fig. 5.10) as this SAM lacks any absorption bands because the molecule does not contain any chromophores. The main features of the dielectric layer also visible in all other DR spectra are a background increasing towards higher photon energies and additional peaks in regions where the reflectivity of the gold substrate changes strongly, i.e. at 2.6 eV and 3.5 eV [9].

We start our discussion of the spectra of the R-Az6 SAMs with CF_3-Az6 because for this compound we have most complementary optical data measured on other states of the same compound. The DR spectra and an absorbance spectrum of the compound in solution are shown in Fig. 5.11. The spectrum in solution shows the typical absorption bands of azobenzenes: The dominating S_2 (π–$\pi^\star$) excitation, the weak S_1 (n–$\pi^\star$) excitation and the S_3 absorption band due to higher (π–$\pi^\star$)

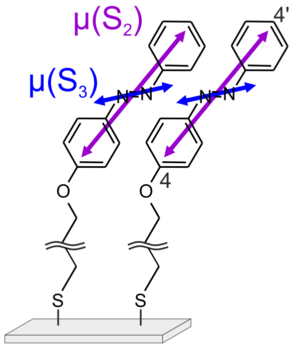

Figure 5.12: Orientation of optical transition dipole moments $\mu(S_2)$ and $\mu(S_3)$ for the R-Az6 SAMs: Orientations from DFT-calculations performed in the group of Karsten Reuter [9].

excitations (cf. Sec. 2).

In the SAM the S_2 absorption band is shifted towards higher photon energies compared to the solution (hypsochromic, i.e. blue shift), whereas the S_3 band is shifted towards lower photon energies (bathochromic, i.e. redshift). We also observed similar but smaller shifts of these bands for polycrystalline films and solutions of aggregates as shown on the same graph.

These results are in line with earlier research on monolayers of azobenzene derivatives on water [108] and on microcrystals and SAMs of H-Az10 [4] on semitransparent gold substrates where a blue shift of the S_2 band was observed. The S_2 band position of the microcrystals was in between that of the solution and the SAM. These findings were attributed to the formation of H-aggregates. Indeed, our observations are explained well by the molecular exciton model [18, 20, 109]: The transition dipole moments (TDMs) for the S_2 and S_3 transitions of an isolated molecule lie in the aromatic plane as shown in Fig. 5.12. The chromophores in the SAM are standing predominantly upright. Hence, in a 2D arrangement the S_2 TDMs, which are almost parallel to the axis that connects the C4 and C4' atoms, form an H-aggregate leading to the observed blue shift of the corresponding band. The excitation of a band is strongest when the electric field of the incident light is parallel to the TDM; therefore, the S_2 transition is pronounced in the p-pol spectra, but hardly[7] visible in the s-pol. spectrum.

The S_3 TDMs are oriented roughly parallel to the N=N bond and are head-to-tail aligned. Thus, they form a J-aggregate resulting in a red-shifted aggregate band. Because the S_3 TDM (as the N=N bond) has an orientation almost parallel to the surface, it is only slightly more intense in the p-pol than in the s-pol spectra. In J-aggregates vibrational excitations are suppressed [110]; therefore, the absorption fine structure of the S_3 band becomes visible in the SAM as well as in the polycrystalline film and the aggregates in solution.

The position of the S_1 transition in the SAM can not be determined from the spectra due to strong artefact peaks caused by the large slope of the reflectivity of the substrate around 2.5 eV—the onset of the absorption of gold.

Figure 5.10 shows DR spectra of all 3 R-AzO6 SAMs. As we have shown, their molecular orientation is very similar and thus the orientation of their TDMs in SAMs. Hence, we expect them to form similar aggregates. Only the position of the S_2 aggregate band varies depending on the substituent and reflects the relative positions of the absorption of the free molecules in solution. The excitonic shifts and peak

---

[7] While there is no indication of a peak in the s-pol. spectrum at the position where the S_2 peak maximum is observed in the p-pol. spectrum, at about 3.8 eV a small broad peak is visible, that may be interpreted as the H-aggregate peak of molecules with a deviating orientation and larger variations in their orientation, e.g. at defects.

Table 5.5: Peak positions and excitonic shifts of the S_2 band: Peak positions are maxima directly read from the spectra. Peak positions in ethanolic solution are given for comparison. The excitonic shift is computed as the difference to the value in solution.

		S_2 (eV)	S_2 (nm)	S_2 in solution (eV)	S_2 in solution (nm)	excitonic shift (eV)	excitonic shift (nm)
H-Az6	SAM	4.26	291	3.57	347	0.69	56
CF_3-Az6	SAM	4.17	297	3.50	354	0.67	57
	polycrystalline film	4.07	305	3.50	354	0.57	49
	aggregates in solution	4.04	307	3.50	354	0.54	47
CN-Az6	SAM	4.01	309	3.41	364	0.61	55

Table 5.6: Photon doses applied in photoisomerization experiments of R-Az6 SAMs. The illumination was conducted in normal incidence.

λ nm	photon dose J cm^{-2}	photon dose photons cm^{-2}
366	> 0.2	$> 4 \times 10^{17}$
460	> 8	$> 2 \times 10^{19}$

positions are given in Tab. 5.5. The smaller excitonic shift of the aggregates in solution and the polycrystalline film may be explained by a different structure of CF_3-Az6 in the solid state where the S_2 TDMs are aligned differently than in the SAM where the substrate enforces a parallel structure.

5.2.5 Photoisomerization Behaviour

SAMs of all three R-Az6 compounds were irradiated with UV (366 nm) and blue (460 nm) light and did not show any significant changes in the DR spectra nor did the polycrystalline film or the solution of CF_3-Az6 aggregates. The photon doses employed (Tab. 5.6) were well above those required to reach the photostationary states in solution. Photoisomerization of SAMs was also attempted in the S_2 aggregate band at 308 nm and in the S_3 band at 254 eV where photoisomerization can also be induced (cf. Sec. 2) in solution. Further experiments in our group [10] show that also in the crystalline film and in aggregates in solution the photoisomerization is suppressed. In ethanolic solution with a water content adjusted so that CF_3-Az6 coexists in aggregates and as free molecules (in a nonequilibrium state slowly forming further aggregates) we could demonstrate reversible photoisomerisation of the free molecule by UV and blue light while the aggregates did not show any photoresponse [10, Fig. 8]. These findings are in line with earlier research, were photoisomerization of azobenzenealkanthiols was found to be suppressed in the SAM and in the crystalline state [4, 21]. More recently in a photoemission experiment less than 1% of the molecules in an azobenzenealkanthiol SAM were found to be susceptible to photoisomerization [111]—a number below the detection limit of our DR spectroscopy set up.

We conclude that in phases exhibiting excitonic coupling the photoisomerization is suppressed.

Reasons for the Suppressed Photoisomerization Deexcitatation of the S_2 state of the azobenzene chromophore by charge transfer of the excited electron or hole into the substrate does not seem a likely cause for the suppressed isomerization, because the alkyl chain acts as a tunnelling barrier. The isolating properties of upright alkyl chains were demonstrated for SAMs of alkanethiolates with nitrile headgroup: The charge transfer time of an electron in an unoccupied state of the nitrile group into unoccupied states of the metal substrate, was measured using the Auger core-hole clock method. It was found to increase from 14 fs for a C2 chain to 100 fs for a C4 chain [86, 87]. These results are in line with recent results from our group where charge transfer times for the excited state in CF_3-Az3 where determined by 2-photon photoemission and the core hole clock method [112]. The time required for the photoisomerization of azobenzene is of the order of 1 ps [35]. Thus, for these systems with short linker chains de-excitation to the substrate would explain a reduction of the photoisomerization cross section by several orders of magnitude and the isomerization would be unobservable in the experiments described in this work. However, if we extrapolate the increase in charge transfer time with chain length exponentially, for the C6 chain the charge transfer time and the time required for the photoisomerization should be of the same magnitude and the photoisomerization should become observable. Finally, the effective photoisomerization we observed in diluted chromophore SAMs (cf. Sec. 5.5) demonstrates that it is not charge transfer that inhibits the photoisomerization in longer chained single component azobenzene alkanethiolate SAMs.

The suppressed photoisomerization in all systems that show excitonic coupling may lead to the presumption that the excitonic coupling is the cause for the failure of the investigated SAMs to switch. Another explanation frequently assumed in literature is steric hindrance. Based on our experiments we can not discern between the two possible causes, because the dense packing in these films suggesting steric hindrance is a prerequisite for the excitonic coupling. In the following we discuss the two options:

When exciting the system in the aggregate band we have to assume that the photoisomerization is influenced by the delocalized nature of the aggregate excitation. This delocalized state would have to decay into a localized excitation in order to induce the isomerization of an individual molecule. We do not want to speculate further about such processes. However, in the SAMs there is some absorbance at the position of the S_2 band in solution, which we attribute to chromophores in locations of incomplete order. These molecules should isomerize when excited at 366 nm. This leaves us with steric hindrance as the more likely cause for the failure of the R-Az6 SAMs to switch.

What is meant by steric hindrance? Naively one would assume there is simply not enough room for the chromophores in the *cis* state in the SAM, i.e. the *cis* state is not a sufficiently deep minimum in the potential surface. However, for the SAMs investigated here, calculations have shown that this is not the case [113]. Hence, steric hindrance may only describe a situation where, even tough there is enough room for a final all-*cis* state, there may not be enough space in the *trans* layer for the movement, i.e. the activation barrier for the isomerization requires more energy than is available in the photoexcited state.

5.3 Aromatic Linker

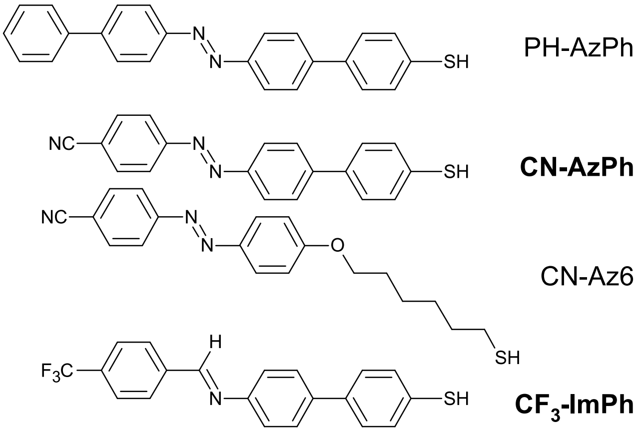

Figure 5.13: SAM forming thiols with aromatic linker: Ph-AzPH, the azobenzene derivative for which photoismerizable SAMs have been reported; CN-AzPh, the azobenzene SAM with aromatic linker investigated in this chapter; CN-Az6, the analogue compound to SZa with alkyloxy linker already discussed in Sec. 5.2; and CF_3-ImPh, an imine with aromatic liker also investigated in this chapter.

For SAMs of Ph-AzPh (Fig. 5.13) effective photoisomerization has been reported [6, 83, 84]. Therefore, we also investigated azobenzene SAMs with aromatic linkers. The molecule CN-AzPh was chosen, because the CN substituent allows to obtain additional orientational information from the NEXAFS spectra as already discussed for CN-Az6, the analogue molecule with an aliphatic hexyloxy linker. CF_3-ImPh, an imine with aromatic linker was also investigated because it was available earlier. Imines possess a π system that is isoelectrical to that of azobenzenes and also show photoisomerization. However, the *cis-trans* isomerization barrier is lower than for azobenzenes and consequently the *cis* form can not be expected to be stable at room temperature.

Compared to the R-Az6 SAMs, which could all be prepared in the same way from ethanolic solutions, the solubility of CN-AzPh and CF_3-ImPh in ethanol is lower; thus individual preparation methods had to be developed (cf. Sec. 7.2.5).

Even though photoisomerization for SAMs of these compounds could not be demonstrated the comparison of spectra of CN-AzPh with CN-Az6 gives valuable insight on the influence of the aromatic linker on the XP and NEXAFS spectra.

Structurally it is an interesting question how the plane of the phenyl linker unit is oriented with respect to the plane of the azobenzene chromophore: X-ray diffraction on solid biphenyl shows that the two rings are in the same plane [114]. For crystals of the thioacetate precursor of Ph-AzPh a planar sturcture was observed, while for the 2,2'-substituted compound a twisted conformation is expected [84]. Based on the structural similarity of CN-AzPh and CF_3-ImPh to Ph-AzPh we assume an all planar structure for these compounds.

5.3.1 XPS

S2p Figure 5.14 shows S2p spectra of the two SAMs with aromatic linker. The spectra of CN-AzPh and CF_3-ImPh were fitted using a single doublet on a background comprising linear and Shirley components. The S2p$_{3/2}$ peak is located at a binding energy of 161.88±0.01 eV (FWHM <0.6 eV) for both compounds. No peaks at higher binding energies were observed, showing that we were able to produce SAMs free of unbound thiol or disulphide. The frequently observed peak at about 161 eV commonly assigned to atomic sulphur is below the detection limit.

A spectrum of CN-Az6, already discussed in detail in Sec. 5.2.1 is shown for

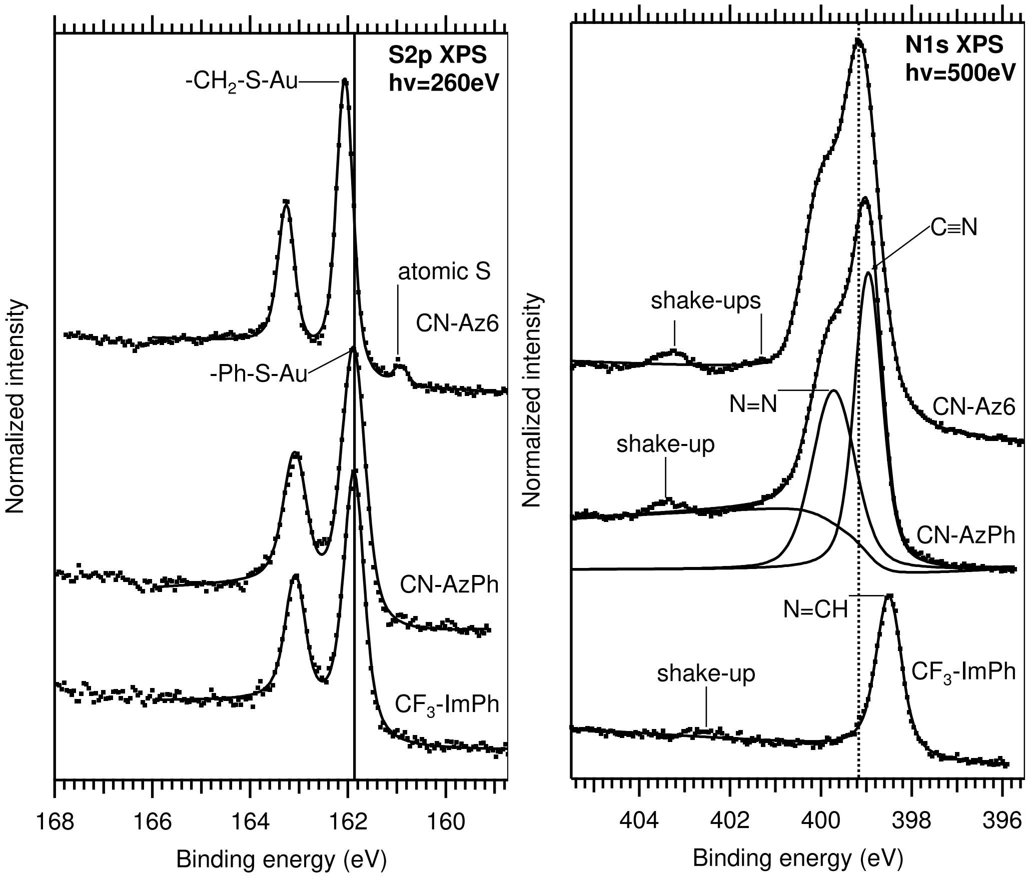

Figure 5.14: S2p and N1s XP spectra: Intensities were normalized to the right background.

Table 5.7: N1s XPS peak parameters: All energies in eV.

	NN / NCH	FW	CN	FW	shake ups		optical transitions	
	BE	HM	BE	HM	BE (shift)[b]	BE (shift)[b]	n->$\pi^\star$	π->$\pi^\star$
CN-Az6	400.0	0.9	399.1	0.9	401.03 (1.9)[c]	403.2 (3.2)[c]	2.8[a]	3.6[a]
CN-AzPh	399.7	1.1	399.0	0.7	—	403.4 (3.7)[c]		3.4[a]
CF$_3$-ImPh	398.5	0.7	—	—	—	402.6 (4.1)		

[a] solution in cyclohexane

[b] Shifts are given with respect to the azo (NN) peak.

[c] Due to the broad structure the shake-ups of the NN and CN photoemission peaks can not be separated. Therefore, the difference to the NN peak given here will underestimate the shift.

comparison. We note that the S2p$_{3/2}$ peak of the two SAMs with aromatic linker is shifted towards lower binding energies by about 0.2 eV, while the peaks of the two aromatic compounds have the same binding energy. The difference can be explained by the higher electron density in the vicinity of the aromatic system. The S2p binding energies of the two SAMs with aromatic linker are the same for the same reason as the R-Az6 and C12 SAMs all have the same S2p binding energy (cf. Sec. 5.2.1).

N1s All nitrogen atoms in CN-AzPh are located in the chromophore, which is identical to that oft the reference compound CN-Az6. Hence, the spectra look almost identical and the spectrum of CN-AzPh was decomposed into 2 peaks representing

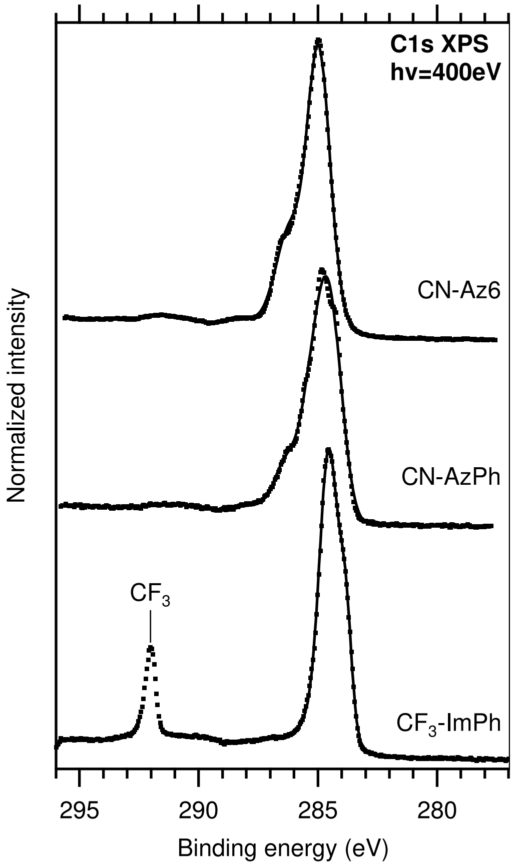

Figure 5.15: C1s XP spectra: Intensities were normalized to the right background.

Table 5.8: C1s XPS peak parameters: All energies in eV.

	p1 BE	FW HM	p2 BE	FW HM	p3 BE	FW HM	CF_3 BE	FW HM
CN-Az6	284.9	1.1	285.4	1.7	286.5	0.9	—	—
CN-AzPh	284.5	1.2	285.3	1.1	286.3	1.1	—	—
CF_3-ImPh	283.8	0.6	284.5	1.0	—	—	292.0	0.6

the CN- and NN-nitrogen in the same way as CN-Az6.

The imine CF_3-ImPh only contains a single N atom. Thus, the spectrum could be fitted with a single Voigt peak on a background comprising a Shirley and a linear component. The peak position of the imine group is shifted by 1.2 eV with respect to that of the diazo group in CN-AzPh (Tab. 5.7). However, about 0.4 eV of the observed shift can be attributed to the different substituents, as for the otherwise identical molecules CN-Az6 and CF_3-Az6 exchanging the CN for a CF_3 group shifts the N1s peak of the NN group by 0.4 eV (cf. Tab. 5.2). For all 3 compounds a shake-up is observed.

C1s Figure 5.15 shows C1s XP spectra of the three compounds. Again the spectrum of CN-AzPh is very similar to that of CN-Az6. All spectra were fitted with the same empirical decomposition already described for CN-Az6 in Sec. 5.2.1.

The main peak in the spectrum of CF_3-ImPh does not show the shoulder at high binding energies observed for the R-Az6 and CN-AzPh SAMs attributed to the CN and -C-O groups. Thus, the main peak was fitted with two peaks only. In addition

Table 5.9: Average orientations in the SAM: Values in parentheses were computed according to Eq. 5.1 from the measured data using the mean of α_C and α_N.

	α_C (deg)	α_N (deg)	β (deg)	γ (deg)	ϑ (deg)
CN-Az6	72±5	73±5	59±5	(60±8)	(37±6)
CN-AzPh	64±5	62±5	59±5	(49±7)	(43±6)
CF_3-ImPh	65±5	66±5	—	—	—

the peak of the CF_3 group is observed at about 292 eV. All peak parameters are given in Tab. 5.8.

5.3.2 NEXAFS

Figure 5.16 shows NEXAFS spectra at the N1s and C1s edge of the two SAMs with aromatic linker and CN-Az6 for comparison. Data were processed as described in 4.2 and 7.8. Orientational angles were obtained from the spectra in the same way as for the aliphatic compounds (cf. Sec. 5.2.2.2) and are shown in Tab. 5.9. We note that the SAMs with aromatic linker have a less upright orientation. Spectral features are discussed in the following.

CN-AzPh The spectra of CN-AzPh are similar to those of CN-Az6, which were discussed in detail in 5.2.2: In the C1s spectrum the low energy structure at $284 - 286$ eV is assigned to the C1s to LUMO+0,1,2. The shoulder at the low energy side of the structure in CN-Az6 is not visible in CN-AzPh. This is explained by the fact that CN-AzPh in contrast to CN-Az6 possesses no oxygen bridge, and thus the corresponding initial state effects are not observable at the neighbouring C core. Compared to CN-Az6 the polarization contrast is reduced indicating a less upright orientation for CN-AzPh. The peak at 286.7 eV is attributed to the transition in the localised π bond of the C≡N group. It exhibits the same vibrational progression as in CN-Az6 with the same splitting of 0.25 ± 0.05 eV. Toward higher energies the C1s spectra of CN-AzPh are similar to those of CN-Az6, because the linker in both compounds contribute little to the spectra due to the dampening of the Auger electrons from the linker by the chromophore. Differences in the polarization contrast can be explained by the different orientation.

The N1s spectrum of CN-AzPh is almost identical to that of CN-Az6. We observe the sharp transition to the LUMO at 398.4 eV, followed by the transition to the $\pi^\star$ orbital of the localised π bond of the CN group at 399.6 eV with its vibrational progression with the same splitting as in the C1s spectra, and the transitions to the LUMO+3,4.

CF_3-ImPh The C1s spectra of the imine are very similar to that of CF_3-Az6 (Fig. 5.4). The CF_3 group leads to similar $\sigma^\star$ structures in the spectra of both compounds. In the spectrum of the imine the LUMO structure is observed at the same position as for CF_3-Az6. However, unlike the spectra of the azobenzenes it possesses a pronounced twofold structure, where the maximum is observed at the low energy side of the structure. In the following we give a tentative explanation for this observation. For an unambiguous assignment, however, a calculation would be required. If we assume the general appearance of the LUMO orbitals to be similar to those of the azobenzenes (Fig. 5.6), the LUMO has a high density at the bridge C atom, which is not present in the azobenzenes. Thus, we would expect a larger contribution of this transition in the imine compared to the azobenzene. For the

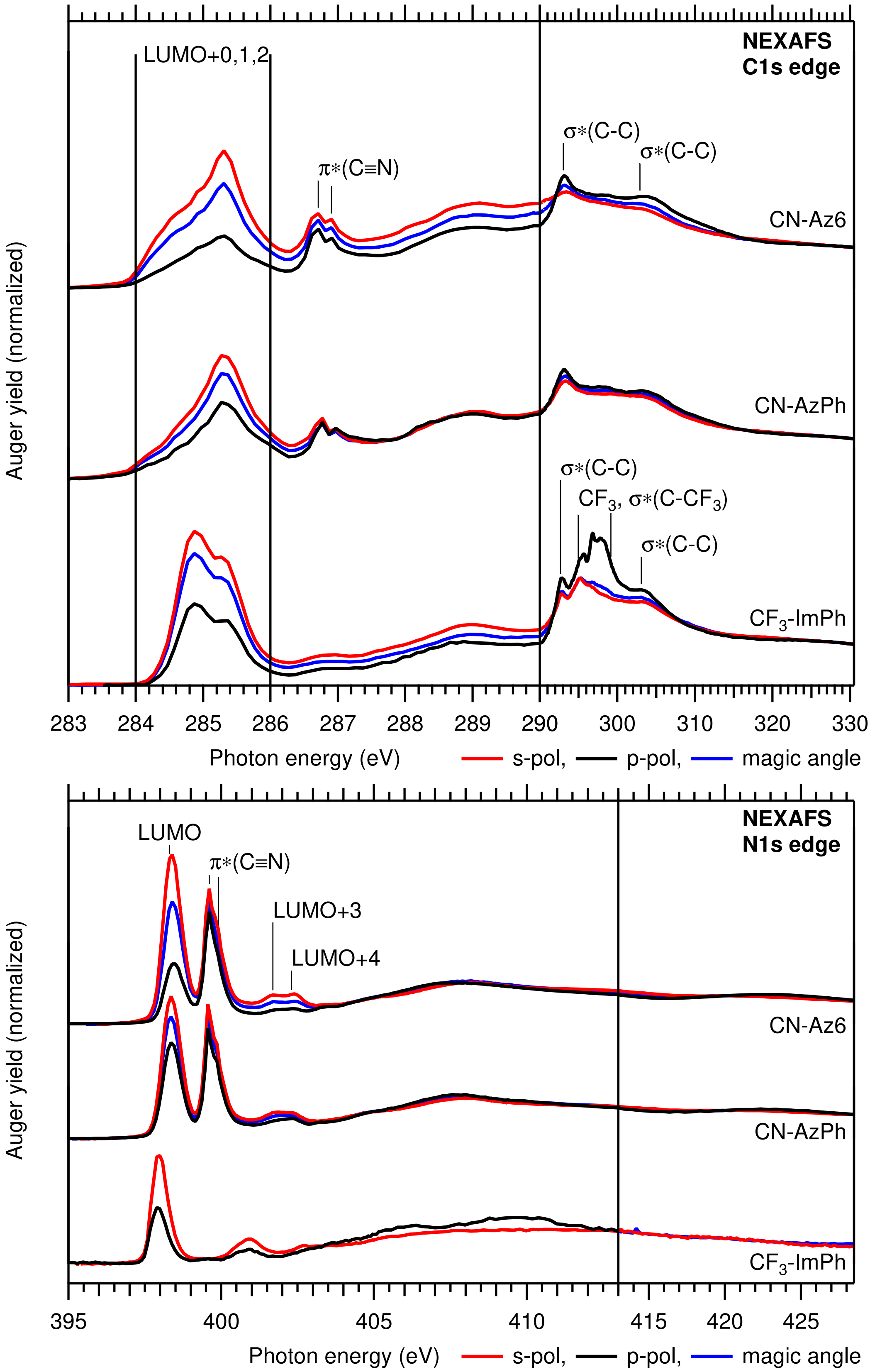

Figure 5.16: C1s and N1s NEXAFS spectra of the SAMs with aromatic linker and CN-Az6 for comparison.

same reason the energetic position of the LUMO transition is effected more than that of the LUMO+1,2 located at the rings rather than the bridge. Apparently the C1s→LUMO transition is shifted to higher energies.

The N1s spectrum consists of the transitions from the N atom in the imine bridge, which is the only N core in the molecule, and is very similar to that of CF_3-Az6 (cf. Fig. 5.4). We observe a pronounced transition to the LUMO at 398.0 eV followed by features in the range of 400–403 eV attributed to transitions to the higher LUMOs. The N1s transitions to the LUMOs of the imine are shifted towards lower energies with respect to those of the azobenzenes. This is opposite to the shift of the LUMO transition observed in the C1s spectrum.

5.3.3 Optical Properties and Photoisomerization

Photoisomerization for CN-AzPh and CF_3-ImPh was attempted in NEXAFS experiments using illumination with 366 nm and 460 nm. No significant changes in the spectra were observed upon illumination. However, illumination was always conducted before—not during—the NEXAFS scans. In the light of later experiments on the photoisomerizable H-Az11/C12 mixed SAMs where photoisomerization was not observed in NEXAFS due to a reduced lifetime of the *cis* form in vacuum (cf. Sec. 5.5.5), these results are of limited significance.

Only a single DRS photoisomerization experiment was performed for CN-AzPh where no isomerization was observed. However, this result should be confirmed by future experiments. It is not clear why for SAMs of Ph-AzPh unlike for SAMs of R-Az6 photoisomerization could be observed in the literature. Even though the reported lattice vectors for Ph-AzPh are slightly larger than those reported for the related R-Az6 SAMs (cf. Tab. 5.4) this does not seem to be a likely cause.

Due to the lower *cis-trans* activation barrier of imines compared to azobenzenes we did not expect the isomerization to be observable at room temperature. Hence, we did not conduct any DRS photoismerization experiments for CF_3-ImPh, as our set-up does not allow measurements at low temperatures.

5.4 Mixed Chromophores

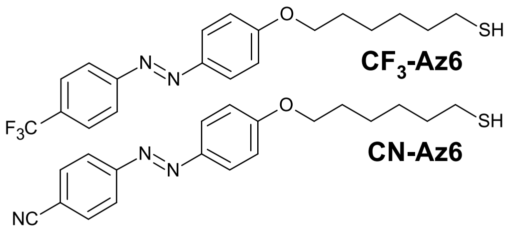

Figure 5.17: Thiols used in the mixing experiment.

In this chapter we will investigate mixed SAMs formed by coadsorption of the two azobenzenealkanetiols CF_3-Az6 and CN-Az6 (Fig. 5.17). They are prepared by incubating the gold substrate in a mixed solution of the two components with a constant total thiol concentration.

The preparation of mixed SAMs by coadsorption has so far been mainly studied on simple alkanethiols with variations in the chain length [59] or carrying small head groups [45]. If the two molecules are more different they usually do not form mixtures on the surface and a single component SAM of the preferentially adsorbed species is formed [115]. The formation of SAMs is based on attractive interactions between the molecules on the surface. The preferential adsorption can be explained by assuming the interactions between the two species A and B forming a hierarchy, e.g. AA $>$ BB $>$ AB leading to preferential adsorption of A. Thus, two thiols with almost identical structure should be very likely to mix on the surface.

CF_3-Az6 and CN-Az6 only differ by their end groups. From our investigations of single component SAMs (Sec. 5.2) we know that both form well ordered SAMs with the same structure. The different substituents can be used as markers in XPS experiments allowing to quantify both components independently at the surface. Thus, these two compounds are an ideal prototype system for a coadsorption experiment. While exchanging the end group does not alter the structure it changes the dipole moment and the optical adsorption. Hence, the system allows to investigate the influence of the environment on molecules of either kind.

In the following we will show that CF_3-Az6 and CN-Az6 indeed form mixed SAMs without phase separation with the same structure as the single component SAMs. The composition at the surface can be tuned to any value between the two pure layers as a function of the composition of the adsorption solution. Only slight preferential adsorption of one component is observed, and the relation can be fitted well with an adsorption model assuming the same interactions between like and unlike molecules (AA = BB = AB). DR spectra reveal strong excitonic coupling also in the mixed SAM. As the mixed SAMs are equally densely packed as the single component SAMs, no photoisomerization was observed as expected.

5.4.1 XPS

The series of spectra recorded for the mixed SAM has the primary purpose to quantify the two components on the surface, i.e. to obtain the composition on the surface as a function of the composition of the adsorption solution. Spectra of the single component SAMs have already been discussed in Sec. 5.2.1. In contrast to the spectra discussed so far, the spectra shown in the following were recorded using a monochromatized laboratory Al K_α X-ray source ($h\nu$=1486.7 eV).[8] The XPS study was

---

[8] The radiation from the laboratory source is not polarized in contrast to the synchrotron experiments, where p-polarized light was used, and the kinetic energy oft the photoelectrons is of the

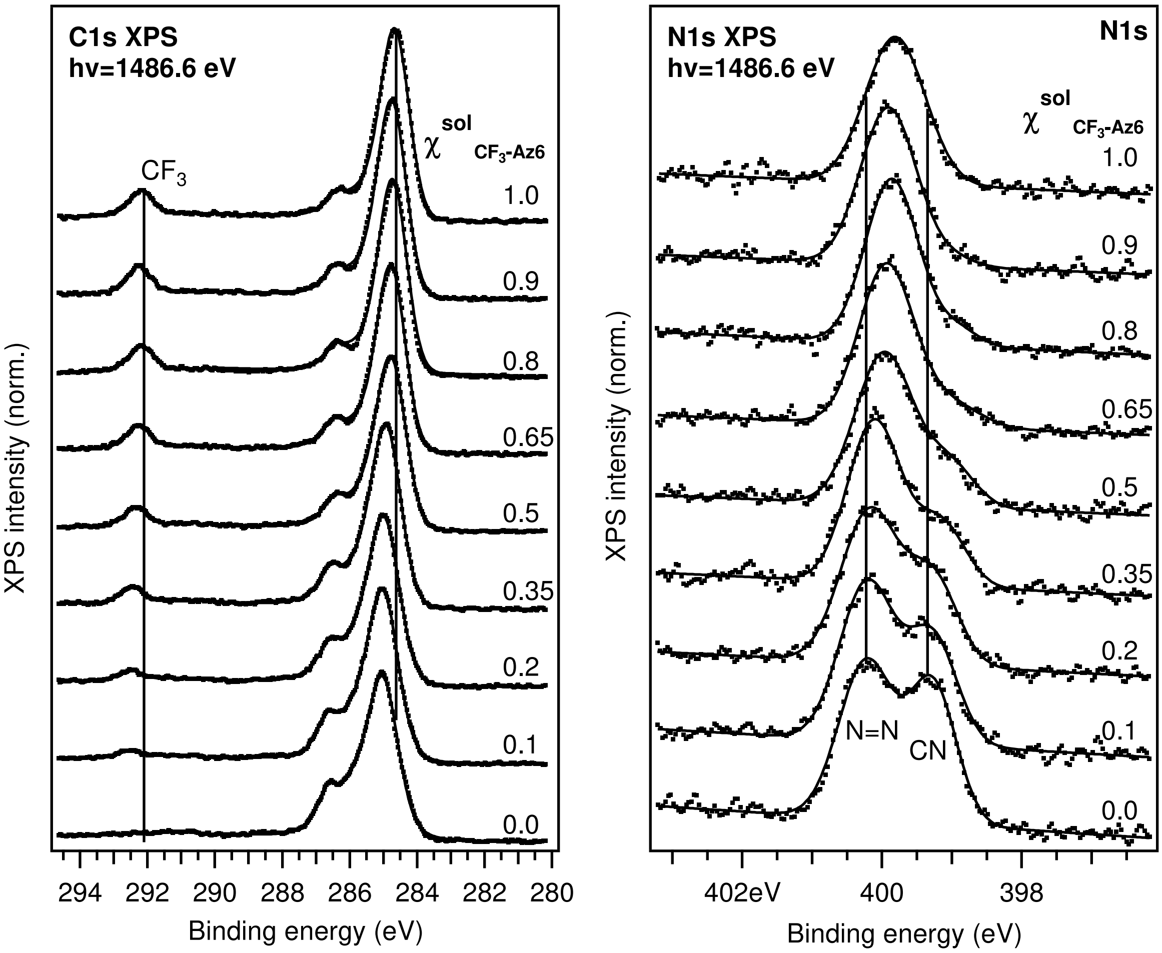

Figure 5.18: XP spectra of SAMs produced from solutions with varying mole fractions $\chi^{\mathrm{sol}}_{\mathrm{CF_3\text{-}Az6}}$ of CF$_3$-Az6, starting with a pure CF$_3$-Az6 layer (top) and ending with a pure CN-Az6 layer ($\chi^{\mathrm{sol}}_{\mathrm{CF_3\text{-}Az6}}$=0%). All spectra were normalized to the integral of the Au4f peak recorded on each sample.

performed in close cooperation with D. Przyrembel, who did all the measurements with the laboratory source. The XP spectra are very similar to those obtained using synchrotron radiation.[9]

In the following, we will first give a qualitative description of the spectra, before we discuss the composition at the surface and peak shifts in detail. Figure 5.18 shows series of C1s and N1s spectra for SAMs produced from solutions with various mole fractions of the two components, starting with a pure layer of CF$_3$-Az6 ($\chi^{\mathrm{sol}}_{\mathrm{CF_3\text{-}Az6}}$ =

---

order 1 keV as compared to 100 eV in the synchrotron experiments. Therefore, in the spectra recorded with the laboratory source the signal from the lower parts of the layer is less dampened. The lower cross section at higher photon energies and lower intensity of the laboratory source lead to a worse signal to noise ratio, most noticeable for the S2p spectra. Unlike the spectra recorded at the synchrotron, those acquired using the laboratory source are quantitative. (cf. Sec. 4.1.9)

[9] Apart from the slightly lower resolution the only noticeable difference is observed in the N1s spectrum of CN-Az6. Here the the intensity of the peaks attributed to the azo (N=N) and nitril (C≡N) nitrogen differs from that observed in spectra recorded using synchrotron radiation. The differences are due to different attenuation of photoelectrons emitted from different depths within the SAM caused by the higher photon energy and lack of polarization of the X-rays from the laboratory source.

100%) at the top and ending with a pure layer of CN-Az6 ($\chi^{\mathrm{sol}}_{\mathrm{CF_3\text{-}Az6}} = 0\%$) at the bottom. When we compare the spectra in the series we observe:

With decreasing mole fraction of CF_3-Az6 in solution,

- the intensity of the CF_3 peak in the C1s spectrum decreases.
- the intensity of the nitrile component in the N1s spectrum increases.
- the azo component of the N1s peak and the whole C1s main peak structure shift continuously towards higher binding energies between the positions of the pure components.
- the nitrile component of the N1s peak and the CF_3 peak in the C1s spectrum also shift towards higher binding energies.

From these observations we can already infer that we achieved a mixture at the surface, i.e. both components are found at the surface. The composition in the SAM can be tuned as it changes continuously with the composition in solution. We have obtained a real mixture on short range, i.e. we do not observe large domains of the single components as this would not lead to continuous peak shifts but a linear combination of the spectra of the single component SAMs.

On each sample S2p spectra were recorded. They uniformly show a single doublet at a binding energy of 162 eV independent of the composition of the adsorption solution. No atomic sulphur or unbound thiol was observed at a detection limit of 5%.

Composition at the surface Now we look at the composition at the surface more quantitatively. In order to obtain peak areas from the spectra they were analysed as follows: F1s, O1s, and the CF_3-component of the C1s spectrum were fitted using a single Gaussian on a linear background. The C1s main peak was decomposed into three components as described in Sec. 5.2.1 by fitting three Gaussians on a linear background. These peak and background models are less involved than those used to fit spectra obtained at the synchrotron and reflect the lower instrumental resolution and lower signal to noise ratio of the spectra recorded using the laboratory source.

Figure 5.19 shows peak areas as a function of the composition of the adsorption solution. All areas were normalized to the Au 4f peak areas measured on the same sample. For O, F, and the CF_3-C integrals from the fit were used. The N peak is difficult to decompose into the azo and nitrile components especially for SAMs with low CN-Az6 content. Therefore, the total area of the N1s structure was obtained by subtracting a linear background and integrating the measured data.

Since each molecule contains one oxygen atom, the uniformity of the O1s intensity, which has a standard deviation below ±0.08, demonstrates a constant coverage independent of the SAM composition. The normalized areas of the F1s and C1s(CF_3) directly represent the surface fraction of CF_3-Az6. The N1s integral consists of the contributions of the nitrile group on a constant background from the azo group. Thus, the variation on top of this background reflects the CN-Az6 fraction on the surface. It decreases accordingly towards higher CF_3-Az6 fractions.

For all mixtures we find a higher fraction of CF_3-Az6 on the surface than in solution, i.e. we observe preferential adsorption of CF_3-Az6.

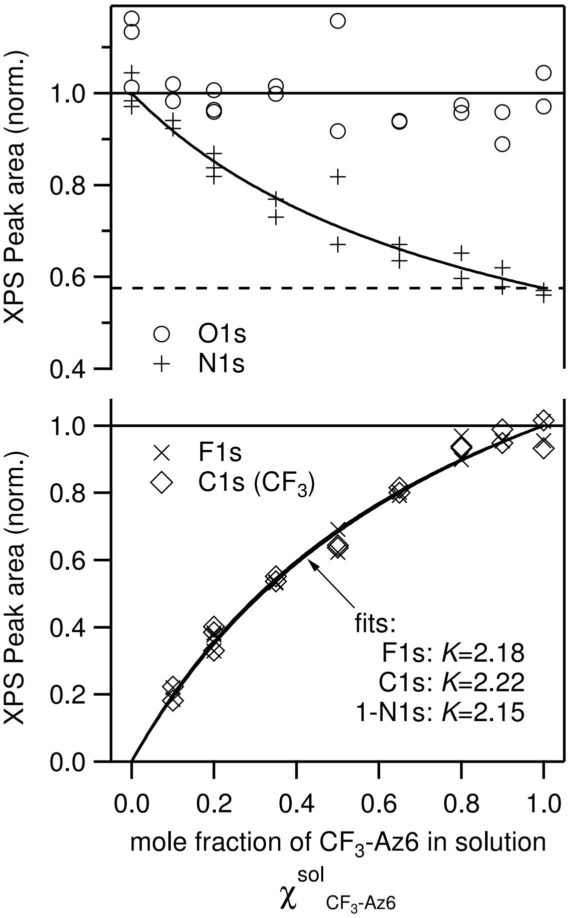

Figure 5.19: XPS intensities as a function of the mole fraction $\chi^{\mathrm{sol}}_{\mathrm{CF_3\text{-}Az6}}$ of CF_3-Az6 in solution. Solid lines are fits to Eq. 5.6. All spectra were normalized to the intensity of the Au4f levels of the substrate of the same sample and to the intensities of pure SAMs of CF_3-Az6 for F1s and C1s (CF_3) spectra, and CN-Az6 for N1s as obtained from the fits. For O1s the mean of all samples was used. The dashed line indicates the contribution of the azo nitrogen to the total nitrogen integral. The peak areas in the lower panel correspond to mole fraction $\chi^{\mathrm{ads}}_{\mathrm{CF_3\text{-}Az6}}$ of CF_3-Az6 fraction on the surface.

Adsorption Model The adsorption behaviour can be modelled, if we assume that the SAM is in thermodynamic equilibrium with the adsorption solution. Since the total coverage is independent of the SAM composition, the exchange reaction of the two adsorbed compounds A and B can be written as a simple 1:1 exchange:

$$\mathrm{A}^{\mathrm{ads}} + \mathrm{B}^{\mathrm{sol}} \rightleftharpoons \mathrm{A}^{\mathrm{sol}} + \mathrm{B}^{\mathrm{ads}}; \qquad K = \frac{c_{\mathrm{A}}^{\mathrm{sol}} c_{\mathrm{B}}^{\mathrm{ads}}}{c_{\mathrm{A}}^{\mathrm{ads}} c_{\mathrm{B}}^{\mathrm{sol}}} \tag{5.2}$$

with the equilibrium constant K and the concentrations in solution $c_{\mathrm{A/B}}^{\mathrm{sol}}$ and on the surface $c_{\mathrm{A/B}}^{\mathrm{ads}}$. Expanding with the constant total concentrations in solution c_0^{sol} and on the surface c_0^{ads}:

$$c_0^{\mathrm{sol}} = c_{\mathrm{A}}^{\mathrm{sol}} + c_{\mathrm{B}}^{\mathrm{sol}}; \qquad c_0^{\mathrm{ads}} = c_{\mathrm{A}}^{\mathrm{ads}} + c_{\mathrm{B}}^{\mathrm{ads}}, \tag{5.3}$$

we replace the concentrations c_i by mole fractions $\chi_i = \frac{c_i}{c_0}$, and use

$$\chi_{\mathrm{B}}^{\mathrm{sol}} = 1 - \chi_{\mathrm{A}}^{\mathrm{sol}} \quad \text{and} \quad \chi_{\mathrm{B}}^{\mathrm{ads}} = 1 - \chi_{\mathrm{A}}^{\mathrm{ads}}. \tag{5.4}$$

$$K = \frac{c_{\mathrm{A}}^{\mathrm{sol}} c_{\mathrm{B}}^{\mathrm{ads}}}{c_{\mathrm{A}}^{\mathrm{ads}} c_{\mathrm{B}}^{\mathrm{sol}}} = \frac{c_{\mathrm{A}}^{\mathrm{sol}} c_{\mathrm{B}}^{\mathrm{ads}}}{c_{\mathrm{A}}^{\mathrm{ads}} c_{\mathrm{B}}^{\mathrm{sol}}} \frac{c_0^{\mathrm{ads}} c_0^{\mathrm{sol}}}{c_0^{\mathrm{sol}} c_0^{\mathrm{ads}}} = \frac{\chi_{\mathrm{A}}^{\mathrm{sol}} \chi_{\mathrm{B}}^{\mathrm{ads}}}{\chi_{\mathrm{A}}^{\mathrm{ads}} \chi_{\mathrm{B}}^{\mathrm{sol}}} = \frac{\chi_{\mathrm{A}}^{\mathrm{sol}} (1 - \chi_{\mathrm{A}}^{\mathrm{ads}})}{\chi_{\mathrm{A}}^{\mathrm{ads}} (1 - \chi_{\mathrm{A}}^{\mathrm{sol}})} \tag{5.5}$$

The XPS intensity I_{A} of the adsorbed species A is proportional to the surface concentration and thus to the surface molar fraction of that component $\chi_{\mathrm{A}}^{\mathrm{ads}}$. Thus,

		slope / eV
F1s		-0.49 ± 0.04
C1s	(CF_3)	-0.49 ± 0.04
N1s	(CN)	-0.48 ± 0.06
N1s	(NN)	-0.49 ± 0.02
C1s	(main)	-0.38 ± 0.02
O1s		-0.32 ± 0.04
S2p		0

Table 5.10: Slopes of fits from Fig. 5.20 (right).

we get for the XPS intensity I_A of the adsorbed species A:

$$I_\mathrm{A} \propto \chi_\mathrm{A}^\mathrm{ads} = \frac{K\chi_\mathrm{A}^\mathrm{sol}}{1+(K-1)\chi_A^\mathrm{sol}} \tag{5.6}$$

Eq. 5.6 was fitted to the peak integrals of F1s and C1s(CF_3) and [1-N1s(CN)] shown in Fig. 5.19[10] with K and the intensity for $\chi_{\mathrm{CF_3\text{-}Az6}}^\mathrm{ads} = 100\%$ as free parameters. For nitrogen the offset caused by the nitrile group, i.e. intensity for $\chi_{\mathrm{CF_3\text{-}Az6}}^\mathrm{ads} = 0\%$ was an additional free parameter.[11] The fits all yield an average equilibrium constant of $K = 2.2 \pm 0.2$ indicating the preferential adsorption of CF_3-Az6; thus for a 1:1 mixture in solution a surface ratio of $\chi_{\mathrm{CF_3\text{-}Az6}}^\mathrm{ads}$=69% is obtained. Nonetheless any desired surface composition can be obtained by adjusting the composition of the adsorption solution.

The peak areas of the C1s(CF_3) and F1s spectra only depend on the CF_3-Az6 concentration, whereas the N1s peak area above the azo background depends only on the CN-Az6 concentration.

In the derivation of equation (5.6) we assumed a constant equilibrium constant K independent of the surface composition, i.e. that the SAM behaves as an ideal two-dimensional solution [45]. This implies that the adsorption energies of the two components do not depend on the number of like and unlike molecules in the vicinity of the molecule to be exchanged. I.e. the interactions between CF_3-Az6/CF_3-Az6, CF_3-Az6/CN-Az6 and CN-Az6/CN-Az6 must be very similar.

Peakshifts — Influence of the enviroment Figure 5.20 (left) shows XPS binding energies as a function of the mole fraction $\chi_{\mathrm{CF_3\text{-}Az6}}^\mathrm{ads}$ of CF_3-Az6 in the SAM. The continuous shift of the binding energy with the composition of the SAM is clearly visible for all elements. Even though the relevant quantity to discuss this data is the composition of the *SAM*, in the right figure the same data is plotted again as a function of the composition of the adsorption *solution*. Although the observed linear relationship is most probably coincidental, it allows to quantify the peak shifts as slopes of the linear fits (Tab. 5.10).

We note that the shift in XPS binding energy is constant for all cores in the extended π-system of the chromophore, while it is lower for the C1s main peak, which is dominated by the cores of the aromatic system but contains some contributions of

---

[10] For the figure the data was scaled, setting the intensity obtained from the fit for $\chi_{\mathrm{CF_3\text{-}Az6}}^\mathrm{ads} = 100\%$ to 1. Correspondingly, for the [1-N1s] data the intensity obtained from the fit for $\chi_{\mathrm{CF_3\text{-}Az6}}^\mathrm{ads} = 0\%$ was subtracted as an offset.

[11] As CN-Az6 contains 3 and CF_3-Az6 2 nitrogen atoms, this offset should be about 66 %. However, due to the stronger attenuation of the electrons emitted from the azo nitrogen compared to the nitrile nitrogen, a lower value is observed.

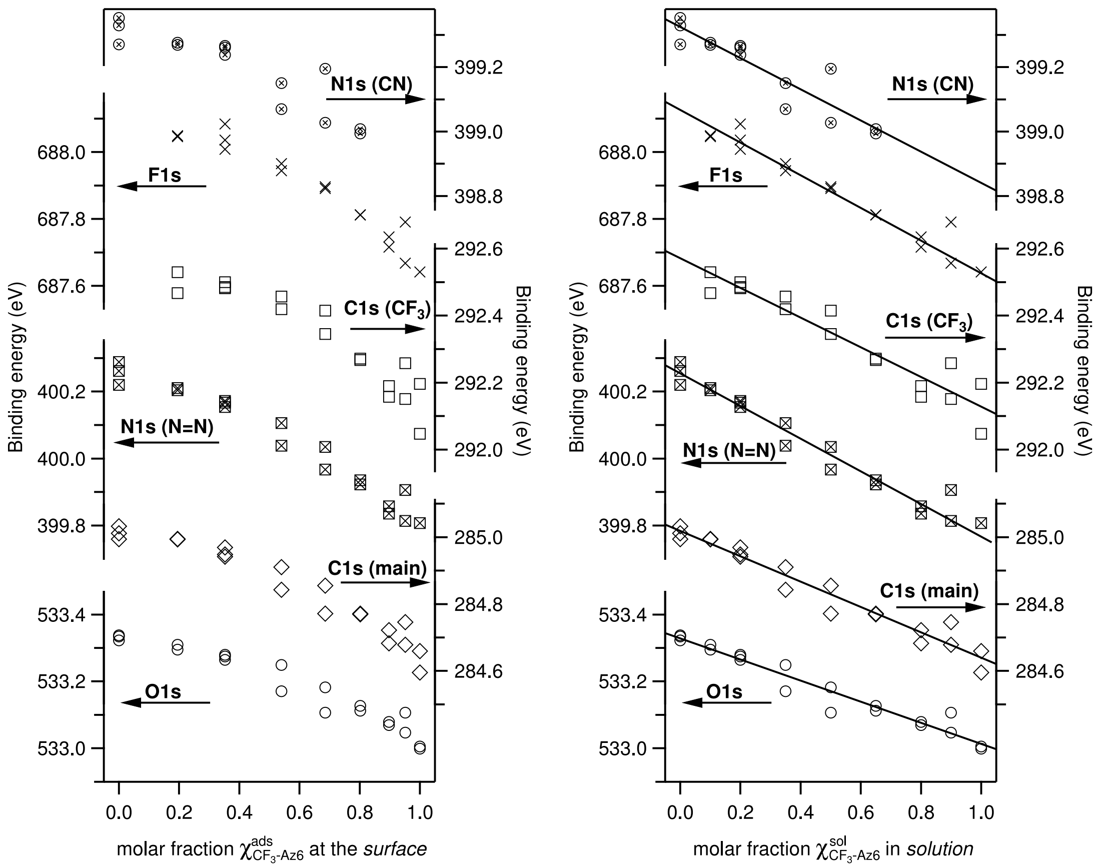

Figure 5.20: XPS binding energies as function of the *surface* mole fraction $\chi^{\mathrm{ads}}_{\mathrm{CF_3\text{-}Az6}}$ (*left*) and the mole fraction $\chi^{\mathrm{sol}}_{\mathrm{CF_3\text{-}Az6}}$ in the adsorption *solution* (*right*). Solid lines are linear fits to the data.

the linker chain, and the O1s core, which is located at the bottom of the aromatic system. As discussed already, the BE of the S atom directly bound to the metal substrate does not shift due to Fermi level pinning.

The observation of continuous peak shifts as a function of the composition of the SAM without broadening rather than a linear combination of the spectra of the two components, suggests that the peak positions depend on a local potential [116] created by the wider environment of the core probed.

In a simplistic model the SAM is described as isolated from the metal surface and polar groups in a SAM are described as dipole layers, which introduce steps in the local potential [117]. In this model the potential step is proportional to the dipole surface density. Thus, we would expect a linear relation between the surface molar fraction $\chi^{\mathrm{ads}}_{\mathrm{CF_3\text{-}Az6}}$ and the observed peak shifts. Fig. 5.20 shows a clear deviation from this model.

A more severe problem with this approach is the question, how to couple the potential of the dipole layer that describes the SAM to the Fermi level of the substrate, which is the reference for the BE. It has been proposed to couple the vacuum potential of the SAM to the vacuum level of the metal substrate, which in turn is coupled to the substrate's Fermi level [118]. For simple alkanethiolate SAMs this model has later been refined [116].

Following the approach of directly coupling the vacuum levels the dipole layer would have no effect on cores on the substrate side of the dipole layer. If we try to describe the polar end groups CF_3 and CN as a dipole layer on top of the SAM in contrast to the observation we would expect little or no peak shifts for cores in the chromophore. Assuming dipoles extending into the chromophore could explain peak shifts in the chromophore, but would lead to a dependence of the shift on the position of the core within the chromophore. Most remarkably, however, we observe the same peak shift for the out most atoms of the SAM (F and the CN N), which should be centres of negative charge, as for the NN N in the middle of the chromophore.

Thus, the author was unable to construct a conclusive qualitative model of the local potential in the mixed SAM. Nonetheless, assuming a plane averaged local potential to describe the photoemission in these mixed SAMs appears to be a valid approach. DFT calculations including slaps of the metal substrate [119–121] may allow to model the local potential.

5.4.2 NEXAFS

Figure 5.21 shows C1s and N1s spectra of pure CF_3-Az6 and CN-Az6 SAMs and a mixed SAM prepared from solutions with a 1:1 mixture of the two components. The spectra of the pure SAMs of CF_3-Az6 and CN-Az6 have already been discussed in Sec. 5.2.2. In addition here we want to draw attention to a small energetic difference between the N1s to LUMO $\pi^\star$ transition observed at 398.3 eV for CF_3-Az6 compared to 398.4 eV for CN-Az6. This difference of 0.1 eV is much smaller—and probably within the errors of the method—than the corresponding difference of 0.9 eV for the azo nitrogen in the N1s XP spectra (cf. Fig. 5.18). This difference can be explained as follows: In XPS the difference in the local potential caused by the different end groups in the two molecules leads to a corresponding difference in the work function. In NEXAFS, however, the change in the local potential shifts the initial and final states involved in the transition in a similar manner.

In the case of the mixed SAM the C1s and N1s spectra can be described as a linear combination of the spectra of the single components (Fig. 5.22). This substantiates that the molecules have the same orientation in the mixed SAM as in the single component SAMs. From the coefficient of the fit of the spectra of the pure layers to the mixed layer the mole fractions in the mixed SAM $x = \chi^{\text{ads}}_{\text{CF}_3\text{-Az6}}$ can be obtained as follows: The edge jump in NEXAFS is proportional to the amount of the relevant element at the surface if dampening is disregarded. The spectra were normalized to an edge jump of 1. As both molecules are very similar and have a similar orientation the dampening can be assumed to be the same. Both molecules have the same number of C atoms. Thus, we obtain the following linear relationship for the C1s NEXAFS spectra A, where the surface mole fraction of CF_3-Az6 is $x = \chi^{\text{ads}}_{\text{CF}_3\text{-Az6}}$:

$$x \cdot A_{\text{CF}_3\text{-Az6}} + (1-x) \cdot A_{\text{CN-Az6}} = A_{\text{mixed SAM}} \tag{5.7}$$

For the N1s spectra we have to take into account that the spectra are normalized to 1 and both molecules have a different number of nitrogen atoms. Thus, we have to weight the spectra of the pure compounds with 2 for CF_3-Az6 and 3 for CN-Az6:

$$2x \cdot A_{\text{CF}_3\text{-Az6}} + 3(1-x) \cdot A_{\text{CN}_3\text{-Az6}} = \big(2x + 3(1-x)\big) \cdot A_{\text{mixed SAM}} \tag{5.8}$$

The following values were obtained for the mixed layer prepared form a solution with $\chi^{\text{sol}}_{\text{CF}_3\text{-Az6}} = 50\%$:

	C1s, p-pol	C1s, s-pol	N1s, s-pol	N1s,p-pol
$\chi^{\text{ads}}_{\text{CF}_3\text{-Az6}} = x =$	69%	69%	62%	66%

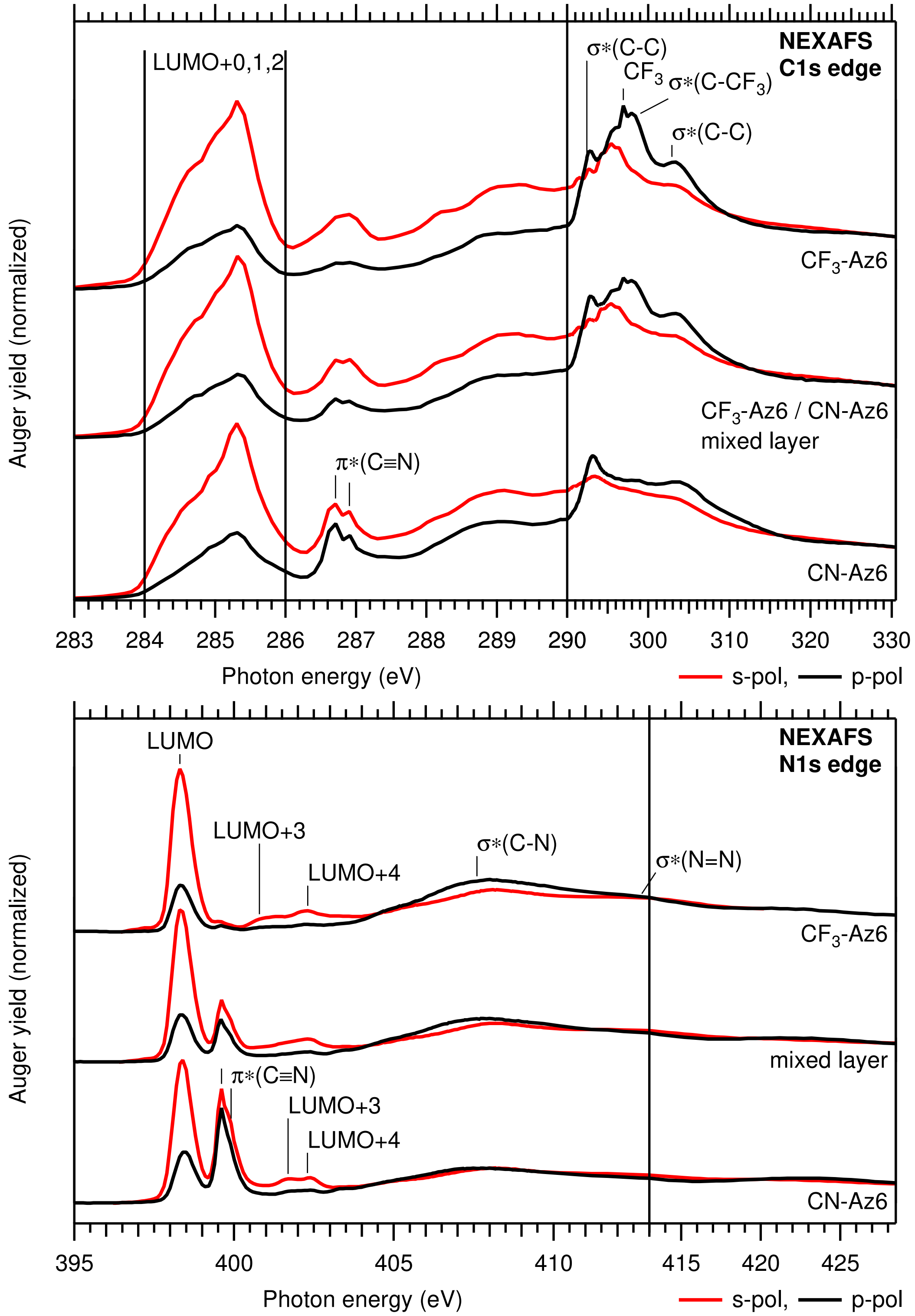

Figure 5.21: C1s and N1s NEXAFS of SAMs of CF_3-Az6, CN-Az6 and a mixed SAM prepared from solution with a 1:1 mixture ($\chi^{\mathrm{sol}}_{\mathrm{CF_3\text{-}Az6}} = 50\%$). Note that, due to preferential adsorption, the molar fraction of CF_3-Az6 at the surface is higher than in solution as discussed in the text.

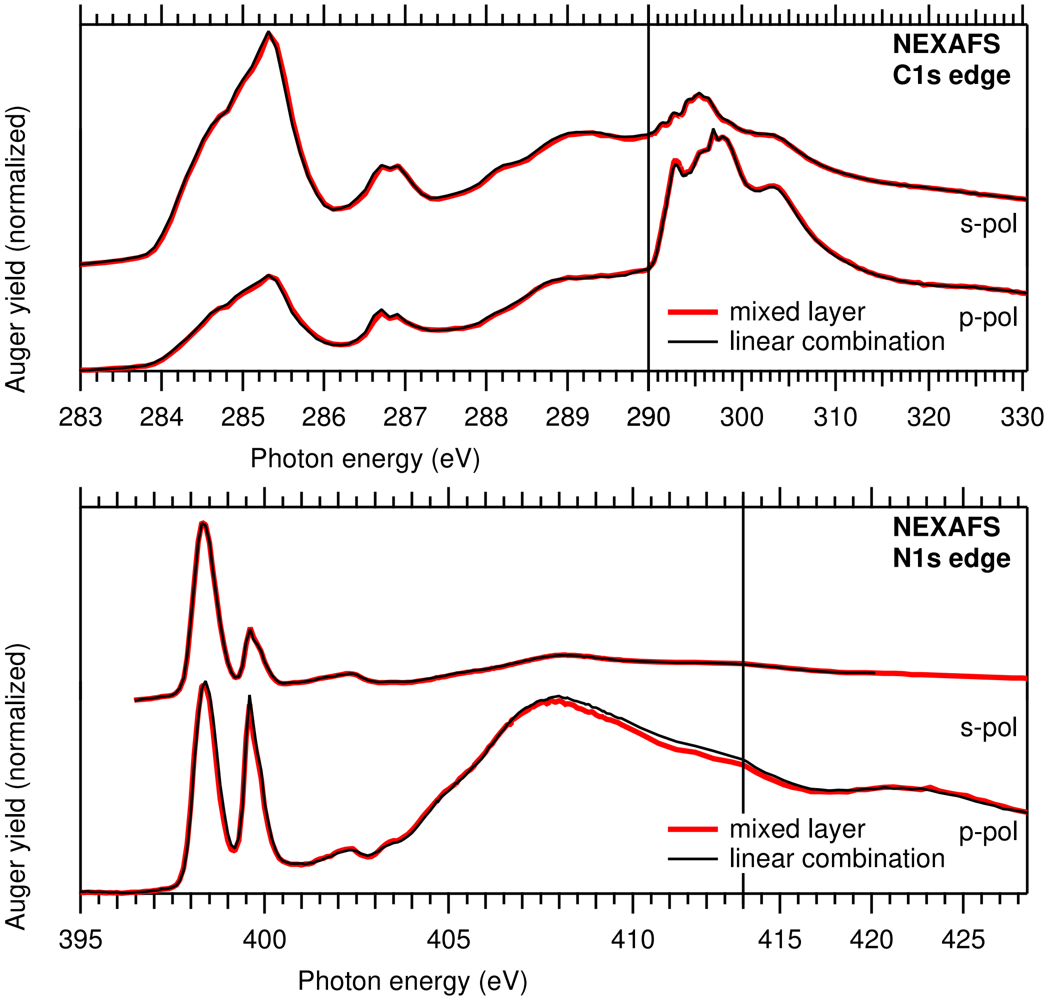

Figure 5.22: C1s and N1s NEXAFS of a mixed SAM prepared from a solution of CF_3-Az6 and CN-Az6 1:1 ($\chi^{\mathrm{sol}}_{\mathrm{CF_3\text{-}Az6}} = 50\%$) (red) and best fits of linear combinations of the pure compounds (black). From the fit a surface molar fraction of ($\chi^{\mathrm{ads}}_{\mathrm{CF_3\text{-}Az6}} = 69 \pm 2\%$) was obtained (see text).

The deviation of the values obtained at the C and N edge can be explained if we consider the dampening. Auger electrons originating from the additional N atom in the CN group of CN-Az6 are less attenuated by the layer than electrons originating from the azo group deeper in the layer. Thus, the weight of the CN-Az6 spectra in the decomposition should be increased to a value larger than 3. This would result in a higher$\chi^{\mathrm{ads}}_{\mathrm{CF_3\text{-}Az6}}$. Therefore, we state the value obtained at the C edge with an error estimated from the deviation of the two values measured at the N edge as our best estimate: $\chi^{\mathrm{ads}}_{\mathrm{CF_3\text{-}Az6}} = (69 \pm 2)\%$. This is in excellent agreement with the value of 69% expected for a sample prepared from 50% solution based on the fits of the XPS peak areas.

We summarise that both the pure components and the mixture have a similar orientation. A mixed phase with deviating orientation is not formed. However, from the NEXAFS data alone we can not infer that there is a mixed phase, as a mixture of single component domains would result in the same spectra. The composition of the SAM obtained from the NEXAFS spectra confirms the results obtained from the quantitative XPS.

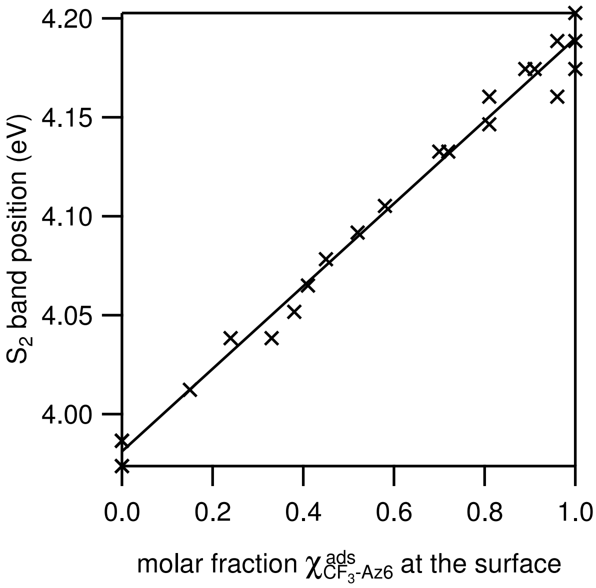

Figure 5.23: S_2 band position as a function of the surface molar fraction $\chi^{ads}_{CF_3\text{-}Az6}$. S_2 Band positions are maxima directly read from the DR spectra measured using p-polarized light. The solid line is a linear fit to the data (offset: $3.981 \pm 0.004\,eV$, slope $0.209 \pm 0.005\,eV$).

5.4.3 Optical Properties

Figure 5.24 shows DR spectra of the mixed and single component SAMs.[12] The spectra of the pure components were already discussed in Sec. 5.2.4. Here we are most interested in the S_2 aggregate band observable in the spectra measured using p-polarized light. With decreasing molar fraction of $\chi^{ads}_{CF_3\text{-}Az6}$ on the surface the S_2 band position shifts gradually from that of the pure CF_3-Az6 SAM to that of the pure CN-Az6 (0% CF_3-Az6) SAM without changing its width significantly. This is a further indication for real mixing of the two components at a molecular level rather than the formation of larger domains: The excited states in the aggregate band are delocalized over many molecules. The continuous shift of the band position with the composition of the SAM indicate that coupling takes place between unlike chromophores. This would not be possible in a scenario with larger clusters of the individual components, which should lead to a linear combination of the spectra of the single components that should become visible as a broadening of the peak.

The position of the S_2 band as a function of the composition of the SAM is shown in Fig. 5.23. We observe a linear relation between the band position and $\chi^{ads}_{CF_3\text{-}Az6}$. This linear relation indicates that both components contribute equally to the aggregate.

5.4.4 Photoisomerization Behaviour

Photoisomerization has been attempted for all $\chi^{ads}_{CF_3\text{-}Az6}$ shown in Fig. 5.23 using the same conditions as for the single component R-Az6 SAMs (cf. Sec. 5.2.5). No significant changes in the spectra were observed for any composition. This result is not unexpected as the structure of the SAM is the same as for the single component SAMs, which do not photoisomerize, and the S_2 aggregate absorption peak behaves like that of a single component SAM with a chromophore with an intermediate position of the S_2 transition.

Therefore, the results obtained on this mixed SAM do not help to differentiate between steric hindrance and excitonic coupling as reasons for the inhibited photo-

---

[12] DRS measurements were performed in close collaboration with T. Moldt.

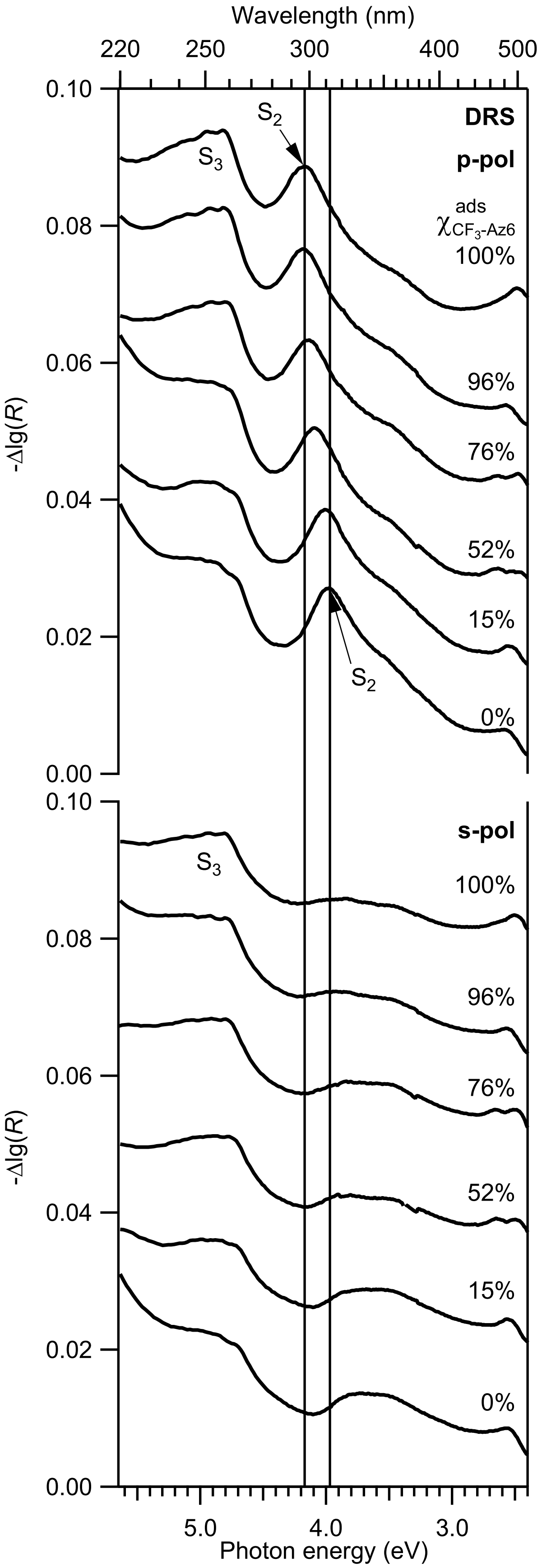

Figure 5.24: DR spectra of CF_3-Az6/CN-Az6 mixed SAMs for different molar fractions $\chi^{\mathrm{ads}}_{\mathrm{CF_3\text{-}Az6}}$ on the surface. Measured at an angle of incidence of 45° using p-polarized *(top)* and s-polarized *(bottom)* light.

isomerization. However, by exchanging one of the components in the mixture by one with an adsorption energy further apart from that of the other while maintaining the structure of the SAM, we might be able to gain more insight into this question. The increased difference in adsorption energy should reduce the excitonic coupling. Stilbenes with a structure corresponding to the R-Az6 azobenzens are promising candidates for such an experiment.

5.5 Diluted Chromophores

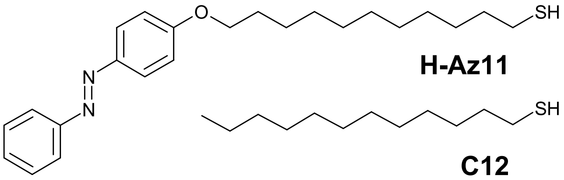

Figure 5.25: Thiols used for the formation of SAMs with diluted chromophores: H-Az11 the thiol carrying the linker chain and 1-dodecanethiol (C12) used as spacer.

In Sec. 5.2.5 we have shown that single component azobenzenealkanethiolate SAMs do not photoisomerize—presumably due to steric constraints. Thus, it appears desirable to produce SAMs with a lower chromophore density. However, as the formation of SAMs is based on the attractive interactions between the molecules, the surface will always be completely covered. One approach pursued to reduce the chromophore density is to attach the chromophores to a linker with a larger footprint [122]. In another study a photoisomerizable SAM was produced by adsorption from a solution of the *cis* isomer [123]. This SAM was found to have a lower density and to be less ordered than a SAM of the *trans* isomer of the same compound, which did not switch. Placing the chromophore carrying alkanethiol on a curved surface, i.e. on gold nanoparitcles, also reduces the chromophore density. For H-Az11 (Fig. 5.25), the compound used in the work presented in this chapter, reversible photoisomerization could be demonstrated on nanoparticles [82, 85].

The approach we followed is to produce mixed SAMs where the chromophore-carrying thiol is diluted with a chromophore-free spacer. A simple alkanethiole (C12, Fig. 5.25) was used as spacer molecule. The formation of mixed SAMs by co-adsorption with molecules strongly differing in their structure is often hampered by strong preferential adsorption of one component. Hence, many researchers employed asymmetric disulphides comprising the chromophore carrying thiol and a simple alkanethiol as spacer to ensure both components are delivered to the surface [14, 15, 21–23]. For these systems photoisomerization was demonstrated. However, this technique leads to SAMs with a fixed 1:1 ratio of the two components. Similar photoisomerizable SAMs were produced by coadsorption [24–26]. This approach, we followed, allows to produce SAMs of arbitrary composition. We were able to produce mixed SAMs of H-Az11 and C12 very similar to those formed from an asymmetric disulphide by Ah Qune and coworkers [22].

In the following we will show that this system forms mixed SAMs without phase separation where the chromophore density can be tuned from 0 to 100% chromophore coverage via the composition of the adsorption solution. The composition at the surface as a function of the composition of the adsorption solution was obtained by quantitative XPS. Unlike in the previous mixing experiment (cf. Sec. 5.4) where two very similar molecules were mixed, the data obtained could not be fitted with a model assuming same interactions between the two different molecules at the surface. Extending the model to allow for different interactions between the two pairs of like and between unlike molecules, the data could be described well. Like the other azobenzene alkanethiolate SAMs investigated in this work (cf. Sec. 5.2) the structure of the undiluted layer of H-Az11 exhibits a predominantly upright orientation of the chromophore. With decreasing chromophore density the azobenzene moieties are tilted more towards the surface. A strong shift of the aggregate band in the optical spectra of mixed SAMs compared to the pure chromophore SAMs demonstrates that excitonic coupling can be tuned by the chromophore density. Already for minor dilu-

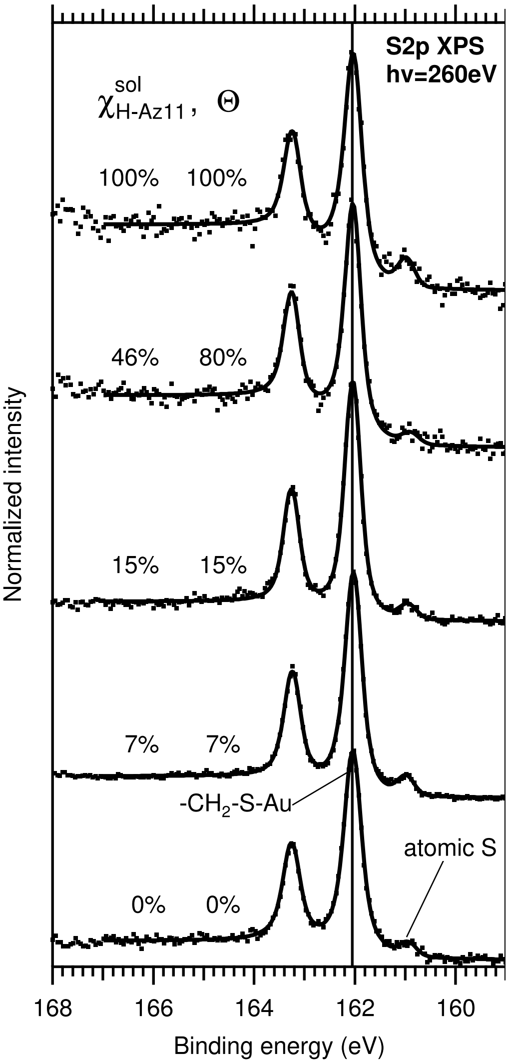

Figure 5.26: S2p XPS spectra of H-Az11/C12 mixed SAMs: Intensities were normalized to the total peak area for display. Data was measured on the same samples as the NEXAFS spectra. The surface coverages Θ were estimated from the molar fraction $\chi^{sol}_{\text{H-Az11}}$ of H-Az11 in the adsorption solution using Fig. 5.29.

tions efficient photoisomerization upon illumination with UV light is demonstrated. Unlike in solution the reverse process induced by blue light is almost complete. We suggest a cooperative mechanism to explain this observation.

5.5.1 XPS

S2p Figure 5.26 shows S2p XP spectra of the two pure components and for different mixed SAMS. The spectra are very similar to those of the R-Az6 SAMs and are decomposed similarly into two peaks.[13] For all concentrations the parameters of the main component were within 162.03 ± 0.02 eV and FWHM 0.40 ± 0.02 eV and 160.95 ± 0.10 eV for the minor component in agreement with the values for the R-Az6 SAMs. This agreement is expected as the thiolate binding energy is pinned to the Fermi level of the substrate and the chemical environment of the S atom is the same in all alkyl thiolate SAMs.

As for R-Az6 the main component at 162 eV is assigned to the desired thiolate bound to gold and the minor component at 161 eV is attributed to the undesired

---

[13] For the main component a Voigt line profile was used. The minor component was fitted using a Gaussian. During the fit all parameters but the width of the minor component were free. For the minor component a FWHM of 0.38 eV was used.

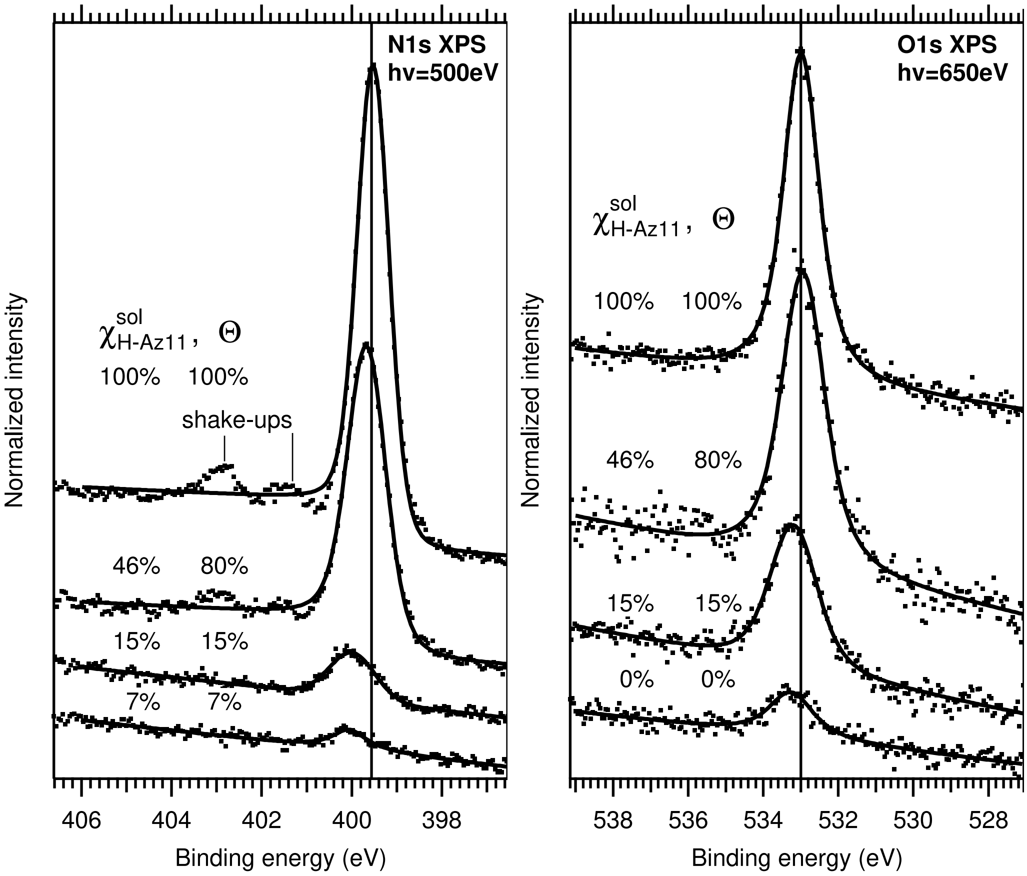

Figure 5.27: N1s and O1s XP spectra of H-Az11/C12 mixed SAMs: Intensities were normalized to the right background. Note that even though a decreasing peak intensity with decreasing surface coverage Θ is correctly reproduced, relative intensities are not comparable in these conditions. Data was measured on the same samples as the NEXAFS spectra. The surface coverages Θ were estimated from the molar fraction $\chi^{\mathrm{sol}}_{\mathrm{H\text{-}Az11}}$ of H-Az11 in the adsorption solution using Fig. 5.29.

atomic sulfur. In all cases the peak area of the atomic sulphur is less than 10% of the total peak area. It is unclear why such a high content of atomic sulphur compared to the spectra shown for the R-Az6 SAMs is present.[14] Peaks at higher binding energies corresponding to unbound thiolate/disulphide were not observed. In this series of spectra the dependence of the XPS background on the thickness of the adsorbate layer is very notable (cf. Fig. 4.3). Therefore, in Fig. 5.26 spectra were normalized to the total peak area.

N1s Figure 5.27 (left) shows N1s spectra for pure and diluted H-Az11 SAMs. The spectrum of the pure H-Az11 SAM is almost identical to that of H-Az6 described

---

[14] An H-Az6-SAM analysed in the same beam-time also showed high amounts of atomic sulfur, suggesting some problem during that beamtime, like substrates with a higher contamination. The atomic sulfur is not caused by beam damage as the spectra shown are sums of 5 scans and no increase in the atomic sulphur peak was observed with exposure. When the H-Az11/C12 system was investigated again [37, SI] in a later beamtime the amounts of the minor components were generally below the detection limit of 2%. Due to the lower signal to noise ratio of the S2p spectra recorded using our laboratory X-ray source the detection limit for the minor component is about 10%. Thus, it can not be said whether SAMs prepared for the UV/vis and quantitative XPS experiments suffered from the same problem.

Table 5.11: XPS Peak Parameters: All Energies in eV.

$\chi^{\text{sol}}_{\text{H-Az11}}$	Θ	N BE	FWHM	O BE	FWHM	C1 BE	FWHM	C2 BE	FWHM	C3 BE	FWHM
100%	100%	399.5	0.8	533.0	1.1	284.3	0.6	284.8	0.8	286.2	0.8
46%	80%	399.7	1.0	533.0	1.4	284.5	0.7	284.9	0.9	286.3	0.9
15%	15%	400.0	1.1	533.1	1.4	284.7	0.7	285.0	0.9	285.5	0.7
7%	7%	400.1	1.0	—	—	284.7	0.8	285.0	0.9	—	—
0%	0%	—	—	533.3	1.4	284.8	0.9	284.9	1.1	—	—

in detail in Sec. 5.2.1: We observe a single peak and shake-ups. All spectra were fitted using a Voigt peak on a combination of Shirley type and linear background. With increasing dilution the peak position shifts continuously towards higher binding energies (Tab. 5.11). This continuous shift indicates largely statistical mixing of the two components.

O1s Figure 5.27 (right) shows O1s spectra for pure and diluted H-Az11 SAMs. The spectrum of the pure H-Az11 SAM is almost identical to that of H-Az6 described in detail in Sec. 5.2.1. All spectra were fitted using a Voigt peak on a linear background. With increasing dilution the peak position also seems to shift towards higher binding energies (Tab. 5.11). However, this shift is less pronounced than for the N1s spectra. This observation is in line with the results obtained for the CF_3-Az6/CN-Az6 system where the extend of the peaks shift decreases with increasing distance of the probed atom to the surface.

For the peak in the pure C12 SAM (0% H-Az11) sample we do not have an explanation. In the XPS experiments conducted later to investigate the surface coverage as a function of the composition in solution using the Al K_α-source no oxygen was observed for 0% samples.

C1s Figure 5.28 shows C1s spectra for pure and diluted H-Az11 SAMs. The spectrum of the pure H-Az11 SAM is almost identical to that of H-Az6 described in detail in 5.2.1 and was fitted using the same decomposition into three Voigt peaks and a Shirley background. The spectra of the diluted SAMs were fitted in the same way. The spectra of the pure C12 SAM and the $\chi^{\text{sol}}_{\text{H-Az11}}$=7% SAM were fitted with two peaks only. This empirical decomposition allows to fit the data well, but is only a rough approximation of the physical model. As the parameters of the main peaks are highly correlated their individual positions are not very meaningful. However, a shift of both main peaks towards smaller energies is clearly observed (see also Tab. 5.11) and of similar magnitude as for the N1s peak.

Composition on the Surface In order to investigate the chromophore density Θ in the SAM as a function of the composition of the adsorption solution quantitative XP spectra were acquired in a similar manner [82] as for the CF_3-Az6/CN-Az6 system using a monochromatized Al $K\alpha$ source.[15] As H-Az11 and C12 lack additional markers, only the N1s spectra can be used to quantify the amount of H-Az11 on the surface. Unlike for the CF_3-Az6/CN-Az6 mixed SAMS we have to expect deviations from a 1:1 exchange reaction as discussed in the next section. Thus, the amount of

---

[15] The XPS measurements with the laboratory X-ray source were performed by D. Przyrembel.

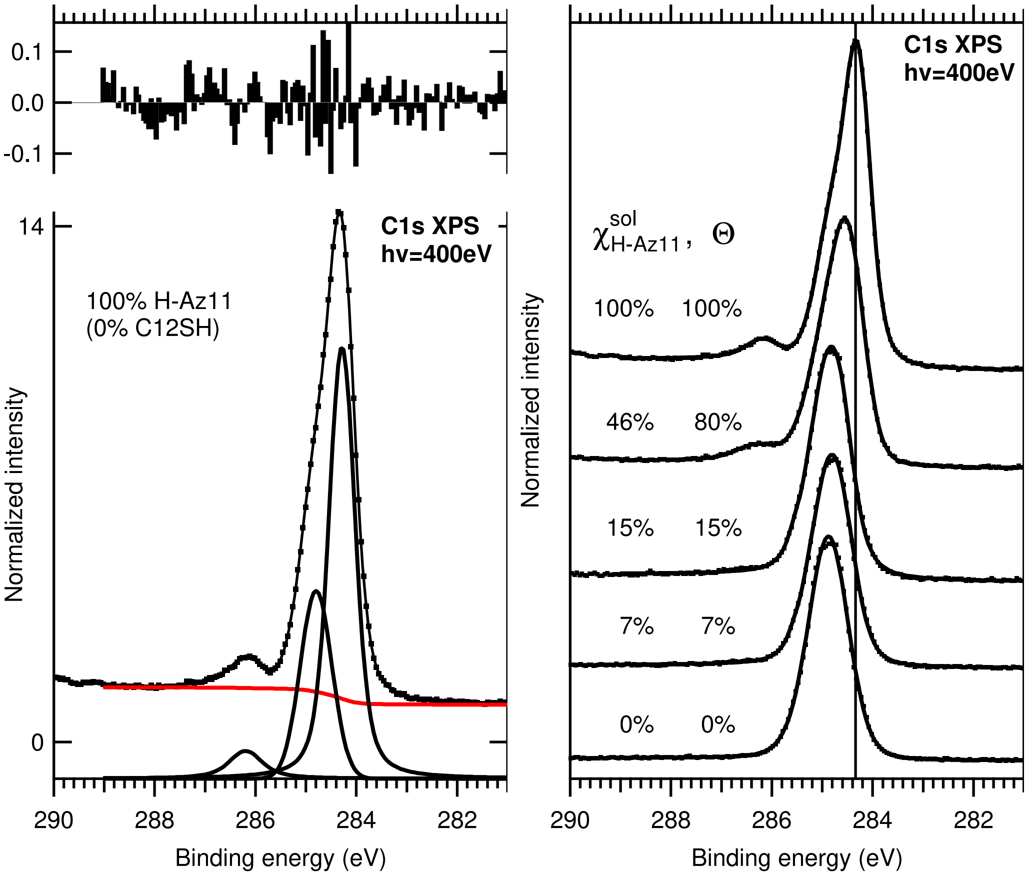

Figure 5.28: C1s-XP spectra of H-Az11/C12 mixed SAMs: Intensities were normalized to the right background. Data was measured on the same samples as the NEXAFS spectra. **left:** Decomposition and residuals for a 100% H-Az11 sample. **right:** Spectra of various concentration of the chromophores: The surface coverages Θ were estimated from the molar fraction $\chi^{\mathrm{sol}}_{\text{H-Az11}}$ of H-Az11 in the adsorption solution using Fig. 5.29.

C12 in the SAM can not be determined. Hence, we describe the composition at the surface by the relative surface coverage Θ of H-Az11 compared to a 100% H-Az11 SAM.

We assume that differences in attenuation of the N1s electrons as a result of different coverage can be neglected as the N=N bridge is located in the outer part of the molecule and the kinetic energy of the electrons is relatively high. Thus, Θ can be obtained as the N1s peak area normalized to a 100% H-Az11 SAM.

Figure 5.29 shows the H-Az11 coverage Θ in the SAM as a function of the molar fraction $\chi^{\mathrm{sol}}_{\text{H-Az11}}$ in the adsorption solution. For small $\chi^{\mathrm{sol}}_{\text{H-Az11}}$the composition of the SAM resembles that in solution (diagonal line). For higher $\chi^{\mathrm{sol}}_{\text{H-Az11}}$a preferential adsorption of H-Az11 is observed.

The van der Waals interactions between neighbouring C12 molecules and between H-Az11 and C12 should be very similar because the chain length is nearly the same. Between H-Az11 molecules, however, there will be additional π-π interactions between the chromophores. This explains the preferential adsorption of H-Az11. In the following we will try to model this behaviour:

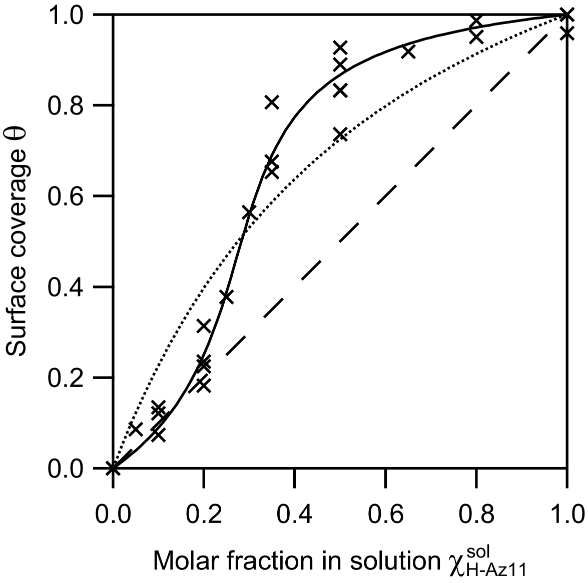

Figure 5.29: Surface coverage Θ as a function of the molar fraction of H-Az11 $\chi^{\mathrm{sol}}_{\text{H-Az11}}$ in the adsorption solution. The diagonal corresponds to a model without preferential adsorption, i.e. the composition on the surface is the same as in solution. The dotted line is a fit of Eq. 5.11, the model assuming same interactions between like and unlike molecules. The solid line is a fit of Eq. 5.19, a model allowing different interactions between the two pairs of like molecules and between unlike molecules.

5.5.2 Adsorption Model

In the literature we find the following footprints for the two components:

simple alkanethiols [105]	0.217 nm^2
H-Az11 [102, 103]	0.242 nm^2

The values differ by about 10%. Thus, we can hope for a reasonable description of the data when we assume a 1:1 exchange reaction in the following as we did for the CF$_3$-Az6/CN-Az6 system. In the case of a 1:1 exchange the surface coverage becomes equal to the surface molar fraction:

$$\Theta = \chi^{\mathrm{ads}}_{\text{H-Az11}} \tag{5.9}$$

We express the equilibrium constant K for the adsorption process using the mole fractions in solution $\chi^{\mathrm{sol}}_{\mathrm{A}}$ and at the surface $\chi^{\mathrm{ads}}_{\mathrm{A}}$ of the component A (H-Az11) only in the same way as for the CF$_3$-Az6/CN-Az6 system discussed in the previous section (cf. Eq. 5.5):

$$\mathrm{A}^{\mathrm{ads}} + \mathrm{B}^{\mathrm{sol}} \rightleftharpoons \mathrm{A}^{\mathrm{sol}} + \mathrm{B}^{\mathrm{ads}}; \qquad K = \frac{c^{\mathrm{sol}}_{\mathrm{A}} c^{\mathrm{ads}}_{\mathrm{B}}}{c^{\mathrm{ads}}_{\mathrm{A}} c^{\mathrm{sol}}_{\mathrm{B}}} = \frac{\chi^{\mathrm{sol}}_{\mathrm{A}}(1-\chi^{\mathrm{ads}}_{\mathrm{A}})}{\chi^{\mathrm{ads}}_{\mathrm{A}}(1-\chi^{\mathrm{sol}}_{\mathrm{A}})} \tag{5.10}$$

Solving this equation for $\chi^{\mathrm{ads}}_{\mathrm{A}}$ we obtain:

$$I_{\mathrm{A}} \propto \chi^{\mathrm{ads}}_{\mathrm{A}} = \frac{K\chi^{\mathrm{sol}}_{\mathrm{A}}}{1 + (K-1)\chi^{\mathrm{sol}}_{A}} \tag{5.11}$$

Fitting this simple equation (fit result $K = 2.64$), that described the data in the case of the CF$_3$-Az6/CN-Az6 excellently, fails completely in the current case (dotted line in Fig. 5.29). Such deviations from the behaviour of an ideal two-dimensional solution are the typical situation in mixed SAMs [45]. Apparently the assumption that the equilibrium constant does not depend on the surface mole ratio, implying that all interactions between neighbouring molecules are equal, does not hold true for the current case as discussed in the previous section. Thus, a more elaborate model is required:

The next more complex model is one assuming different interactions between the two kinds of same molecules (AA and BB) and different molecules (AB). The energy gained by the exchange reaction (Eq. 5.6) can thus be written as:

$$\Delta_R E = \underbrace{\chi_{\mathrm{A}}^{\mathrm{ads}} E_{\mathrm{AA}} + \chi_{\mathrm{B}}^{\mathrm{ads}} E_{\mathrm{AB}}}_{\substack{\text{Energy gained by bringing} \\ \text{1 A \textit{to} the surface}}} \underbrace{-\chi_{\mathrm{A}}^{\mathrm{ads}} E_{\mathrm{AB}} - \chi_{\mathrm{B}}^{\mathrm{ads}} E_{\mathrm{BB}}}_{\substack{\text{Energy lost by removing} \\ \text{1 B \textit{from} the surface}}} + \Delta_R E_0 \tag{5.12}$$

Where E_{ij} are the interaction energies between the different molecules in the SAM, and $\Delta_R E_0$ contains all contributions that do not depend on the composition of the SAM, e.g. differences in interactions with the solvent. Using $\chi_{\mathrm{A}}^{\mathrm{ads}} = 1 - \chi_{\mathrm{B}}^{\mathrm{ads}}$ we obtain:

$$\Delta_R E = \chi_{\mathrm{A}}^{\mathrm{ads}} E_{\mathrm{AA}} + (1 - \chi_{\mathrm{A}}^{\mathrm{ads}}) E_{\mathrm{AB}} - \chi_{\mathrm{A}}^{\mathrm{ads}} E_{\mathrm{AB}} - (1 - \chi_{\mathrm{A}}^{\mathrm{ads}}) E_{\mathrm{BB}} + \Delta_R E_0 \tag{5.13}$$

$$\Delta_R E = \chi_{\mathrm{A}}^{\mathrm{ads}} (E_{\mathrm{AA}} - 2E_{\mathrm{AB}} + E_{\mathrm{BB}}) + (E_{\mathrm{AB}} - E_{\mathrm{BB}} + \Delta_R E_0) \tag{5.14}$$

Assuming that entropic contributions are negligible or follow the same pattern as the naive energies E_i we replace them by the Gibbs free energies, i.e. $\Delta_R E = \Delta_R G$ and use

$$K = e^{\frac{-\Delta_R G}{kT}} \tag{5.15}$$

to obtain the equilibrium constant K for the exchange reaction. It can be rewritten by introducing K_x and K_1 as follows:

$$K = (K_x)^{\chi_{\mathrm{A}}^{\mathrm{ads}}} K_1, \qquad K_x = e^{\frac{E_{\mathrm{AA}} - 2E_{\mathrm{AB}} + E_{\mathrm{BB}}}{kT}}, \quad K_1 = e^{\frac{E_{\mathrm{AB}} - E_{\mathrm{BB}} + \Delta_R E_0}{kT}} \tag{5.16}$$

$$(K_x)^{\chi_{\mathrm{A}}^{\mathrm{ads}}} K_1 = \frac{\chi_{\mathrm{A}}^{\mathrm{sol}} (1 - \chi_{\mathrm{A}}^{\mathrm{ads}})}{\chi_{\mathrm{A}}^{\mathrm{ads}} (1 - \chi_{\mathrm{A}}^{\mathrm{sol}})} \tag{5.17}$$

$$\Leftrightarrow \chi_{\mathrm{A}}^{\mathrm{ads}} \left(1 - \chi_{\mathrm{A}}^{\mathrm{sol}}\right) (K_x)^{\chi_{\mathrm{A}}^{\mathrm{ads}}} K_1 = \chi_{\mathrm{A}}^{\mathrm{sol}} (1 - \chi_{\mathrm{A}}^{\mathrm{ads}}) \tag{5.18}$$

This equation has no analytical solution for the dependent variable $\chi_{\mathrm{A}}^{\mathrm{ads}}$, and thus was fitted as an implicit function:

$$\chi_{\mathrm{A}}^{\mathrm{ads}} \left(\chi_{\mathrm{A}}^{\mathrm{sol}}\right) \tag{5.19}$$

to the data in Fig. 5.29 (solid line). The agreement with the data is good. The parameters obtained by the fit are $K_1 = 1.42$ and $K_x = 0.0765$. In principle Eq. 5.16 should allow to obtain information on the interaction energies E_{AA}, E_{BB}, E_{AB} or ratios of them. However, additional assumptions are required to solve the equations.

Similar adsorption behaviour as observed for the mixed SAMs discussed in this work has been described in literature [45, 61, 124] and deviations from the model assuming same interactions have been discussed [59]. A model similar to Eq. 5.19 has been developed in [125] and refined and fitted to experimental data in [126]. In the future the role of the entropy [127] and its influence on the derivation of Eq. 5.19 should be discussed.

5.5.3 NEXAFS (Molecular Orientation)

Figure 5.30 shows C1s and N1s NEXAFS spectra of pure H-Az11, C12 SAMs and mixed SAMs with different surface coverages Θ of H-Az11. The surface coverages Θ were estimated from the molar fraction $\chi_{\mathrm{H\text{-}Az11}}^{\mathrm{sol}}$ in the adsorption solution using Fig. 5.29.

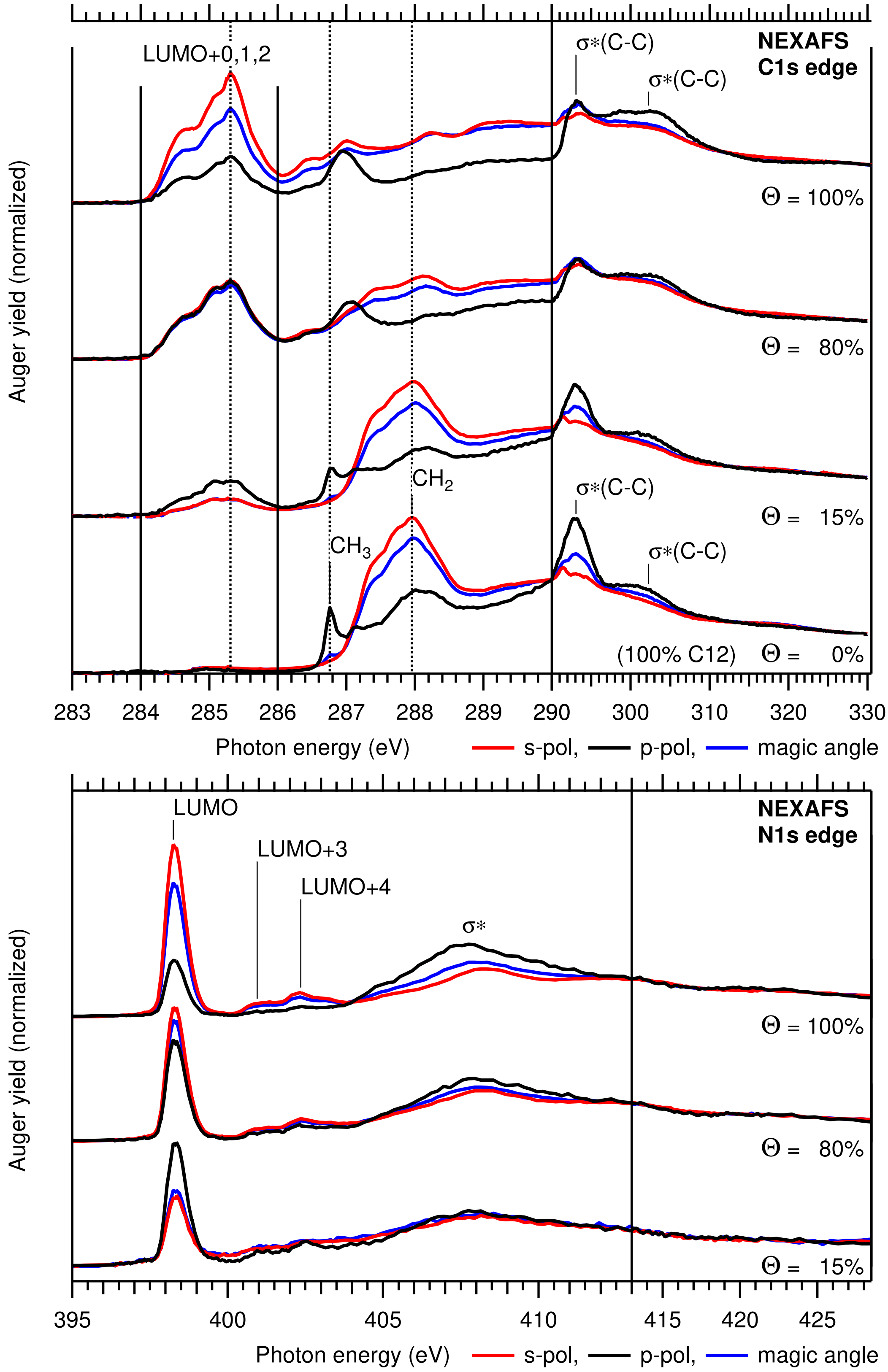

Figure 5.30: C1s and N1s NEXAFS of SAMs of mixed H-Az11/C12 SAMs with different surface coverages Θ of H-Az11.

$\chi^{\mathrm{sol}}_{\mathrm{H\text{-}Az11}}$	Θ	α / deg C1s	α / deg N1s
100%	100%	71±5	73±5
46%	80%	55±5	59±5
15%	15%	42±5	45±5

Table 5.12: Avarage orientations α (cf. Fig. 5.8) of chromophores in diluted SAMs with various chromophore coverages Θ: Note that the values given are *average* orientations only and do not describe the orientation of individual molecules. The values given are for the samples shown. Sample to sample variations were below 1° for the pure H-Az11 SAM. For the mixed SAMs sample to sample variation were higher (below 3°) as expected as the orientation depends strongly on the surface concentration. The stated error of 5° includes systematic contributions.

Pure Components The C1s spectrum of C12 has already been discussed in Sec. 5.2.2. The main features are the sharp $\sigma^\star$ (CH_3) resonance at 286.7 eV only visible in the p-polarized spectrum and the broader structure around 288 eV, which is most pronounced in the s-polarized spectrum and originates from the chain.

NEXAFS spectra of H-Az11 are very similar to those of H-Az6 also discussed in 5.2.2. The C1s spectrum shows the lowest energy absorption structure in the range from 284 to 286 eV with the threefold substructure assigned to the C1s to LUMO+0,1,2 transitions. As the spectra of C12 show no absorption in this region below 286 eV, this transition can be used to infer the orientation of the chromophore also in the mixed SAM. The spacer does not contain any nitrogen, hence the N1s spectra of the mixed layers only reflect the structure of the chromophore.

Mixed SAMs If we compare the N1s spectra for SAMs with decreasing chromophore coverage, we see that the polarization contrast at the N1s to LUMO resonance decreases and is inverted at even lower coverages. This suggests that the chromophores are oriented predominantly upright in the pure H-Az11 while their average orientation becomes more and more tilted as the chromophore concentration in the SAM decreases.

Looking at the C1s spectra the same behaviour is observed for the C1s to LUMO+0,1,2 transitions as expected. In the spectra for Θ=15% we see the spectrum of the spacer superimposed on the spectrum of the tilted chromophore. In the spectra for Θ=80% the $\sigma^\star$(CH_3) resonance is not visible any more and the features of the spacer chain between 286.5 and 288.5 eV are dampened. This strong dampening can be explained by the high density of more upright oriented chromophores sticking out of the linkers. At this coverage a more correct picture would be a SAM of the chromophore intermixed with few spacers.

From the N1s to LUMO and C1s to LUMO+0,1,2 transitions the average tilt angles α of the aromatic plane were calculated in the same way as for H-Az6 in Sec. 5.2.2 and are given in Tab. 5.12. NEXAFS spectroscopy averages over a macroscopic area of the sample. Thus, a *mean* tilt angle α is obtained without information on how much the individual chromophore in the mixed SAM deviates from this average. The values for pure H-Az11 are in good agreement with those obtained for H-Az6 implying a similar structure.

This observed bending down of the chromophores with increasing dilution would not occur in the case of the formation of densely packed domains. This and the

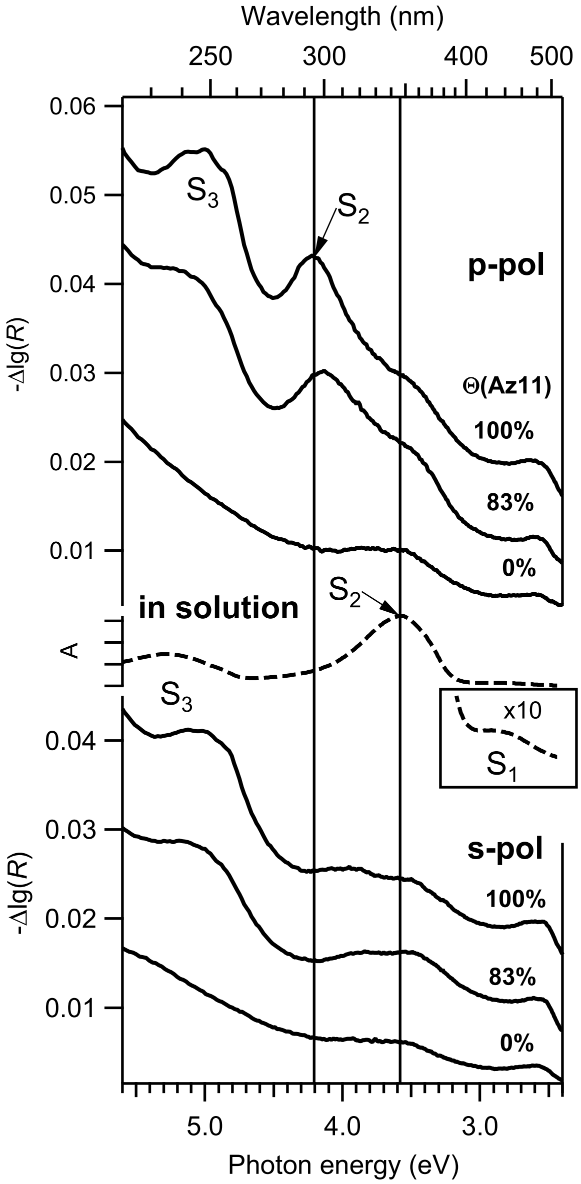

Figure 5.31: DR spectra of H-Az11 for different coverages Θ: Measured at an angle of incidence of 45° using p-polarized *(top)* and s-polarized *(bottom)* light. An absorbance spectrum of *trans*-H-Az11 in methanol *(middle)* is shown for comparison. The inset shows the upscaled S_1 absorption band in solution.

fact, that unlike for the CF_3-Az6/CN-Az6 mixed SAMs the NEXAFS spectra of H-Az11/C12 can not be expressed as linear combinations of the spectra of the pure SAMs corroborates the largely statistical mixing.

As H-Az11 like H-Az6 lacks an additional substituent that would allow to obtain an additional angle from the NEXAFS measurements the orientation of the mixed layers can not be determined in more detail.

5.5.4 Optical Properties

Figure 5.31 shows DR spectra of mixed and single component SAMS measured with p- and s-polarized light.[16] As discussed already in Sec. 5.2.4 the general shape of the spectra is caused by the SAM acting as a dielectric layer and is thus best observed for the pure C12 (0% H-Az11) SAM, which contains no chromophores. The spectra of the 100% H-Az11 SAM are very similar to that of H-Az6 discussed in Sec. 5.2.4: As in solution the main absorption bands are the S_2 and S_3 transitions while the S_1

---

[16] DRS measurements were performed in close collaboration with T. Moldt.

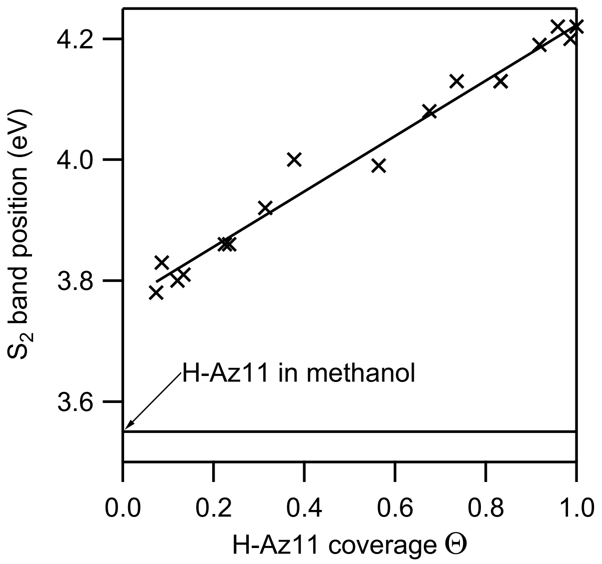

Figure 5.32: S_2 band position in mixed SAMs as a function of chromophore coverage Θ: The data points are maxima directly read from the p-pol spectra in Fig. 5.31. The solid line is a linear fit to the data. The band position in methanol (3.55 eV) is shown for comparison.

transition is weak and can hardly be separated from the drop in the spectrum due to the effect of the dielectric layer at 2.6 eV. The shifts in the band positions compared to solution indicate the formation of aggregates and are described by the excitonic coupling of the transition dipole moments (TDMs). Due to their different orientation the S_2 TDMs in the SAM form H-aggregates leading to a hypsochromic (blue) shift of 0.64 ± 0.1 eV, while the S_3 TDMs form J-aggregates, and thus lead to a bathochromic (red) shift. The excitation of a band is strongest when the electric field vector of the light is parallel to the TDM. Thus, the S_3 band with its TDM approximately parallel to the N=N bond has a similar intensity in the spectra measured using s- and p-polarized light, whereas the S_2 band is much more pronounced in the p-polarized spectra.

For the mixed SAMs the p-polarized DRS signal of the S_2 band increases with increasing coverage and the shifts of the S_2 and S_3 bands also increase. Figure 5.32 shows a plot of the observed S_2 band positions as a function of the chromophore coverage Θ on the surface. For $\Theta \rightarrow 0$ one might expect an S_2 band position similar to that of free H-Az11 in solution. However, a linear fit yields an offset of 0.21 ± 0.02 eV. This value is one order of magnitude larger than typical solvatochromic effects (cf. Chap. 2). We conclude that the chromophores in the SAM form small aggregates even for very low chromophore densities.[17] This view is corroborated by the fact that models of azobenzene dimers and oligomers [128] predict an excitonic shift of this order of magnitude.

We note that in addition to the blue-shifted part of the S_2 band the p-polarized spectra also show a signal in the energy range of the S_2 band of the H-Az11 monomer in solution.

5.5.5 Photoisomerization

The photoisomerization of azobenzenes in solution has already been discussed in Chap. 2 and is shown again in Fig. 5.33 (bottom): Upon UV illumination a photostationary state (PSS) predominantly consisting of the *cis* isomer is reached. Illu-

---

[17] The formation of larger aggregates would contradict the previously shown XPS and NEXAFS results and not explain the continuous shift of the band position.

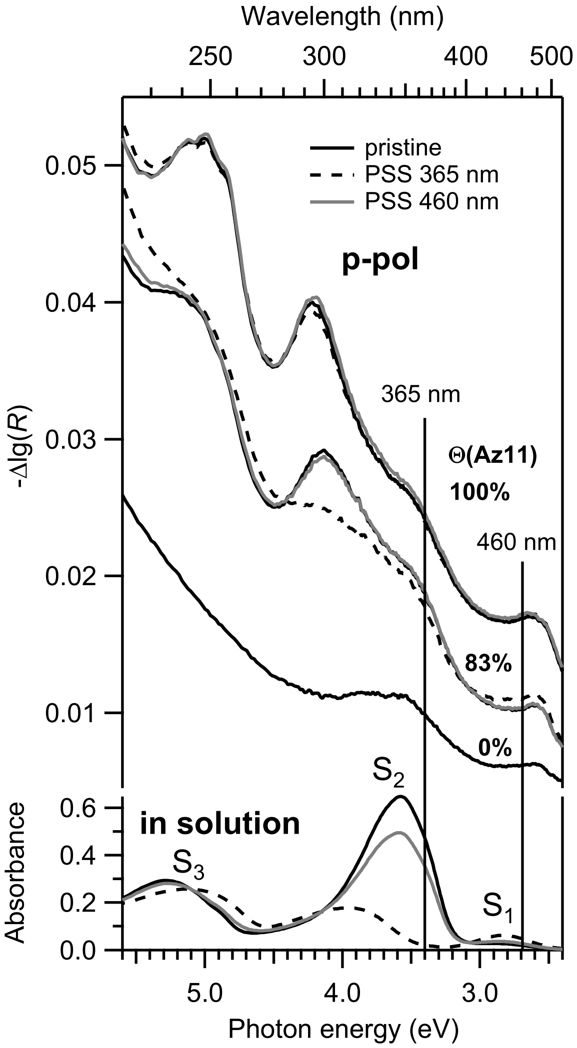

Figure 5.33: Photoisomerization of H-Az11 SAMs for different coverages Θ: DR spectra, measured at an angle of incidence of 45° using p-polarized light; pristine and photostationary states (PSS) after illumination with UV (365 nm) and blue (460 nm) are shown. Absorbance spectra of H-Az11 in methanol *(bottom)* are shown for comparison. The illumination wavelengths are indicated by vertical lines.

mination with blue light leads to another PSS, which is distinct from the initial pure *trans* state and still contains a fraction of the *cis* isomer.

For the 100% H-Az11 SAM illumination with UV light only leads to minor changes in the spectrum, as expected from the results of the other single component azobenzene alkanethiolate SAMs. The lower-coverage SAMs, however, exhibit pronounced photoisomerization as becomes apparent from the change in the DR signal of the S_2 band. For decreasing coverage, i.e. increasing dilution of H-Az11 a larger fraction of the chromophores is isomerized. Illumination with blue light leads to a spectrum indistinguishable from the pristine spectrum within the reproducibility of the measurement. This behaviour is in contrast to that of the solution where illumination with blue light leads to a PSS that contains significant amounts of the *cis* isomer. SAMs in the UV PSS were stable for several hours in the dark. Thus, we can neglect thermal relaxation during the time of the experiment. Several switching cycles were performed; no appreciable fatigue was observed (Fig. 5.34).

The photon doses used in the isomerization experiments (Tab. 5.13) were sufficient to reach the PSSs, and are equivalent to seconds to minutes with the LED lamps. For the mixed SAMs doses of about 10 times that required in solution were necessary.[18]

---

[18] The time to reach the PSS is ill defined. Half-lives would be a better measure, however, the focus

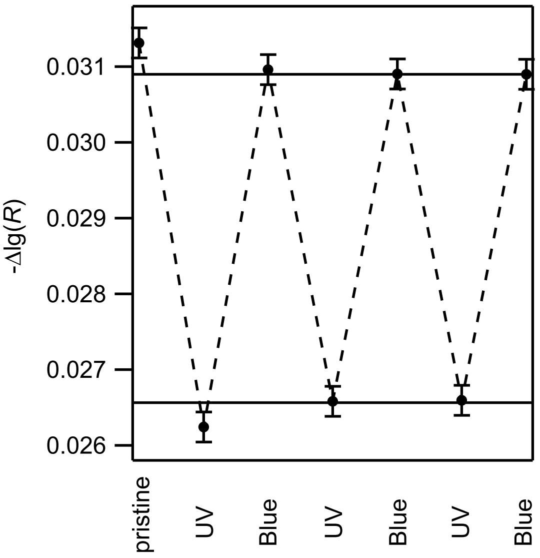

Figure 5.34: Reversibility of photoisomerisation: sample: Θ(H-Az11) = 83%. Data points were extracted from the p-polarized DR spectra at the S_2 band maximum (4.13 eV, 300 nm), recorded for the pristine SAM and the photostationary states. Horizontal lines are a guide to the eye.

Table 5.13: Photon doses applied in the photoisomerization experiment: Photon doses in photons $\cdot$ cm^{-2}. The illumination was conducted in normal incidence. The doses applied correspond to minutes of illumination with the LED sources used. In solution and for the mixed SAMs of all coverages investigated a photostationary state was reached, whereas higher doses only resulted in minor changes of the undiluted 100% H-Az11 SAM.

	UV (365 nm)	blue (460 nm)
H-Az11 / methanol	3×10^{17} (PSS)	9×10^{17} (PSS)
100% H-Az11 SAM	1×10^{19} (minor effects)	1×10^{19}
H-Az11 / C12 SAMs	6×10^{18} (PSS)	8×10^{18} (PSS)

Proposed Mechanism The center wavelength of the UV light source used is 365 nm close to the S_2 absorption maximum in solution. However, we observed that the main changes in the spectra upon illumination at this wavelength occur in the S_2 aggregate band around 295 nm. This difference is large compared with the full width at half maximum of 9 nm of the LED source.

A response of the aggregate band when exciting the monomer suggests a stepwise isomerization process of aggregate stacks within the mixed SAM: Chromophores at the edge of an aggregate should absorb at wavelength closer to that of the monomer. Isomerization of such an edge chromophore opens space allowing a neighbour to isomerize and alters its neighbours absorption and thereby making it susceptible to the UV light. This describes a scenario, where chromophores in the aggregates of which the SAM is composed switch one after another in a domino-like fashion.

A blue PSS almost identical to the pristine *trans* state fits well in this picture: We can neglect thermal relaxation from the *cis* into the *trans* state during the experiment, because spectra of mixed SAMs in the UV PSS were stable for several hours after the exposition. Thermal effects neglected, the composition of the blue PSS depends on the absorption cross section σ and photoisomerization quantum yield Φ (cf. Sec. 2). The preferential adsorption of H-Az11 and the zero-density offset of the S_2 band position with respect to that in solution indicate that there is an additional

---

of the experiment was to investigate PSSs. Kinetic studies are currently under way.

energetic gain for *trans* molecules in aggregate stacks. This gain will increase the energy difference between *cis* and *trans* state further while the *cis* to *trans* isomerization progresses. Thus, the potential landscape will change in a way that increases the likelihood to decay into the *trans* state with increasing *trans* content in the stack. Hence, the mechanism proposed above describes a cooperative process.

Photoisomerization in NEXAFS It has been attempted to measure NEXAFS spectra on isomerized layers. Even though reversible photoisomerization could be demonstrated using DRS before and after the NEXAFS measurements, NEXAFS spectra of layers irradiated with UV light in the same conditions as for the DRS experiments or in the vacuum chamber were indistinguishable from spectra of pristine (*trans*) layers. This lead to the assumption that the vacuum might somehow influence the isomerization. And indeed it could be demonstrated using DRS that a SAM in the UV PSS switches back to the *trans* state upon exposure to vacuum for $<$90 min, while the UV PSS is stable for hours in ambient conditions.

Later NEXAFS spectra of the UV PSS were successfully recorded by illuminating the SAM during the measurement and the differences in the thermal relaxation constant between ambient and vacuum were attributed to a water layer stabilizing the *cis* form in air [37].

In the light of these results, earlier experiments conducted in the cause of this work attempting to detect switching of single component SAMs by NEXAFS have limited significance, because the illumination was always conducted before the measurement.

5.6 Conclusion

In this chapter we have presented results on four different kinds of azobenzene-based SAMs on gold: single component azobenzene alkanethiolate SAMs (R-Az6); a single component azobenzene SAM with aromatic linker (CN-AzPh) and an imine with aromatic linker (CF_3-ImPh); mixed SAMs consisting of two azobenzene alkanethiolates, which only differ by a substituent in the chromophore; and mixed SAMs where the chromophores of an azobenzene alkanethiolate are laterally diluted by an alkanethiolate spacer (H-Az11/C12). In the following we will summarize our results with respect to the molecular structure on the surface, the coadsorption process that leads to the mixed SAMs, the optical properties, and the photoisomerization behaviour:

Molecular Structure The azobenzene chromophore is planar in the *trans* form. Using NEXAFS spectroscopy we obtained two parameters describing the orientation of the chromophore plane with respect to the surface: α, the angle between the surface normal and the normal of the chromophore and ϑ, the angle between the bond axis to the CF_3 or CN substituent in CF_3-Az6 and CN-Az6. We found that the chromophores are oriented predominantly upright. There are two possible orientations of the diazo (N=N) bridge in the chromophore plane. Of these, the structure with the diazo bridge more parallel to the surface appears more likely, as DR spectroscopy results suggest. Within error, the molecular orientations of all 4 single component azobenzene alkanethiolates were found to be similar. The lateral structure of azobenzene alkanethiolate SAMs is known form AFM/STM measurements. Combining this data with our results on the molecular orientation we constructed a structural model for the R-Az6 SAMs.

For the SAMs with aromatic linkers (CN-AzPh and CF_3-ImPh), we found that the chromophores have a less upright orientation than in the azobenzene alkanetiolate SAMs.

Because single component CF_3-Az6 and CN-Az6 SAMs showed the same orientation, they were an ideal prototype system for a coadsorption experiment. The molecular orientations in the mixed SAMs were found to agree with those of the corresponding single component SAMs, and the NEXAFS spectra of the mixed SAMs are a linear combination of the spectra of the single component SAMs. In contrast, the XP spectra of the mixed SAMs can not be described as a linear combination of the single component SAMs. Rather, the peaks shift continuously with the composition as the peak positions depend on the effect of the local potential created by the neighbouring molecules. These observations show that we achieved a real mixture on short range, i.e. we do not observe large domains of the single components as this would not lead to continuous peak shifts but a linear combination. The composition in the SAM can be tuned arbitrarily as it changes continuously with the composition in solution.

For the diluted chromophore SAM (H-Az11/C12) we observed an increasing tilt of the azobenzene chromophore with increasing dilution of the chromophores on the surface. This bending down of the chromophores is compatible with a model where the chromophores stick out of a densely packed alkanethiolate SAM. For these SAMs XPS measurements show that the chromophore density can be tuned from 0% to 100% via the composition of the adsorption solution, and no phase separation occurs.

Thermodynamics of Coadsorption Using quantitative XPS we measured the composition of mixed SAMs formed by coadsorption as a function of the composition of the adsorption solution. Generally, the composition of a mixed SAM does not resemble that of the solution and depends on the energetics of the SAM formed. Assuming an equilibrium between SAM and the adsorption solution we developed a model describing the composition of mixed SAMs as a function of the composition of the adsorption solution based on the interactions between the different molecules in the SAM. The assumption of same interactions between like and unlike molecules leads to the simple model (Eq. 5.6), which describes the experimental data observed for the CF_3-Az6/CN-Az6 SAMs well. For the H-Az11/C12 SAMs, the model was extended to allow for different interactions between the two pairs of like molecules and between unlike molecules (Eq. 5.19). In both cases simple preferential adsorption of one component was observed.

Optical Properties Using DR spectroscopy with polarized light we investigated the optical properties of the azobenzene alkanethiolate SAMs (R-Az6 and H-Az11). We observed pronounced excitonic coupling in these densely packed SAMs: The S_2 band is blue-shifted by $\approx 0.6\,\mathrm{eV}$, compared to the transition of the free molecule in solution, and is only visible in the spectra obtained using p-polarized light. For the S_3 band a less pronounced redshift is observed, and the band is only slightly more pronounced in the spectrum recorded using p-polarized light compared to the spectrum recorded using s-polarized light.

DFT calculations provided the orientations of the TDMs within the chromophores. Combining this information with the structural model described above allows us to understand the observations qualitatively:

The blueshift of the S_2 band indicates that the S_2 TDMs form an H-aggregate, i.e. the TDMs are oriented parallel. The excitation of a band is strongest, if the electrical field vector of the light is parallel to the TDM. Because, the S_2 TDMs are oriented along the long axis of the chromophore, the fact that the S_2 band is only visible in the spectra obtained using p-polarized light, corroborates the upright orientation of the chromophore.

The redshift of the S_3 band indicates the formation of a J-aggregate, i.e. the S_3 TDMs are head-tail aligned. The S_3 TDMs are oriented roughly parallel to the N=N bond. Within our structural model of the SAM, the head tail alignment is better for the structure with the N=N bond more parallel to the surface. The fact that the S_3 band is visible in spectra recorded using light of either polarization, indicates that the TDM has still a significant component perpendicular to the surface.

The SAMs show the same substituent effects than the respective compounds in solution: The S_2 band of H-Az6 is located at the shortest wavelength followed by CF_3-Az6 and CN-Az6. The CF_3-Az6/CN-Az6 mixed SAMs allowed to study the excitonic coupling of two different chromophores as a function of their relative fractions on the surface, while the same geometrical structure is maintained independent of the composition at the surface. With decreasing fraction of one component, we observed a continuous shift of the S_2 band position from that of the one component to that of the other. This shift is linear with the composition of the SAM. Thus, both components contribute equally to the aggregate. The continuous shift is a further indication for real mixing of the two components on a molecular level rather than the formation of larger domains.

For the diluted chromophore SAM (H-Az11/C12), we observed a decrease in intensity of the S_2 band with decreasing H-Az11 coverage Θ. With decreasing coverage, the position of the S_2 aggregate band shifts linearly towards longer wavelength. For $\Theta \to 0$ one might expect no aggregate formation and thus an S_2 band position close to that of the free molecule in solution. However, we observed an offset and conclude that the chromophore in the SAM must form dimers or small aggregates even for low coverages.

Photoisomerization Behaviour and Mechanism We irradiated all single component azobenzene alkanethiolate SAMs (R-Az6 and H-Az11) and the mixed chromophore SAMs (CF_3-Az6/CN-Az6 SAMs) with UV (365 nm) and blue (460 nm) light, and did not observe any significant changes in the DR spectra. The photon doses employed were well above those required to reach the photostationary states of the *cis–trans* isomerization in solution. Photoisomerization was also not observed for (CF_3-Az6) in crystalline films or aggregates in solution. We conclude that in densely packed chromophore phases the photoisomerization is suppressed. One might assume that excitonic coupling is the cause for the suppressed photoisomerization. Another possible cause is steric hindrance. Based on our experiments we can not discern between the two possible causes, because the dense packing in the layers suggesting steric hindrance is also a prerequisite for the excitonic coupling. As detailed in the text, steric hindrance appears to be the more likely cause.

The dilution of the chromophores in the H-Az11/C12 mixed SAM should reduce both possible causes. And indeed, we observed photoisomerization already for minor dilutions of the chromophore at photon doses only one order magnitude above those required in solution. We could show that the isomerized layers are stable for several hours in the dark and could perform several isomerization cycles without any appreciable fatigue. This is one of the few cases for which effective photoisomerization of azobenzene chromophores in SAMs was demonstrated.

Although we illuminated with a UV wavelength close to the S_2 absorption maximum in solution, we observed that the main changes in the spectra occur in the S_2 aggregate band. This suggests a stepwise isomerization process of aggregate stacks within the mixed SAM: Isomerization of a chromophore at the edge of an aggregate stack opens space allowing a neighbour to isomerize and alters its neighbours absorption making it susceptible to the UV light. Thus, the chromophores in the aggregates switch one after another in a domino-like fashion.

Unlike in solution, the PSS under blue illumination is nearly indistinguishable from the pristine SAM. The preferential adsorption of H-Az11 and the observation of small aggregates for low coverages indicate that there is an energetic gain for *trans*-molecules neighbouring other *trans*-molecules. This gain will increase the energy difference between *cis* and *trans* state while the *cis* to *trans* isomerization progresses. Hence, the mechanism describes a cooperative process.

Chapter 6

TBI/Au(111)

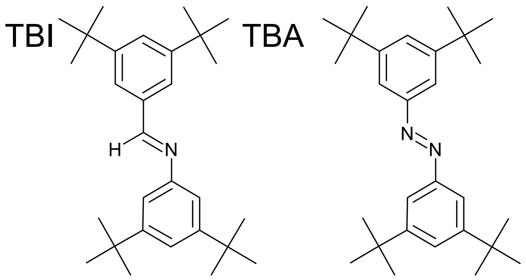

Figure 6.1: Structural formulas of TBI ((*E*)-3,5-di-*tert*-butyl-N-(3,5-di-l*tert*-butyl-benzylidene)aniline) and TBA (*E*-3,3',5,5'-tetra-*tert*-butyl-azobenzene).

6.1 Introduction

As discussed in the previous chapter, decoupling the frontier orbitals of azobenzene based molecular switches from the metal substrate is essential to maintain the photoisomerizability at the surface. So far we have discussed SAMs where the azobenzene moiety is decoupled from the surface by the thiolate linker. In these SAMs the chromophores are standing nearly upright. This upright orientation in densely packed SAMs, however, inhibits the photoisomerization in single component SAMs through sterical hindering or coupling of chromophores. Isomerization could only be induced in two-componental mixed SAMs where the lateral distance between the chromophores was increased by spacer molecules.

Another method to decouple the chromophore from the gold substrate is to attach bulky end groups to the chromophore. In TBA (structure Fig. 6.1)—also investigated in the cause of this work [27, 28], however, not part of this thesis—*tert*-butyl groups are attached in *meta* position. These molecules are deposited on the surface by physical vapour deposition and orient themselves flatly on the surface. This orientation has the advantage that there is no additional space requirement during the isomerization and coupling between chromophores is weak. Even though the decoupling from the surface is not as good as for the SAMs, TBA could be isomerized successfully at the surface and a photostationary state with up to 70% *cis* isomer was achieved. However, the process is much less efficient than for the SAMs, and a different, substrate mediated mechanism [129] is assumed.

TBI (structure Fig. 6.1) is the imine analogue of TBA. Compared to azobenzenes with *cis*–*trans* thermal activation barriers of $\approx 1\,\mathrm{eV}$ [39] in solution the activation barriers for N-benzylideneaniline and derivatives including TBI itself are only $\approx 0.6\,\mathrm{eV}$ [130–132]. Furthermore, the predicted energy difference between *cis* and *trans* isomer are in the case of TBI [132, 133] ≈ 0.25 eV for the free molecule and 0.4 eV for the adsorbed molecule on Au(111), whereas for TBA [133, 134] 0.3–0.6 eV (free molecule) and 0.5–1.0 eV (Au(111)) are predicted. The reduced activation energy allows for a rapid interconversion of the two TBI isomers at room temperature, while the reduced energetic difference between the isomers allows to shift the equilibrium from one isomer to the other by small changes in the environment of the molecule. In the following we will demonstrate that a change in coverage is sufficient to drive the equilibrium from *trans* to *cis* and back to *trans*, provided that enough thermal energy is available to overcome the activation barrier.

At low temperatures (210 K) multilayers adsorb in the *trans* configuration, the ground state of the free molecule. At elevated temperature (313 K) sufficient activation energy is available and the molecules can thus toggle between the two conformations. The equilibrium state observed at this temperature is a *cis* layer, whereas at higher temperatures (333 K) a *trans* layer is observed. Both layers are densely packed. The space occupied by a *trans* molecule, however, is about 1.5 times larger than that required by a *cis* molecule. Since the *cis* layer has a significantly higher density than the *trans* layer, the favoured molecular conformation is not only determined by the energy of the individual adsorbed molecule, but is determined by the adsorption energy of the whole layer. Apparently, the gain in total adsorption energy in the *cis* layer due to the higher coverage outweighs the lower adsorption energy of this less favourable conformation for the individual molecule. However, for the adsorption–desorption equilibrium that determines the coverage, i.e. how many molecules stay on the sample, the relevant quantity is the adsorption energy of the individual molecule. It is higher for the *trans* form, and thus at higher temperatures this form is found on the surface.

The data presented in the following has already been shown in [133] and was re-evaluated[1] for the present work.

6.2 TDS and Sample Preparation

Layers of TBI were prepared by vapour deposition onto a freshly prepared (111) surface of a gold single crystal that could be held at various temperatures as described in Sec. 7.3. At a sample temperature of 210 K approximately 2 monolayers (ML) of TBI were deposited onto the substrate. Figure 6.2 shows the TD spectrum of such a multilayer (**M**). The peak in the range 280–330 K shows zero-order desorption typical for multilayers. Here the molecules of the second and higher[2] layers desorb. The following broad structure is assigned to the first monolayer where the molecules are in direct contact with the metal substrate and are more strongly bound.

---

[1] The present analysis deviates in the following aspects from that given in [133]: In [133] a background had been silently subtracted from the NEXAFS data. Thus, the angles obtained in Tab. 6.2 differ from those in the earlier publication. Qualitatively, however, the orientation obtained is not at variance with [133]. In the earlier publication the TDS spectra shown in Fig. 6.3 of this work were normalized at about 500 K. The difference—though only visible for layer **T**—also leads to a difference in the coverage $\Theta_\mathbf{B}$ within the error of the method. This deviation in $\Theta_\mathbf{B}$ propagates into the relative surface coverages $^{\rho_{cis}}/_{\rho_{trans}}$ (Eq. 6.4), because Eq. 6.3 is sensitive to small changes in this parameter.

[2] The second layer does not necessarily form a closed layer but growth of the third layer may start before the second layer is complete.

[3] The TDS spectra chosen are for the samples for which NEXAFS and XPS data will be presented in the following. For layer **T** the TDS spectrum was recorded with a different sensitivity. Therefore, the spectrum shown for layer **T** is that of a different sample, for which a sample of type **C** was prepared in sequence. The intensity ratio of the latter two spectra at 500 K was used to scale

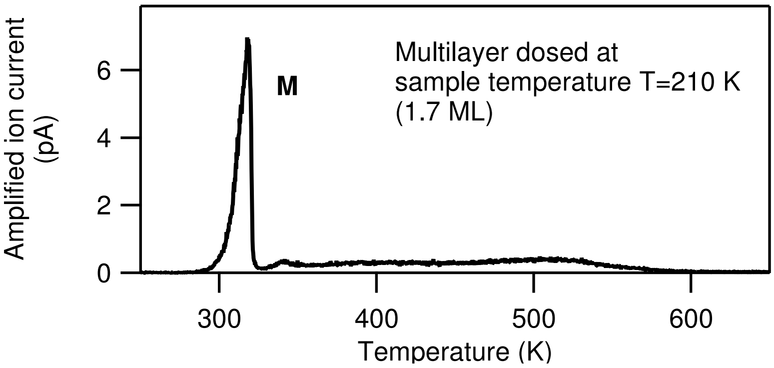

Figure 6.2: TDS of TBI on Au (111): Multilayer **M** adsorbed at substrate temperature of 210 K, m/e=57.

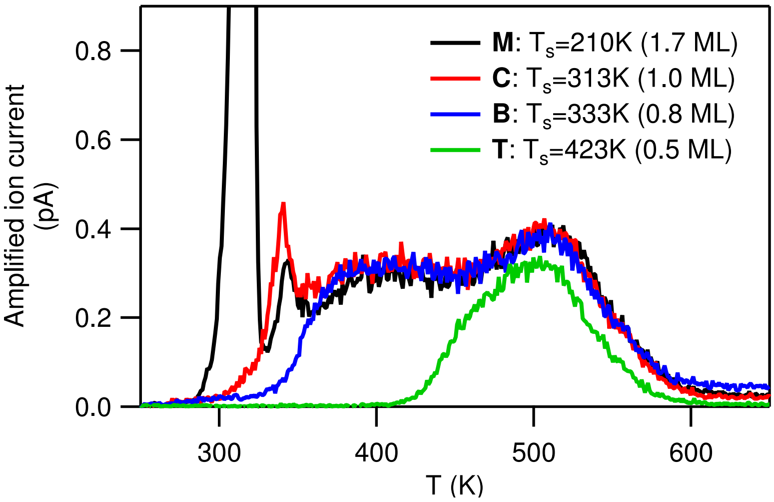

Figure 6.3: TDS of TBI on Au(111): m/e=57, Offsets were corrected to 0 at the beginning of the spectra. The spectra are otherwise unscaled.[3]

The TD spectrum of the multilayer **M** is shown again on an enlarged scale in Fig. 6.3. The very broad temperature interval of 320–600 K during which the monolayer desorbs and the threefold substructure indicate that the monolayer runs through several structures during the desorption process. The sharp peak at the onset of the monolayer desorption, here at 320 K, is frequently observed for aromatic adsorbate layers and generally attributed to a compressed structure [135]. Typically in the compressed structure molecules are shifted to less favourable adsorption sites so that more molecules can be placed in direct contact with the surface [136]. For the present case of TBI the molecule even changes its configuration in the compressed layer as we will show in the following section.

In order to investigate the monolayer and the other structures that are formed during the TDS of the multilayer they had to be prepared individually. This was done at first by *partial desorption*, i.e. a TD spectrum of a multilayer was recorded up to a temperature before the onset of desorption of the respective species, where the heating ramp was aborted and the sample was cooled again. Alternatively TBI was dosed onto the substrate held at constant temperature until *saturation coverage* was reached. The latter method leads to the same overall structures, as proved by

---

the spectrum of **T** relative to the spectrum of **C** on the graph. The two spectra of samples of type **T** were indistinguishable apart from the scaling.

NEXAFS. Because the layers prepared by saturation coverage were found to show more reproducible and more pronounced structures, this method was used for the layers discussed in the following.

In addition to the spectrum of the mutilayer, Fig. 6.3 shows TD spectra of various (sub-) monolayers prepared by the saturation coverage method. The coverage for the different structures given in the figure were obtained by comparing TDS peak integrals. The values are relative to the full monolayer **C** (with compression peak) for which a coverage $\Theta = 1.0$ monolayer (ML) was defined. Layer **B** approximates a full layer without the compression peak. Layer **T** has a low coverage high temperature structure. When a similar amount of TBI as in layer **T** was adsorbed at the temperature at which the multilayer is prepared, a less ordered structure, which also shows some signal in the multilayer desorption range, was obtained (not shown).

6.3 Molecular Orientation and NEXAFS

6.3.1 Theory

In order to extract molecular orientations from the NEXAFS data DFT calculations were performed in the group of Karsten Reuter to obtain possible adsorption geometries and frontier orbitals of the contemplable structures [133]. Here we briefly summarize the results necessary for the discussion of the NEXAFS data:

A search for ground and metastable states of TBI in the gas phase was performed: For the ground state a *trans* configuration with one phenyl moiety twisted by 40° about the axis of the other was found. This configuration is chiral and consists of 2 energetically degenerate isomers and will henceforth be denoted as *twisted-trans*. The *cis* configuration is metastable. However, ground state-conformations of related azobenzene derivatives, adsorbed on metal surfaces, have been found to differ from solution [137], and STM results on TBI [138] in a submonolayer regime indicate a planar structure similar to that observed for TBA [27, 28]. Thus, in addition to the 2 gas-phase structures a *planar-trans* configuration was considered for the search of the preferred adsorption sites, suspecting that such a configuration could be stabilized at the surface by the enhanced van der Waals interaction with both phenyl moieties. The resulting optimised adsorbed geometries are shown in Fig. 6.4.

For these geometries the LUMOs required for the analysis of the NEXAFS spectra were calculated and are shown in Fig. 6.5 for the *planar-trans* and the *cis* configuration.

6.3.2 NEXAFS

Figure 6.6 shows NEXAFS spectra of the layers for which TD spectra were displayed in Fig. 6.3. Data were processed as described in 4.2 and 7.8. We start our discussion with the spectra recorded at the nitrogen edge. Here the analysis is facilitated by the fact that the molecule contains only a single nitrogen atom. Therefore, transitions are only possible into states that have sufficient density at that core. From the plots of the molecular orbitals in Fig. 6.5 it is obvious that for both conformers only the LUMO and LUMO+3 have significant density at the N atom. Thus, the N1s transitions to these states are the main features in the spectra of all layers. The peak positions for these transitions are given in Tab. 6.1. For the *cis* configuration the LUMO is located at the phenyl ring at the C-side of the imine bridge, whereas the LUMO+3 is located at the phenyl ring located at the N-side of the imine bridge.

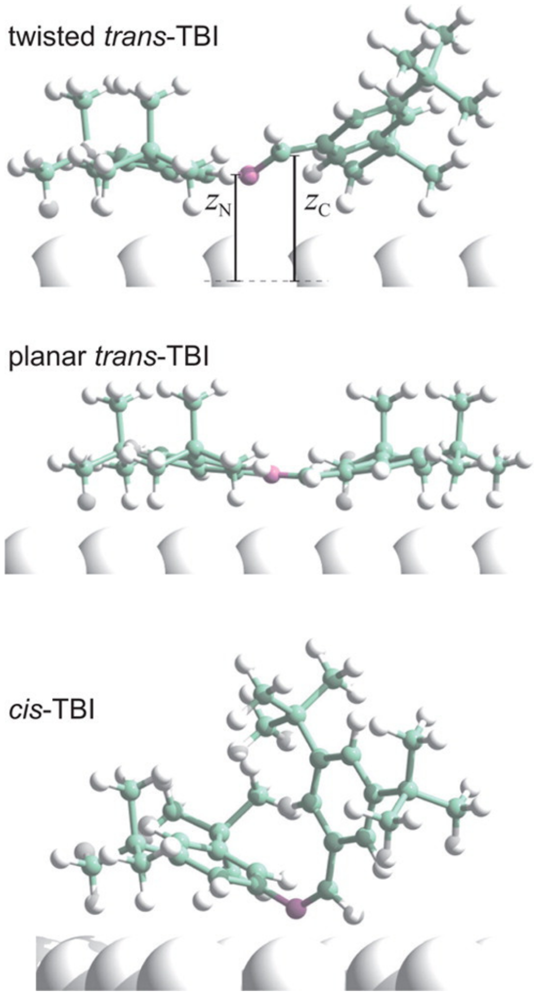

Figure 6.4: Calculated adsorption geometries of TBI on Au(111) in the twisted trans, planar trans, and cis configuration: In contrast to the gas phase, where the twisted *trans* form is favoured, adsorbed on Au(111) the planar *trans* form is observed. Figure from [133].

Thus, the orientation of the transition dipole moments to these orbitals allows us to obtain individual orientations for the two different rings in this configuration. For the *planar-trans* form, however, both orbitals extend over both rings even though they are not entirely symmetric.

In contrast to the N1s edge at the C1s edge transitions to all 4 LUMOs are possible and form one overlapping structure. Thus, we can obtain less information from the polarization dependence of these spectra. However, for the *planar-trans* configuration all TDMs should point in the same direction and the orientation should be the same as obtained from N1s spectra. In addition to the $\pi^\star$ transitions, the C1s spectra show $\sigma^\star$ resonances and other features not relevant for the analysis of the molecular structure, which we will not discuss further.

In the following we will discuss the spectra and structure of all layers qualitatively before we will give a detailed analysis of the molecular orientation of the pure layers **C** and **T** in Sec. 6.3.3.

Layer T The transitions to both the LUMO and LUMO+3 show up as strong absorption peaks only for p-polarized X-rays, whereas there is hardly any intensity in the spectrum recorded using s-polarized X-rays. This implies an orientation of the whole aromatic system of the adsorbed molecule almost parallel to the surface.

Of the three adsorption structures considered this observation is only compatible with the *planar-trans* configuration. Thus, we conclude: The low coverage, high

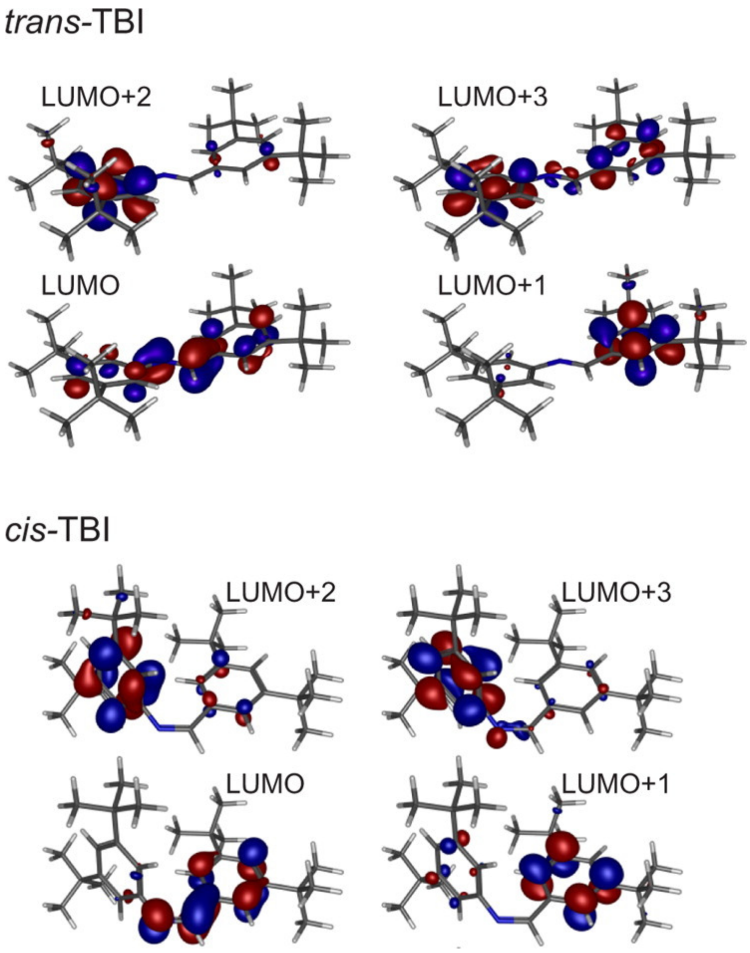

Figure 6.5: Contour plots of the LUMOs of TBI in the *planar-trans-* and in the *cis*-configuration. Only the LUMO and LUMO+3 have significant electron density at the nitrogen atom (marked by blue sticks). Figure from [133].

Table 6.1: N1s NEXAFS peakpositions: Positions of the $\pi^\star$ transitions. Values are maxima directly read from the spectra measured using p- and s-polarized light. For layer **C** the LUMO+3 transition shifts slightly when going from p- to s-polarized light. For layer **T** values are from p-polarized spectrum, because the peak has only little intensity in the s-polarized spectra. The apparent shift of the transition to the LUMO in the s-pol spectrum for this layer is most likely explained by the contribution of traces of *cis* molecules. For the flat topped LUMO+3 transition of layer **T** the middle of the flat top was visually estimated.

	LUMO / eV	LUMO+3 / eV
M	398.0	401.2
C	398.5	401.6 (p-pol), 401.4 (s-pol)
T	397.9	401.3

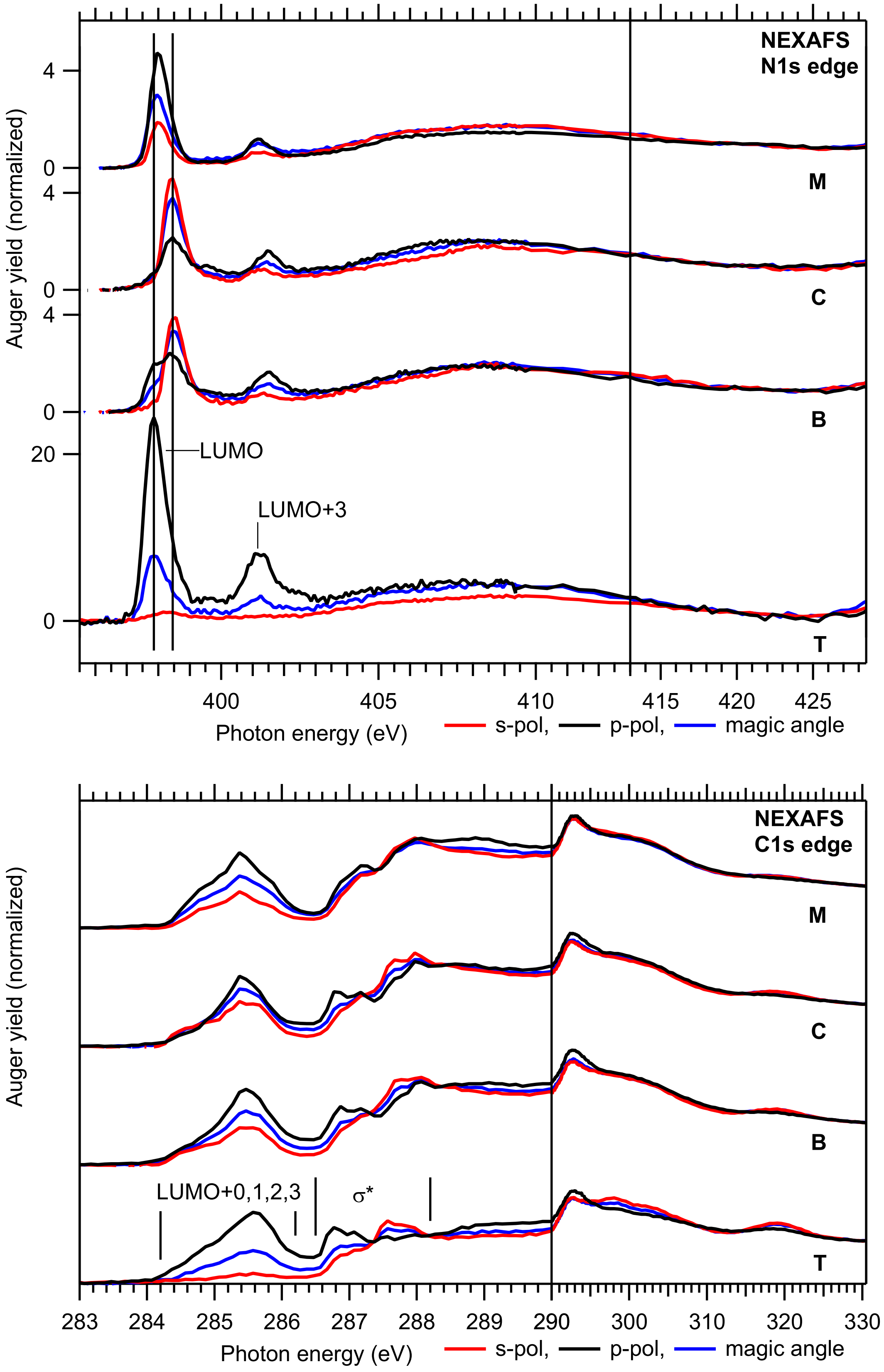

Figure 6.6: NEXAFS spectra of TBI on Au(111).

temperature layer **T** consists of TBI in this *planar-trans* configuration.

Layer C For this densely packed layer the N1s spectra lock distinctly different compared to layer **T**: Both the transitions to the LUMO and LUMO+3 are shifted towards higher photon energies; there is only little intensity at the position of the LUMO transition in layer T; and the transition to the LUMO shows an inverse polarization contrast, whereas the polarization contrast of the LUMO+3 transition has the same orientation as in layer T but is slightly weakened. Even though the transitions to the individual LUMOs in the C1s spectra overlap, the inverted polarization contrast of the LUMO transition is visible in the left peak of the LUMO structure.

From the energy shifts in the N1s spectra we conclude that both layers **C** and **T** consist of different TBI species. The different polarization contrast observed for the two transitions leads to the conclusion that molecules can not be planar any more, and thus both rings must have different orientations with respect to the surface. While the aniline moiety, i.e. the aromatic ring attached to the N of the imine bridge, is only slightly tilted with respect to the surface, the benzylidene moiety must be strongly tilted. (cf. angles in Tab. 6.2). Of the three adsorbed structures considered (cf. Fig. 6.4) only the *cis* configuration is compatible with these observations. The adsorption geometry with the aniline moiety predominantly parallel to the metal surface enables a strong interaction of the N atom with the substrate and may thus be favoured.

We conclude that layer **C** consists of the *cis* isomer.

Layer B The N1s spectra of the layer show contributions of both structures: **C** and **T**. Thus, we assume that the layer consists of a mixture of the two layers. As the spectra are normalized to the total coverage, the composition of the layer can be obtained by comparing the peak heights in the spectra of layer B and C. The LUMO transition in the s-pol spectra are most suitable for this approach, as they can be attributed solely to the *cis* species.[4] This results in a peak ratio and thus in a surface molar fraction of the *cis* species in this mixed layer **B** of $\chi_{cis} = 83 \pm 9\%$. This ratio can also be obtained from the XPS spectra discussed in 6.4. A comparison of the results will be given in 6.6.

Layer M The N1s NEXAFS spectrum is different from those of Layers **C** and **T**: The LUMO transition is observed at an intermediate energy and the spectra can not be described as a superposition of the spectra of **C** and **T**. The polarization dependence of the LUMO and LUMO+3 transitions are similar. The higher peak intensity in the s-pol spectra compared to layer **T** indicates that the aromatic rings are tilted slightly more out of a parallel orientation to the surface than in layer **T**.

The comparable tilt angles for both aromatic rings suggest that the majority of molecules adopt the *trans* configuration. From TDS we know that the second layer is more weakly bound than the first layer. Thus, we hypothesise that this multilayer dosed at low temperatures consists of a *planar-trans* monolayer, which is covered by an adlayer with the molecular axis parallel to the surface, but with molecules in the *twisted-trans* configuration similar to that of the free molecule.

---

[4] In Principle the spectra of layer **B** should be a linear combination of the spectra of **C** and **T**. This analysis has been attempted. However, due to the inaccuracies of the normalisation, especially severe for the particular low coverage of layer **T**, this approach leads to inconsistent results. The approach chosen, comparing the peak heights in the s-polarized spectra of **C** and **B**, does not require to use spectra of **T**.

Table 6.2: Molecular orientation: Theoretical values from [133]: Out-of-horizontal phenyl plane bend angles for the two phenyl rings of TBI: α_C for the benzylidene moiety, i.e. the phenyl ring attached to the C of the imine bridge, and α_N for the aniline moiety, i.e. the ring attached to the N of the imine bridge. Experimental values are orientations of TDMs obtained from the NEXAFS N1s transitions to the LUMO and LUMO+3 and C1s transitions averaged over the LUMO+0–3 structure. The angles were computed as described in Sec. 4.2.5 and Sec. 7.8.

layer	assumed adsorption geometry	theory α_C	theory α_N	N1s→ LUMO	N1s→ LUMO+3	C1s→ LUMO+0–3
	twisted-trans	32.5	10.3			
M	*trans + twisted-trans*			41±5	48±5	
C	*cis*	82.0	26.6	68±5	46±5	
T	*planar-trans*	11.5	10.8	<10	<10	25±5

Note that the angles obtained for layer M from the NEXAFS spectra can not be compared to the values obtained from the DFT calculations, because the theoretical values are for molecules in direct contact with the substrate, whereas for the experiment we expect a superposition of the signals from the first layer in *planar-trans* configuration and the *twisted-trans* molecules on top. In addition, the calculated *planar-trans* adsorption geometry is based on the interaction of the molecule with the gold substrate— the interaction of the second with the first layer will be different.

6.3.3 Molecular Orientation: Details

To obtain the orientations of the phenyl rings of TBI in the different layers the polarization dependence of the LUMO and LUMO+3 transitions in the N1s spectra and the LUMO+0–3 structure in the C1s spectra were analysed as described in Sec. 4.2.5. As the individual transitions of the C1s to LUMO+0–3 structure could not be separated, integrals of the whole structure were used leading to an avarage orientation of the 4 TDMs for each core involved. The resulting angles between the TDM and the surface normal are given in Tab. 6.2 and are compared to theoretical predictions for the out-of-horizontal phenyl plane bend angles of the two different phenyl moieties: α_C for the benzylidene moiety, i.e. the phenyl ring attached to the C of the imine bridge, and α_N for the aniline moiety, i.e. the ring attached to the N of the imine bridge.

The exact determination of the angles of the TDMs is impaired by background effects. The extent to which spectra are affected increases with decreasing coverage. Thus, the effects are more noticeable for the thin TBI layers than the thicker SAMs discussed in previous chapters. As the molecule contains only one N atom the N1s spectra are more affected than the C1s spectra and the problem is most pronounced for layer **T**, which has the lowest coverage of all structures investigated. The background effects manifest in a nonconstant spectrum in the post-edge region and hence interfere with the normalisation of the spectra. These uncertainties have a strong influence on α.

Layer T We propose a *planar-trans* configuration for this layer. In an ideally planar configuration both rings have the same orientation $\alpha_C = \alpha_N$. However, the structure predicted by the DFT calculations is slightly bent, allowing for an increased interaction of the N with the substrate. The predicted angles for the two rings primarily indicate this bend rather than a tilt of the whole molecule with respect to the surface (cf. Fig. 6.4 and Tab. 6.2).

In the *planar-trans* configuration the LUMO and LUMO+3 orbitals both extend over both rings even though they are distributed unequally (cf. Fig. 6.5). Thus, the transitions to these orbitals can not be used to obtain individual orientations for the two rings. However, since the structure is essentially planar, all $\pi^\star$ TDMs should point approximately into the same direction and we should obtain a similar average out-of-horizontal phenyl plane bend angle from the N1s to LUMO, N1s to LUMO+3 and the averaged C1s to LUMO+0–3 transitions.

The N1s LUMO+3 resonance is not visible in the s-pol spectrum even though it has nonzero intensity in this region. This suggests the existence of a background on which the $\pi^\star$ resonances are superimposed. For the s-pol spectrum the LUMO resonance appears shifted towards its position for the *cis* form in layer **C**, suggesting that part of the intensity arises from traces of *cis* molecules in the layer. Both effects lead to an overestimation of α. Therefore, we state the value of 10° obtained from the analysis of these N1s resonances as an upper limit. This value below the theoretical prediction appears plausible, because the rings are bent towards each other, the $\pi^\star$ orbitals extend over both rings, and thus the TDMs should be tilted less than the individual rings.

In contrast, the average orientation obtained from the C1s to LUMO+0–3 transitions yields a value of 25° significantly above the prediction. However, the ratio of s- and p-pol spectrum (not shown) is constant over the whole structure. This indicates that all 4 TDMs have the same orientation and also suggests a planar structure.

The discrepancy between the angles obtained from the N1s and C1s spectra may not be explained by background effects. Several other effects might play a role: The LUMOs were computed for the neutral molecule. The core hole, however, will distort the orbitals. For the N1s transitions it is located at the N atom in the imine bridge, whereas for the C1s transitions the core hole on average is located further out in the rings. The problems concerning the normalisation may have added different systematic errors to the N1s and C1s spectra.

Layer C We proposed a *cis* configuration for this layer. In this configuration the two rings are twisted with respect to each other. This twist reduces the conjugation of the two aromatic rings. The resulting LUMO and LUMO+3 are predominantly located at one of two rings, respectively. Thus, the orientations of the respective TDMs can be compared to α_C and α_N obtained from the DFT calculations. These experimental values differ significantly form the DFT predictions. However, the assignment of the *cis* configuration to the molecules in this layer still appears more likely than the *twisted-trans* form, which would also be compatible with the values obtained, in a different adsorption geometry than that predicted though. The assignment of the *cis* form is further corroborated by STM results.[5] The average orientation obtained from the C1s to LUMO+0–3 transitions lies in between the two orientations obtained from the N1s spectra as expected.

The deviation of the experimentally obtained angles from the prediction may have several reasons: First, the angles not only depend on the configuration of the molcule, i.e. *cis* but as much on the actual adsorption geometry. As the calculations were performed for an individual molecule on a nonreconstructed surface it is not unlikely

---

[5] STM results see 6.5 The STM image shows a mixed layer similar to layer **B** consisting of molecules in the *cis* and *planar-trans* forms. The NEXAFS spectra of layer **B** can be described as a superposition of the spectra of **T** and **C**. Thus, **C** should consist of the *cis* conformer.

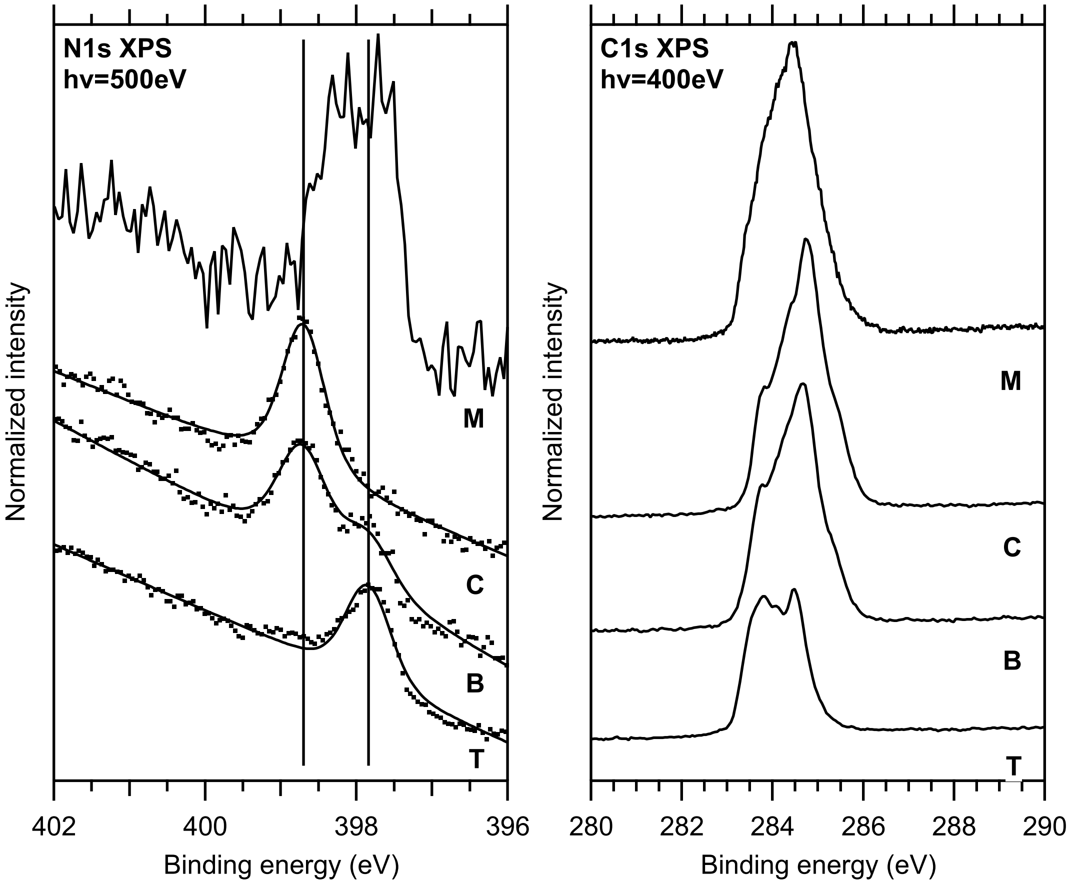

Figure 6.7: XPS spectra of TBI: N1s specta (*left*) and C1s spectra (*right*).

that the results deviate from the observed behaviour in a densely packed layer on a surface that shows the typical herringbone reconstruction of Au(111).[6] Second, as already discussed for layer **T**, the calculations are for the neutral molecule and the core hole may distort the orbitals. Also normalisation issues may play a role.

6.4 XPS

Figure 6.7 shows N1s and C1s spectra of the various layers. As we assume that both layers **C** and **T** purely consist of *cis* and *trans* molecules, respectively, we expect a single peak in the N1s spectra of these layers. The shift of approximately 1 eV towards higher binding energies of the peak of the *cis* species in **C** compared to the *trans* species in **T** can be explained by the increased interaction of the N atom with the metal due to the reduced distance to the substrate in the *cis* form (2.3 Å (*cis*) vs. 3.2 Å (*trans*), theoretical values from [133]). The spectrum of layer **T** exhibits a small feature at the position of the peak in layer **C**, which is assigned to small amounts of *cis* molecules present in this layer.

The N1s spectra of the mixed layer **B** can be fitted with two peaks at the same positions as in the pure layers. In the monolayer regime dampening of the signal should not differ much for the two species. Thus, the composition is directly given

---

[6] From the STM image of a layer similar to **B** it is apparent that the adsorption follows the reconstruction. Thus, it appears likely that the reconstruction also survives in the case of layer **C**.

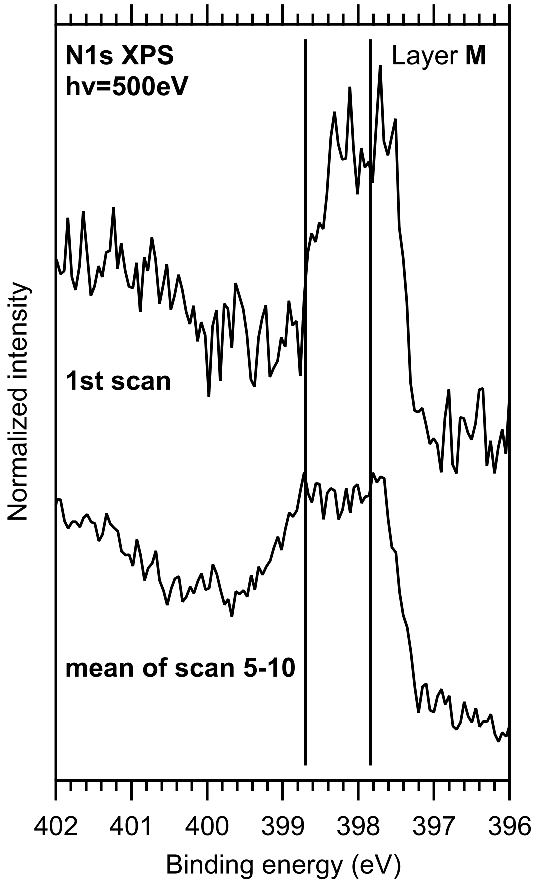

Figure 6.8: Effect of X-ray exposure on the Multilayer **M**: N1s XPS spectra of a pristine layer and after several scans. The vertical bars indicate the positions of the *cis* and *trans* monolayers **C** and **T** as in Fig. 6.7. Upon X-ray exposure the peak not only broadens, but also shifts towards lower binding energies, i.e. towards the position of the *cis* monolayer. This suggests that the change is not only due to conventional beam damage, but arises partly from a *trans–cis* isomerization induced by the secondary electrons.

by the peak areas and we obtain a surface molar fraction of $\chi_{cis} = 72 \pm 8\%$[7] for the *cis* species in the mixed layer.

The spectrum of the multilayer **M** shows strong X-ray induced changes while the spectra are recorded (Fig. 6.8). They are most probably caused by secondary electrons, which may lead to beam damage or other structural changes. Layer **M** is much more sensitive to these effects than the monolayers. Presumably excitations, which lead to the damage, are quenched by interactions with the substrate in the monolayers. Thus, in Fig. 6.7 we show a single scan for the monolayer while several scans were averaged for the other spectra. The spectrum of **M** shows a broader flat topped peak structure with a centre in between the positions of the *cis* and *trans* monolayer, a high intensity at the position of the *trans* peak and little intensity at the position of the *cis* molecules. This is compatible with our view of a multilayer with a flat *trans* layer at the metal interface and a twisted *trans* layer on top.

The C1s spectra also shown in Fig. 6.7 exhibit pronounced differences between the different layers. However, unlike the N1s spectra where the signal arises from a single atom in the molecule, the C1s spectra are a complex superposition of the overlapping signals of all the different C atoms in the molecule (aromatic, aliphatic,

---

[7] The peak width of the smaller peak is highly correlated with the amplitude of the larger. Thus, naive application of error propagation leads to a rel. error of 37%. To estimate the error, shape and width were set fixed to (a) the values obtained from the fit to layer C and (b) to a gaussian shape and mean width of those obtained from the fits of layer C and B. (The shape of the peak of layer T varied widely even between different spots on the same sample—probably due to artefacts fortunately only present in layer C). The difference between the values obtained from the two fit variants, was larger then the error obtained from the fit errors of either fit variants and is given as our estimate.

aliphatic close to surface). Thus, no further analysis has been attempted.

6.5 STM

A mixed *trans*/*cis* monolayer similar[8] to layer **B** has been investigated by STM in the group of Leonhard Grill [133]. The image is shown in Fig. 6.9. Mainly the *tert*-butyl groups are imaged. For *trans*-TBI they show up as 4 dark-gray protrusions, whereas for the *cis* molecules the *tert*-butyl groups of the ring twisted with respect to the surface show up as white spots. These assignments are shown in the bottom part of the figure where a magnified section of the image is overlaid with structural formulas of the *trans* and *cis* forms. These results corroborate the structures assigned on the bases of the NEXAFS results: A *planar-trans* configuration and a *cis* configuration with one ring plane parallel to the surface and the other one twisted upwards.

A more detailed analysis of the image reveals that the molecules arrange following the herringbone reconstruction of the surface. At this coverage *cis* molecules are mainly observed on the herringbone ridges. For each molecule with *cis* configuration the azimuthal orientation of the neighbouring *trans* molecules changes with respect to the row direction. This lateral stacking allows a dense packing in the mixed layer. The analysis yields an area $1.6\pm0.1\,\mathrm{nm}^2$ for the *trans* molecule, whereas the *cis* form occupies only $1.1\pm0.1\,\mathrm{nm}^2$ resulting in a relative surface density $\rho_{cis}/\rho_{trans} = 1.5\pm0.1$.

6.6 Relative Surface Densities of the two Isomers

The relative surface densities of the two isomers in the mixed layer **B** can also be deduced from XPS and NEXAFS data: Combining the composition and the coverages of **B** with those of the pure *cis* layer **C**, the relative space requirements of the two species in the mixed film can be obtained according to the following considerations.

First we define some quantities needed in the derivation: The composition of the film is described by the *surface molar fractions* of the components $\chi_i = N_i/N$, where N_i is the number of molecules of species i and N the total number of molecules on the sample. The *total coverage* $\Theta_\mathbf{B} = N/A$ of layer **B** is the total number of TBI molecules N on the sample surface A. The *partial coverages* of the components $\Theta_i = N_i/A$ is the number N_i of molecules of the respective species per sample area. In contrast to the partial coverage, which is defined with respect to the total sample surface A, the *surface densities* $\rho_i = N_i/A_i$ are defined with respect to the surface A_i occupied by the respective species. The space requirement of a *trans* molecule relative to a *cis* molecule is given by the inverse ratio ρ_{cis}/ρ_{trans} of the two surface densities. This is the quantity we seek for.

We assume that layer **B** completely covers the sample surface. Thus, the sum of the areas occupied by the two species is the total sample area. Using this relation we obtain:

$$1 = \frac{A_{trans}}{A} + \frac{A_{cis}}{A} = \frac{N_{trans}}{A}\frac{A_{trans}}{N_{trans}} + \frac{N_{cis}}{A}\frac{A_{cis}}{N_{cis}} = \frac{\Theta_{trans}}{\rho_{trans}} + \frac{\Theta_{cis}}{\rho_{cis}} \tag{6.1}$$

Layer **C** is also assumed to be complete and to consist of *cis* molecules only. We further assume that the surface density of the *cis* molecules is the same in layer **C**

---

[8] The layer was prepared by dosing a multilayer at T = 300 K and subsequent annealing at 390 K for 10 min.

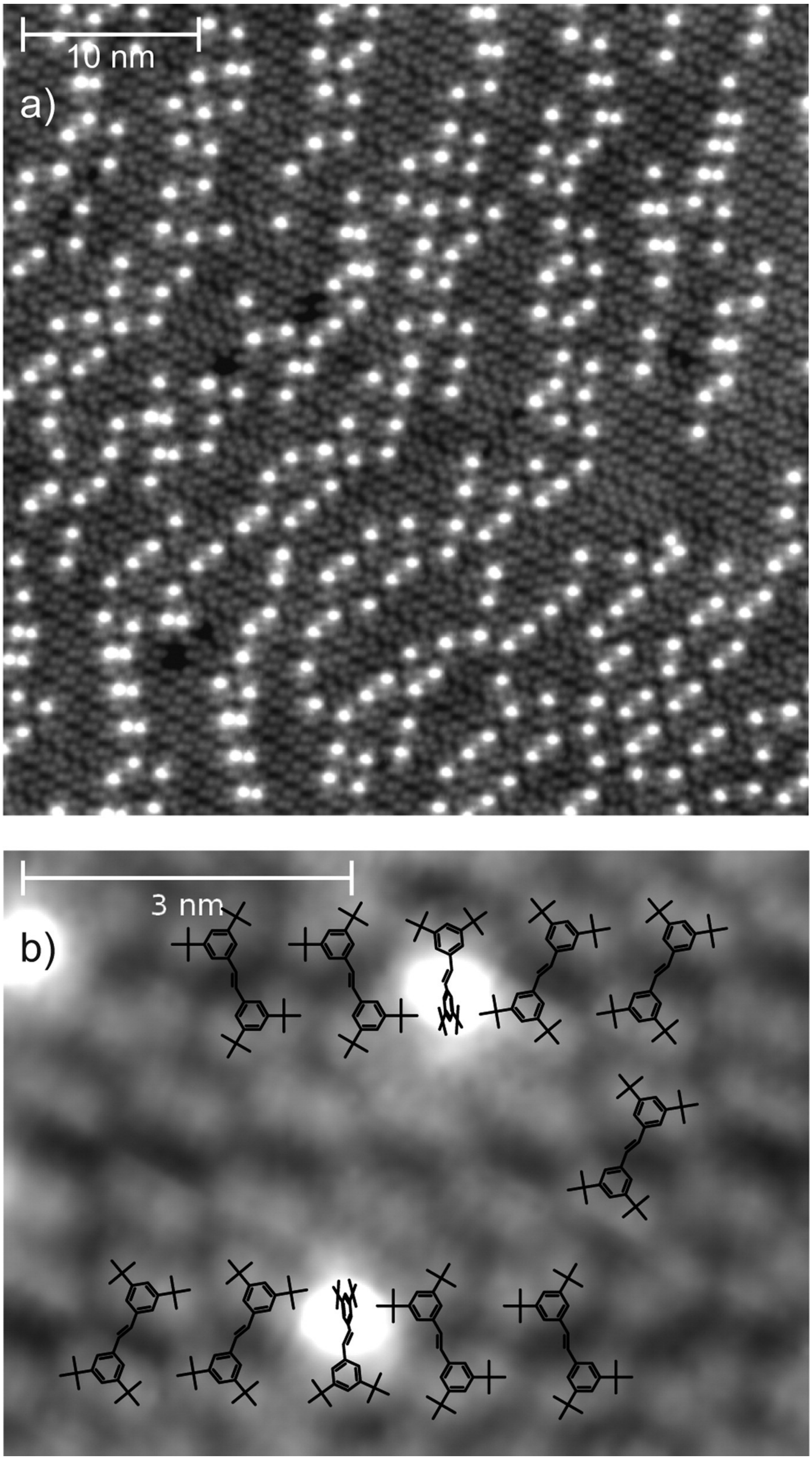

Figure 6.9: STM image of a TBI layer similar to **B**: Overview *(top)* and magnified section overlaid with structures of the proposed *planar-trans* and *cis* adsorption geometries *(bottom)*, Figure from [133].

as in the mixed layer **B**. Thus, the total coverage $\Theta_{\mathbf{C}}$ of layer **C** equals the surface density of the *cis* species. This leads for the following relation:

$$\frac{\Theta_{trans}}{\rho_{trans}} + \frac{\Theta_{cis}}{\rho_{cis}} = 1 = \frac{\Theta_{\mathbf{C}}}{\rho_{cis}} \quad \Rightarrow \quad \frac{\rho_{cis}}{\rho_{trans}} = \frac{\Theta_{\mathbf{C}} - \Theta_{cis}}{\Theta_{trans}} \tag{6.2}$$

Using $\Theta_{trans} = \Theta_{\mathbf{B}} - \Theta_{cis}$ and $\Theta_{cis} = \chi_{cis}\Theta_{\mathbf{B}}$ we obtain:

$$\frac{\rho_{cis}}{\rho_{trans}} = \frac{\Theta_{\mathbf{C}} - \chi_{cis}\,\Theta_{\mathbf{B}}}{(1-\chi_{cis})\,\Theta_{\mathbf{B}}} \tag{6.3}$$

With the reference coverage $\Theta_{\mathbf{C}} = 1$ and $\Theta_{\mathbf{B}} = 0.8 \pm 0.1$ obtained from TDS we obtain the following relative surface densities using the two different values for the coverage $\chi_{cis}^{\mathrm{NEXAFS}} = 83 \pm 9\%$ and $\chi_{cis}^{\mathrm{XPS}} = 72 \pm 8\%$:

$$\frac{\rho_{cis}}{\rho_{trans}} = 2.5 \pm 0.2 \text{ for } \chi_{cis}^{\mathrm{NEXAFS}} \quad \text{and} \quad \frac{\rho_{cis}}{\rho_{trans}} = 1.9 \pm 0.4^{9} \text{ for } \chi_{cis}^{\mathrm{XPS}} \tag{6.4}$$

$$\text{compared to} \quad \frac{\rho_{cis}}{\rho_{trans}} = 1.5 \pm 0.1 \text{ from STM.} \tag{6.5}$$

The value obtained from the STM image probably describes the actual situation in the mixed layer best. Of the two indirectly obtained values the one based on the XPS results appears most reliable. However, the method described above may lead to a systematic underestimation of the space required by a *cis* molecule for the following reason: We assume that the space requirements of the *cis* molecule are the same in the pure *cis* layer **C** as in the mixed layer **B**. The STM image shows that the *cis* molecules in the mixed layer adsorb at the herringbone ridges only and are separated by trans molecules. In a pure *cis* layer the *cis* molecules must also adsorb at other positions without *trans* molecules inbetween. The resulting structure is probably less dense.

6.7 Conclusion

Based on the evaluation of the NEXAFS data, TBI in layer **T** clearly possesses a *planar-trans* configuration similar to that of TBA [27, 28]. This adsorption behaviour of TBI is confirmed by HREEL spectroscopy [133]. Also based on HREEL measurements, similar adsorption geometries were found for the related molecules TBA [139, 140], dimethoxy-TBA [141], and tetra-*tert*-butyl-stilbene [140] on Au(111). From STM studies at submonolayer coverage we know that at low temperatures TBI molecules aggregate in well ordered islands in the *planar-trans* configuration [138]. Further XPS and NEXAFS experiments on annealed layers show no indication of a different species up to 500 K, where the detection limit was reached due to desorption. In addition, NEXAFS measurements show that multilayers of type **M** (adsorbed at 210 K) are in the *trans* configuration. These findings lead to the conclusion, that the *planar-trans* configuration is the stable isomer of TBI on Au(111).[10]

---

[9] Due to the large errors in the input variables, Gaussian error propagation based on a linear approximation of the function could not be applied, and errors were calculated using intervals. Due to the different behaviour of the function in different regions, the errors for the two results differ, even though the errors of the input values are similar.

[10] This result is not at variance with previous STM data [138], which report on a *cis* species upon annealing of a submonolayer of TBI at 500 K. At the very low coverage studied in the STM experiment the molecules are absorbed at the herringbone ridges of the reconstructed Au(111) surface. There may be a small amount of reactive sites below the detection limit of our NEXAFS experiment at which the *cis* configuration of TBI may be favoured in layer **T**.

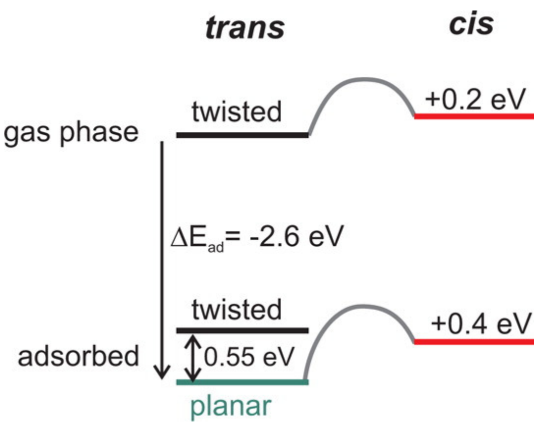

Figure 6.10: DFT-D energetics of TBI on Au(111): Figure from [133].

However, the NEXAFS data for the monolayer **C** with the highest coverage, prepared at a sample temperature in between that of layer **T** and **M**, indicates a twisted species. Comparison with theoretical predictions and the STM image for the mixed layer allow us to conclude that layer **C** consists almost completely of molecules in *cis* configuration.

Which effects stabilise the *cis* configuration in layer **C**, i.e. why is the *cis* configuration the thermodynamic equilibrium state? Figure 6.10 shows an energy-level diagram for the two isomers adsorbed on the surface and in the gas phase obtained from DFT calculations. Even though the calculated adsorption energy is likely overestimated [133], the relative positions of the energies allow to explain the observed behaviour: The adsorption energies $\Delta_{\text{ads}}E$ for the *trans* and *cis* form are the differences of the energies of the ***trans*** molecule in the gas phase $E^{\text{gas}}_{\boldsymbol{trans}}$ to the respective adsorbed species:

$$\Delta_{\text{ads}}E_{trans} = E^{\text{ads}}_{trans} - E^{\text{gas}}_{\boldsymbol{trans}} \tag{6.6}$$
$$\Delta_{\text{ads}}E_{cis} = E^{\text{ads}}_{cis} - E^{\text{gas}}_{\boldsymbol{trans}} \tag{6.7}$$

This adsorption energy is larger for the *trans* form than for the *cis* form. However, it is not the adsorption energy of the individual molecule that determines the equilibrium state for a full layer but the total adsorption energy for the whole layer:

$$\Delta_{\text{ads}}E^{\text{tot}}_{trans} = N_{trans}\ \Delta_{\text{ads}}E_{trans} = A\ \rho_{trans}\ \Delta_{\text{ads}}E_{trans} \tag{6.8}$$
$$\Delta_{\text{ads}}E^{\text{tot}}_{cis} = N_{cis}\ \Delta_{\text{ads}}E_{cis} = A\ \rho_{cis}\ \Delta_{\text{ads}}E_{cis} \tag{6.9}$$

The smaller footprint of the *cis* form allows for a higher density ρ_{cis} of the *cis* monolayer, i.e. a larger number N_{cis} of molecules on the same sample surface A. As long as the gain in total adsorption energy due to this larger number of adsorbed molecules in the *cis* layer overcompensates the decreased adsorption energy for the individual molecule, the *cis* layer is stable:

$$\Delta_{\text{ads}}E^{\text{tot}}_{cis} > \Delta_{\text{ads}}E^{\text{tot}}_{trans} \quad \Rightarrow \quad \frac{\rho_{cis}}{\rho_{trans}} > \frac{\Delta_{\text{ads}}E_{trans}}{\Delta_{\text{ads}}E_{cis}} \tag{6.10}$$

So far we have discussed the equilibrium state. However, in order to obtain the equilibrium state, it also has to be kinetically achievable. Hence, we have to consider the activation barriers of the isomerization and the energy for the competing desorption: During preparation of the multilayer **M** at low temperatures the thermal energy is insufficient to enable the isomerization. Hence, the first layer of the multilayer **M** adsorbed at lower temperatures remains in *trans* configuration,

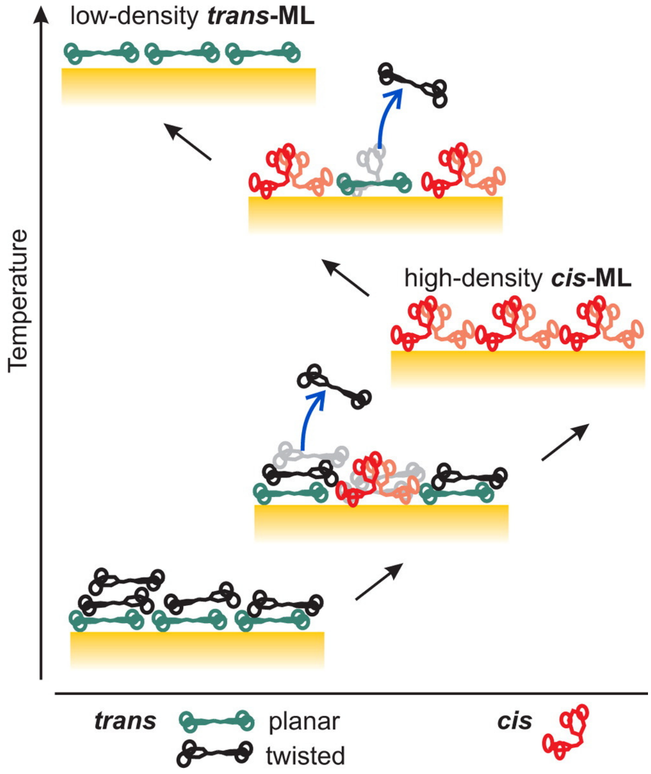

Figure 6.11: Schematics of the temperature and coverage driven isomerization of TBI on Au(111): Adsorbed at low temperatures, the molecules on the surface switch from *trans* to *cis* and back to *trans* when continuously increasing the temperature due to the change of coverage and supply of activation energy. Figure from [133].

while more molecules are adsorbed on top. The adsorption energy is larger than the activation barrier for the *trans* to *cis* isomerization.[11] Thus, thermal isomerization at the surface is possible without desorption. During a TDS heating ramp the activation energy is supplied, molecules from the multilayer isomerize, and a *cis* monolayer is formed, while excess molecules desorb. Upon further heating the *cis* layer partially desorbs and at the now lower coverage the adsorption energy of the individual molecule determines the equilibrium, and thus the *trans* form is favoured. A mixed phase of type **B**, which covers the sample fully, exists until a pure *trans* (sub)-monolayer regime of type **T** is obtained. At coverages below the full *trans* monolayer TBI molecules assemble in well-ordered islands [138]. Theses processes during a TDS heating ramp are sketched in Fig. 6.11.

---

[11] The *cis* to *trans* activation energy of free TBI in the gas phase and solution is expected to be about 0.6 eV[132] and is expected to be even lower for the adsorbed molecule in analogy to TBA on Au(111) [129, 142]. For the *trans* to *cis* isomerization relevant for the process discussed the energy difference of the adsorbed *planar-trans* and *cis* state has to be added to this value. Both, the activation barrier and the energy difference between the two adsorbed isomers is larger for TBA (cf. Sec. 6.1), and thus the temperature and coverage dependent isomerization is only observed for TBI.

Chapter 7

Methods and Materials

7.1 General

All work involving azo compounds was carried out in yellow light with a cut-off wavelength of 500 nm.[1]

7.2 SAM preparation

7.2.1 Glassware Preparation and Plastic Disposables

Reusable glassware was cleaned using an alkaline lab cleaner in an immersion bath at 60 °C. After rinsing with tap water, the glassware was immersed into 0.1 M hydrochloric acid followed by three baths of de-mineralized water and allowed to dry in air. The effectiveness of the cleaning procedure was checked by rinsing samples of the glassware with ethanol or acetonitrile and recording UV/vis spectra down to 200 nm.

Disposable glassware and PP products (pipette tips, syringes, syringe filters, reaction vessels) were checked for extractables using the same procedure. For syringes we were not able to find a brand that did not release intolerable amounts of substances absorbing at low wavelength. Thus, disposable syringes were disassembled and cleaned using the same procedure as for the glassware. Alternatively, single items were rinsed with the solvent to be used in the experiment.

7.2.2 Weighing and Liquid Handling

The typically required sub-mg amounts of thiols were weight using aluminium weighing boats and the reverse weighing technique on a Satorius micro balance. Where the concentration of the solution was determined photometrically, less accurate balances were used.

Volumes for the preparation of SAMs and dilution of samples for photometric determinations were generally measured using air displacement pipettes with disposable PP tips. For acetonitrile, due to the high vapour pressure, direct displacement pipettes[2] with disposable PP tips were used.

---

[1] fluorescent light tubes *Narva* colour *yellow special*

[2] Gilson, Microman positive displacement pipettes

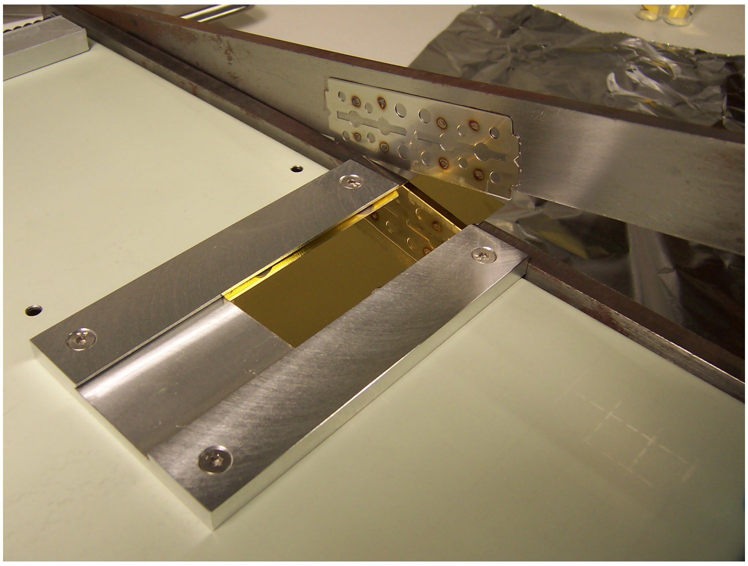

Figure 7.1: Cutting device for Mica Substrates: A paper cutter was equipped with a guide to hold the mica and an extra long razor blade spot-welded to the guillotine-knife. Razor blade: Type JT1, JT3, Art. No 3811, Jaguar Stahlwarenfabrik GmbH & Co. KG, Solingen, Germany, $l \approx 65\,\text{mm}$, $d = 0.15\,\text{mm}$. Thinner blades were found to be less suitable.

7.2.3 Substrates

Epitaxial gold on mica, (25 x 75) mm, 300 nm gold was obtained from Georg Albert, PVD-Beschichtungen, Silz, Germany. These were annealed by the manufacturer to give large Au(111) terraces. The substrates were cut into (25 x 10) mm pieces for UV/vis measurements and (12 x 10) mm pieces for XPS and NEXAFS measurements using a modified paper cutter (Fig. 7.1). Cut substrates were stored under argon in the vials later used for immersion.

7.2.4 SAM forming Thiols and Solvents

Structural formulas can be found in Fig. 5.1. If published, synthesis are referenced in the following. Generally HPLC-grade solvents were used for SAM preparation.

H-Az6 (6-[4-[2-phenyldiazenyl]phenoxy]-1-hexanethiol,
CF_3-Az6 (6-[4-[2-[4-(trifluoromethyl)phenyl]diazenyl]phenoxy]-1-hexanethiol [10], and
CN-Az6 (4-[2-[4-[(6-mercaptohexyl)oxy]phenyl]diazenyl]-benzonitrile) [95],
were prepared by Dr. W. Freyer in our group.

H-Az11 (11-[4-(2-phenyldiazenyl)phenoxy]-1-undecanethiol [82, SI] was a courtesy of R. Klajn, Weizmann Institute of Science, Department of Organic Chemistry, 76100 Rehovot, Israel. The compound is also commercially available (ProChimia Surfaces Sp. z o.o., Sopot, Poland, http://www.prochimia.com).

CN-AzPh (4-[(E)-[4-[(6-sulfanylhexyl)oxy]phenyl]diazenyl]benzonitrile) [143] was prepared by S. Zarwell in the group of K. Rück-Braun, Technische Universität Berlin, Institut für Chemie.

CF_3-ImPh (4'-[(E)-[4-(trifluoromethyl)benzylidene]amino]biphenyl-4-thiol) was prepared in the group of Rainer Haag, Freie Universität Berlin, Institut für Chemie und Biochemie.

C12 (1-dodecanethiol (98%) was used as obtained from Alfa Aesar.

7.2.5 Sample Preparation

7.2.5.1 General Procedure

For incubation it is desirable to use vessels with no neck to facilitate the later removal of the substrates and an inner diameter small enough so that samples are forced in an upright position and can not lie flat on the ground. For immersion at ambient temperature flat bottom glass vials[3] were chosen and covered with cover slips to limit evaporation during incubation.

Substrates were immersed into 0.1 mM adsorption solutions of the respective thiols. After 20–24 h samples were removed using cover slip tweezers touching them at the front and the back at the upper edge, and rinsed using a glass Pasteur pipette with the same solvent as for the immersion. Care was taken to also flush the tweezers. Following this, samples were taken with a second pair of tweezers at the other side and rinsed again. Finally they were blown dry with argon taking care to dry the space in between the tweezers without blowing solvent onto the sample and placed in fresh vials and stored under argon.

7.2.5.2 Single Component R-Az6 SAMs

Generally batches of 2–4 ml of 1 mM stock solution were prepared by dissolving the appropriate amount of the thiol in ethanol. Sonication and when necessary warming to 40 ℃ was done to aid dissolution. Stock solutions were stored up to 2 weeks in a refrigerator at 8 ℃ and were diluted to 0.1 mM adsorption solutions as needed.

7.2.5.3 Mixed Chromophore SAMs (Mixed R-Az6 SAMs)

Mixed SAMs of H-Az6/CN-Az6 and CF_3-Az6CN-Az6 were prepared from solutions in ethanol with a total thiol concentration of 0.1 mM . These adsorption solutions were prepared from 1 mM stock solutions. Incubation time was 24 ± 1 h.

For the CF_3-Az6/CN-Az6 XPS-experiment a single batch of stock solution was prepared for each compound in order to minimize random errors related to varying concentrations. The solution was split into 1.5 ml lots. These were stored in a freezer at below -18 ℃. Prior to use, vials containing stock solutions were warmed to 40 °C to ensure complete solution of the precipitate and allowed to cool to room temperature. Partly used vials were then stored in a fridge at 8 ℃. When diluting the solutions the same pipette was used for both components, when necessary, pipetting several times in order to minimize the influence of systematic errors of the pipette.

For the H-Az6/CN-Az6 experiments samples for XPS- and UV-measurements were cut from the same piece of gold substrate and were immersed back to back into the same solution. For the CF_3-Az6/CN-Az6 UV/vis-experiment and the H-Az6/CN-Az6 UV/vis- and XPS-experiments the concentration-ratio in the working

---

[3] Roth Art. No.: H306.1, borosilicate glass, flat bottom, 4 ml, o.d. 14.5 mm, i.d. 12 mm. The polythene stoppers included with the vials were not used as UV/vis spectra showed that they contained substances extractable with ethanol.

Table 7.1: Absorption Coefficients of the R-Az6 Thiols: Stated errors are standard deviations of 4–5 samples.

compound	solvent	$\lambda_{\max}$	$\varepsilon_{\max}$ / $10^3\,\mathrm{cm^2\,mmol^{-1}}$
H-Az6	methanol	347	27.3 ± 0.3
H-Az6	ethanol	347	27.1 ± 0.2
CF_3-Az6	ethanol	354	27.0 ± 0.1
CN-Az6	ethanol	364	30.4 ± 0.3

solutions was obtained by fitting UV-spectra of the adsorption solutions with a linear combination of reference spectra of the individual compounds.

UV/vis Reference Spectra and Absorption Coefficients Reference spectra were obtained from ≈ 0.03 mM solutions of the individual compounds with known concentration. For these reference samples the compounds were dried in vacuum above P_2O_5 for 24 h at room temperature. To the appropriate amounts for 20–40 ml (0.2–0.4 mg) the required volume of solvent was added by weight. The results are given in Tab. 7.1.

Stability of Stock Solutions As disulphides are a common impurity in thiols and adsorb much less than thiols [61] stock solutions of CF_3-Az6 and CN-Az6 were analysed by ultra high performance liquid chromatography (UPLC) using an acetonitrile/water gradient as eluent and a reverse phase column.[4] Both thiol and disulphide carry the same chromophore; thus UV-absorption could be used to quantify the amount of disulphide. For both compounds less than 2% of the chromophores were found to be disulphide.

7.2.5.4 Diluted Chromophore SAMs (H-Az11/C12 Mixed SAMs)

Mixed SAMs of H-Az11/C12 were prepared from adsorption solutions in methanol with a total thiol concentration of 0.1 mM. Adsorption solutions were prepared from stock solutions (see below). Incubation time was 20 ± 0.5 h. Samples for XPS- and UV-measurements were cut from the same piece of gold substrate and were immersed back to back into the same solution. Methanol rather than ethanol was chosen as solvent because it was used in earlier work by Klajn et al. that led to the current cooperation.

Stock Solutions of H-Az11 Stock solutions of H-Az11 were prepared by sonication of the appropriate amount of the compound to give a nominally $0.4\,\mathrm{mmol\,l^{-1}}$ solution and warming the solution to 40°C. A small amount of a disperse solid residue remains. We assume this residue is the corresponding disulphide. The suspension was filtered through a 0.2 µm PTFE-membrane syringe filter. The purity of the filtrate was checked by ultrahigh-performance liquid chromatography. The Filtrate was used as stock solution. Due to the unknown amount of residue filtered off, the concentration of this stock solution had to be determined photometrically, as described below.

For the determination the solution was diluted to a nominal concentration of $0.03\,\mathrm{mmol\,l^{-1}}$ and the absorbance in the main band was compared to the absorbance coefficient of H-Az6 in methanol (Tab. 7.1), a compound with the same chromophore

---

[4] Analysis were performed by J. Leistner in the group of S. Hecht.

that dissolves completely and shows an absorbance spectrum indistinguishable from the one of H-Az11.

Solubility of H-Az11 The solubility of H-Az11 in methanol is low and it is easily underestimated due to the presence of the insoluble disulphide. We determined a solubility of $0.54 \pm 0.02\,\mathrm{mmol\,l^{-1}}$ in the following way: H-Az11 was repeatedly added to the solution and the resulting suspension was filtered until the absorbance of the filtrate remained constant.

Stock Solutions of C12 $1\,\mathrm{mmol\,l^{-1}}$ stock solutions of 1-dodecanethiol (C12) were prepared by diluting the liquid compound by volume assuming a density of $0.845\,\mathrm{g\,cm^{-3}}$ [144] in 2 steps: 8 µl were measured using microcapillary glass pipettes with plunger and diluted to $10\,\mathrm{mmol\,l^{-1}}$. This solution was then further diluted to $1\,\mathrm{mmol\,l^{-1}}$.

7.2.5.5 SAMs of CN-AzPh

CN-AzPh is less soluble in ethanol than the R-Az6 compounds. For the data shown, $0.1\,\mathrm{mmol\,l^{-1}}$ adsorption solutions were directly prepared by sonication of the appropriate amount of the compound for 30 min at room temperature. No undissolved residue remained. TLC analysis of the solutions always showed a second component, which we attribute to the corresponding symmetrical disulphide. We were not always able to produce solutions of the desired concentration, presumably due to an increased disulphide content. In future experiments, one should thus aim at a higher nominal concentration and filter off the residue followed by a photometric determination of the concentration as described for H-Az11.

Preparation from the Corresponding Disulfide SAMs of CN-AzPh were also prepared from solutions in a 1:1 mixture of ethanol and THF. The solubility in THF is much higher, however, analysis by TLC (below) revealed that CN-AzPh in THF is quantitatively transformed to the disulphide. The oxidation to the disulphide is most likely due to peroxides generally present in THF. The highest purity qualities of THF commercially available are specified to contain $< 40\,\mathrm{mg l^{-1}}$ of peroxides—more than sufficient to oxidize a $1\,\mathrm{mmol\,l^{-1}}$ solution of the thiol completely.

However, XPS and NEXAFS spectra of SAMs prepared from the solutions in ethanol/THF were indistinguishable from samples prepared from ethanol. Disulphides and thiols are expected to lead to the same SAM, however, the adsorption of disulphides is expected to be less efficient. Apparently in this case the concentration of $0.1\,\mathrm{mmol\,l^{-1}}$ nominal thiol concentration corresponding to $0.05\,\mathrm{mmol\,l^{-1}}$ disulphide and the immersion time of 24 h is sufficient to produce a SAM of similar quality than from ethanol.

Thin-Layer Chromatography (TLC) The image of the TLC plate in Fig. 7.2 shows the formation of disulphides in THF: After the substrates with the SAMs had been removed after 24 h, the adsorption solutions in ethanol and in THF/ethanol 1:1 were evaporated at room temperature by means of a nitrogen stream. The dry residues and a sample of the pristine substance were dissolved in chloroform and applied to the plate. The pristine substance shows two bands. The upper band is the main component and is assigned to the thiol. We assign the lower band to the disulphide. The residue of the solution in THF only shows a single component

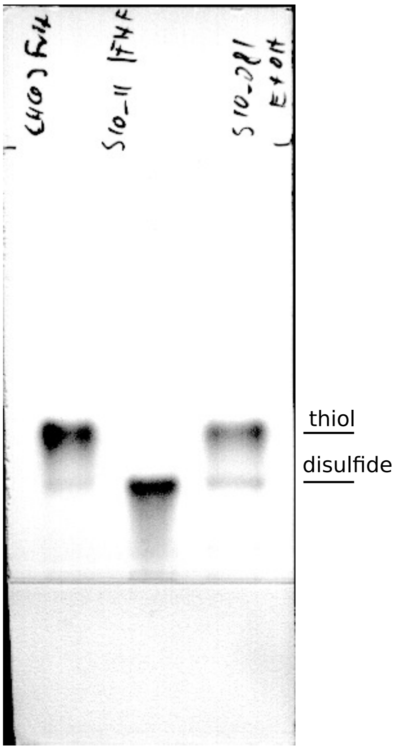

Figure 7.2: TLC of CN-AzPh: pristine compound *(left)*, residue from solution in THF *(middle:)*, and residue from solution in ethanol *(right)*. Adsorbent: silica gel 60, mobile phase: CH_2Cl_2/benzene 1:1. Blue channel of an image acquired using an office flat-bed scanner.

at the position of the disulphide, whereas the sample from the ethanolic solution appears nearly unaffected after 24 h. We conclude that in THF the thiol is completely oxidized to the disulphide while the compound is stable in ethanol for the duration of the adsorption process. Further experiments show that the oxidation in THF is complete within the time required to evaporate the solvent.

7.2.5.6 SAMs of CF_3-ImPh

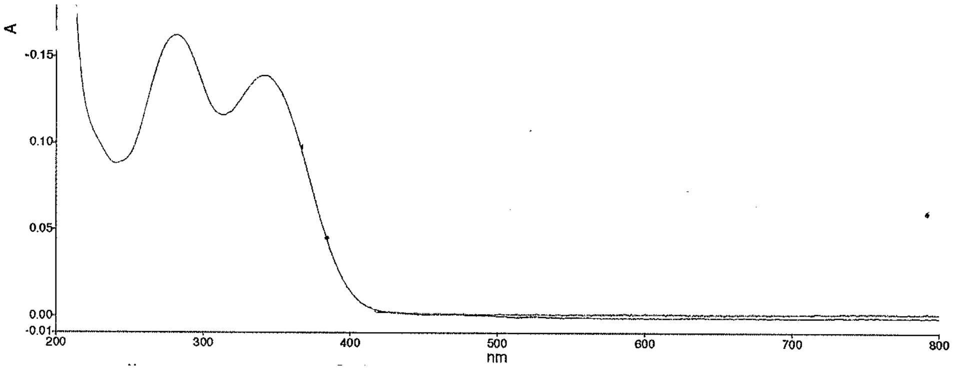

Figure 7.3: UV spectrum of a saturated solution of CF_3-ImPh in acetonitrile.

The solubility of CF_3-ImPh in ethanol was found to be very low. In acetonitrile the solubility is higher but well below the desired concentration of $0.1\,\mathrm{mmol\,l^{-1}}$ for the adsorption solution. Figure 7.3 shows a UV/vis spectrum of a saturated solution in acetonitrile. Using the absorption coefficient of the related imine 4-benzylidenamino-biphenyl[5] the concentration of the saturated solution was estimated as $8 \cdot 10^{-3}$ mM.

---

[5] $\epsilon_{\max} = 17.6 \cdot 10^3\,\mathrm{cm^2\,mmol^{-1}}$ at $\lambda_{\max} = 335\,\mathrm{nm}$ in dimethylformamide from [145].

Adsorption solutions were prepared from saturated solutions as follows: In a 14 ml centrifuge tube a small amount of the compound was dispersed in acetonitrile by sonication for 15 min at room temperature. The suspension was centrifuged for 15 min at 5500 rpm and the supernatant solution was siphoned off using a pipette. This saturated solution was diluted 1:1 with acetonitrile in order to prevent precipitation due to evaporation losses and used as adsorption solution.

Frequently, when preparing SAMs of this compound, excessive amounts of atomic sulphur were observed in S2p XP spectra at binding energy of 161 eV. In hindsight we have to assume that part of the undissolved residue consists of the corresponding disulphide for which we expect a lower solubility than for the thiol. Thus, we may not always have obtained a saturated solution and the observed excessive amounts of atomic sulphur—relative to the bond thiolate–may be due to incomplete coverage or a reduced ability of the thiol to displace atomic sulphur present on the pristine substrate due to a too dilute adsorption solution. For the concentration estimated above the absorption solution only contains a marginal excess of the thiole (cf. Sec. 3).

For future experiments the saturation concentration or the absorbance of a saturated solution should be determined as described for H-Az11 in order to ensure a reproducible concentration of the adsorption solution. For convenience the centrifugation should be replaced by filtration with syringe filters.

Imines are sensitive to acids; thus the formation of disulphides could not be investigated by TLC on silica gel.

7.3 Preparation of Layers of TBI and TDS

Crystal A square gold crystal ($10 \times 10 \times 2\,\mathrm{mm}^3$) with (111) surface was mounted with tantalum[6] wire to an LN_2 cooled manipulator as shown in Fig. 4.19.[7] The temperature was measured using a Type K thermocouple stuck in a hole at the side of the crystal. The crystal was heated by a current through the tantalum wires controlled by an Eurotherm 900 EPC PID controller.

The crystal was prepared by repeated sputter-anneal cycles (argon, acceleration voltage 0.8 kV, ion current 8 µA, sputter time 10 min, anneal temperature 610 °C, heating, $1.75\,\mathrm{K\,s^{-1}}$, cooling $1.5\,\mathrm{K\,s^{-1}}$, time at anneal temperature 10 min) until the pattern of the herringbone reconstruction of the (111) surface [146, Fig. 7] became visible in the LEED image (Fig. 7.4). Prior to each deposition the crystal was prepared by a single sputter anneal cycle.

Deposition of TBI (*E*)-3,5-di-*tert*-butyl-N-(3,5-di-*tert*-butyl-benzylidene)aniline (TBI) [132] was prepared by Ying Luo in the group of Rainer Haag, Freie Universität Berlin, Institut für Chemie und Biochemie and was deposited from an evaporator similar[8] to that described in Appendix A. The evaporator was pumped separately

---

[6] Tantalum forms alloys with gold. Thus, generally, gold crystals can not be mounted using tantalum. For this set-up, however, no problems were encountered. Tungsten wire can not be used for this purpose, as it becomes brittle after the first annealing.

[7] The figure shows an earlier version of the holder with a round crystal.

[8] The evaporator used in the experiment was a predecessor of the one described in the appendix. No aluminium foil was used to couple the crucible to the heating element of which the temperature was measured. Hence, the actual crucible temperatures may have been below the value given and differences in the rates between runs may partly be due to varying crucible temperatures. Also the long equillibration time of 30 min prior to deposition was only required because of the worse thermal coupling of the crucible to the heating element compared to the current design.

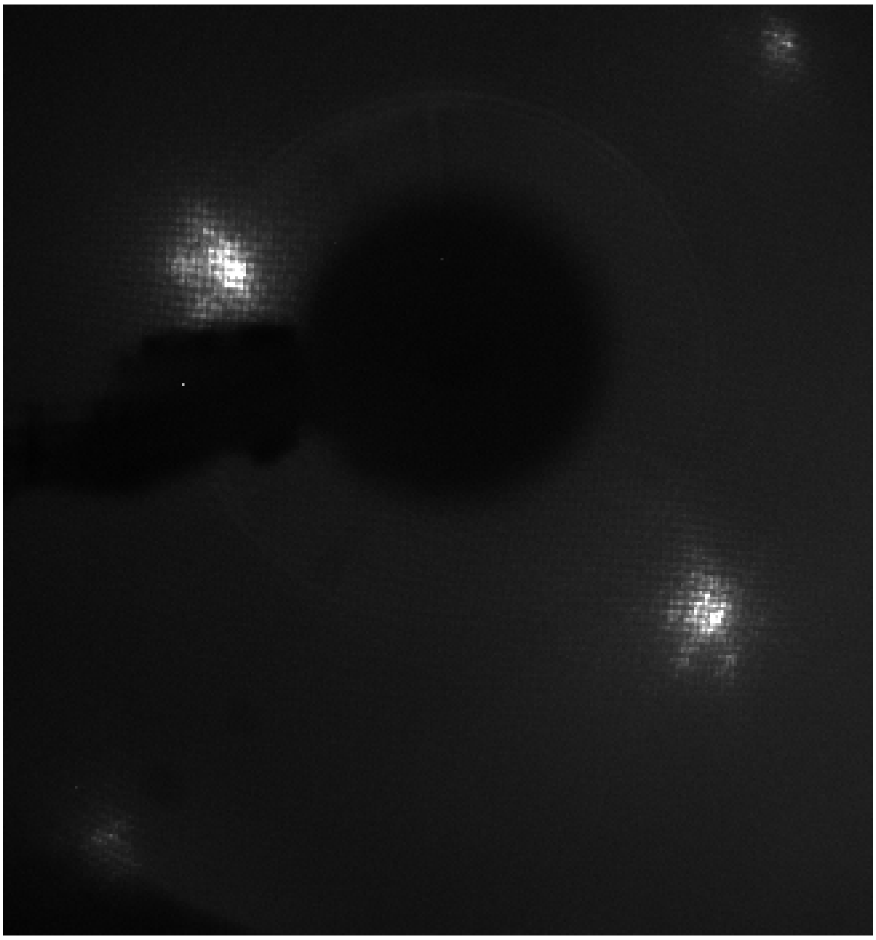

Figure 7.4: LEED pattern of reconstructed Au(111) surface at room temperature, energy 77.5 V.

from the chamber and was connected via a valve to the preparation chamber. It could be moved in evaporation position into the chamber via a linear motion.

The evaporator-set-up was baked for 36 h at 145 ℃. After filling the crucible 2–3 mm high with TBI, the evaporator-set-up was baked at 65 ℃ (measured at crucible) for 36 h.

Before deposition the evaporator was allowed to equilibrate at 85 ℃ for 30 min in order to ensure a stable rate. The sample was held at the desired deposition temperature, retraced from the deposition position, and its surface turned away from the evaporator. Then, the valve to the preparation chamber was opened and the evaporator was moved into evaporation position. The shutter was opened for ≈1 min in order to evaporate directly into the mass spectrometer to determine the evaporation rate. This value was used to adjust the exposition times determined by test evaporations and TDS prior to the experiment. Then, the sample was moved into evaporation position and turned face towards the evaporator. The shutter was opened for the calculated time, then the evaporator was retracted and the valve to the preparation chamber was closed. The sample was left for further 5 min at the deposition temperature and then allowed to cool with $1\,\mathrm{K\,s^{-1}}$ to the measurement temperature.

TDS A Pfeiffer PrismaPlus QMG 220 PT M25 252 quadrupole mass spectrometer (open ion source, yttriated iridium filament) was used. The mass of the parent ion, i.e. the ion of the nondissociated molecule, exceeded the range of m/e=200 amu of the QMS. Therefore, we chose the *tert*-butyl-ion (M+=57 amu) as prominent fragment for the TDS (Mass spectra: Fig. 4.2.3.1). Spectra with m/e=197 amu were recorded in parallel and show the same behaviour at a higher noise level. The auto range feature was disabled and TD spectra were recorded with fixed amplification and an integration time of 0.2 s per data point. The data was binned later for display. The spectrometer was warmed up for 2 h before usage and protected by a shutter during deposition. For TDS the sample was moved to a defined vertical distance underneath the TDS. A sufficient distance of the sample to the ionisation cell of the QMS is important in order to avoid readsorption of molecular fragments that escape from the ionisation cell. TD spectra were recorded with a heating ramp of $1\,\mathrm{K\,s^{-1}}$.

7.4 UV/vis Spectroscopy in Solution

Spectra were recorded using a Perkin Elmer Lambda 850 spectrometer with the following settings: monochromator slit widths equivalent to 2 nm optical resolution, 1 data point per nm, integration time 0.04 s per data point. With these settings a spectrum for the range 200–800 nm could be recorded in 40 s.

Generally fused silica cells were used. For photometric determinations disposable UV cells[9] were used. Cells had a path length of 10 mm.

7.5 Preparation of the *cis* Form of H-Az6

(From the authors *Diplomarbeit*) For Figs. 2.3 and 2.4 the pure *cis* form of Az20 was prepared by thin layer chromatography (TLC) as follows: A solution of Az20 in $CHCl_3$ was applied in a stripe onto a standard silica gel 60 TLC sheet. After the sheet had dried, it was irradiated for a few minutes at 366 nm using a TLC lamp. Following development in benzene/$CHCl_3$ 7+3, the sheet was dried in vacuum. It was then masked with a piece of black cardboard so that only the sides were left uncovered. In the light of a desk lamp the positions of the *cis* ($R_f = 0.08$) and the trans from ($R_f = 0.61$) were marked. The area containing the *cis* form was cut out and the sides that had been exposed to light were cut off broadly. Finally the *cis* form was eluted with ethanol and the UV/vis spectrum of the solution was recorded.

The whole procedure took less than about half an hour. It can therefore be assumed that only traces of the *trans* form are formed in the solution due to the thermal back reaction. This was confirmed by TLC of the solution, which was concentrated by evaporating the solvent with nitrogen after the spectrum had been recorded.

Because the solution of the *cis* form obtained in this way has an unknown concentration, its spectrum was scaled to align with the isosbestic points of the photoisomerization experiment.

7.6 Differential Reflectance (DR) Spectroscopy

Spectra were recorded using a Perkin Elmer Lambda 850 spectrometer equipped with rotatable Glan-Taylor polarizers and a home-built reflection unit. The set-up and

---

[9] semi-micro disposable UV cells, Brand GmbH & Co. KG, Germany, Cat. No. 759150.

Table 7.2: Illumination Conditions

	λ nm	FWHM nm	Intensity mW cm^{-2}
blue (LED-Array, R-Az6)	460	26	15.3 ± 0.4
blue (LED-Array, H-Az11 / C12)	460	26	12.2 ± 0.2
UV (TLC-Lamp, R-Az6)	366	42[a]	0.8 ± 0.4
UV (Thorlabs LED, H-Az11 / C12)	365	9	6.8 ± 0.2

[a] The spectrum of the TLC lamp shows a sharp peak on top of a broad peak. The majority of the intensity is in the broad peak, hence the FWHM of the broad structure is given.

measurement principle are described in 4.4.

The spectrometer was allowed to warm up for 2 h before measurement and spectra were acquired using the following settings: Monochromator slit widths equivalent to 2 nm optical resolution, 1 data point per nm, integration time 1 or 2 s per data point for the spectra shown, 0.2 s for preliminary measurements, common beam depolarizer in the beam (on). The lamp changeover from the tungsten lamp used at long wavelengths to the deuterium lamp used for short wavelengths was at its default value of 319.2 nm. The filters used to suppress higher orders were set to change at their default wavelength. Sample- and reference beam attenuators were not used (set to 100%). The common beam mask was fully open (100%) resulting in a spot size of $4 \times 12\,\mathrm{mm}^2$ on the sample, where the width is controlled by the monochromator slit and the hight is controlled by the common beam mask.

Spectra were recorded for s- and p- polarized light corresponding to nominal rotations of the polarizers of 0° and 90°. At 2 s per data point the total acquisition time for the 220–600 nm range and a single polarization was 13 min.

7.7 Photoisomerization Experiments

DR spectroscopy photoisomerization experiments of SAMs were conducted as follows: After a spectrum of the pristine SAM had been recorded, the sample holder was removed from the spectrometer and placed underneath the respective light source. Then, the sample was illuminated for 10 min in normal incidence and a spectrum of the irradiated SAM was recorded.

The following light sources were used: Blue light was delivered by an LED array intended for decorative purposes (nominal electrical power consumption 2.1 W). The distance was chosen so that the divergent beams of the individual sources overlapped, and the spot appeared visually homogeneous over the full size of the sample.

For the experiments on R-Az6 and mixed R-Az6 SAMs UV light from a TLC lamp (low pressure mercury discharge lamp with fluorescent coating and filter) was used. For the experiments on H-Az11/C12 collimated UV light from a Thorlabs M365L2 LED module with an aspheric condenser lens (f=40 mm) was used. Table 7.2 gives wavelength, spectral width, and intensity on the sample for these sources. The power at the position of the sample surface was measured using a Coherent Fieldmaster powermeter with LM-10 Sensor (diameter of active area 17.8 mm) for the R-Az6 experiments and a Melles Griot 13PEM001 powermeter (diameter of active area 10.0 mm) for the H-Az11/C12 experiments. Wavelength and spectral

Table 7.3: Beamlines and Photon Energy Corrections (in eV).

	beamline	system	$h\nu$ corr. N1s	 C1s
2009, May	U41	CF_3-ImPh (NEXAFS)	0.38	0.26
2009, August	UE52 SGM	R-Az6	-0.31	-0.09
2010, June	UE52 SGM	TBI, CN-AzPh, CF_3-ImPh(XPS)	-0.14	0.07
2011, March	UE52 SGM	H-Az6 (NEXAFS C1s)	0	0.11
2012, June	UE56-2 PGM-2	H-Az11 / C12	0.35	0.26

Table 7.4: XPS Photon Energies (in eV).

	$h\nu$	harmonic
S2p	260	1st
C1s	400	3rd
N1s	500	3rd
O1s	650	3rd

width were obtained from spectra recorded using an Avaspec 2048 spectrometer.

7.8 NEXAFS and XP spectra

Photoelectron spectra and Auger electrons for partial yield NEXAFS were recorded at the synchrotron facility BESSY II using an Omicron EA125 hemispherical electron analyser with a five channel detector. Beamlines and time of measurement for the spectra presented in this work are given in Tab. 7.3. The width of the monochromator excit slit was 20 µm at the UE52 and 30 µm at the UE56 beamlines. The measurement geometries for XPS (Fig. 4.1b) and NEXAFS (Fig. 4.9) have already been shown in the experimental section. Each spectrum was recorded on a different spot in order to minimize radiation damage. All measurements were performed on samples cooled to below 165 K using liquid nitrogen in order to reduce radiation damage further. The exit slit of the electron analyser was in the fully open position for all measurements.

XPS All XP binding energies were referenced to the substrate's Au4f$_{7/2}$ peak at a binding energy of 83.95 eV [65]. XP spectra were recorded using vertically polarized radiation, and the following electron analyser settings: central analyser energy (CAE, path energy) 5 eV, step size 0.05 eV, and dwell time 0.2 s. For C1s spectra one scan was sufficient, for the other elements typically 5 scans measured on the same spot were summed resulting in a total integration time of 1 s per data point. Due to the lower coverage in the TBI experiments more scans were summed: 5 scans for the C1s spectra, 10–25 scans for the N1s spectra. With these settings the energy resolution was limited by the electron analyser. Table 7.4 gives photon energies and diffraction order of the beamline monochromator used for XPS.

Quantitative XPS measurements of the mixed SAMs series were performed at room temperature in a laboratory UHV setup equipped with a monochromatized X-ray source (VG Scienta MX650, Al Kα, $h\nu$=1486.7 eV) and a high-resolution hemispherical electron analyzer (VG Scienta SES-200). The radiation was focused on a sample area of $3 \times 9\,\mathrm{mm}^2$. The measurement geometry is given in Fig. 4.1a. The total energy resolution was better than 0.4 eV.

Table 7.5: NEXAFS Normalization Parameters.

		normalization intervals left	normalization intervals right	interval for carbon dip corr.
R-Az6	N1s	396.0–397.0	419.5–420.5	—
	C1s	280.0–281.0	328.0–329.0	280.0–281.0
CN-AzPh/ CF_3-ImPh	N1s	396.0–397.0	419.5–420.5	—
	C1s	280.1–281.1	328.0–329.0	not corr.
H-Az11 / C12	N1s	395.9–396.9	424.4–425.4	—
	C1s	280.3–281.3	328.3–329.3	280.3–281.3
TBI	N1s	396.0–397.0	419.5–420.5	—
	C1s	280.0–281.0	328.0–329.0	280.0–281.0

NEXAFS Both C1s and N1s spectra were recorded using horizontally polarized light of the 1st harmonic of the beamline monochromator. To detect the Auger electrons the analyser's pass energy was set to its maximum value of 50 eV for maximum transmission. This setting corresponds to a 5 eV wide electron energy detection window (Fig. 4.10). Spectra were recorded at nominal electron kinetic energies, i.e. not corrected for the analyser work function, of 259 eV for C1s and 377 eV for N1s spectra. A Hamamatsu G2119-01 photodiode with $10 \times 10\,\mathrm{mm}^2$ active area connected to a Keithley Model 6514 Electrometer was used to measure the X-ray flux. The photon energy was scanned stepwise, integration time was 1 s per data point. Generally the LUMO region (C1s: 280–295 eV, N1s: 392–410 eV) was scanned with 0.1 eV, the rest of the spectrum (C1s: 294–330 eV, N1s: 409–430 eV) with 0.5 eV steps. The total acquisition time is significantly larger than the sum of the integration times due to time required for the measurement of the diode current and the movements of monochromator and undulator. Thus, it took about 20 min to record a C1s scan.

The parameters used for the normalization of the spectra are given in Tab. 7.5. For the carbon dip correction described in Sec. 4.2.3.3, resonant photoemission (RPE) spectra were recorded after each NEXAFS scan at 281 eV photon energy with the following analyser settings: CAE 50 eV (same as for NEXAFS scan), nominal electron energy range 250–285 eV, dwell time 0.2 s, and step size 0.5 eV. The integration intervals for the RPE spectra are given in Tab. 7.5. For all measurements a degree of polarization P=0.96 was assumed for the synchrotron radiation.

Sample rotations β for near p-polarized geometries (Fig. 4.9) and intervals for the determination of the molecular orientations α are given in Tab. 7.6.

Photon Energy Calibration C1s Spectra were referenced to the $\pi^\star$ resonance of highly oriented pyrolytic graphite (HOPG) at 285.38 eV as described in Sec. 4.2.4 (beamtimes 2012-06, 2011-03). For beamtimes where no measurement of HOPG was available, spectra of a SAM that was also measured in one of the beamtimes with HOPG reference were manually aligned to the corrected spectra and the offset determined that way.

For N1s spectra no absolute reference measurements were available. For comparison, all spectra were referenced arbitrarily to the beamtime 2011-03.

Table 7.6: NEXAFS Parmeteres for Determination of Orientational Angle α.

		interval for determination of α		β (p-pol)
R-Az6	N1s	398.5–399.0		18.5°
	C1s	284.5–285.8		
H-Az6	C1s			1°
CN-AzPh	N1s	398.2–398.7		20°
	N1s (CN)	399.4–400.0		
	C1s	284.4–285.7		
CF_3-ImPh	N1s	397.6–398.7		10°
	C1s	284.8–286.1		
H-Az11 / C12	N1s	397.4–398.9		0°
	C1s	284.8–286.1		
TBI		(LUMO)	(LUMO+3)	18.5°
–Layer M	N1s	397.1–399.0	400.5–402.1	
–Layer C	N1s	398.0–399.2	400.7–402.5	
–Layer T	N1s	396.9–399.1	401.2–402.9	
–Layer T	C1s	284.0–286.3		

Appendix A

Evaporator for Organic Molecules

Abstract

A new miniature evaporation source for deposition of thin films of organic molecules in UHV operating in the temperature range of 60°C–250°C is presented. Design goals were the use of miniature crucibles allowing stable operation with sub-mg fillings and the exact temperature control of the crucible while maintaining easy exchange of crucibles. The design is based on a copper cylinder electrically isolated by a 0.1 mm thin boron-silicate glass sleeve from a heating filament made of a high-temperature spring alloy. An inexpensive boron-silicate glass crucible with only 2.4 mm inner diameter is thermally coupled to the copper cylinder by a peace of aluminium foil. 2 crucibles can be fitted onto a DN40CF base flange. This design is based on nonradiative heat transport, and thus requires reduced filament temperatures thereby eliminating the need for a water cooled shield. We present temperature measurements performed in the crucible demonstrating the excellent thermal coupling. A stable deposition rate is reached within 5 min after the set temperature is reached. In addition, we show the thickness distributions of layers prepared using the device. The thickness distributions were obtained by a novel method based on the optical absorbance of dye layers deposited on transparent substrates measured using an inexpensive flatbed scanner.

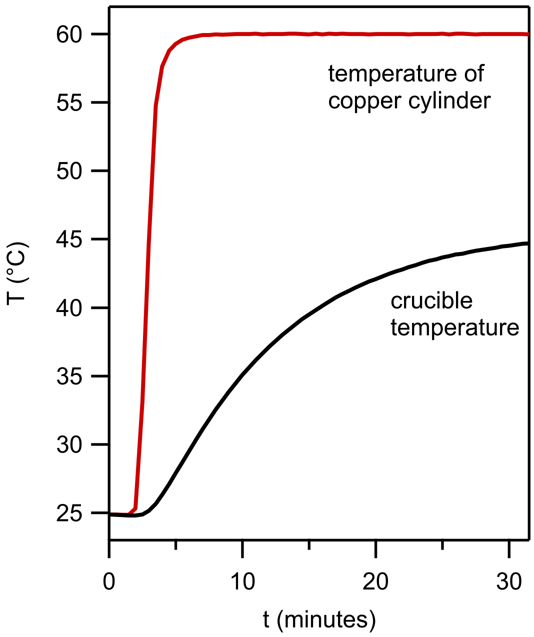

Figure A.1: Temperature in the crucible and at the heating element for the proposed design without thermal conductor to fill the gap.

A.1 Introduction

The fabrication of thin layers of organic compounds in a regime of (sub-) monolayers to a few nm thickness becomes increasingly important in current research, such as molecular switches or organic semiconductors. In basic research commonly small samples of about 10 mm diameter are employed, new compounds are often only available in small quantities, several compounds shall be evaporated interchangeably, and compounds of interest may degrade during the optimization of the deposition. Thus, evaporators that can be refilled and baked without breaking the vacuum of the analytical system are required. They should posses easily exchangeable crucibles, preferably made of quartz or glass to avoid reactions with a wide variety of evaporants. The crucibles should be of miniature size to allow stable operation with sub-mg fillings and several crucibles should fit onto a single DN40CF flange. Many compounds need to be evaporated at relatively low temperatures of 60–250 °C. Most evaporators are designed to operate at higher temperatures and rely on radiative heat transport, which becomes ineffective at these low temperatures. Therefore, special solutions are required.

A key element for a stable deposition rate is a stable temperature in the crucible, because the deposition rate depends exponentially on the crucible temperature. PID controllers make it easy to stabilize the temperature at the point of measurement. In many designs aimed at higher temperature ranges, the temperature is not measured directly at the crucible but at some element close to it. Radiative heat transport quickly leads to a thermal equilibrium between the crucible and the measurement point. Thus, a stable temperature at the measurement point corresponds to a stable temperature in the crucible and will lead to a stable deposition rate. When such devices are used at lower temperatures than intended, thermal equilibrium is reached only slowly and it is difficult to obtain a stable rate.

In a common set-up[1] a crucible is inserted into a graphite heating-element. There is a minimal gap between crucible and heating element. At higher temperatures

---

[1] Miniature Knudsen-Cell (K-Cell), tectra GmbH, Frankfurt/M, Germany

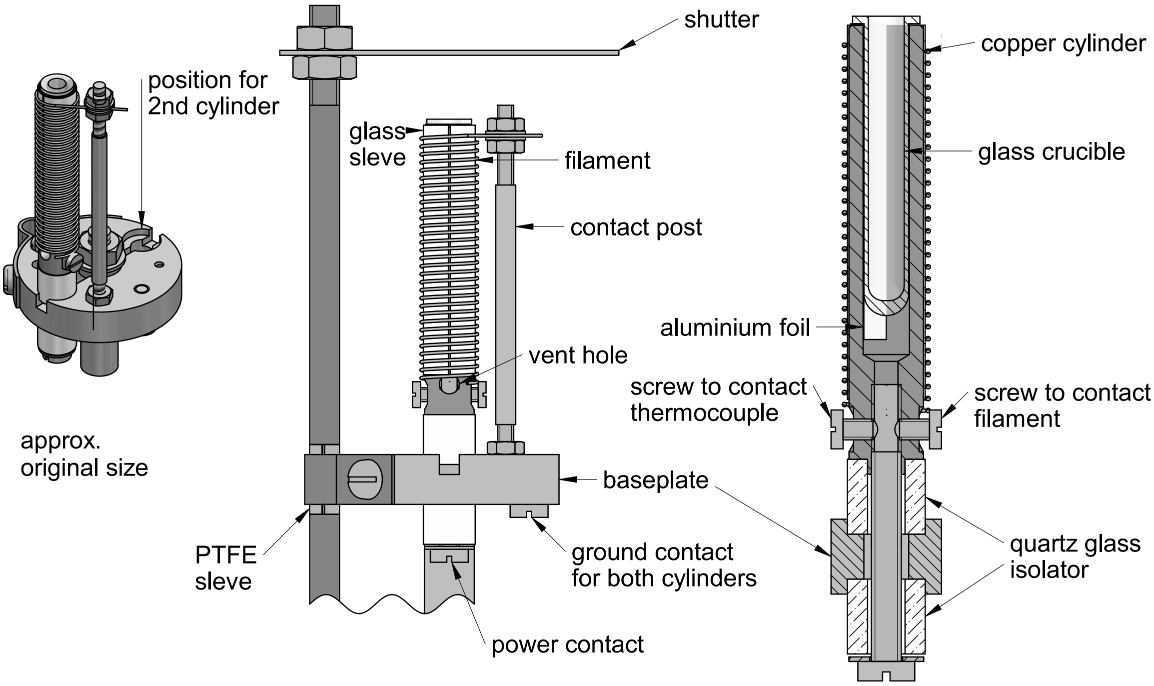

Figure A.2: Evaporator head.

thermal radiation nontheless ensures effective heat transport and the temperature measured at the heating element is representative for the crucible. At lower temperatures the inevitable gap between heating element and crucible in such designs inhibits fast thermal equilibration. This effect is shown strikingly in Fig. A.1, which compares the temperature in the crucible to that of the heating element. In order to use such a design at lower temperatures some flexible heat conductor is required to fill the gap. In a commercial design for the temperature range 15–300 ℃[2] a liquid metal conductor is used to couple a quartz crucible to the heating element. Here we present a simpler design where a miniature crucible is effectively coupled to the heating element by crumpled aluminium foil. The design is entirely based on nonradiative heat transport and can therefore be used without a water cooled shield.

A.2 Evaporator Design

Evaporator Head Figure A.2 shows the evaporator head. The baseplate is mounted electrically isolated from the chamber and can accommodate 2 cylindrical heating elements. Each heating element consists of a copper cylinder, which is electrically and thermally isolated by a quartz tube section from the base plate. Quartz rather than alumina was chosen for its about 10-fold lower thermal conductivity [41]. A slotted, 0.1 mm thin borosilicate glass sleeve electrically isolates the copper cylinder from the filament, whereas the spring force of the sleeve ensures tight thermal contact. The filament is wound to a slightly smaller diameter than the copper cylinder and is held in tight contact by its spring force. It is made from a high-temperature spring alloy, which does not loose its resilience during operation. One end of the filament is screwed to the copper cylinder, which in turn is connected to the supply lead

---

[2] Organic Material Effusion Cell (OME), Dr. Eberl, MBE Komponenten GmbH, Weil der Stadt, Germany

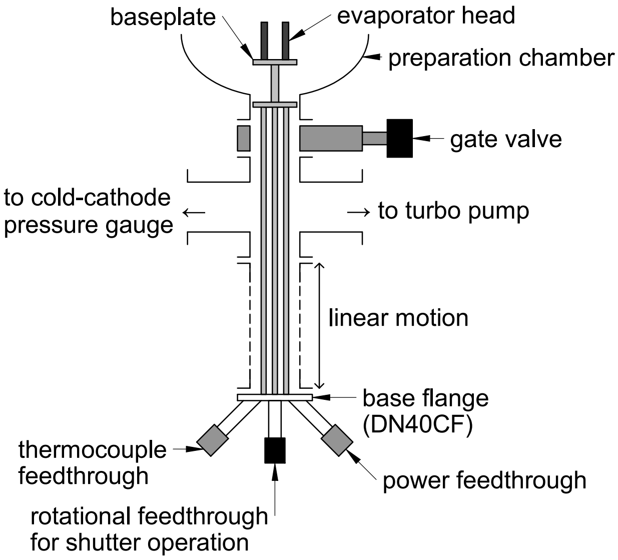

Figure A.3: Evaporator system.

by the same screw that holds it mechanically. The other end of the filament is connected to the baseplate via a contact post placed besides the heating element. The temperature of the copper cylinder is measured by a type K thermocouple screwed to the coper cylinder. A shutter is held by a bracket at the side of the baseplate, electrically insulated by a piece of slotted PTFE.

A glass crucible with 2.4 mm inner diameter is thermally coupled to the copper cylinder by a piece of crumpled aluminium foil as described in Sec. A.3. The thermal coupling achieved this way is so good that the temperature measured at the copper cylinder is representative for the crucible. Hence, it is not necessary to attach a thermocouple to the crucible itself.

Evaporator System The evaporator head is integrated into an assembly, which is connected via a gate valve to the preparation chamber and can be pumped and baked separately (Fig. A.3). A linear motion allows to move the evaporator into the preparation chamber for deposition.

The baseplate of the evaporator head is mounted electrically isolated via a tripodal structure to the DN40CF base flange, which accommodates a magnetically coupled rotational feedthrough for the shutter, a thermocouple, and a power feedthrough—all on NW16CF flanges. Because the evaporator system has to be detached from the preparation chamber each time the crucibles have to be changed, good mechanical protection of the feedthroughs is important. Therefore, feedthroughs with MIL-C-5015 type connectors (6 pin) on the air side were chosen. Even though it would be possible to make all connections via a single feedthrough,[3] 2 separate feedthroughs were chosen for ease of assembly.

This assembly is inserted into a linear motion, which is connected via a DN40CF cross piece and the gate valve to the preparation chamber. With the linear motion fully extended the evaporator head sits below the gate valve. The evaporator system

---

[3] A MIL-C-5015 K type thermocouple feedthrough could be used for both: power connections and temperature control. In this case the power connections had to be made via the alumel pins of the thermocouple pairs leaving the corresponding chromel pins unused. Thus, a 6 pin feedthrough would accommodate power connections for 1 heating element and 1 thermocouple and a 10 pin feedthrough would accommodate power connections for 2 heating elements (3 alumel pins) and 2 thermocouples.

operation up to 150 °C:	
current	0.38 A
voltage at filament	4.1 V
operation up to 250 °C:	
current	0.50 A
voltage at filament	5.5 V
proportional band	7 K
integral time	34 s
derivative time	6 s
PWM cycle time	0.5 s

Table A.1: Electrical and PID parameters.

is pumped by a turbo pump (DN63CF) connected via an adapter to the cross piece and the pressure is measured using a cold-cathode pressure gauge.

Controller The temperature is controlled by pulse width modulation (PWM) of a DC current using a Eurotherm 3508 temperature controller directly connected to a solid state relay[4], which modulates the output of an adjustable laboratory power supply. Alternatively, the evaporator was controlled via a controllable power supply connected to the analogue output of the PID controller. For operation up to 250 °C, the unmodulated current was adjusted below the point where the onset of red-glow of the filament becomes visible on the cylinder in complete darkness. For operation up to 150 °C lower currents are sufficient. Care has to be taken not to heat the filament too much as it may relax and loose its springiness at too high temperatures. PID parameters were obtained using the auto-tune function of the controller. Typical values for the electrical and PID parameters are given in Tab. A.1.

A.3 Operation

Preparation for Deposition Before filling the crucibles the evaporator system was backed at 150°C for 24 h. After cool down a pressure below 1×10^{-9} mbar was reached in the evaporator system.

In order to fill the crucibles the evaporator system was vented via the flood valve of the turbo pump, the turbo pump was removed and the evaporator system was detached below the gate valve. The crucibles were removed, filled ≈ 2 mm high with the evaporant, and inserted with a fresh piece of aluminium foil as described below. Thereafter, the system was remounted, evacuated and baked at a temperature below the evaporation temperature. Due to the reduced bake-out temperature longer bake-out times were used. For example, for the depositon of TBI at a crucible temperature of 85°C (Sec. 7.3) the system was baked for 36 h at 65°C (measured at crucible). After the bake out, while the walls of the system were still warm, the evaporator was repeatedly heated at maximum power to the desired evaporation temperature and allowed to cool down in order to degas the system.

Deposition For deposition, the crucible was heated to the desired temperature. Then the gate valve to the preparation chamber was opened, the evaporator was moved into the chamber into deposition position (typical distance from sample to

---

[4] Crydom MPDCD3

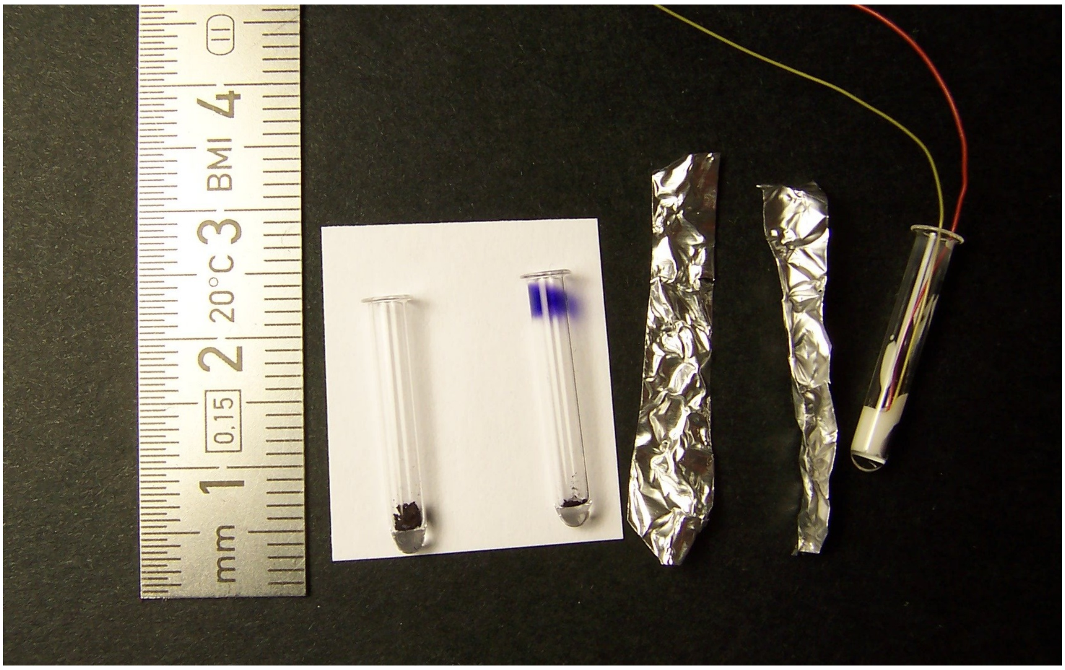

Figure A.4: Crucible after deposition of the test dye, crucible after deposition with insufficient thermal contact, aluminium foil used as flexible thermal conductor, pre-formed aluminium foil, crucible with type K thermocouple glued to the bottom (from left to right).

crucible opening: 70–90 mm), and the shutter was opened to measure the deposition rate or start the deposition. When the calculated deposition time had elapsed, the shutter was closed, the heating of the evaporator was turned off, the evaporator was retracted from the preparation chamber, and the gate valve was closed.

Mounting the Crucible A piece of aluminium foil[5] is crumpled up and straightened again. From the so-prepared foil a piece of approximately 5 mm × 30 mm is cut (Fig. A.4). The foil is then pre-wound around an 1.5 mm Allen key and inserted into the copper cylinder. Then the crucible is forced into the assembly, while the foil is still held at the outer end. The excess foil is torn off at the edge of the lip of the crucible. Generally, for ease of handling 20 µm thick aluminium foil was used, however, we achieved an equally well thermal coupling with foils of 15 µm and 30 µm thickness. In order to ensure the best possible thermal contact, the foil should be cut to the largest width that still allows the crucible to be pressed into the cylinder. Use a new piece of foil for each remount. Condensation of the evaporant near the rim is a sign for insufficient thermal contact (Fig. A.4).

A.4 Performance

A.4.1 Temperature Control and Rate Stability

In order to measure the temperature in the crucible a type K thermocouple made from ⌀ 0.08 mm wire was glued to the bottom of a crucible using Loctite Hysol 9492 epoxy adhesive (Fig. A.4). The epoxy was cured for 5 h at 150 °C. The temperature

---

[5] Al-content > 99%, 20 µm×450 mm×150 m, Carl Roth GmbH + Co. KG, Karlsruhe, Germany, Art. No. 0954.1

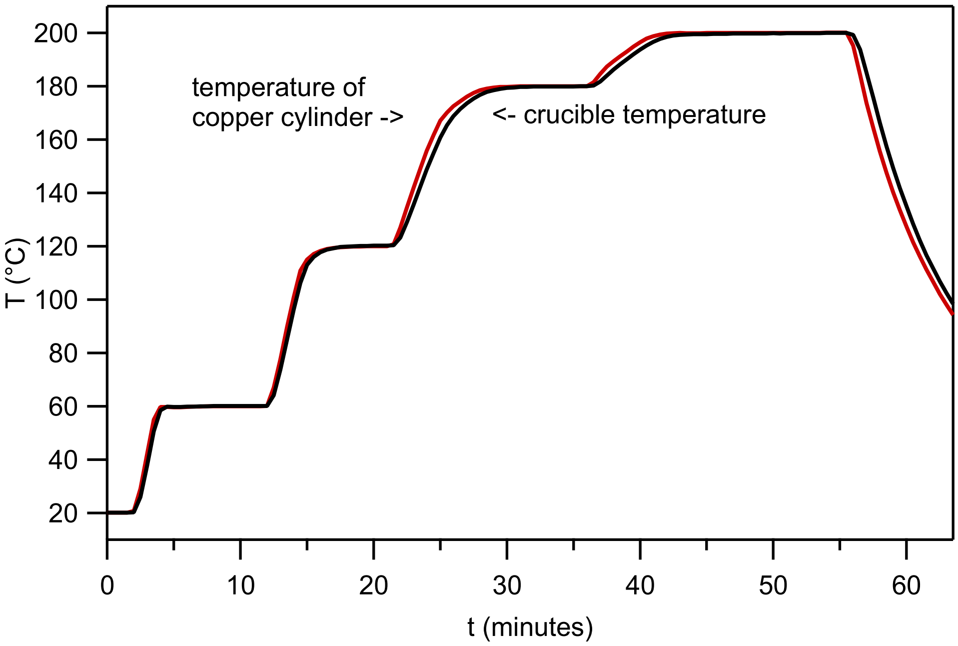

Figure A.5: Temperature in the crucible and in the copper cylinder during a heat-up cycle for a crucible mounted with aluminium foil as thermal conductor.

in the crucible was recorded using a second Eurotherm 3508 temperature controller. The measurements were conducted at a pressure of 10^{-6} mbar. An apparent temperature difference of $\approx 1\,\mathrm{K}$ between the crucible and at the copper cylinder was observed at room temperature (in thermal equilibrium). In the data shown, it was corrected by adding a constant offset.

Figure A.1 shows the temperature at the copper cylinder and in the crucible for a crucible inserted into the copper cylinder *without* aluminium foil. The temperature in the crucible only slowly approaches an equilibrium well below the desired temperature. In this situation it will take long until a stable deposition rate is obtained and the temperature at the copper cylinder is not a good measure for the actual temperature in the crucible. In contrast, when the crucible is mounted *with* aluminium foil, it is thermally coupled well to the copper cylinder (Fig. A.5). Thus, the temperature in the crucible almost instantaneously follows that of the copper cylinder and the temperature measured at the copper cylinder is representative for the crucible temperature. The good temperature control indeed quickly leads to a stable rate as is shown in Fig. A.6: Only 5 minutes after the heating element has reached the set temperature a stable rate is obtained.

A.4.2 Thickness Distribution

In order to estimate the homogeneity of the deposited layers it is important to know the spatial thickness distribution of layers produced using the device. To obtain this information, a test dye was evaporated onto microscope slides and the thickness was measured as absorbance of the so-prepared layers (Sec. A.5). Figure A.7 shows the thickness distributions for layers prepared on samples mounted in various distances l to the opening of the crucible. Independent of the distance l, the distributions exhibit a homogeneous plateau corresponding to the width of the crucible (2.4 mm). Outside the plateau the layer thickness rapidly declines. This behaviour is typical for tubular crucibles. For a crucible to sample distance of $l = 83\,\mathrm{mm}$, the thickness

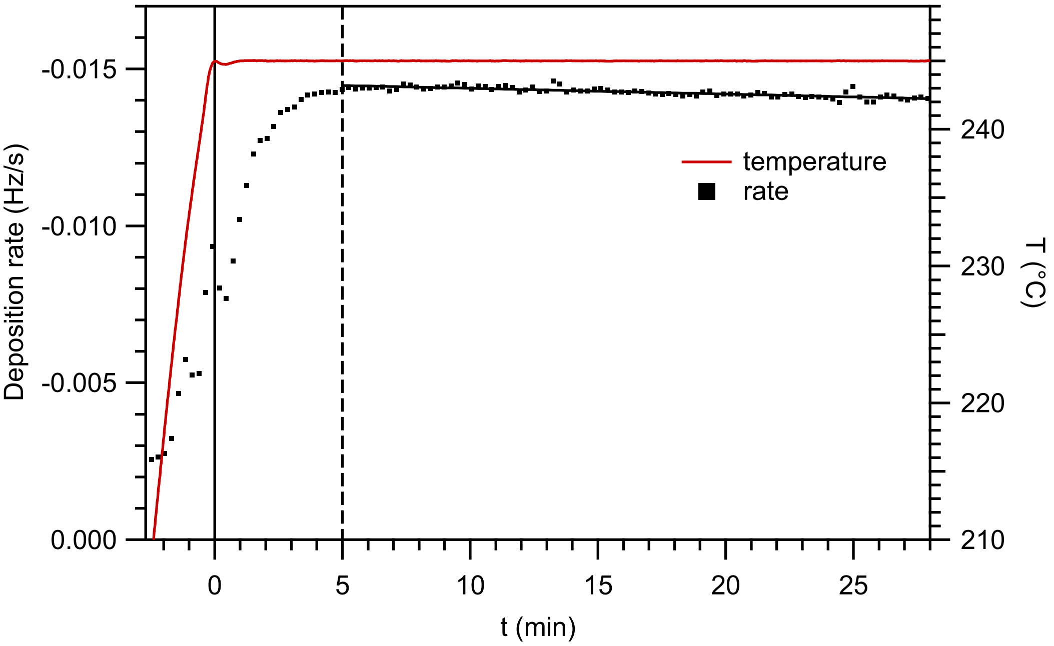

Figure A.6: Temperature and deposition rate as a function of time: The black solid line is a linear fit to the rate. 5 minutes after the evaporator has reached the set temperature, a stable rate is obtained, which drops linearly by only 2.5% within 20 minutes. Evaporant: α-sexithiophene, set crucible temperature: 245 °C, rate recorded using a quartz microbalance with standard 6 MHz gold coated quartz sensor connected to a Sycon Instruments STM-2XM/MF controller. The recorded frequency was averaged in 16 s intervals and differentiated to obtain the rate.

at the border is 95% of that in the centre for a 5 mm diameter sample and 83% for a 10 mm diameter sample. For the measurements shown, care was taken not to contaminate the crucible walls when filling it with the test dye. As material sticking to the walls widens the distribution, the homogeneity given above is a lower limit for the expected homogeneity in normal operation.

If larger areas of homogeneous deposition are required, shorter crucibles could be used. Another possibility may be to insert a quartz wool plug into the opening of the crucible. This approach is currently followed in our group in order to keep the evaporant in the crucible when the evaporator is mounted horizontally. However, no measurements of the thickness distribution of this set-up were made so far.

A.5 Measuring the Thickness Distribution

To measure the thickness distribution of evaporated layers is nontrivial. Thickness distributions measured using a quartz microbalance moved in the sample plane are broadened by the finite size of the sensor (14 mm for typical 6 MHz sensors), which is even larger than the size of typical samples for the intended use of the evaporator. Interferometric methods require substrates with thickness variations much smaller than the differences to be detected and expensive equipment not typically available in UHV laboratories.

Here we present a method based on measuring the absorbance of dye layers evaporated onto microscope slides using an inexpensive flatbed scanner, which allows scans in transmission mode. For solutions the Beer-Lambert law, i.e. the proportionality between the thickness of the liquid and its absorbance can generally be

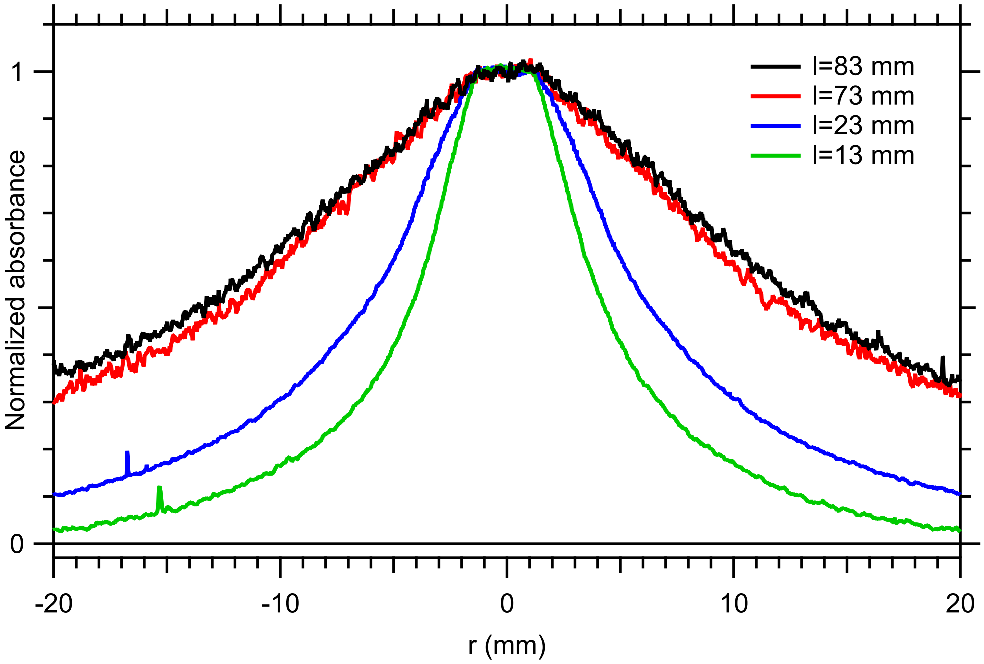

Figure A.7: Thickness distributions measured as absorbances of the layers for samples in various distances l to the crucible opening.

assumed. For solid layers, however, changes in the reflective properties or scattering due to nonideal layer growth might render this relationship invalid.

For the intended use of the evaporator—the preparation of layers of only a few monolayers—it can be assumed that the device is operated in a regime where collisions in the gas phase are not relevant for the shape of the thickness distribution. However, for the samples used to measure the distribution, macroscopic amounts of dye had to be evaporated in order to obtain sufficient absorbance. This requires larger deposition rates, which correspond to higher pressures in the crucible that may lead to a broadening of the thickness distribution.

In the following we will present the method, show that the absorbance is sufficiently proportional to the thickness, and evaluate the limit until which pressure broadening does not influence the distribution.

Method The dye 2,9,16,23-tetra-*tert*-butyl-29H,31H-phthalocyanine [6] was used in the evaporation experiments as obtained. The experiments were performed without bake out of the chamber or the evaporator at a pressure of $< 2 \cdot 10^{-7}\,\mathrm{mbar}$. The dye was evaporated onto microscope slides, which were at room temperature. The crucibles were filled $\approx 2\,\mathrm{mm}$ high. Material sticking to the walls of the crucibles leads to a broadening of the thickness distribution. This was avoided by filling the crucibles through a 1.8 mm o.d. cannula. For each experiment a fresh crucible was used, because evaporation rates decreased significantly over the extended evaporation times of up to 16 h. We attribute this to the fact that smaller particles are consumed more rapidly than larger ones, and thus the surface at which sublimation takes place is reduced.

The absorbance profiles were obtained from scans performed using a Canon Canoscan 8400F flatbed scanner, which allows scans in transmission mode. Paper labels

---

[6] 97%, CAS [35984-93-1], Sigma-Aldrich, Art. No. 423157

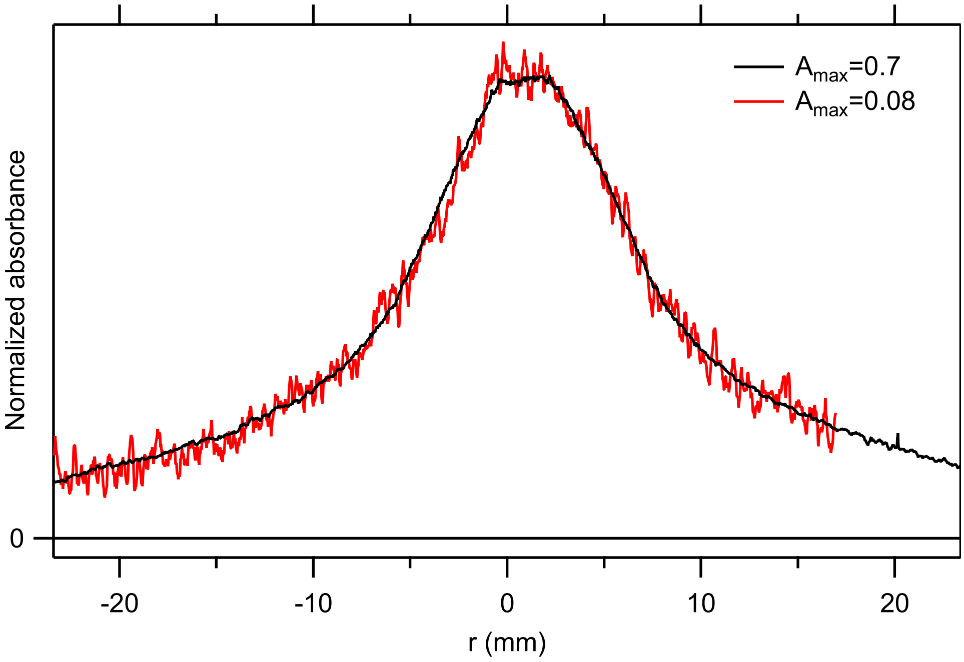

Figure A.8: Linearity of the absorbance with the layer thickness: Normalized absorbance profiles of samples with a maximum absorbance A_{max} differing by one order of magnitude. The agreement of the profiles verifies that the absorbance of the dye layer is proportional to its thickness. Crucible temperature: 150 ℃.

were attached to both ends of the microscopy slides in order to lift them off the glass plate of the scanner to avoid Newton's rings. Samples were scanned at a resolution of 1200 dpi, with the gamma value set to γ=1, and all image optimization turned off. For the analysis, the green channels of the images were used. The position of the maximum of the absorbance was determined by fitting a 2-dimensional Gaussian. Profiles were obtained along sections trough the maximum. The profiles are means of 5 points perpendicular to the direction of the section. The brightness values I were converted to absorbances A using

$$A = -\lg \frac{I}{I_0}, \tag{A.1}$$

where I_0 is a white value obtained as the mean of the brightness values of an uncoated region on the sample. The sections were normalized to a mean around the maximum.

Linearity of the Absorbance The linearity of the absorbance obtained using the scanner was confirmed by scanning a stepped gray wedge. In order to show that the proportionality between layer thickness and absorbance is sufficient for our purpose, we prepared two layers: one with approx. 10-fold the thickness of the other. Figure A.8 shows that their normalized absorbance profiles are in excellent agreement. As a nonlinearity in the absorbance would have lead to a distortion of the shape depending on the absolute absorbance, we have shown that the absorbance is sufficiently linear with thickness.

Pressure Broadening Figure A.9 shows that at the crucible temperatures used in these experiments no significant broadening of the profiles due to excessive pressure

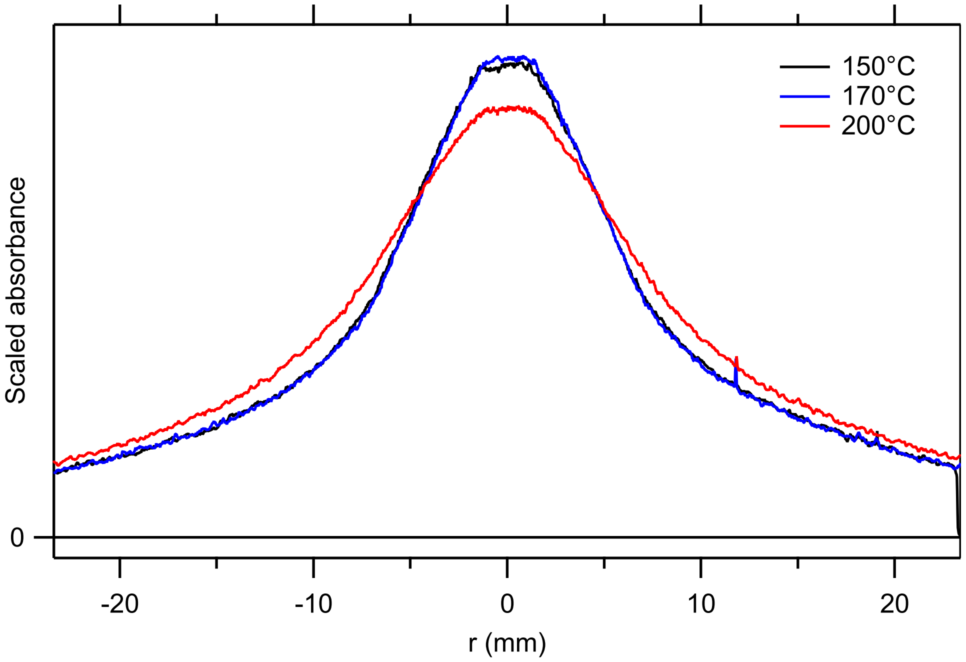

Figure A.9: Pressure broadening of the thickness profile: Absorbance profiles of samples prepared at different crucible temperatures in otherwise identical conditions. All profiles were scaled onto the profile at 150℃ by a least-squares fit.

in the crucible occurs: Profiles of samples prepared at 150 ℃ and 170 ℃ agree well, whereas a profile of a sample prepared at 200 ℃ shows significant broadening.

A.6 Acknowledgement

The author wants to thank Dr. W. Freyer, who suggested the test dye, R. Pesslin, who suggested the use of the Inconel alloy used for the filament and who manufactured the copper cylinders, and R. Grosser, who reassembled and rewired the evaporator innumerous times. S. Kijak prepared the samples for Fig. A.7. I thank K. Zielke and W. Bronsch for allowing me to record the data presented in Fig. A.6 at their set-up and Dr. M. Bernien for proof-reading of this appendix.

A.7 Drawings and Assembly Notes

A.7.1 Assembly and Manufacturing Notes

Dimensions Due to the tolerances of the ceramic and glass parts the following dimensions have to be adjusted to the measured dimensions of these parts: The diameter of the copper cylinder needs to be slightly larger than the inner diameter of the glass sleeve to ensure a firm contact. The counterbores in the baseplate need to be adjusted in order to center the quartz and ceramic isolators properly.

Mounting the Glass Sleeve The copper cylinder possesses a chamfer at the rim to aid insertion. It is wetted with a few drops of isopropyl alkohol for lubrication and forced top-first into the glass sleeve.

Mounting the Baseplate to the Central Pole Take care to centre the screw so that no electrical contact is made to the baseplate.

Mounting the Copper Cylinder Assembly to the Baseplate The copper cylinder is mounted as shown in the drawing. The cable to connect it to the power supply is inserted between the screw-head and the metal washer. Take care to centre the screw so that no electrical contact is made to the baseplate.

Filament The filament was made from ⌀ 0.3 mm 2.4669 (Inconel X750) wire[7] by winding the wire around an M5 thread on the lathe. Alternatively filaments can be custom made by spring manufacturers. To mount the filament it is widened by partially unwinding it, pushed over the copper cylinder assembly, and is allowed to snap back.

Thermocouples and Electrical Connections Thermocouple wires were ⌀ 0.25 mm single strand PFA insulated type K.[8] The thermocouple is formed by spot-welding, the excess wire is trimmed behind the weld spot, and the thermocouple is screwed to the copper cylinder. Note that it must not touch the filament. Electrical connections were made by ⌀0.5 mm diameter single strand, PFA insulated copper wire.

---

[7] Obtained from Vogelsang Edelstähle, Hagen, Germany

[8] OMEGA Engineering, INC., Stamford, Connecticut, USA, Art. No. IEC-TFCY-010 and IEC-TFAL-010

A.7.2 Assembly and Bill of Materials

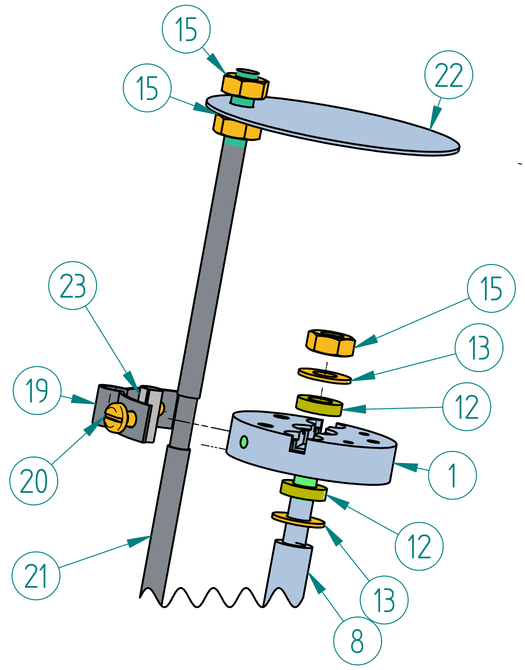

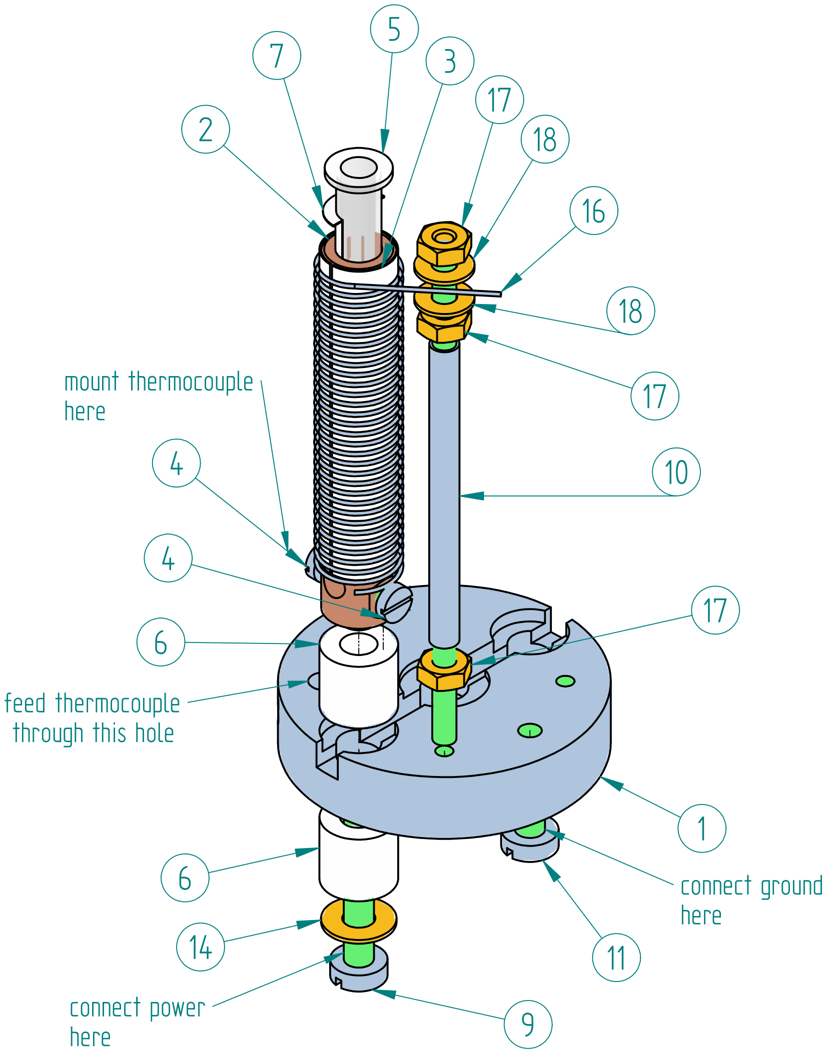

Pos.	Title	Qty.	Pos.	Title	Qty.
1	base plate	1	13	Washer ISO 7089 – 3 – A2	2
2	copper cylinder	**1**	14	Washer ISO 7089 – 2 – A2	1
3	glass sleve	**1**	15	Hexagon nut ISO 4032 – M3 – 6 – A2	3
4	Screw ISO 1207 – M1.4 x 2 – A2	**2**	16	filament	**1**
5	crucible	**1**	17	Hexagon nut ISO 4032 – M1.6 – A2	**3**
6	fused silica tube section	**2**	18	Washer ISO 7089 – 1.6 – A2	**2**
7	aluminium foil	**1**	19	shutter guide	1
8	central pole	1	20	Screw ISO 1580 – M2 x 3 – A2	2
9	Screw ISO 1207 – M2 x 12 – A2	**1**	21	shutter pole	1
10	contact pole	**1**	22	shutter	1
11	Screw ISO 1207 – M2 x 5 – A2	1	23	PTFE tube section, slotted	1
12	ceramic washer for M3	2			

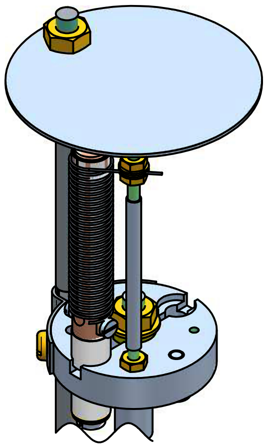

Double quantities in **bold** if two heating elemensts are required

A.7.3 Ceramics and Glass Parts

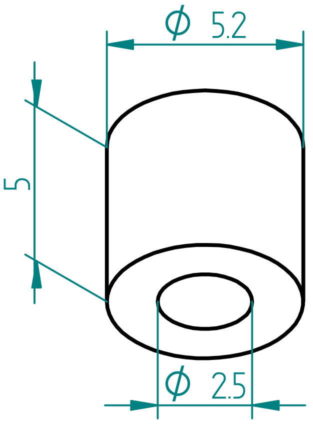

fused silica tube section

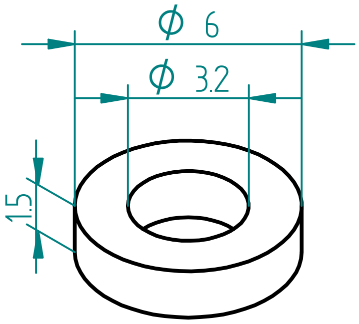

ceramic washer for M3
aluminium oxide ceramics
tectra GmbH, Frankfurt/M, Germany

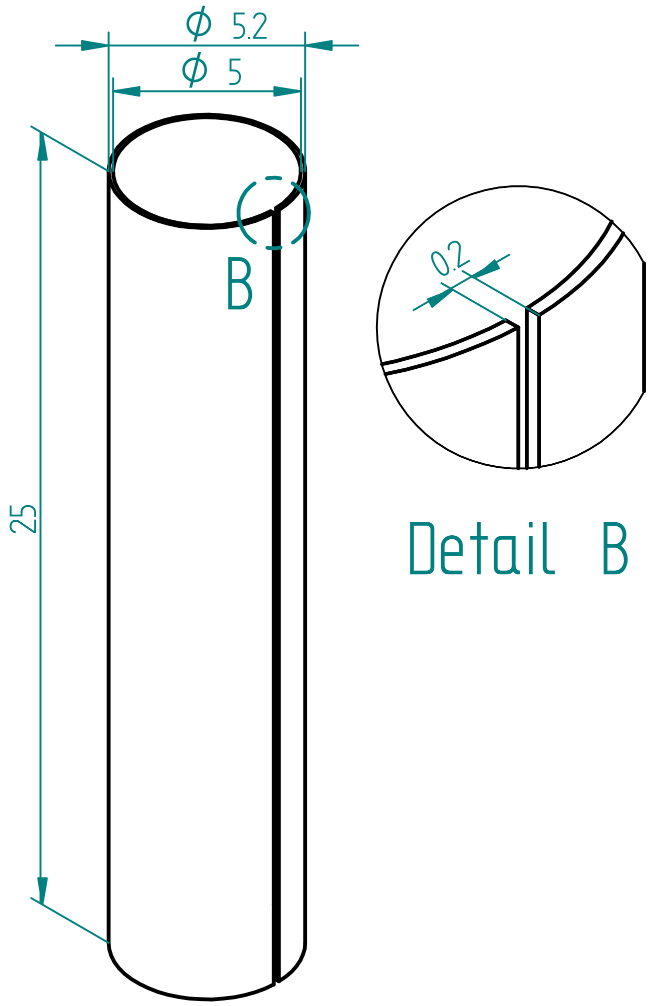

glass sleve
Borosilicat glass 3.3, laser cut
Hilgenberg GmbH, Malsfeld, Germany
(custom made)

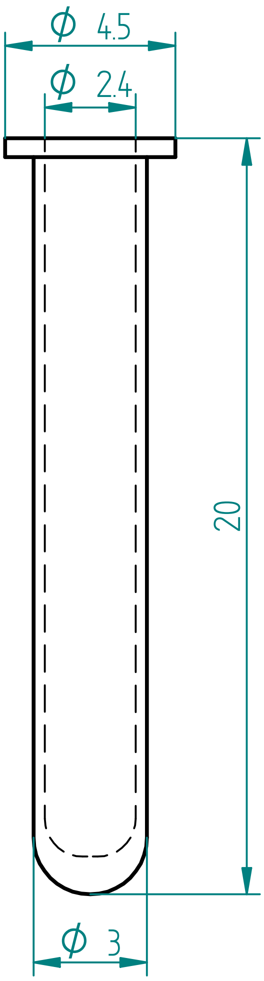

crucible (Mikroreagenzgläser mit aufgebördeltem Rand)
Borosilicat glass 3.3
Hilgenberg GmbH, Malsfeld, Germany
(custom made)

5:1

A.7.4 Stainless Steel Parts, PTFE Sleve and Filament

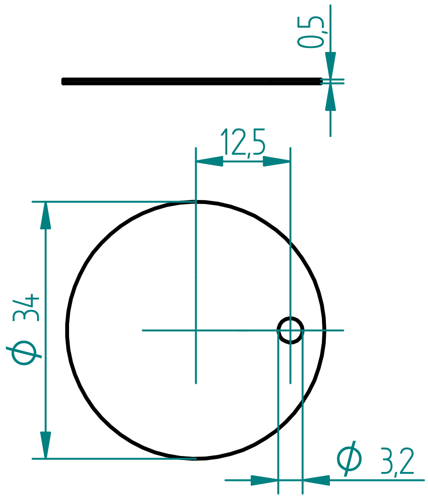

shutter
stainless steel

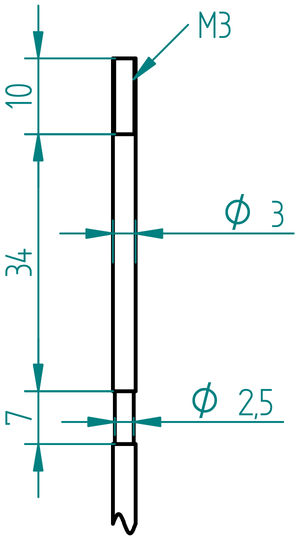

shutter pole
stainless steel

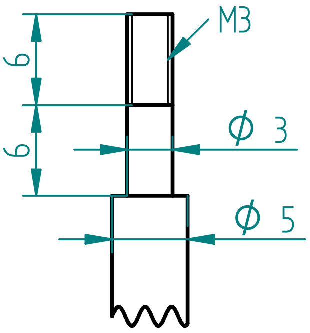

central pole
stainless steel

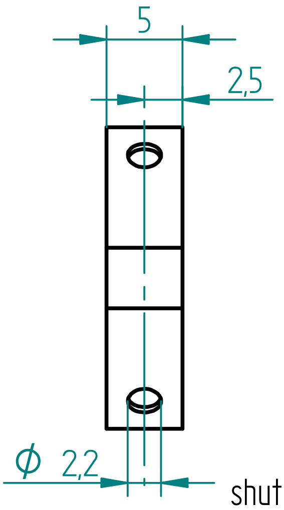

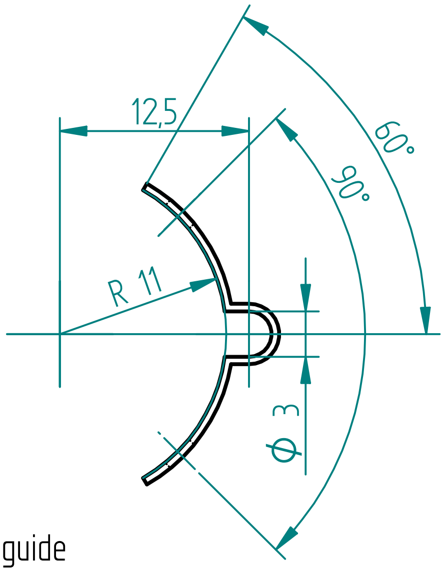

shutter guide
stainless steel

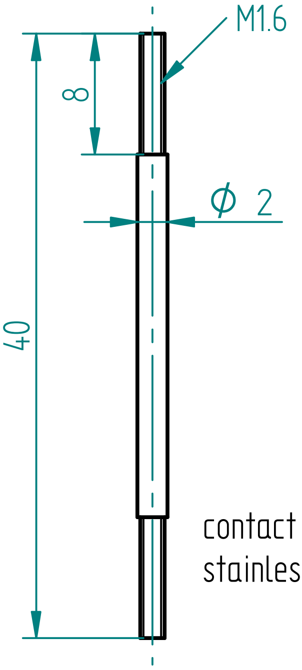

contact pole
stainless steel

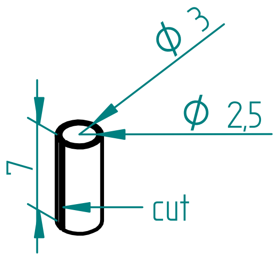

PTFE tube section, slotted

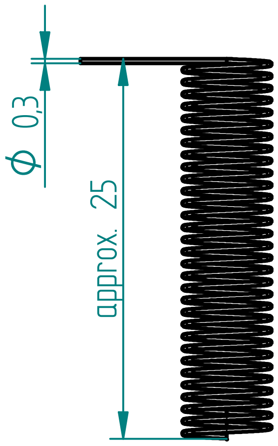

filament
2.4669 (Inconel X750) wire
wound around an M5 thread

A.7.5 Copper Cylinder

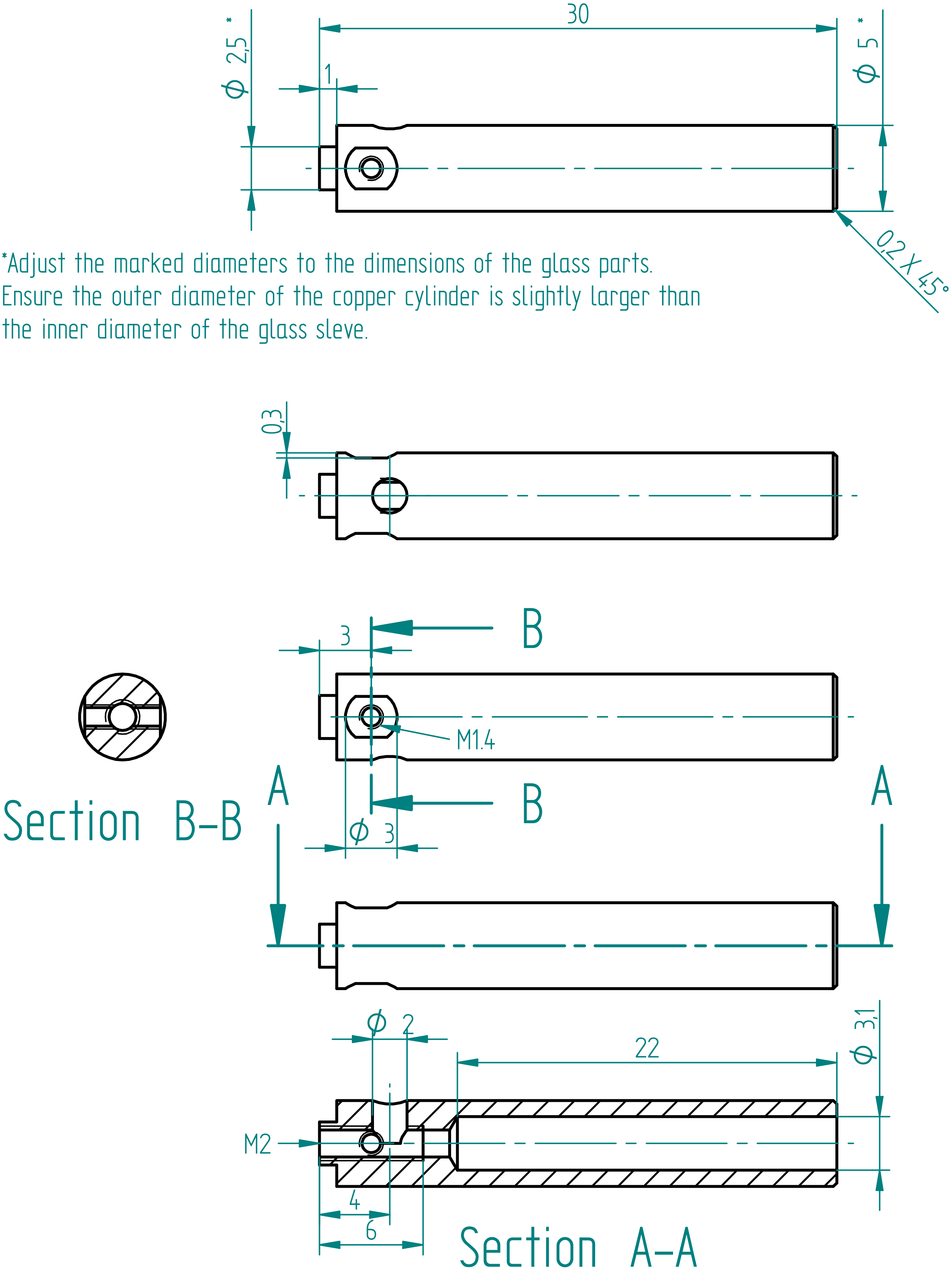

*Adjust the marked diameters to the dimensions of the glass parts.
Ensure the outer diameter of the copper cylinder is slightly larger than
the inner diameter of the glass sleve.

copper cylinder
OFHC copper

3:1

A.7.6 Base Plate

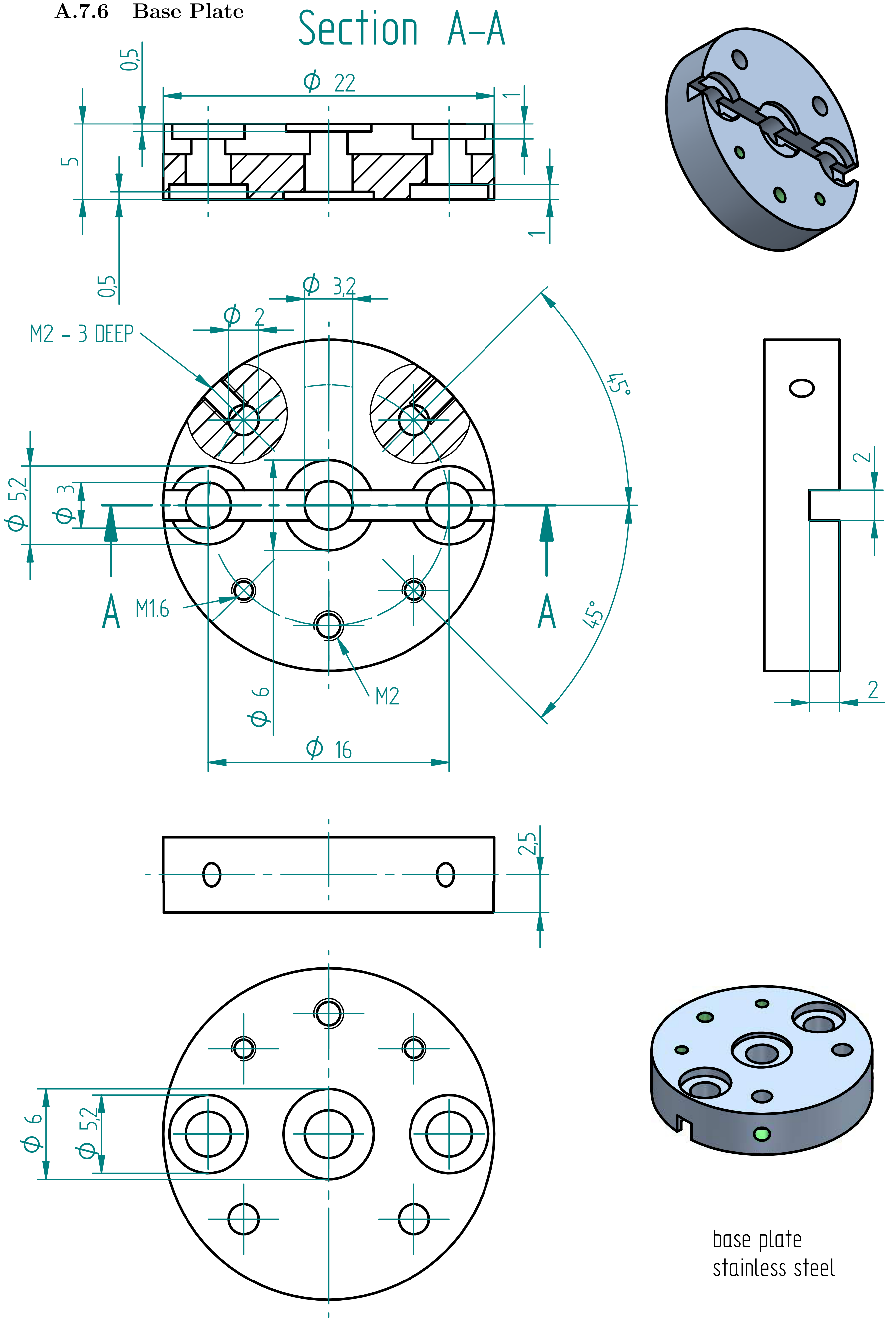

base plate
stainless steel

Bibliography

[1] C. Vericat, M. E. Vela, G. Benitez, P. Carro and R. C. Salvarezza. 'Self-assembled monolayers of thiols and dithiols on gold: new challenges for a well-known system'. In: *Chem. Soc. Rev.* **39** (2010), 1805–1834. DOI: `10.1039/b907301a` (cit. on pp. 5, 17–19)

[2] M. Wolf and P. Tegeder. 'Reversible molecular switching at a metal surface: A case study of tetra-tert-butyl-azobenzene on Au(111)'. In: *Surf. Sci.* **603** (2009), 1506–1517. DOI: `10.1016/j.susc.2008.11.049` (cit. on pp. 5, 55)

[3] M. J. Cook, A.-M. Nygard, Z. Wang and D. A. Russel. 'An evanescent field driven mono-molecular layer photoswitch: coordination and release of metallated macrocycles'. In: *Chem. Commun.* (2002), 1056–1057. DOI: `10.1039/B201870P` (cit. on pp. 6, 69)

[4] R. Wang, T. Iyoda, L. Jiang, D. A. Tryk, K. Hashimoto and A. Fujishima. 'Structural investigation of azobenzene-containing self-assembled monolayer films'. In: *J. Electroanal. Chem.* **438** (1997), 213–219. DOI: `10.1016/S0022-0728(96)05031-0` (cit. on pp. 6, 68–69, 71–72)

[5] N. R. Krekiehn, M. Müller, U. Jung, S. Ulrich, R. Herges and O. M. Magnussen. 'UV/Vis spectroscopy studies of the photoisomerization kinetics in self-assembled azobenzene-containing adlayers'. In: *Langmuir* **31** (2015), 8362–8370. DOI: `10.1021/acs.langmuir.5b01645` (cit. on p. 6)

[6] G. Pace, V. Ferri, C. Grave, M. Elbing, C. von Hänisch, M. Zharnikov, M. Mayor, M. A. Rampi and P. Samorì. 'Cooperative light-induced molecular movements of highly ordered azobenzene self-assembled monolayers'. In: *Proc. Natl. Acad. Sci. U. S. A.* **104** (2007), 9937–9942. DOI: `10.1073/pnas.0703748104` (cit. on pp. 6–7, 56, 68, 75)

[7] G. Kalyuzhny, A. Vasevich, G. Ashkenasy, A. Shanzer and I. Rubinstein. 'UV/vis spectroscopy of metalloporphyrin and metallophthalocyanine monolayers self-assembled on ultrathin gold films'. In: *J. Phys. Chem. B* **104** (2000), 8238–8244. DOI: `10.1021/jp0010785` (cit. on pp. 6, 69)

[8] D. Brete. 'Azobenzene-alkanthiols self-assembled on gold: Molecular switching investigated by UV/vis and NEXAFS spectroscopy'. Diplomarbeit (MA thesis). FU-Berlin, 2007 (cit. on pp. 6, 12–13, 69)

[9] C. Gahl, R. Schmidt, D. Brete, E. R. McNellis, W. Freyer, R. Carley, K. Reuter and M. Weinelt. 'Structure and excitonic coupling in self-assembled monolayers of azobenzene-functionalized alkanethiols'. In: *J. Am. Chem. Soc.* **132** (2010), 1831–1838. DOI: `10.1021/ja903636q` (cit. on pp. 6, 68–71)

[10] W. Freyer, D. Brete, R. Schmidt, C. Gahl, R. Carley and M. Weinelt. 'Switching behavior and optical absorbance of azobenzene-functionalized alkanethiols in different environments'. In: *J. Photochem. Photobiol., A* **204** (2009), 102–109. DOI: `10.1016/j.jphotochem.2009.02.018` (cit. on pp. 6, 69–70, 72, 130)

[11] R. Forker, M. Gruenewald and T. Fritz. 'Optical differential reflectance spectroscopy on thin molecular films'. In: *Annu. Rep. Prog. Chem., Sect. C: Phys. Chem.* **108** (2012), 34–68. DOI: `10.1039/C2PC90002E` (cit. on pp. 6, 51–52)

[12] L. Sun, S. Berkebile, G. Weidlinger, M. Denk, R. Denk, M. Hohage, G. Koller, F. P. Netzer, M. G. Ramsey and P. Zeppenfeld. ‘Layer resolved evolution of the optical properties of α-sexithiophene thin films’. In: *Phys. Chem. Chem. Phys.* **14** (2012), 13651–13655. DOI: `10.1039/C2CP42270K` (cit. on p. 6)

[13] K. Tamada, J. Nagasawa, F. Nakanishi and K. Abe. ‘Structure and Growth of Hexyl Azobenzene Thiol SAMs on Au(111)’. In: *Langmuir* **14** (1998), 3264–3271. DOI: `10.1021/la971348j` (cit. on p. 6)

[14] K. Tamada, H. Akiyama and T. Wei. ‘Photoisomerization reaction of unsymmetrical azobenzene disulfide self-assembled monolayers studied by surface plasmon spectroscopy: Influences of side chain length and contacting medium’. In: *Langmuir* **18** (2002), 5239–5246. DOI: `10.1021/la0157667` (cit. on pp. 6, 8, 56, 93)

[15] H. Akiyama, K. Tamada, J. Nagasawa, K. Abe and T. Tamki. ‘Photoreactivity in self-assembled monolayers formed from asymmetric disulfides having para-substituted azobenzenes’. In: *J. Phys. Chem. B* **107** (2003), 130–135. DOI: `10.1021/jp026103g` (cit. on pp. 6, 8, 56, 93)

[16] A. S. Davydov. *Theory of molecular excitons.* Plenum Press, New York, 1971 (cit. on p. 7)

[17] A. S. Davydov. ‘The theory of molecular excitons’. In: *Sov. Phys. Usp.* **7** (1964), 145. DOI: `10.1070/PU1964v007n02ABEH003659` (cit. on p. 7)

[18] M. Kasha. ‘Energy transfer mechanisms and the molecular exciton model for molecular aggregates’. English. In: *Radiat. Res.* **20** (1963), 55–70. DOI: `10.2307/3571331` (cit. on pp. 7, 71)

[19] M. Kasha, H. R. Rawls and M. Ashraf El-Bayoumi. ‘The exciton model in molecular spectroscopy’. In: *Pure Appl. Chem.* **11** (1965), 371–392. DOI: `10.1351/pac196511030371` (cit. on p. 7)

[20] E. G. McRae and M. Kasha. ‘The molecular exciton model’. In: *Physical Processes in Radiation Biology.* Ed. by L. Augstein, R. Mason and B. Rosenberg. 1964, 23–42. DOI: `10.1016/B978-1-4831-9824-8.50007-4` (cit. on pp. 7, 71)

[21] S. D. Evans, S. R. Johnson, H. Ringsdorf, L. M. Williams and H. Wolf. ‘Photoswitching of azobenzene derivatives formed on planar and colloidal surfaces’. In: *Langmuir* **14** (1998), 6436–6440. DOI: `10.1021/la980450t` (cit. on pp. 8, 56, 72, 93)

[22] L. F. N. Ah Qune, H. Akiyama, T. Nagahiro, K. Tamada and A. T. S. Wee. ‘Reversible work function changes induced by photoisomerization of asymmetric azobenzene dithiol self-assembled monolayers on gold’. In: *Appl. Phys. Lett.* **93** (2008), 083109. DOI: `10.1063/1.2969468` (cit. on pp. 8, 56, 93)

[23] T. Nagahiro, H. Akiyama, M. Hara and K. Tamada. ‘Photoisomerization of azobenzene containing self-assembled monolayers investigated by Kelvin probe work function measurements’. In: *J. Electron Spectrosc. Relat. Phenom.* **172** (2009), 128–133. DOI: `10.1016/j.elspec.2009.02.009` (cit. on pp. 8, 56, 93)

[24] A. S. Kumar, T. Ye, T. Takami, B.-C. Yu, A. K. Flatt, J. M. Tour and P. S. Weiss. ‘Reversible photo-switching of single azobenzene molecules in controlled nanoscale environments’. In: *Nano Lett.* **8** (2008), 1644–1648. DOI: `10.1021/nl080323%2B` (cit. on pp. 8, 93)

[25] U. Jung, O. Filinova, S. Kuhn, D. Zargarani, C. Bornholdt, R. Herges and O. Magnussen. ‘Photoswitching behavior of azobenzene-containing alkanethiol self-assembled monolayers on Au surfaces’. In: *Langmuir* **26** (2010), 13913–13923. DOI: `10.1021/la1015109` (cit. on pp. 8, 93)

[26] D. T. Valley, M. Onstott, S. Malyk and A. V. Benderskii. ‘Steric hindrance of photoswitching in self-assembled monolayers of azobenzene and alkane thiols’. In: *Langmuir* **29** (2013), 11623–11631. DOI: `10.1021/la402144g` (cit. on pp. 8, 93)

[27] R. Schmidt, S. Hagen, D. Brete, R. Carley, C. Gahl, J. Dokić, P. Saalfrank, S. Hecht, P. Tegeder and M. Weinelt. 'On the electronic and geometrical structure of the *trans*- and *cis*-isomer of tetra-*tert*-butyl-azobenzene on Au(111)'. In: *Phys. Chem. Chem. Phys.* **12** (2010), 4488–4497. DOI: `10.1039/B924409C` (cit. on pp. 8, 55, 111, 114, 125)

[28] R. Schmidt. 'Selbstorganisation und Photoisomerisation von Azobenzolderivaten auf Au(111)-Oberflächen'. PhD thesis. Fachbereich Physik der Freien Universität Berlin, 2011. URL: `http://www.diss.fu-berlin.de/diss/receive/FUDISS_thesis_000000024687` (cit. on pp. 8, 19, 31, 35, 45, 60–62, 65–67, 111, 114, 125)

[29] H. Fliegl, A. Köhn, C. Hättig and R. Ahlrichs. 'Ab initio calculation of the vibrational and electronic spectra of *trans*- and *cis*-Azobenzene'. In: *J. Am. Chem. Soc.* **125** (2003), 9821–9827. DOI: `10.1021/ja034433o` (cit. on p. 11)

[30] L. Briquet, D. P. Vercauteren, E. A. Perpète and D. Jacquemin. 'Is solvated *trans*-azobenzene twisted or planar?' In: *Chem. Phys. Lett.* **417** (2006), 190–195. DOI: `10.1016/j.cplett.2005.09.119` (cit. on p. 11)

[31] G. C. Hampson and J. M. Robertson. 'Bond lengths and resonance in the *cis*-azobenzene molecule'. In: *J. Chem. Soc.* (1941), 409–411. DOI: `10.1039/JR9410000409` (cit. on p. 11)

[32] T. Ishikawa, T. Noro and T. Shoda. 'Theoretical study of the photoisomerization of azobenzene'. In: *J. Chem. Phys.* **115** (2001), 7503–7513. DOI: `10.1063/1.1406975` (cit. on p. 11)

[33] G. Füchsel, T. Klamroth, J. Dokić and P. Saalfrank. 'On the electronic structure of neutral and ionic azobenzenes and their possible role as surface mounted molecular switches'. In: *J. Phys. Chem. B* **110** (2006), 16337–16345. DOI: `10.1021/jp060969v` (cit. on p. 12)

[34] J. Griffiths. 'Photochemistry of azobenzene and its derivatives'. In: *Chem. Soc. Rev.* **1** (1972), 481–493. DOI: `10.1039/CS9720100481` (cit. on p. 11)

[35] I. Conti, M. Garavelli and G. Orlandi. 'The different photoisomerization efficiency of azobenzene in the lowest $n\pi^*$ and $\pi\pi^*$ singlets: The role of a phantom state'. In: *J. Am. Chem. Soc.* **130** (2008), 5216–5230. DOI: `10.1021/ja710275e` (cit. on pp. 11–12, 73)

[36] H. Rau. 'Azo compounds'. In: *Photochromism*. Ed. by H. Dürr and H. Bouas-Laurent. Amsterdam: Elsevier Science, 2003. Chap. 4, 165–192. ISBN: 978-0-444-51322-9. DOI: `10.1016/B978-044451322-9/50008-7` (cit. on p. 12)

[37] T. Moldt, D. Przyrembel, M. Schulze, W. Bronsch, L. Boie, D. Brete, C. Gahl, R. Klajn, P. Tegeder and M. Weinelt. 'The role of adventitious water on the photoisomerization of azobenzene-functionalized self-assembled monolayers'. In: *Phys. Chem. Chem. Phys.* (2016). submitted (cit. on pp. 14, 95, 106)

[38] H. M. D. Bandara and S. C. Burdette. 'Photoisomerization in different classes of azobenzene'. In: *Chem. Soc. Rev.* **41** (2012), 1809–1825. DOI: `10.1039/C1CS15179G` (cit. on p. 14)

[39] J. Dokić, M. Gothe, J. Wirth, M. V. Peters, J. Schwarz, S. Hecht and P. Saalfrank. 'Quantum chemical investigation of thermal cis-to-trans isomerization of azobenzene derivatives: Substituent effects, solvent effects, and comparison to experimental data'. In: *J. Phys. Chem. A* **113** (2009), 6763–6773. DOI: `10.1021/jp9021344` (cit. on pp. 14–15, 111)

[40] D. M. Shin and D. G. Whitten. 'Solvent-induced mechanism change in charge-transfer molecules. Inversion versus rotation paths for the Z → E isomerization of donor-acceptor substituted azobenzenes'. In: *J. Am. Chem. Soc.* **110** (1988), 5206–5208. DOI: `10.1021/ja00223a058` (cit. on p. 15)

[41] D. R. Lide, ed. *CRC Handbook of chemistry and physics, internet version 2005*. CRC Press, 2005 (cit. on pp. 15, 145)

[42] C. Reichardt. 'Solvatochromic Dyes as Solvent Polarity Indicators'. In: *Chem. Rev.* **94** (1994), 2319–2358. DOI: 10.1021/cr00032a005 (cit. on pp. 15–16)

[43] J. C. Love, L. A. Estroff, J. K. Kriebel, R. G. Nuzzo and G. M. Whitesides. 'Self-assembled monolayers of thiolates on metals as a form of nanotechnology'. In: *Chem. Rev.* **105** (2005), 1103–1169. DOI: 10.1021/cr0300789 (cit. on p. 17)

[44] L. H. Dubois and R. G. Nuzzo. 'Synthesis, structure and properties of model organic surfaces'. In: *Annu. Rev. Phys. Chem.* **43** (1992), 437–463. DOI: 10.1146/annurev.pc.43.100192.002253 (cit. on p. 17)

[45] C. D. Bain, J. Evall and G. M. Whitesides. 'Formation of monolayers by the coadsorbtion of thiols on gold: Variation in the head group, tail group, and solvent.' In: *J. Am. Chem. Soc.* **111** (1989), 7155–7164. DOI: 10.1021/ja00200a039 (cit. on pp. 17, 21, 81, 85, 98–99)

[46] J. B. Schlenoff, M. Li and H. Ly. 'Stability and self-exchange in alkanethiol monolayers'. In: *J. Am. Chem. Soc* **117** (1995), 12528–12536. DOI: 10.1021/ja00155a016 (cit. on p. 17)

[47] S. Narasimhan and D. Vanderbilt. 'Elastic stress domains and the herringbone reconstruction on Au(111)'. In: *Phys. Rev. Lett.* **69** (Sept. 1992), 1564–1567. DOI: 10.1103/PhysRevLett.69.1564 (cit. on p. 18)

[48] F. Reinert and G. Nicolay. 'Influence of the herringbone reconstruction on the surface electronic structure of Au(111)'. In: *Appl. Phys. A: Mater. Sci. Process.* **78** (2004), 817–821. DOI: 10.1007/s00339-003-2436-6 (cit. on p. 18)

[49] P. Kowalczyk. 'High temperature STM/STS investigations of resonant image states on Au(1 1 1)'. In: *Appl. Surf. Sci.* **253** (2007), 4036–4040. DOI: 10.1016/j.apsusc.2006.08.033 (cit. on p. 18)

[50] D. G. Castner, K. Hinds and D. W. Grainger. 'X-ray photoelectron spectroscopy sulfur 2p study of organic thiol and disulfide binding interactions with gold surfaces'. In: *Langmuir* **12** (1996), 5083–5086. DOI: 10.1021/la960465w (cit. on p. 18)

[51] B. J. Lindberg, K. Hamrin, G. Johansson, U. Gelius, A. Fahlman, C. Nordling and K. Siegbahn. 'Molecular spectroscopy by means of ESCA II. Sulfur compounds. Correlation of electron binding energy with structure'. In: *Physica Scripta* **1** (1970), 286. DOI: 10.1088/0031-8949/1/5-6/020 (cit. on p. 18)

[52] G. Liu, J. A. Rodriguez, J. Dvorak, J. Hrbek and T. Jirsak. 'Chemistry of sulfur-containing molecules on Au(1 1 1): thiophene, sulfur dioxide, and methanethiol adsorption'. In: *Surf. Sci.* **505** (2002), 295–307. DOI: 10.1016/S0039-6028(02)01377-8 (cit. on p. 18)

[53] A. Shaporenko, A. Terfort, M. Grunze and M. Zharnikov. 'A detailed analysis of the photoemission spectra of basic thioaromatic monolayers on noble metal substrates'. In: *J. Electron Spectrosc. Relat. Phenom.* **151** (2006), 45–51. DOI: 10.1016/j.elspec.2005.10.008 (cit. on p. 18)

[54] P. Cyganik, M. Buck, T. Strunskus, A. Shaporenko, J. D. E. T. Wilton-Ely, M. Zharnikov and C. Wöll. 'Competition as a design concept: Polymorphism in self-assembled monolayers of biphenyl-based thiols'. In: *J. Am. Chem. Soc.* **128** (2006), 13868–13878. DOI: 10.1021/ja0640647 (cit. on p. 18)

[55] A. A. Dameron, L. F. Charles and P. S. Weiss. 'Structures and displacement of 1-adamantanethiol self-assembled monolayers on Au(111)'. In: *J. Am. Chem. Soc.* **127** (2005), 8697–8704. DOI: 10.1021/ja042621o (cit. on p. 19)

[56] K. Heister, D. L. Allara, K. Bahnck, S. Frey, M. Zharnikov and M. Grunze. 'Deviations from 1:1 compositions in self-assembled monolayers formed from adsorption of asymmetric dialkyl disulfides on gold'. In: *Langmuir* **15** (1999), 5440–5443. DOI: 10.1021/la9902385 (cit. on p. 20)

[57] R. K. Smith, S. M. Reed, P. A. Lewis, J. D. Monnell, R. S. Clegg, K. F. Kelly, L. A. Bumm, J. E. Hutchison and P. S. Weiss. 'Phase separation within a binary self-assembled monolayer on Au{111} driven by an amide-containing alkanethiol'. In: *J. Phys. Chem. B* **105** (2001), 1119–1122. DOI: `10.1021/jp0035129` (cit. on p. 20)

[58] C. D. Bain and G. M. Whitesides. 'Formation of two-component surfaces by the spontaneous assembly of monolayers on gold from solutions containing mixtures of organic thiols'. In: *J. Am. Chem. Soc.* **110** (1988), 6560–6561. DOI: `10.1021/ja00227a044` (cit. on p. 21)

[59] C. D. Bain and G. M. Whitesides. 'Formation of monolayers by the coadsorbtion of thiols on gold: Variation in the length of the alkyl chain'. In: *J. Am. Chem. Soc.* **111** (1989), 7164–7175. DOI: `10.1021/ja00200a040` (cit. on pp. 21, 81, 99)

[60] C. D. Bain, E. B. Troughton, T. Tao, J. Evall, G. M. Whitesides and R. G. Nuzzo. 'Formation of monolayer films by the spontaneous assembly of organic thiols from solution onto gold'. In: *J. Am. Chem. Soc.* **111** (1989), 321–335. DOI: `10.1021/ja00183a049` (cit. on p. 21)

[61] C. D. Bain, H. A. Biebuyck and G. M. Whitesides. 'Comparison of self-assembled monolayers on gold: Coadsorption of thiols and disulfides'. In: *Langmuir* **5** (1989), 723–727. DOI: `10.1021/la00087a027` (cit. on pp. 21, 99, 132)

[62] C. D. Bain and G. M. Whitesides. 'Modeling organic surfaces with self-assembled monolayers'. In: *Angew. Chem., Int. Ed. Engl.* **28** (1989), 506–512. DOI: `10.1002/anie.198905061` (cit. on p. 21)

[63] S. Hüfner. *Photoelectron spectroscopy.* 2nd ed. Springer series in solid-state sciences. Springer, 1996 (cit. on p. 23)

[64] A. Nilsson. 'Applications of core level spectroscopy to adsorbates'. In: *Journal of Electron Spectroscopy and Related Phenomena* **126** (2002), 3–42. DOI: `10.1016/S0368-2048(02)00141-X` (cit. on p. 23)

[65] M. P. Seah, I. S. Gilmore and G. Beamson. 'XPS: binding energy calibration of electron spectrometers—re-evaluation of the reference energies'. In: *Surf. Interface Anal.* **26** (1998), 642–649. DOI: `10.1002/(SICI)1096-9918(199808)26:9<642::AID-SIA408>3.0.CO;2-3` (cit. on pp. 24, 139)

[66] W. Domcke, L. S. Cederbaum, J. Schirmer and W. von Niessen. 'Negative shake-up energy in core ionization'. In: *Phys. Rev. Lett.* **42** (Apr. 1979), 1237–1241. DOI: `10.1103/PhysRevLett.42.1237` (cit. on pp. 25, 60)

[67] S. Doniach and M. Sunjic. 'Many-electron singularity in X-ray photoemission and X-ray line spectra from metals'. In: *J. Phys. C: Solid State Phys.* **3** (1970), 285. DOI: `10.1088/0022-3719/3/2/010` (cit. on p. 26)

[68] D. A. Shirley. 'High-resolution X-ray photoemission spectrum of the valance bands of gold'. In: *Phys. Rev. B: Condens. Matter Mater. Phys.* **5** (1972), 4709–4714. DOI: `10.1103/PhysRevB.5.4709` (cit. on pp. 26, 32)

[69] F. Chesneau, J. Zhao, C. Shen, M. Buck and M. Zharnikov. 'Adsorption of long-chain alkanethiols on Au(111): A look from the substrate by high resolution X-ray photoelectron spectroscopy'. In: *J. Phys. Chem. C* **114** (2010), 7112–7119. DOI: `10.1021/jp100522n` (cit. on p. 28)

[70] P. Feulner, T. Niedermayer, K. Eberle, R. Schneider, D. Menzel, A. Baumer, E. Schmich, A. Shaporenko, Y. Tai and M. Zharnikov. 'Strong temperature dependence of irradiation effects in organic layers'. In: *Phys. Rev. Lett.* **93** (2004), 178302. DOI: `10.1103/PhysRevLett.93.178302` (cit. on pp. 31, 62)

[71] R. Schmidt, E. McNellis, W. Freyer, D. Brete, T. Gießel, C. Gahl, K. Reuter and M. Weinelt. 'Azobenzene-functionalized alkanethiols in self-assembled monolayers on gold'. In: *Appl. Phys. A: Mater. Sci. Process.* **92** (2008), 267–275. DOI: `10.1007/s00339-008-4829-z` (cit. on pp. 31, 64)

[72] F. Schreier. 'The Voigt and complex error function: A comparison of computational methods'. In: *J. Quant. Spectrosc. Radiat. Transfer* **48** (1992). Special Issue Conference on Molecular Spectroscopic Databases, 743–762. DOI: `10.1016/0022-4073(92)90139-U` (cit. on p. 31)

[73] *Igor technical notes: #026: The Voigt profile.* Part of the documentation of the data analysis software *Igor Pro.* WaveMetrics, Inc. Portland, USA, May 2006 (cit. on p. 31)

[74] F. Schreier. 'Optimized implementations of rational approximations for the Voigt and complex error function'. In: *J. Quant. Spectrosc. Radiat. Transfer* **112** (2011), 1010–1025. DOI: `10.1016/j.jqsrt.2010.12.010` (cit. on p. 31)

[75] B. Henke, E. Gullikson and J. Davis. 'X-ray interactions: photoabsorption, scattering, transmission, and reflection at E=50–30000 eV, Z=1–92'. In: *Atomic Data and Nuclear Data Tables.* Atomic Data and Nuclear Data Tables **54** (1993), 181–342. DOI: `10.1006/adnd.1993.1013` (cit. on p. 33)

[76] J. Stöhr. *NEXAFS spectroscopy.* 1st ed. Springer Series in Surface Sciences 25. Springer, Corrected Printing 1996 (cit. on pp. 33–34, 36, 39–40, 45, 64–65)

[77] M. Piantek. 'Switchable molecules on metallic surfaces studied by core-level spectroscopies'. PhD thesis. Fachbereich Physik der Freien Universität Berlin, 2009. URL: `http://www.diss.fu-berlin.de/diss/receive/FUDISS_thesis_000000017823` (cit. on p. 35)

[78] N. I. of Standard (NIST). 'NIST X-ray Photoelectron spectroscopy database: NIST standard reference database 20, version 4.1 (web version)'. URL: `http://srdata.nist.gov/xps/` (cit. on p. 40)

[79] P. E. Batson. 'Carbon 1 *s* near-edge-absorption fine structure in graphite'. In: *Phys. Rev. B: Condens. Matter Mater. Phys.* **48** (July 1993), 2608–2610. DOI: `10.1103/PhysRevB.48.2608` (cit. on p. 44)

[80] J. Stöhr and D. A. Outka. 'Determination of molecular orientation on surfaces from the angular dependence of near-edge X-ray-absorption fine-structure spectra'. In: *Phys. Rev. B: Condens. Matter Mater. Phys.* **36** (1987), 7891–7905. DOI: `10.1103/PhysRevB.36.7891` (cit. on pp. 45–46, 62)

[81] A. de Jong and J. Niemantsverdriet. 'Thermal desorption analysis: Comparative test of ten commonly applied procedures'. In: *Surf. Sci.* **233** (1990), 355–365. DOI: `10.1016/0039-6028(90)90649-S` (cit. on p. 49)

[82] T. Moldt, D. Brete, D. Przyrembel, S. Das, J. R. Goldman, P. K. Kundu, C. Gahl, R. Klajn and M. Weinelt. 'Tailoring the properties of surface-immobilized azobenzenes by monolayer dilution and surface curvature'. In: *Langmuir* **31** (2015), 1048–1057. DOI: `10.1021/la504291n` (cit. on pp. 52–53, 93, 96, 130)

[83] V. Ferri, M. Elbing, G. Pace, M. D. Dickey, M. Zharnikov, P. Samorì, M. Mayor and M. A. Rampi. 'Light-powered electrical switch based on cargo-lifting azobenzene monolayers'. In: *Angew. Chem., Int. Ed.* **47** (2008), 3407–3409. DOI: `10.1002/anie.200705339` (cit. on pp. 56, 75)

[84] M. Elbing, A. Blaszczyk, C. von Hänisch, M. Mayor, F. Violetta, C. Grave, M. A. Rampi, G. Pace, P. Samorì, A. Shaporenko and M. Zharnikov. 'Single component self-assembled monolayers of aromatic azo-biphenyl: Influence of the packing tightness on the SAM structure and light-induced molecular movements'. In: *Adv. Funct. Mater.* **18** (2008), 2972–2983. DOI: `10.1002/adfm.200800652` (cit. on pp. 56, 75)

[85] J. Zhang, J. K. Whitesell and M. A. Fox. 'Photoreactivity of self-assembled monolayers of azobenzene or stilbene derivatives capped on colloidal gold clusters'. In: *Chem. Mater.* **13** (June 2001), 2323–2331. DOI: `10.1021/cm000752s` (cit. on pp. 56, 93)

[86] P. Kao, S. Neppl, P. Feulner, D. L. Allara and M. Zharnikov. ‘Charge transfer time in alkanethiolate self-assembled monolayers via resonant auger electron spectroscopy’. In: *J. Phys. Chem. C* **114** (2010), 13766–13773. DOI: `10.1021/jp1042816` (cit. on pp. 57, 73)

[87] S. Neppl, U. Bauer, D. Menzel, P. Feulner, A. Shaporenko, M. Zharnikov, P. Kao and D. L. Allara. ‘Charge transfer dynamics in self-assembled monomolecular films’. In: *Chem. Phys. Lett.* **447** (Oct. 2007), 227–231. DOI: `10.1016/j.cplett.2007.09.013` (cit. on pp. 57, 66, 73)

[88] N. Martensson, S. Svensson and U. Gelius. ‘Single and double shake-up processes in the Ne 1s photoelectron spectrum’. In: *Journal of Physics B: Atomic and Molecular Physics* **20** (1987), 6243–6255. DOI: `10.1088/0022-3700/20/23/016` (cit. on p. 60)

[89] K. Heister, L. S. O. Johansson, M. Grunze and M. Zharnikov. ‘A detailed analysis of the C 1s photoemission of n-alkanethiolate films on noble metal substrates’. In: *Surf. Sci.* **529** (2003), 36–46. DOI: `10.1016/S0039-6028(03)00299-1` (cit. on p. 60)

[90] D. Nordfors, A. Nilsson, N. M. rtensson, S. Svensson, U. Gelius and S. Lunell. ‘Experimental and INDO/CI calculated gas phase C1s shake-up spectra of C_6H_6, C_6H_5OH, and $C_6H_5CH_5OH$’. In: *J. Chem. Phys.* **88** (1988), 2630–2636. DOI: `10.1063/1.454043` (cit. on p. 62)

[91] M. Weinelt, N. Wassdahl, T. Wiell, O. Karis, J. Hasselström, P. Bennich, A. Nilsson, J. Stöhr and M. Samant. ‘Electronic structure of benzene on Ni(100) and Cu(110): An x-ray-spectroscopy study’. In: *Phys. Rev. B: Condens. Matter Mater. Phys.* **58** (Sept. 1998), 7351–7360. DOI: `10.1103/PhysRevB.58.7351` (cit. on p. 62)

[92] M. Shibuta, N. Hirata, R. Matsu, T. Eguchi and A. Nakajima. ‘Charge Separation at the Molecular Monolayer Surface Observation and Control of the Dynamics’. In: *J. Phys. Chem. Lett.* **3** (2012), 981–985. DOI: `10.1021/jz3002579` (cit. on p. 62)

[93] G. Hähner, C. Wöll, M. Buck and M. Grunze. ‘Investigation of intermediate steps in the self-assembly of n-alkanethiols on gold surfaces by soft X-ray spectroscopy’. In: *Langmuir* **9** (1993), 1955–1958. DOI: `10.1021/la00032a005` (cit. on pp. 62, 66)

[94] M. Zharnikov and M. Grunze. ‘Spectroscopic characterization of thiol-derived self-assembling monolayers’. In: *J. Phys.: Condens. Matter* **13** (2001), 11333–11365. DOI: `10.1088/0953-8984/13/49/314` (cit. on p. 62)

[95] D. Brete, D. Przyrembel, C. Eickhoff, R. Carley, W. Freyer, K. Reuter, C. Gahl and M. Weinelt. ‘Mixed self-assembled monolayers of azobenzene photoswitches with trifluoromethyl and cyano end groups’. In: *J. Phys.: Condens. Matter* **24** (2012), 394015. DOI: `10.1088/0953-8984/24/39/394015` (cit. on pp. 64, 130)

[96] R. Püttner, C. Kolczewski, M. Martins, A. S. Schlachter, G. Snell, M. Sant’Anna, J. Viefhaus, K. Hermann and G. Kaindl. ‘The C 1s NEXAFS spectrum of benzene below threshold: Rydberg or valence character of the unoccupied σ-type orbitals’. In: *Chem. Phys. Lett.* **393** (2004), 361–366. DOI: `10.1016/j.cplett.2004.06.053` (cit. on p. 64)

[97] H. Ågren, V. Carravetta, O. Vahtras and L. G. M. Pettersson. ‘Orientational probing of polymeric thin films by NEXAFS: Calculations on polytetrafluoroethylene’. In: *Phys. Rev. B: Condens. Matter Mater. Phys.* **51** (June 1995), 17848–17855. DOI: `10.1103/PhysRevB.51.17848` (cit. on p. 65)

[98] I. Ishii, R. McLaren, A. P. Hitchcock, K. D. Jordan, Y. Choi and M. B. Robin. ‘The σ^* molecular orbitals of perfluoroalkanes as studied by inner-shell electron energy loss and electron transmission spectroscopies’. In: *Can. J. Chem.* **66** (1988), 2104–2121. DOI: `10.1139/v88-336` (cit. on p. 65)

[99] N. Ballav, B. Schüpbach, S. Neppl, P. Feulner, A. Terfort and M. Zharnikov. ‘Biphenylnitrile-based self-assembled monolayers on Au(111): Spectroscopic characterization and resonant excitation of the nitrile tail group’. In: *J. Phys. Chem. C* **114** (2010), 12719–12727. DOI: `10.1021/jp1045386` (cit. on p. 65)

[100] S. Carniato, V. Ilakovac, J.-J. Gallet, E. Kukk and Y. Luo. 'Hybrid density-functional theory calculations of near-edge x-ray absorption fine-structure spectra: Applications on benzonitrile in gas phase'. In: *Phys. Rev. A: At., Mol., Opt. Phys.* **71** (2005), 022511. DOI: `10.1103/PhysRevA.71.022511` (cit. on p. 66)

[101] S. Carniato, R. Taïeb, E. Kukk, Y. Luo and B. Brena. 'N-K near-edge x-ray-absorption fine structures of acetonitrile in gas phase'. In: *J. Chem. Phys.* **123** (2005), 214301. DOI: `10.1063/1.2104327` (cit. on p. 66)

[102] H. Wolf, H. Ringsdorf, E. Delamarche, T. Takami, H. Kang, B. Michel, C. Gerber, M. Jaschke, H.-J. Butt and E. Bamberg. 'End-group-dominated molecular order in self-assembled monolayers'. In: *J. Phys. Chem.* **99** (1995), 7102–7107 (cit. on pp. 68, 98)

[103] M. Jaschke, H. Schönherr, H. Wolf, H.-J. Butt, E. Bamberg, M. K. Besocke and H. Ringsdorf. 'Structure of alkyl and perfluoroalkyl disulfide and azobenzenethiol monolayers on gold(111) revealed by atomic force microscopy'. In: *J. Phys. Chem.* **100** (1996), 2290–2301. DOI: `10.1021/jp952355o` (cit. on pp. 68, 98)

[104] S. C. B. Mannsfeld, T. W. Canzler, T. Fritz, H. Proehl, K. Leo, S. Stumpf, G. Goretzki and K. Gloe. 'The structure of [4-(phenylazo)phenoxy]hexane-1-thiol self-assembled monolayers on Au(111)'. In: *J. Phys. Chem. B* **106** (2002), 2255–2260. DOI: `10.1021/jp012771a` (cit. on p. 68)

[105] W. B. Caldwell, D. J. Campbell, K. Chen, B. R. Herr, C. A. Mirkin, A. Malik, M. K. Durbin, P. Dutta and K. G. Huang. 'A highly ordered self-assembled monolayer film of an azobenzenealkanethiol on Au(111): Electrochemical properties and structural characterization by synchrotron in-plane X-ray diffraction, atomic force microscopy, and surface-enhanced raman spectroscopy'. In: *J. Am. Chem. Soc.* **117** (1995), 6071–6082. DOI: `10.1021/ja00127a021` (cit. on pp. 68, 98)

[106] M. Wanunu, A. Vaskevich and I. Rubinstein. 'Widely-applicable gold substrate for the study of ultrathin overlayers'. In: *J. Am. Chem. Soc.* **126** (2004), 5569–5576. DOI: `10.1021/ja0396448` (cit. on p. 69)

[107] I. Doron-Mor, Z. Barkay, N. Filip-Granit, A. Vaskevich and I. Rubinstein. 'Ultrathin gold island films on silanized glass. morphology and optical properties'. In: *Chem. Mater.* **16** (2004), 3476–3483. DOI: `10.1021/cm049605a` (cit. on p. 69)

[108] J. Heesemann. 'Studies on monolayers. 1. Surface tension and absorption spectroscopic measurements of monolayers of surface-active azo and stilbene dyes'. In: *J. Am. Chem. Soc.* **102** (1980), 2167–2176. DOI: `10.1021/ja00527a004` (cit. on p. 71)

[109] M. Kasha. 'Classification of Excitons'. In: *Physical Processes in Radiation Biology.* Ed. by L. Augstein, R. Mason and B. Rosenberg. 1964, 17–19. DOI: `10.1016/B978-1-4831-9824-8.50006-2` (cit. on p. 71)

[110] A. Eisfeld and J. S. Briggs. 'The J- and H-bands of organic dye aggregates'. In: *Chem. Phys.* **324** (2006), 376–384. DOI: `doi:10.1016/j.chemphys.2005.11.015` (cit. on p. 71)

[111] N. Heinemann, J. Grunau, T. Leißner, O. Andreyev, S. Kuhn, U. Jung, D. Zargarani, R. Herges, O. Magnussen and M. Bauer. 'Reversible switching in self-assembled monolayers of azobenzene thiolates on Au (111) probed by threshold photoemission'. In: *Chem. Phys.* **402** (2012), 22–28. DOI: `10.1016/j.chemphys.2012.03.025` (cit. on p. 72)

[112] C. Gahl, R. Schmidt, D. Brete, S. Paarmann and M. Weinelt. 'Charge-transfer dynamics in azobenzene alkanethiolate self-assembled monolayers on gold'. In: *Surface Science* **643** (2016), 183–189. DOI: `10.1016/j.susc.2015.08.028` (cit. on p. 73)

[113] E. McNellis. 'Private communication' (cit. on p. 73)

[114] J. Trotter. 'The crystal and molecular structure of biphenyl'. In: *Acta Crystallogr.* **14** (Nov. 1961), 1135–1140. DOI: `10.1107/S0365110X6100334X` (cit. on p. 75)

[115] A. Ulman. 'Formation and structure of self-assembled monolayers'. In: *Chem. Rev.* **96** (1996), 1533–1554. DOI: 10.1021/cr9502357 (cit. on p. 81)

[116] Y. Ge, T. Weidner, H. Ahn, J. E. Whitten and M. Zharnikov. 'Energy level pinning in self-assembled alkanethiol monolayers'. In: *J. Phys. Chem. C* **113** (2009), 4575–4583. DOI: 10.1021/jp809975x (cit. on p. 86)

[117] O. M. Cabarcos, A. Shaporenko, T. Weidner, S. Uppili, L. S. Dake, M. Zharnikov and D. L. Allara. 'Physical and electronic structure effects of embedded dipoles in self-assembled monolayers: Characterization of mid-chain ester functionalized alkanethiols on Au{111}'. In: *J. Phys. Chem. C* **112** (2008), 10842–10854. DOI: 10.1021/jp801618j (cit. on p. 86)

[118] H. Ahn, M. Zharnikov and J. E. Whitten. 'Abnormal pinning of the Fermi and vacuum levels in monomolecular self-assembled films'. In: *Chem. Phys. Lett.* **428** (2006), 283–287. DOI: 10.1016/j.cplett.2006.07.053 (cit. on p. 86)

[119] L. Wang, G. M. Rangger, L. Romaner, G. Heimel, T. Bučko, Z. Ma, Q. Li, Z. Shuai and E. Zojer. 'Electronic structure of self-assembled monolayers on Au(111) surfaces: The impact of backbone polarizability'. In: *Adv. Funct. Mater.* **19** (2009), 3766–3775. DOI: 10.1002/adfm.200901152 (cit. on p. 87)

[120] O. T. Hofmann, D. A. Egger and E. Zojer. 'Work-function modification beyond pinning: When do molecular dipoles count?' In: *Nano Lett.* **10** (2010), 4369–4374. DOI: 10.1021/nl101874k (cit. on p. 87)

[121] B. Kretz, D. A. Egger and E. Zojer. 'A toolbox for controlling the energetics and localization of electronic states in self-assembled organic monolayers'. In: *Adv. Sci.* **2** (2015). DOI: 10.1002/advs.201400016 (cit. on p. 87)

[122] U. Jung, S. Kuhn, U. Cornelissen, F. Tuczek, T. Strunskus, V. Zaporojtchenko, J. Kubitschke, R. Herges and O. Magnussen. 'Azobenzene-containing triazatriangulenium adlayers on Au(111): Structural and spectroscopic characterization'. In: *Langmuir* **27** (2011), 5899–5908. DOI: 10.1021/la104654p (cit. on p. 93)

[123] T. Weidner, F. Bretthauer, N. Ballav, H. Motschmann, H. Orendi, C. Bruhn, U. Siemeling and M. Zharnikov. 'Correlation between the molecular structure and photoresponse in aliphatic self-assembled monolayers with azobenzene tailgroups'. In: *Langmuir* **24** (2008), 11691–11700. DOI: 10.1021/la802454w (cit. on p. 93)

[124] S. Chen, L. Li, C. L. Boozer and S. Jiang. 'Controlled chemical and structural properties of mixed self-assembled monolayers by coadsorption of symmetric and asymmetric disulfides on Au(111)'. In: *J. Phys. Chem. B* **105** (2001), 2975–2980. DOI: 10.1021/jp0040650 (cit. on p. 99)

[125] J. P. Folkers, P. E. Laibinis, G. M. Whitesides and J. Deutch. 'Phase behavior of two-component self-assembled monolayers of alkanethiolates on gold'. In: *J. Phys. Chem.* **98** (1994), 563–571. DOI: 10.1021/j100053a035 (cit. on p. 99)

[126] F. T. Oyerokun, R. A. Vaia, J. F. Maguire and B. L. Farmer. 'Role of solvent selectivity in the equilibrium surface composition of monolayers formed from a solution containing mixtures of organic thiols'. In: *Langmuir* **26** (2010), 11991–11997. DOI: 10.1021/la101464j (cit. on p. 99)

[127] C.-A. Palma, M. Cecchini and P. Samorì. 'Predicting self-assembly: from empirism to determinism'. In: *Chem. Soc. Rev.* **41** (2012), 3713–3730. DOI: 10.1039/C2CS15302E (cit. on p. 99)

[128] M. Utecht, T. Klamroth and P. Saalfrank. 'Optical absorption and excitonic coupling in azobenzenes forming self-assembled monolayers: a study based on densitiy functional theory'. In: *Phys. Chem. Chem. Phys.* **13** (2011), 21608–21614. DOI: 10.1039/c1cp22793a (cit. on p. 103)

[129] S. Hagen, P. Kate, F. Leyssner, D. Nandi, M. Wolf and P. Tegeder. 'Excitation mechanism in the photoisomerization of a surface-bound azobenzene derivative: Role of the metallic substrate'. In: *J. Chem. Phys.* **129** (2008), 164102. DOI: `10.1063/1.2997343` (cit. on pp. 111, 127)

[130] E. Fischer and Y. Frei. 'Photoisomerization equilibria involving the C=N double bond'. In: *J. Chem. Phys.* **27** (1957), 808–809. DOI: `10.1063/1.1743834` (cit. on p. 111)

[131] G. Wettermark, J. Weinstein, J. Sousa and L. Dogliotti. 'Kinetics of *cis-trans* isomerization of *para*-substituted N-benzylideneanilines'. In: *J. Phys. Chem.* **69** (1965), 1584–1587. DOI: `10.1021/j100889a023` (cit. on p. 111)

[132] Y. Luo, M. Utecht, J. Dokić, S. Korchak, H.-M. Vieth, R. Haag and P. Saalfrank. '*cis-trans* isomerisation of substituted aromatic imines: A comparative experimental and theoretical study'. In: *ChemPhysChem* **12** (2011), 2311–2321. DOI: `10.1002/cphc.201100179` (cit. on pp. 111–112, 127, 135)

[133] C. Gahl, D. Brete, F. Leyssner, M. Koch, E. R. McNellis, J. Mielke, R. Carley, L. Grill, K. Reuter, P. Tegeder and M. Weinelt. 'Coverage- and temperature-controlled isomerization of an imine derivative on Au(111)'. In: *J. Am. Chem. Soc.* **135** (2013), 4273–4281. DOI: `10.1021/ja309330e` (cit. on pp. 112, 114–116, 119, 121, 123–127)

[134] E. R. McNellis, C. Bronner, J. Meyer, M. Weinelt, P. Tegeder and K. Reuter. 'Azobenzene versus 3,3',5,5'-tetra-tert-butyl-azobenzene (TBA) at Au(111): Characterizing the role of spacer groups'. In: *Phys. Chem. Chem. Phys.* **12** (2010), 6404–6412. DOI: `10.1039/c001978j` (cit. on p. 112)

[135] T. Vondrak and X.-Y. Zhu. 'Two-photon photoemission study of heterogeneous electron Transfer: C_6F_6 on Cu(111)'. In: *J. Phys. Chem. B* **103** (1999), 3449–3456. DOI: `10.1021/jp9846983` (cit. on p. 113)

[136] W. Huber, M. Weinelt, P. Zebisch and H.-P. Steinrück. 'Azimuthal reorientation of adsorbed molecules induced by lateral interactions: benzene/Ni(110)'. In: *Surf. Sci.* **253** (1991), 72–98. DOI: `10.1016/0039-6028(91)90582-D` (cit. on p. 113)

[137] M. Piantek, J. Miguel, A. Krüger, C. Navío, M. Bernien, D. K. Ball, K. Herrmann and W. Kuch. 'Temperature, surface, and coverage-induced conformational changes of azobenzene derivatives on Cu(001)'. In: *J. Phys. Chem. C* **113** (2009), 20307–20315. DOI: `10.1021/jp907641f` (cit. on p. 114)

[138] J. Mielke, F. Leyssner, M. Koch, S. Meyer, Y. Luo, S. Selvanathan, R. Haag, P. Tegeder and L. Grill. 'Imine derivatives on Au(111): Evidence for "inverted" thermal isomerization'. In: *ACS Nano* **5** (2011), 2090–2097 (cit. on pp. 114, 125, 127)

[139] L. Óvári, M. Wolf and P. Tegeder. 'Reversible changes in the vibrational structure of tetra-*tert*-butylazobenzene on a Au(111) surface induced by light and thermal activation'. In: *J. Phys. Chem. C* **111** (2007), 15370–15374. DOI: `10.1021/jp075274o` (cit. on p. 125)

[140] F. Leyssner, S. Hagen, L. Óvári, J. Dokić, P. Saalfrank, M. Peters, S. Hecht, T. Klamroth and P. Tegeder. 'Photoisomerization ability of molecular switches adsorbed on Au(111): comparison between azobenzene and stilbene derivatives'. In: *J. Phys. Chem. C* **114** (2010), 1231–1239. DOI: `10.1021/jp909684x` (cit. on p. 125)

[141] L. Óvári, J. Schwarz, M. V. Peters, S. Hecht, M. Wolf and P. Tegeder. 'Reversible isomerization of an azobenzene derivative adsorbed on Au(1 1 1): Analysis using vibrational spectroscopy'. In: *Int. J. Mass Spectrom.* **277** (2008), 223–228. DOI: `10.1016/j.ijms.2008.04.024` (cit. on p. 125)

[142] R. J. Maurer and K. Reuter. 'Bistability loss as a key feature in azobenzene (non-)switching on metal surfaces'. In: *Angew. Chem., Int. Ed.* **51** (Nov. 2012), 12009–12011. DOI: `10.1002/anie.201205718` (cit. on p. 127)

[143] S. Zarwell. 'Photoschalter-Linker-Konjugate: Design, Synthesen und Charakterisierungen'. PhD thesis. Technische Universität Berlin, 2011 (cit. on p. 130)

[144] *1-dodecanethiol, 98%.* Online catalog. www.alfa.com, Art. No. A12741, CAS 112-55-0. Alfa Aesar (cit. on p. 133)

[145] V. Farcasan and A. Donea. 'Schiff's bases and benzylamies from 2-phenyl-4-(4'-amino-phenyl)- thiazole and 4-aminobiphenyl. Some UV data'. In: *Studia Univ: Bebes-Bolyai, Chemia* **25** (1980), 76–80 (cit. on p. 134)

[146] M. A. Van Hove, R. J. Koestner, P. C. Stair, J. P. Bibérian, L. L. Kesmodel, I. Bartoš and G. A. Somorjai. 'The surface reconstructions of the (100) crystal faces of iridium, platinum and gold: I. Experimental observations and possible structural models'. In: *Surf. Sci.* **103** (1981), 189–217. DOI: `10.1016/0039-6028(81)90107-2` (cit. on p. 135)

Summary

Photo-responsive molecular switches are a promising class of materials. In this work two types of systems, in which the molecular switches were adsorbed on a surface, are investigated: self-assembled monolayers (SAMs) of azobenzenes on gold and (sub)monolayers of TBI (*E*)-3,5-di-*tert*-butyl-N-(3,5-di-*tert*-butyl-benzylidene)aniline[1] vapour-deposited on gold.

Azobenzene SAMs SAMs of azobenzene alkanethiolates on Au(111) were investigated by X-ray photoemission spectroscopy (XPS) and near-edge X-ray-absorption fine-structure (NEXAFS) spectroscopy. We found that the chromophores in these SAMs are oriented predominately upright. We developed a structural model of the SAMs by combining the molecular orientation obtained from NEXAFS measurements with AFM/STM data from literature on the lateral structure of the SAMs. The optical properties of the SAMs were investigated by UV/vis differential reflectance (DR) spectroscopy. Strong excitonic coupling of the chromophores was observed in these densely packed layers. The *trans*-*cis* photoisomerization was found to be inhibited in these SAMs—presumably due to steric hindrance or excitonic coupling.

Bicomponent SAMs were prepared by coadsorption from solution. The composition of the SAMs as a function of the ratio of the two components in the solution was analysed by quantitative XPS. We demonstrate that we can arbitrarily tune the composition of the SAM and we present a thermodynamic model describing the relation between the composition of the SAM and the solution. Mixed SAMs comprising two different azobenzene chromophores allowed to study the excitonic coupling in a two-component system.

In order to enable photoisomerization in the SAM, mixed SAMs of azobenzene alkanethiolates diluted with unsubstituted alkanethiolates were produced. Here a dependence of the excitonic coupling on the dilution of the chromophores and efficient photoisomerization was demonstrated.

TBI Aromatic imines are closely related to azobenzenes. In imines the N=N group of azobenzenes is replaced by the isoelectrical CH=N group, which only contains a single N atom. The lower *trans*-*cis* isomerization barrier in imines compared to azobenzenes allows for thermal isomerization near room temperature. The imine TBI adsorbed on Au(111) is partially decoupled form the surface by *tert*-butyl substituents. We show that this compound forms two different stable monolayers: an all-*cis* and an all-*trans* layer. The fraction of the two isomers in the layers of TBI on Au (111) depends on the temperature and the coverage. With increasing temperature and decreasing coverage the compound undergoes isomerization from *trans* to *cis* and back to *trans*. The coverage of the various layers was determined by thermal desorption (TD) spectroscopy. The conformation and adsorption geometry of TBI in the layers was determined from NEXAFS measurements. The conformational transitions are driven by the higher packing density of the less stable *cis* isomer. Furthermore, it is found that in the *cis*-form the phenyl ring attached to the N side of the imine bridge is lying flat on the substrate whereas the other ring is lifted.

In the cause of this work, an evaporator for organic molecules was developed. It is extensively characterized in an appendix.

---

[1] 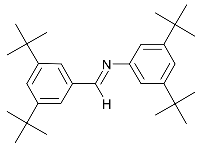

TBI

Zusammenfassung

Photoaktive molekulare Schalter sind eine vielversprechende Gruppe neuer Materialien. In dieser Arbeit wurden zwei verschiedene Arten von auf Oberflächen adsorbierten molekularen Schaltern untersucht: Zum Einen selbstorganisierte Monolagen (SAMs) von Azobenzolen auf Gold sowie auf Gold aufgedampfte (Sub-) Monolagen von (*E*)-3,5-di-*tert*-Butyl-N-(3,5-di-*tert*-butyl-benzyliden)anilin[1].

Azobenzol SAMs Wir haben Azobenzolalkanthiolat SAMs auf Au(111) mittels Röntgennahkantenabsorption (NEXAFS) und Röntgenphotoemissionsspektroskopie (XPS) untersucht und konnten zeigen, dass die Chromophore in diesen SAMs vorwiegend aufrecht orientiert sind. Durch Kombination der Ergebnisse der NEXAFS-Untersuchungen mit Literaturdaten aus AFM/STM-Messungen zur lateralen Struktur konnten wir ein Strukturmodell des SAMs entwickeln. Die optischen Eigenschaften des SAMs wurden mittels UV/Vis-Differenzreflektionsspektroskopie untersucht. Dabei wurde eine starke exzitonische Kopplung der Chromophore in den dicht gepackten SAMs beobachtet. Weiter zeigte sich, dass die *trans–cis*-Photoisomerisation in diesen Schichten, vermutlich auf Grund sterischer Hinderung oder exzitonischer Kopplung, gehemmt ist.

Durch Coadsorption aus Lösung wurden zweikomponentige SAMs hergestellt und ihre Zusammensetzung als Funktion des Verhältnisses der beiden Komponenten in der Lösung mit quantitativem XPS bestimmt. Wir konnten SAMs mit einem beliebigen Verhältnis der beiden Komponeten herstellen und den Zusammenhang zwischen der Zusammensetzung der Lösung und der des SAMs mit einem thermodynamischen Modell beschreiben. Anhand von gemischten SAMs aus zwei verschiedenen Azobenzolchromophoren haben wir die exzitonische Kopplung in einem zweikomponentigen System untersucht.

Um die Photoismerisation in dicht gepackten SAMs zu ermöglichen, haben wir gemischte SAMs aus einem Azobenzolalkanthiolat und einem unsubstituierten Alkanthiolat hergestellt. Dabei wird die Chromophordichte durch die unsubstituierten Alkanthiolate reduziert. Wir konnten zeigen, dass die exzitonische Kopplung von der Chromophordichte abhänging ist und die reduzierte Chromophordichte eine effiziente Photoisomerisation ermöglicht.

TBI Aromatische Imine sind den Azobenzolen ähnlich. Imine besitzen anstelle der N=N-Gruppe der Azobenzole die isoelektrische CH=N-Gruppe, die nur ein einzelnes N-Atom enthält. Die Aktivierungsenergie für die *trans–cis*-Isomerisierung ist in Iminen geringer als in Azobenzolen. Dies ermöglicht eine schnelle thermische Isomerisierung der Imine bei Raumtemperatur. Durch seine *tert*-Butyl-Substituenten ist das Imin TBI teilweise von der Au(111)-Oberfläche entkoppelt. Wir konnten zeigen, dass diese Verbindung auf der Oberfläche zwei unterschiedliche stabile Monolagen ausbilden kann: Eine reine *cis*-Monolage und eine reine *trans*-Monolage. Der Anteil der beiden Isomere in den TBI-Lagen ist von der Temperatur und Bedeckung abhängig. Mit steigender Temperatur und abnehmender Bedeckung erfolgt eine Isomerisierung von *trans* nach *cis* und zurück nach *trans*. Die Bedeckung der verschiedenen Lagen wurde mittels Thermodesorptionsspektroskopie (TDS) bestimmt, die Konformation und die Adsorptionsgeometrie von TBI in den Lagen wurde durch NEXAFS-Messungen bestimmt. Die höhere Packungsdichte des weniger stabilen *cis*-Isomers ist die treibende Kraft der Isomerisierung. Außerdem konnten wir zeigen, dass in der *cis*-Form der Phenylring, der mit dem N-Atom der Imingruppe verbunden ist, flach auf dem Substrat liegt, während der andere Ring absteht.

Im Rahmen dieser Arbeit wurde ein Verdampfer für organische Moleküle entwickelt und ausführlich charakterisiert.

---

[1] 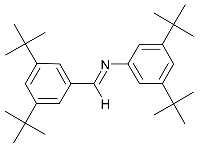

TBI

Selbstständigkeitserklärung

Ich habe alle Hilfsmittel und Hilfen angegeben und versichere auf dieser Grundlage die Arbeit selbstständig verfasst zu haben. Diese Arbeit wurde nicht schon einmal in einem früheren Promotionsverfahren angenommen oder als ungenügend beurteilt.

Daniel Brete

Berlin, den

Publications

1 R. Schmidt, E. McNellis, W. Freyer, D. Brete, T. Gießel, C. Gahl, K. Reuter and M. Weinelt. ‘Azobenzene-functionalized alkanethiols in self-assembled monolayers on gold’. In: *Appl. Phys. A: Mater. Sci. Process.* **92** (2008), 267–275. DOI: `10.1007/s00339-008-4829-z`

2 W. Freyer, D. Brete, R. Schmidt, C. Gahl, R. Carley and M. Weinelt. ‘Switching behavior and optical absorbance of azobenzene-functionalized alkanethiols in different environments’. In: *J. Photochem. Photobiol., A* **204** (2009), 102–109. DOI: `10.1016/j.jphotochem.2009.02.018`

3 C. Gahl, R. Schmidt, D. Brete, E. R. McNellis, W. Freyer, R. Carley, K. Reuter and M. Weinelt. ‘Structure and excitonic coupling in self-assembled monolayers of azobenzene-functionalized alkanethiols’. In: *J. Am. Chem. Soc.* **132** (2010), 1831–1838. DOI: `10.1021/ja903636q`

4 R. Schmidt, S. Hagen, D. Brete, R. Carley, C. Gahl, J. Dokić, P. Saalfrank, S. Hecht, P. Tegeder and M. Weinelt. ‘On the electronic and geometrical structure of the *trans*- and *cis*-isomer of tetra-*tert*-butyl-azobenzene on Au(111)’. In: *Phys. Chem. Chem. Phys.* **12** (2010), 4488–4497. DOI: `10.1039/B924409C`

5 D. Brete, D. Przyrembel, C. Eickhoff, R. Carley, W. Freyer, K. Reuter, C. Gahl and M. Weinelt. ‘Mixed self-assembled monolayers of azobenzene photoswitches with trifluoromethyl and cyano end groups’. In: *J. Phys.: Condens. Matter* **24** (2012), 394015. DOI: `10.1088/0953-8984/24/39/394015`

6 C. Gahl, D. Brete, F. Leyssner, M. Koch, E. R. McNellis, J. Mielke, R. Carley, L. Grill, K. Reuter, P. Tegeder and M. Weinelt. ‘Coverage- and temperature-controlled isomerization of an imine derivative on Au(111)’. In: *J. Am. Chem. Soc.* **135** (2013), 4273–4281. DOI: `10.1021/ja309330e`

7 T. Moldt, D. Brete, D. Przyrembel, S. Das, J. R. Goldman, P. K. Kundu, C. Gahl, R. Klajn and M. Weinelt. ‘Tailoring the properties of surface-immobilized azobenzenes by monolayer dilution and surface curvature’. In: *Langmuir* **31** (2015), 1048–1057. DOI: `10.1021/la504291n`

8 C. Gahl, R. Schmidt, D. Brete, S. Paarmann and M. Weinelt. ‘Charge-transfer dynamics in azobenzene alkanethiolate self-assembled monolayers on gold’. In: *Surface Science* **643** (2016), 183–189. DOI: `10.1016/j.susc.2015.08.028`

9 T. Moldt, D. Przyrembel, M. Schulze, W. Bronsch, L. Boie, D. Brete, C. Gahl, R. Klajn, P. Tegeder and M. Weinelt. ‘The role of adventitious water on the photoisomerization of azobenzene-functionalized self-assembled monolayers’. In: *Phys. Chem. Chem. Phys.* (2016). submitted

Acknowledgement

I thank *Prof. Dr. Martin Weinelt* for the possibility to conduct this work in his research group and for his support and patience. Together with *Dr. Cornelius Gahl* he pursued this project with unrestrained optimism. With their scientific instinct and curiosity they were the source of a never-ending stream of new ideas and cooperations. I am especially indebted to Cornelius. He always took the time it takes to discuss scientific problems in-depth during all stages of this work. His thorough proofreading of this work was also invaluable.

I thank *Prof. Dr. Wolfgang Kuch* for his kind interest in my work and for coassessing this thesis.

The measurements at the synchrotron were a collaborative effort of all who contributed over the years: *Dr. Robert Carley, Dr. Sebastian Hagen, Dr. Cornelius Gahl, Thomas Moldt, Daniel Przyrembel,* and *Dr. Roland Schmidt.*

I want to thank my predecessor *Dr. Roland Schmidt* and my successor *Thomas Moldt.* You were dependable colleagues and good lab mates. The years in which we worked together in the lab were the most productive.

I am indebted to *Daniel Przyrembel*, who did all the XPS measurements with the laboratory X-ray source.

Special thanks go to *Dr. Robert Carley*, who worked very committed with us during several beamtimes even though they were not part of his main project.

Dr. Wolfgang Freyer and *Katrin Herrmann* synthesized many of the azobenzenes investigated in this work. It was Wolfgang's idea to start investigating the optical properties of SAMs and we had many productive discussions on the chemical aspects of the project. During the years at the MBI he supplied me with cake on a regular basis and Katrin—even more regular—provided coffee.

I thank *Dr. Arkadi Rosenfeld*, who allowed us to use his AFM for measurements on gold coated quartz substrates.

Dr. Ying Luo from the group of *Prof. Dr. Rainer Haag* synthesized the compounds TBI and CF_3-ImPh. *Dr. Sebastian Zarwell* from the group of *Prof. Dr. Rück-Braun* synthesized CN-AzPh.

H-Az11 was synthesized in the group of *Dr. Rafal Klajn.* I want to thank him and his group members for the fruitful cooperation.

Dr. Michael Karcher from the group of *Prof. Dr. Fumagalli* spent a lot of time coating many batches of quartz substrates with gold for the UV/Vis transmission mode experiments only briefly mentioned in this work. With his profound knowledge he often was my last resort for questions on mathematical, numerical and instrumental problems.

I have to thank *Dr. Joachim Leistner* from the group of *Prof. Dr. Stefan Hecht* for UPLC/MS measurements, which helped to optimize the preparation of the SAMs.

Dr. Erik McNellis and *Prof. Dr. Karsten Reuter* provided calculations of the electronic structure of the azobenzene derivatives, which were essential for the analysis of the NEXAFS spectra.

I thank *Dr. Felix Leyssner* from the the group of *Prof. Dr. Tegeder* and *Dr. Matthias Koch* from the group of *Prof. Dr. Leonard Grill* for the fruitful cooperation in the TBI project.

During their bachelor theses *Marvin Pohl* contributed to the DR measurements and *Sebastian Kijak* helped to characterize the evaporator for organic molecules.

Dr. Martin Teichmann introduced me to the programming language Python and supported me with advice on numerical and general IT problems.

While we were still at the MBI, our work was supported by *Reinhard Grosser,* who was responsible for the vacuum chamber; *Rainer Schumann* who supported us with urgent supplies and transport; *Roman Peslin,* who machined many parts with outstanding precision, often at short notice; and Kathrein Bäurich, who conducted AFM measurements. I want to thank Reinhard for his dependable service especially during beamtimes and his introduction to vacuum technology and good lab order.

I thank *Dr. Ralph Püttner* for helpful discussions concerning shake-up processes.

I am indebted to *Dr. Matthias Bernien* for many helpful discussions and his help concerning the less documented features of the software Mathematica.

I want to thank all members of the *AG Weinelt* for the pleasant working atmosphere, cross-project help, and moral support.

Finally, I want to thank my parents and friends for their support and patience.